

# Study and characterization of silicon-metal alloy systems for the reactive infiltration process of ceramic matrix composites

THIS IS A TEMPORARY TITLE PAGE  
It will be replaced for the final print by a version  
provided by the service academique.



Thèse n. 8063  
présenté le 2020  
à la Faculté des Sciences de Base  
laboratoire SuperScience  
programme doctoral en SuperScience  
École Polytechnique Fédérale de Lausanne  
pour l'obtention du grade de Docteur ès Sciences  
par

Manoj Naikade

acceptée sur proposition du jury:

Prof. D. Grundler, président du jury  
Dr. L. Weber, Prof. T. J. Graule, directeurs de thèse  
Prof. J.-M. Molina-Jorda, rapporteur  
Dr. A. Passerone, rapporteur  
Prof. V. Michaud, rapporteuse

Lausanne, EPFL, 2020

This page is intentionally left blank.



$$e^{i\pi} + 1 = 0$$

To my grandfather, Kondibhau Ruke...

# Acknowledgements

This thesis work was carried out at the Swiss Federal Laboratories for Materials Science and Technology (Empa), Duebendorf, in the Laboratory for High Performance Ceramics, in collaboration with the École Polytechnique Fédérale de Lausanne (EPFL) and the Institute for Mechanical Engineering and Materials Technology, University of Applied Sciences and Arts of Italian Switzerland (SUPSI).

I am sincerely grateful for the opportunity and continual support and guidance of Prof. Thomas Graule and Prof. Alberto Ortona. I am forever grateful to my thesis director at EPFL, Dr. Ludger Weber, for his encouragement, advice and critical feedback on my dissertation.

Thank you to Dr. Beate Fankhanel, TU Bergakademie Freiberg, Germany for helping in conducting the sessile drop experiments. Thank you to Dr. Rolf Brönnimann for helping with laser ablation; Dr. Annapaola Parrilli, Bekmurza Beisenov, Mahdiah Shakoorioskooie and Rolf Kaufmann, for helping with X-ray analysis in Empa. Thank you to Viktor Lindström and Toni Ivas for helping with the induction furnace. Thank you to Giovanni Bianchi and Luca Cornolti from SUPSI for their support in the work.

I am delighted to have the opportunity to supervise two master students, Caroline Hain and Kaja Kastelik, and I am very grateful for their contribution to this study.

I am pleased to have shared the office space with Tutu Sebastian, Laura Conti, and Hans Jürgen Schindler and am grateful for their support for my experimental work. Thank you, Georgiana Schönberg, for being a great secretary of the lab and easing administrative work.

I am grateful to both my present and former colleagues who have made my stay at Empa cheerful. Thank you to Caroline Durif, Clark Ligon, Domenico Regonini, Eleni Mitrensis, Frank Clemens, Gurdial Bulgan, Gustavo Mata Osoro, Jakob Kübler, Jon Bell, Liliya Vladislavova, Lovro Gorjan, Mark Melnykowycz, Martin Michalek, Michael Stuer, Monika Michalkova, Paulina Ozog, Roland Bächtold, Roman Kubrin, Tony Lusiola, Yang Liu and Yujing Liu.

A special thank you to Amit Korde and Pratyuksh Bansal for proofreading my text. A huge thank you to my dear friends who have kept me inspired on this journey, Paulina Zubrzycka, Punam Sonar, Pradip Zamre, Nur Sena Yuzbasi, Alexandre Guiller, Tutu Sebastian, Pradeep

## Acknowledgements

---

Vallachira, Stefan Pfeiffer, Aniket Mule, Jagannath Biswakarma, Navanshu Ahuja, Wasif Khan, Aditya Burgute and Akshay Natraj.

I am very grateful for the immense support and love of my parents, Mangal and Kondibhau Naikade, my brother Prakash and sister Manisha, my uncle Datta Ruke and last but not least my girlfriend Katrin and her parents Emil and Pauline Fischer.

Finally, I would like to thank the Swiss National Science Foundation (SNSF) for financially supporting the project (Grant number: 163017), the jury members, Prof. em. Dr. Alberto Passerone, Prof. José-Miguel Molina-Jorda and Prof. Véronique Michaud for assessing this work and Prof. Dr. Dirk Grundler for accepting to be the president of the jury.

*Dübendorf, 25 November 2020*

Manoj Naikade

# Abstract

Silicon infiltrated silicon carbide (SiSiC) is one of the most promising and economical non-oxide ceramic matrix composites for high-temperature structural applications. In recent years infiltration by Si-alloys instead of pure Si has become popular to avoid the presence of residual pure Si by replacing it by higher melting silicides. Apart from this beneficial aspect of using Si-alloys, the downsides and limitations have not received much attention and are hence not well understood.

The thesis aims at developing a fundamental understanding of the reactive infiltration of carbonaceous preforms by molten Si-X alloys in general. This is achieved by developing analytical models and designing experiments to individually study various factors like wettability, porosity and pore size distribution, alloy composition, and the preform composition. The near eutectic binary Si-Zr system is used to perform experiments to observe the conjectured phenomena.

Firstly, the wettability of the vitreous C and SiC by Si and Si-8 at. pct Zr alloy was investigated at 1500 °C under static Ar and vacuum environment using the classical sessile drop technique. Both Si and Si-8 at. pct Zr alloy showed good wettability on C and SiC substrates with equilibrium contact angles ranging between 29° and 39°. The measurement of the contact angle and the microstructure of the interface between the liquid droplet and solid surface were studied to understand the fundamental features pertaining to the infiltration process of Si and Si-8 at. pct Zr alloy in carbonaceous C/C or C/SiC preforms. The Si-8 at. pct Zr alloy has a higher initial contact angle and somewhat slower spreading rate compared to Si. The reaction-formed SiC layer was observed on vitreous C with a maximum thickness of ~ 5 µm for both Si and Si-8 at. pct Zr. SiC was observed to be non-reactive to both Si and Si-8 at. pct Zr alloy.

An analytical model for the adequate preform porosity to obtain fully dense SiC composites by infiltration of Si-alloys was formulated for silicide forming alloying elements in general and applied to the Si-Zr binary alloys. The adequate initial pore fraction of the preform increases with the increasing Zr concentration and depends on the C fraction in C/SiC preform. The model gives the range of preform porosity for a given alloy and preform composition resultant silicide phase propensity (in the present case: SiZr or Si<sub>2</sub>Zr) for which volume conservative

reaction transformation is possible.

Early experimental observations suggested that by replacing Si with a Si-alloy with silicide forming elements, the infiltration depth could be substantially limited. This limitation was associated with significant enrichment of silicide forming elements at the infiltration front. We propose the gradual enrichment of silicide forming element at the infiltration front as another process limiting mechanism, different from the well established pore closure at the entrance to the porous preform by excessive carbide formation. This enrichment in silicide forming elements comes by due to the continuous consumption of Si to form SiC at the infiltration front and the concomitant accumulation of the silicide formers in the liquid. An analytical model to obtain the infiltration length in microchannels as well as porous C/SiC preform was developed based on this critical phenomenon of infiltration channel obstruction by the premature formation of solid silicides at the infiltration front. The model reflects all characteristic parameters of the infiltration process, i.e., the temperature, the concentration of silicide former in the initial alloy, the rate of ingress, the composition and size of the particles constituting the preform. The model shows that the Infiltration length decreases with an increasing initial concentration of the silicide forming alloying element and with increasing processing temperature.

Micron-sized glassy C capillaries ranging from 10  $\mu\text{m}$  to 100  $\mu\text{m}$  in thickness manufactured using laser ablation were infiltrated by Si and Si-8 at. pct Zr alloy at 1500  $^{\circ}\text{C}$  and 1700  $^{\circ}\text{C}$  to study the infiltration kinetics as well as the infiltration limiting phenomena. The study showed that to observe the pore closure phenomenon due to the formation of SiC at the entrance to the pore volume with pure Si microchannel with a thickness even lower than 10  $\mu\text{m}$  is needed. In the case of Si-8 at. pct Zr alloy, the pore closure at the entrance was also not observed, but we were able to give evidence of pore-clogging resulting from the Zr enrichment at the infiltration front, ultimately resulting in the precipitation of solid Zr silicides at the infiltration front that blocked the further flow of the alloy.

Finally, C/C and C/SiC performs with various sizes and fraction of graphite powder were infiltrated by Si and Si-8 at. pct Zr alloy at 1500  $^{\circ}\text{C}$  and 1700  $^{\circ}\text{C}$  to make the composites. The porosity of the preforms was analyzed by mercury porosimetry and X-ray computer tomography. It was observed that C/C preforms made from graphite powder having  $d_{90} \geq 44 \mu\text{m}$  can be infiltrated to the whole thickness of approximately 5 mm by Si-8 at. pct Zr alloy, but the residual graphite is unavoidable and C/C preforms were more prone to cracking. The Si-8 at. pct Zr alloy infiltrated C/SiC preforms did not show any cracking. The preforms made from graphite powder with  $d_{90} = 25 \mu\text{m}$  and  $d_{90} = 44 \mu\text{m}$  and graphite mass fraction between 15 and 20 % with a modal pore size of approximately 7  $\mu\text{m}$  resulted in negligible porosity composites. The increase in infiltration temperature to 1700  $^{\circ}\text{C}$  reduced the infiltration length for the C/SiC preforms with a graphite mass fraction of more than 20 % and increased residual porosity in qualitative agreement with the proposed model.

**Keywords:** Silicon carbide, SiC composites, LSI, SiSiC, reactive alloy infiltration, Si-Zr-SiC composites, CMC, ceramic matrix composites

This page is intentionally left blank.

# Contents

<b>Acknowledgements</b>	<b>i</b>
<b>Abstract</b>	<b>iii</b>
<b>List of Figures</b>	<b>xi</b>
<b>List of Tables</b>	<b>xix</b>
<b>1 Introduction</b>	<b>1</b>
<b>2 Theory and related literature</b>	<b>5</b>
2.1 Ceramic matrix composite . . . . .	5
2.1.1 Non-oxide ceramics as the matrix phase . . . . .	6
2.2 Silicon carbide . . . . .	6
2.2.1 Structure of silicon carbide . . . . .	7
2.2.2 Types of silicon carbide ceramics . . . . .	7
2.3 Silicon infiltrated silicon carbide . . . . .	9
2.4 Silicon alloys infiltrated silicon carbide . . . . .	10
2.5 Thermophysical and physicochemical properties of Si . . . . .	16
2.5.1 Oxidation behavior of Si . . . . .	17
2.5.2 Surface tension of Si . . . . .	19
2.5.3 Viscosity of Si . . . . .	21
2.6 Wetting at high temperature . . . . .	24
2.6.1 Sessile drop technique . . . . .	24
2.6.1.1 Other parameters obtained from sessile drop experiments . . . . .	26
2.6.2 Reactive wetting of carbon by Si . . . . .	27
2.6.3 Wetting of SiC by Si . . . . .	32
2.6.4 Kinetic aspect of reactive infiltration . . . . .	33
2.7 The Si-Zr alloy system . . . . .	36
2.8 The C-Si-Zr ternary system . . . . .	38
2.9 Conceptual considerations . . . . .	38
2.9.1 Preform composition . . . . .	38
2.9.2 The use of Si alloys as infiltrants . . . . .	39
2.9.3 Kinetic considerations . . . . .	41
	vii



2.10 Research objectives . . . . .	43
<b>3 Materials and methods</b>	<b>47</b>
3.1 Materials . . . . .	47
3.1.1 Glassy carbon plate . . . . .	47
3.1.2 Silicon . . . . .	47
3.1.3 Si-Zr alloy . . . . .	47
3.1.4 Graphite and SiC powders . . . . .	48
3.1.5 Binder and pore forming agent . . . . .	49
3.1.6 Crucibles . . . . .	49
3.2 Experimental methods . . . . .	50
3.2.1 Sessile drop experiment . . . . .	50
3.2.2 Single capillary microchannel infiltration experiment . . . . .	52
3.2.2.1 Fabrication of microchannel capillaries . . . . .	52
3.2.2.2 Experimental setup . . . . .	53
3.2.2.3 Analysis of the microchannels . . . . .	55
3.2.3 Preform infiltration experiments . . . . .	56
3.2.3.1 Powder mixing and characterization . . . . .	56
3.2.3.2 Fabrication of preforms . . . . .	56
3.2.3.3 Preform characterization . . . . .	57
3.2.3.4 Infiltration setup . . . . .	57
3.2.3.5 Analysis of infiltrated sample . . . . .	58
<b>4 Wetting behavior of Si and Si-Zr alloy on C and SiC</b>	<b>61</b>
4.1 Disclaimer . . . . .	61
4.2 Abstract . . . . .	61
4.3 Introduction . . . . .	61
4.4 Experimental procedure . . . . .	63
4.5 Results . . . . .	64
4.5.1 Surface roughness . . . . .	64
4.5.2 Contact angles under vacuum . . . . .	64
4.5.3 Contact angles under an argon atmosphere . . . . .	65
4.5.4 SEM and EDX analysis . . . . .	66
4.6 Discussion . . . . .	67
4.6.1 Si evaporation in vacuum . . . . .	67
4.6.2 Formation SiC layer before formation of droplet . . . . .	70
4.6.3 Oxidation at liquid surface in Ar atmosphere . . . . .	71
4.6.4 Equilibrium contact angle . . . . .	72
4.6.5 Reaction mechanism at interface . . . . .	73
4.7 Conclusion . . . . .	73
4.8 Outlook . . . . .	74
4.9 Acknowledgment . . . . .	74

<b>5</b>	<b>Analytical modelling pertaining to LSI issues</b>	<b>75</b>
5.1	Ideal preform porosity to obtain fully dense composites . . . . .	75
5.2	Detailed calculation of the phases present . . . . .	80
5.3	Modelling pore clogging in a single carbon microchannel . . . . .	84
5.3.1	Development of the model . . . . .	85
5.3.2	Implications of the model . . . . .	88
5.4	Extension of the model to preform infiltration . . . . .	89
5.4.1	Accounting for arbitrary capillary shape . . . . .	90
5.4.2	Accounting for the presence of SiC particles . . . . .	91
5.4.3	Changes to the guiding equations . . . . .	91
5.4.4	The equivalent pore radius of the preform . . . . .	91
5.4.5	Implication of the model to preform infiltration . . . . .	92
5.5	Differential model for non-isothermal infiltration experiments . . . . .	93
5.5.1	Formulation of the model . . . . .	94
5.5.2	Limits of the differential model . . . . .	97
<b>6</b>	<b>Kinetics of reactive flow of Si and Si-Zr alloy in carbon capillaries</b>	<b>101</b>
6.1	Disclaimer . . . . .	101
6.2	Abstract . . . . .	101
6.3	Introduction . . . . .	101
6.4	Materials and Methods . . . . .	103
6.4.1	Material . . . . .	103
6.4.2	Fabrication of microchannels . . . . .	103
6.4.3	Infiltration setup . . . . .	103
6.4.4	Analyses . . . . .	104
6.5	Results and discussion . . . . .	105
6.5.1	Surface roughness . . . . .	105
6.5.2	Microchannel characterization . . . . .	106
6.5.2.1	Configuration A . . . . .	106
6.5.2.2	Configuration B . . . . .	108
6.5.2.3	Configuration C . . . . .	108
6.5.2.4	Configuration D . . . . .	110
6.5.3	The morphology of reaction layer between silicon and vitreous carbon . . . . .	113
6.5.4	Interpretation of pore closure in Si vs Si-Zr alloy infiltration . . . . .	115
6.6	Conclusion . . . . .	122
<b>7</b>	<b>Reactive infiltration of C/C and SiC/C preforms</b>	<b>123</b>
7.1	Disclaimer . . . . .	123
7.2	Abstract . . . . .	123
7.3	Introduction . . . . .	123
7.4	Materials and methods . . . . .	125
7.4.1	Materials . . . . .	125
7.4.2	Manufacturing of porous preforms . . . . .	125

## Contents

---

7.4.2.1	Powder mixing . . . . .	125
7.4.2.2	Cold pressing of preforms . . . . .	126
7.4.2.3	Hot pressing of preforms . . . . .	126
7.4.2.4	Pyrolysis of preforms . . . . .	126
7.4.3	Infiltration setup . . . . .	127
7.4.3.1	Furnace equipment . . . . .	127
7.4.3.2	Graphite foil crucibles . . . . .	127
7.4.4	Analyses . . . . .	129
7.5	Results . . . . .	129
7.5.1	Particle size and density of powders . . . . .	129
7.5.2	Porosity and pore size distribution by mercury intrusion porosimetry (MIP)	132
7.5.3	Porosity and pore size distribution by X-ray CT . . . . .	134
7.5.4	Infiltration of C-C preforms with near eutectic Si-Zr alloy . . . . .	136
7.5.5	Infiltration of SiC-C preforms with near eutectic Si-Zr alloy . . . . .	138
7.6	Discussion . . . . .	143
7.6.1	Infiltration of the C-C preforms . . . . .	144
7.6.2	Infiltration of the SiC-C preforms . . . . .	146
7.6.3	Banding of the Zr-rich phase . . . . .	150
7.7	Conclusion . . . . .	153
<b>8</b>	<b>Conclusion</b>	<b>155</b>
8.1	Conclusions from this work . . . . .	155
8.2	Outlook . . . . .	157
<b>A</b>	<b>Python codes</b>	<b>161</b>
	<b>Bibliography</b>	<b>185</b>
	<b>Curriculum Vitae</b>	<b>187</b>

# List of Figures

2.1	Weight-specific tensile strength of various classes of materials as a function of temperature [3]. . . . .	6
2.2	Crystal structures for the four most commonly occurring SiC polytypes: (a) 3C, (b) 4H, (c) 6H and (d) 15R. Si atoms in red and C atoms in black (reproduced from [24]). . . . .	8
2.3	Mo-Si phase diagram [71], showing the change of concentration of Mo in different scenario (1) adiabatic SiC formation (2) in real practice situation with heat dissipation (image reproduced from [66]). . . . .	12
2.4	Infiltration depth of Zr as a function of annealing temperature and time (reproduced from [80]). . . . .	15
2.5	Schematic representation of the passive-to-active transition of Si at constant temperature $T$ . (a) the Si/silica/gas three-phase equilibrium at $P_{O_2}^f = P_{O_2}^{f*}$ (b1) , the Si surface is skin free but contains adsorbed oxygen at $P_{O_2}^{f_0} < P_{O_2}^f < P_{O_2}^{f*}$ (b2) a clean, adsorption-free surface is obtained at $P_{O_2}^f < P_{O_2}^{f*}$ (c) Si is oxidized at $P_{O_2}^f > P_{O_2}^{f*}$ (reproduced from [90]). . . . .	18
2.6	The curve (a) represents the variation of the critical partial pressure of oxygen in the furnace ( $P_{O_2}^{f*}$ ) with temperature. The region above the curve defines the passive oxidation state while the one below defines the active oxidation state. The curve (b) represents the variation of the critical partial pressure of oxygen at the Si surface corresponding to Si/silica/gas three-phase equilibrium. $T_{Si}^F$ is the melting point of Si (reproduced from [90]). . . . .	19
2.7	Variation in the equilibrium partial pressure of oxygen at the skin free surface of Si, $P_{O_2}^S$ as a function of the partial pressure of oxygen in the furnace $P_{O_2}^f$ (reproduced from [90]). . . . .	20
2.8	Surface tension of molten Si as a function of partial pressure of oxygen at various temperature [110]. . . . .	22
2.9	Schematic representation of the oscillating viscometer (reproduced from [113]).	23
2.10	Viscosities of molten silicon at different temperature obtained for various materials of crucibles (reproduced from [113]). . . . .	24
2.11	Schematic of liquid droplet on solid substrate showing a non-wetting system on the left and a wetting system on the right. . . . .	25

## List of Figures

2.12 Schematic representation of the melting process of silicon and its spreading on the graphite substrate. (a) before melting, (b) start of melting, (c) during melting, (d) complete melting, (e) during spreading, and (f) stabilization (reproduced from [120]). . . . .	25
2.13 Methods of conducting sessile drop experiments: (a) classical technique, (b) in situ alloy formation, (c) dispensed drop, (d) transferred drop, (e) transferred drop, (f) tilted plate (figure reproduced from [119]). . . . .	27
2.14 SEM micrograph of the reacted interface for a silicon/vitreous carbon couple after 10 min at 1430 °C: (a) at the centre of the interface (equiaxed zone) and (b) in the periphery (columnar zone) [136]. . . . .	29
2.15 Mechanisms at the infiltration front in carbon channel divided in zones I to III. - 1: Si evaporation and diffusion, 2: Si adsorption and nucleation on the C substrate, 3: crystal growth by transversal movement of the two dimensional gas of the impinging Si atoms to the edges of the SiC islands, 4: island growth (Volmer–Weber growth), 5: coalescence of the islands to a continuous SiC layer, 6: partial flaking of the SiC crystals, 7: remaining SiC layer acts as a diffusion barrier, 8: Carbon diffusion along the SiC grain boundaries, 9: pore formation in the SiC layer, 10: silicon diffusion along the SiC grain boundaries (reproduced from [141]). . . . .	31
2.16 The stages of the interaction between molten Si on SiC. The furnace's atmosphere is a source of carbon (figure reproduced from [150]). . . . .	33
2.17 Cross-section of infiltrated channel of diameter 0.5 mm with a dwell time of 24 h at 1450°C. The circle represented with a solid line indicates the initial diameter. The process of C dissolution leads to an increase of the diameter by $9.2 \pm 4 \mu\text{m}$ on average (before $516 \pm 3 \mu\text{m}$ ) [154]. . . . .	34
2.18 Growth of SiC layer at the graphite wall in a Si-Y alloy infiltrated sample after (A) 1 minute, (B) 5 minutes, (C) 10 minutes, (D) 30 minutes, and (E) 180 minutes of reaction time. (figure reproduced from [75]). . . . .	35
2.19 Calculated binary phase diagram of Si and Zr using THERMOCALC. (Thermodynamic database file provided by Chen, H. M., School of Material Science and Engineering, Central South University, China.) . . . . .	37
2.20 Calculated phase diagram of the Si – Zr binary system with experimental data (reproduced from [156]). . . . .	37
2.21 Calculated isothermal section of C–Si–Zr at 1473K with experimental data [161] (reproduced from [160]). . . . .	38
2.22 Example of the desired resultant composition (highlighted in light blue color in Si-Zr equilibrium phase diagram ) of the infiltrant after the reaction with preform, which is beyond the composition where the first silicide is formed. . . . .	40
2.23 Schematic of two limiting cases of Si ingress in C capillary with radius $R$ are triple line controlled characterize by contact angle greater than equilibrium contact angle (left) and viscosity controlled ingress characterized by reaction front being always ahead of the meniscus of Si (right). . . . .	41

2.24	Separation of the parameter space $R, L$ into triple-line reaction controlled (blue) and viscosity controlled combinations (red). The gravity limit indicates the possible filling height at which metallostatic forces equilibrate the capillary forces, which of course depends on the density, the surface tension and the contact angle. . . . .	43
2.25	The quasi-binary cut through the ternary Si-Zr-O system to illustrate that the Zr does not lower the melting temperature of $\text{SiO}_2$ significantly resulting in poor ablation properties. . . . .	44
3.1	The composition of the Si-8 at. pct Zr alloy analyzed with XRD. . . . .	48
3.2	SEM image of (a) TIMREX KS44 graphite particle showing flaky shape particles and (b) SiC F800 showing angular shape particles. . . . .	49
3.3	A custom made alumina tube furnace used for sessile drop experiments showing its major component 1:lights for back illumination, 2: glass sealing window and valves for vacuum and air, 3: alumina tube, 4: turbo molecular pump, 5: insulation, 6: glass sealing window and ND filter, 7: digital camera, 8: furnace controller 9: computer to record images. . . . .	51
3.4	A glassy carbon plate with three laser ablated microchannels with different shapes, and on right are two glassy carbon plates clamped together to make a capillary channel. . . . .	53
3.5	Various configurations of microchannels to achieve different depth, length and tortuosity of the channels. . . . .	54
3.6	Experimental setup used to keep the glassy carbon microchannel upright and infiltrate with Si / near eutectic Si-Zr alloy. . . . .	55
3.7	Crucible setup for the infiltration process; a) graphite foil crucible coated with a BN from inside and a graphite foil cylinder as a wick in the center, b) Si-Zr alloy shards placed into the crucibles, c) placing preform disc on a graphite foil wick. . . . .	58
3.8	Schematics of two alternative crucible setup for the preform infiltration experiments; (a) single use graphite foil (b) multi use graphite crucible coated with BN and graphite foil lining. . . . .	58
4.1	Schematic of metal droplet on substrate placed in a tube furnace with both sides covered by glass to observe and measure the contact angle using a digital camera. . . . .	63
4.2	Development of the contact angle, diameter and height of the droplet of (a) silicon on vitreous carbon (b) $\text{Si}_{0.92}\text{Zr}_{0.08}$ alloy on vitreous carbon (c) silicon on SiC (d) $\text{Si}_{0.92}\text{Zr}_{0.08}$ alloy on SiC with changing temperature and vacuum pressure. . . . .	66
4.3	Development of the contact angle, diameter and height of the droplet of (a) silicon on vitreous carbon (b) $\text{Si}_{0.92}\text{Zr}_{0.08}$ alloy on vitreous carbon (c) silicon on SiC (d) $\text{Si}_{0.92}\text{Zr}_{0.08}$ alloy on SiC with changing temperature and Ar pressure. . . . .	67

## List of Figures

4.4	SEM images of the cross section of (a), (b) the solidified silicon droplet (gray) on vitreous carbon (black) with the visible SiC reaction layer formed at the pure silicon-carbon interface, (c), (d) the solidified $\text{Si}_{0.92}\text{Zr}_{0.08}$ droplet on vitreous carbon (black), exhibiting needle-shaped Si-Zr phase in silicon and the SiC reaction layer formed at the interface. . . . .	68
4.5	SEM images of the cross section of (a), (b) solidified silicon droplet on the SiC substrate showing no reaction layer and slight erosion at interface, (c), (d) the solidified $\text{Si}_{0.92}\text{Zr}_{0.08}$ alloy on the SiC substrate exhibiting needle-shaped Si-Zr phase and slight erosion at the interface. . . . .	68
4.6	EDX analysis of the interface of (a), (b) solidified silicon droplet on the vitreous carbon substrate showing a SiC layer at the Si/C interface, (c), (d) solidified $\text{Si}_{0.92}\text{Zr}_{0.08}$ droplet on the vitreous carbon substrate showing a SiC layer at the C/Si-Zr eutectic phase interface. . . . .	69
4.7	EDX analysis of the interface of (a), (b) solidified silicon droplet on the SiC substrate showing no reaction layer at the Si/SiC interface, (c), (d) solidified $\text{Si}_{0.92}\text{Zr}_{0.08}$ droplet on the SiC substrate showing no reaction layer at the SiC/Si-Zr eutectic phase interface. . . . .	69
4.8	Solidified droplet of Si-Zr alloy on (a) C substrate (b) SiC substrate showing condensed Si near the outside edge of the droplet. . . . .	70
4.9	Schematic of condensation of Si from the surface of metal sample on the C substrate to form thin SiC layer and solid state diffusion through the surface of substrate where metal sample is in contact. . . . .	71
4.10	Silicon droplet on vitreous carbon at 1500 °C, (a) contact angle 40°, (b) pseudo decrease in contact angle to 33° due to evaporation. . . . .	71
4.11	Silicon droplet layer on SiC at 1500 °C with a non-spherical surface due to formation of a solid oxide layer on the surface. . . . .	72
5.1	Evolution of the ideal pore volume fraction with infiltrant concentration in silicide forming element, in the case shown for a preform made of 70 g SiC powder, 20 g graphite and initially 10 g of phenolic resin that after pyrolysis results in 6 g of amorphous carbon. . . . .	80
5.2	Schematic of the carbon microchannel with rectangular cross section <i>we</i> filled with the liquid Si-Zr alloy to a length <i>L</i> . The quantity of silicon atoms, $n_{\text{Si}}$ , that have been consumed so far by the formation of SiC corresponds to a volume of length, $\lambda$ , taking into account the initial concentration of Si, $c_{\text{Si}}$ , and the molar volume. The quantity of zirconium atoms, $n_{\text{Zr}}$ , in that same volume are rejected into the liquid behind and diluted in a volume of length, $\delta$ , that corresponds to the diffusion length. . . . .	85
5.3	Infiltration length calculated using Equation (5.56) for a carbon microchannel with a rectangular cross section and of thickness of 10 $\mu\text{m}$ (a) with increasing temperature, infiltrated by Si-8 at. pct Zr alloy (b) infiltration length as function of initial Si fraction at 1500 °C. . . . .	89

5.4	Schematic representation of the infiltration in a real preform. The infiltration velocity, $v_{inf}$ , is no longer equal to the triple line velocity as in the microchannel model. . . . .	90
5.5	Infiltration length calculated using Equation (5.59) for a SiC-C preform having $R^* = 0.5 \mu\text{m}$ (a) with increasing temperature, infiltrated by Si-8 at. pct Zr alloy (b) with increasing Si fraction infiltrated at $1500^\circ\text{C}$ . . . . .	93
5.6	Evolution of infiltration length, $L$ , and temperature in a non-isothermal infiltration experiment of a Si-8 at.-pct Zr alloy into a microchannel of $10 \mu\text{m}$ thickness. At the beginning the infiltration accelerates since the reaction at the triple line is thermally activated. The change in slope in the green region comes by since the clogging condition $c_{Si} < c_{Si,crit}$ is reached but continuously alleviated by the diffusion of Si to the triple line. After having reached the maximum temperature, the triple line velocity stagnates, yet remains controlled by the Si diffusion regime. In the red domain the triple line is stalled due to solidification of the alloy. . . . .	96
5.7	Evolution of infiltration length, $L$ , and temperature in a non-isothermal infiltration experiment of a Si-8 at.-pct Zr alloy into a microchannel of $10 \mu\text{m}$ thickness. As in the example at $1500^\circ\text{C}$ the infiltration accelerates in the beginning due to thermal activation. The change in slope in the green region comes by since the clogging condition $c_{Si} < c_{Si,crit}$ is reached but continuously alleviated by the diffusion of Si to the triple line. At the peritectic temperature, the critical silicon concentration takes a jump and the triple line is again at its unconstrained speed. After having reached the maximum temperature, the triple line velocity stagnates, yet remains controlled by the Si diffusion regime. . . . .	97
5.8	Evolution of infiltration length, $L$ , with the differential scheme developed for the non-isothermal case applied to the isothermal case by setting the heating rate to 0 and the starting temperature to the isothermal temperature. . . . .	98
6.1	Various configurations of microchannels with their dimensions used in this research. Length indications are in mm. . . . .	105
6.2	Schematic of capillary microchannel assembly by clamping vitreous carbon plate with laser ablated groove together with another vitreous carbon plate. Length indications are in mm. . . . .	106
6.3	Experimental setup of infiltration showing microchannel made by clamping vitreous carbon plates being kept upright by graphite brackets in the graphite crucible. The melting Si or Si-Zr alloy was kept in the BN coated graphite foil crucible in the center. . . . .	106
6.4	Radiograph of microchannels in configuration A showing complete infiltration of all the channels. . . . .	108



## List of Figures

6.5	(a) SEM image showing a cross-section of 1 mm by 0.1mm microchannel infiltrated at 1500 °C in the sample with a grid for reaction layer's thickness measurements (b) Reaction layer thickness along the infiltration length at 15, 25 and 35 mm from the bottom for all 4 channels divided into the left edge (L), middle (M) and right edge (R) and top and bottom laser ablated plate infiltrated by pure Si.	109
6.6	Radiograph of microchannels of configuration B after infiltration by near eutectic Si-8 at-pct Zr alloy. . . . .	110
6.7	SEM image of cross section of 1 mm x 0.025 mm microchannel at 20 mm from the bottom. The lighter part in the middle is Zr rich phase while the reaction layer is mainly SiC with some trapped Zr. . . . .	110
6.8	(a) Radiograph of microchannels of configuration – C after infiltration by near eutectic Si-8 at-pct Zr alloy (b) Phase fraction analysis of 0.01 mm section of the gradient channel. The black fraction represents the Zr-rich phase. . . . .	111
6.9	Radiographs of two samples D1 and D2 after infiltration by Si-8 at-pct Zr alloy at 1500 °C. . . . .	112
6.10	Radiograph of sample D3 showing complete infiltration by pure Si at 1500 °C. .	112
6.11	Radiograph of sample D4 infiltrated by Si-8 at-pct Zr alloy at 1700 °C showed closure of the microchannel at 322 mm. . . . .	112
6.12	BSE image of Si infiltrated 1mm by 0.1mm microchannel sample of configuration –A taken at 15mm from bottom. . . . .	113
6.13	SEM analysis of the reacted interface between silicon and vitreous carbon at 1500 °C, 1 mm x 0.025 mm microchannel sample of configuration A. . . . .	114
6.14	Silicon concentration profile across the reaction zone formed between silicon and vitreous carbon. . . . .	115
6.15	Infiltration length as a function of the initial concentration of Si in the alloy for microchannels with depth $e = 10\mu\text{m}$ and $e = 15\mu\text{m}$ . . . . .	117
6.16	The infiltration length achieved with increasing temperature for the microchannel depth $e = 10\mu\text{m}$ and $e = 15\mu\text{m}$ infiltrated with an Si-Zr alloy with an initial atomic concentration of Si $c_{Si,0} = 0.92$ . . . . .	118
6.17	SEM image of cross section taken at 5 mm from the exit end of 0.01 mm deep microchannel infiltrated with pure Si. . . . .	120
6.18	Si-Zr phase diagram reproduced in Thermocalc using data from [156] showing the alloy composition shift as the alloy flows through microchannel at 1500 °C by a solid arrow and at 1700 °C by a dotted arrow. . . . .	120
6.19	BSE image of the cross section of sample D1, infiltrated at 1500 °C (a) the region near the inlet of the microchannel showing SiC reaction layer and in the middle Si and $\text{ZrSi}_2$ (b) the clogging region showing SiC at the interface and solidified $\text{ZrSi}_2$ in the channel. . . . .	121
6.20	BSE image of the cross section of sample D2, infiltrated at 1500 °C at the end of clogging region with EDX analysis at various points with different contrast. . .	121
6.21	BSE image of the cross section of sample D4, infiltrated at 1700 °C at the end of clogging region with EDX analysis at various points with different contrast. . .	121

7.1	Heating programs used for pyrolysis of the preforms. . . . .	127
7.2	Schematic of heating program used for the reactive melt infiltration process. . .	128
7.3	Schematic of preform infiltration setup using (a) graphite foil crucible (b) graphite crucible with graphite foil lining having inner walls coated with BN. . . . .	128
7.4	SEM images of the TIMREX KS 44 graphite powder (left) and SiC F800 powder (right) showing their flaky and angular shape, respectively. . . . .	129
7.5	The particle size distribution of SiC F800 and TIMREX KS25 powders and their mixtures listed in Table 7.2 as analyzed by laser diffraction. . . . .	131
7.6	The particle size distribution of SiC F800 and TIMREX KS44 powders and their mixtures listed in Table 7.2 as analyzed by laser diffraction. . . . .	132
7.7	Example of the pore size distribution measured via MIP (a) the C-C preform made up of graphite powder TIMREX KS 10 mix pressed at 110 kN and pyrolysed at 1000 °C (b) the SiC-C preform made from powder mix of SiC and C. . . . .	133
7.8	Median pore size and total percentage porosity measure by Hg intrusion with increasing graphite fraction for SiC-C preforms. . . . .	134
7.9	Pore size distribution of SiC-C preforms measured by X-ray CT data for preforms made with mixture of SiC powder and (a) TIMREX KS25 and (b) TIMREX KS44 graphite powder. . . . .	135
7.10	Modal pore size and total porosity of SiC-C preforms with increasing graphite fraction as measured by X-ray CT analysis. . . . .	135
7.11	Preform made with the powder mix C-C_01 at 110 kN pressing force after infiltration (a) bottom surface (b) cross section (c) SEM image of the cross section at the surface where the infiltrating alloy first gets in contact. The arrow indicates the direction of the infiltration. . . . .	136
7.12	Preforms made up from TIMREX KS44 powder showing cracking after infiltration preforms pressed at (a) 90 kN (b) 110 kN force. . . . .	136
7.13	SEM image of the preform made from TIMREX KS44 graphite powder after infiltration showing cracked sample after infiltration. The arrow at the bottom indicates the direction of the infiltration. . . . .	137
7.14	Sample after infiltration of preforms made from TIMREX KS75 powder showing (a) complete infiltration in cross-section with few cracks (b) SEM image showing complete infiltration along the thickness and gradient structure of Zr rich bright phase. The arrow at the bottom indicates the direction of the infiltration. (c) SEM image with higher magnification showing unreacted graphite, SiC, Zr silicide and Si. . . . .	137
7.15	The high resolution SEM images stitched to together to make panorama of the cross section of the SiC-C preforms with increasing mass fraction of TIMREX KS25 graphite powder from 5 to 30 % and infiltrated by near eutectic Si-Zr alloy at 1500 °C. A magnified portion is shown at the bottom marked by red rectangle to illustrate the observed porosity. . . . .	140

## List of Figures

---

7.16 The high resolution SEM images stitched to together to make panorama of the cross section of the SiC-C preforms with increasing mass fraction of TIMREX KS25 graphite powder from 20 to 30 % and infiltrated by near eutectic Si-Zr alloy at 1700 °C. . . . .	141
7.17 The high resolution SEM images stitched to together to make panorama of the cross section of the SiC-C preforms with increasing mass fraction of TIMREX KS44 graphite powder from 20 to 30 % and infiltrated by near eutectic Si-Zr alloy at 1500 °C. . . . .	141
7.18 XRD analysis of SiC/C preforms after infiltration at 1500 °C and 1700 °C showing major phases observed, which were C, Si, Si <sub>2</sub> Zr and some unidentified impurity phases containing Hf, Al and Fe. . . . .	143
7.19 Schematic representation of types of pores (reproduce from [190]). . . . .	144
7.20 Adequate porosity of a C/C preforms with increasing Zr concentration is plotted using Equation (5.19). . . . .	145
7.21 Theoretical initial adequate porosity of the SiC/C preforms with varying graphite fractions to obtain fully dense preforms without residual Si or unreacted C and given silicide phase. Above the line one would expect to get free Si and below the line unreacted C. The measured porosity values are also shown for preforms with TIMREX KS 25 graphite powder mass fractions ranging from 5 to 25 %. . .	147
7.22 (a)SEM image of the SiC_C_07 preform (b) X-ray CT frame showing much larger pores than measured by MIP (median pore diameter = 2 μm). The pores are darkest with both images. . . . .	148
7.23 The calculated terminal infiltration length of the SiC/C preforms for a non-isothermal case, inputting the graphite mass fraction and infiltration temperature values used in this study. . . . .	150
7.24 The calculated terminal infiltration length for an isothermal infiltration case. The temperature has a negative effect on the terminal infiltration depth. . . .	151
7.25 SEM image of the SiC-C preforms with 5 % TIMREX KS25 graphite powder, showing the off-eutectic solidification of Si-8 at. pct Zr alloy in the SiC/C preforms with low C content. . . . .	152
8.1 Experimental setup for induction infiltration experiment (left) and SEM image of the cross-section of the induction infiltrated SiC/C preform with 5 wt.% TIMREX KS 25 graphite powder (right). . . . .	158

## List of Tables

2.1	summary of the surface tension values of Si reviewed by Keene [95]. . . . .	20
2.2	Surface tension of molten silicon measured by different authors. . . . .	21
2.3	The equilibrium contact angles of liquid Si on glassy carbon and graphite substrates. . . . .	28
2.4	Invariant reactions in the Si – Zr system [156, 158]. . . . .	36
2.5	Molar volume of Si, C and SiC calculated from their molecular weight and approximate densities from literature. . . . .	39
2.6	Typical characteristics of the preforms reported by various researchers and their properties after infiltration by a mentioned infiltrant. . . . .	45
3.1	Composition of Si-8 at. pct Zr alloy % provided by CHDR metal, China. . . . .	48
3.2	Typical impurity levels in the TIMREX grade graphite powders. . . . .	49
4.1	Surface roughness of substrates measured by NanoFocus confocal microscope using $\mu$ Soft Analysis XT software. . . . .	64
4.2	The initial and final contact angle of silicon and $\text{Si}_{0.92}\text{Zr}_{0.08}$ on vitreous carbon and SiC substrates and respective temperatures measured under vacuum. . . .	65
4.3	Initial, final and equilibrium contact angle of pure silicon and $\text{Si}_{0.92}\text{Zr}_{0.08}$ on vitreous carbon and SiC substrates and respective temperatures measured under an argon atmosphere. . . . .	66
6.1	Summary of dimensions of microchannels in various configurations. . . . .	104
6.2	Surface roughness of the polished surface and laser ablated surface of glassy carbon plate (measured on 20 $\mu\text{m}$ deep channel) measured by Leica DCM8. . .	107
6.3	Aspect ratio of laser ablated microchannels in vitreous carbon. . . . .	107
7.1	Summary of powder mix used to produce C-C preforms to determine the effect of graphite particle size. . . . .	125
7.2	Summary of powder mix used to make the SiC-C preforms to determine the effect of mass fraction of graphite and SiC powder. . . . .	126
7.3	The particle size distribution of SiC F800, TIMREX KS25, TIMREX KS44 powders and their mixtures with increasing graphite content analyzed after mixing step by laser diffraction along with their skeletal densities measured using He pycnometry and calculated theoretical densities using Equation (7.1). . . . .	131

7.4	Modal pore size and total porosity of C-C preforms with various particle size, pressing force and pyrolysis temperature as measured by Hg intrusion. . . . .	133
7.5	Summary of the results after infiltration of various C-C preforms prepared with different pressing force and pyrolysis temperature. . . . .	138
7.6	Summary of the results of infiltration of SiC-C preforms with near-eutectic Si-Zr alloy at 1500 °C and 1700 °C with their respective densities before and after infiltration calculated by measuring mass, diameter and thickness, and pore and $\text{ZrSi}_2$ volume fraction measured by SEM image grayscale thresholding using Fiji software. The theoretical densities and silicide phase fraction of the completely infiltrated preform calculated by using the formulation in section 5.2 are also given. . . . .	142
7.7	The calculated values of equivalent radius, $R^*$ and SiC propensity factor, $\phi$ in the SiC/C preforms as developed in section 5.4. . . . .	149

# 1 Introduction

Recently, there has been an increasing demand for very high-temperature materials with high resistance to mechanical load, oxidation, abrasion as well as ablation. Numerous public and private entities are now researching and developing such materials for the applications in propulsion and thermal protection systems in the aerospace industry, for kiln furniture, ceramic brake systems, antiballistic plates, components for burners and high-temperature heat exchangers. The typically investigated compliant materials consist of carbides, borides, oxides and nitrides of early transition metals. Some of the promising materials are composites with constituting phases like  $\text{HfB}_2$ ,  $\text{TaB}_2$ ,  $\text{ZrB}_2$ ,  $\text{HfN}$ ,  $\text{TiN}$ ,  $\text{ZrN}$ ,  $\text{ZrC}$ ,  $\text{TiC}$ ,  $\text{HfC}$ ,  $\text{TaC}$  and  $\text{SiC}$ . However, the main difficulty during fabrication arises due to the very high processing temperature and time required to produce these phases. Traditionally the manufacturing involves sintering at very high temperatures with sintering aids because of the extremely high melting temperature of these refractory phases.

Reactive infiltration is rapidly becoming a viable alternative method for the cost-effective manufacturing of various advanced composite materials with the desired microstructure and shape. Some examples of the possible composite materials made by reactive infiltration process are  $\text{Al}_2\text{O}_3$ – $\text{NiAl}$ ,  $\text{TiC}$ – $\text{Al}$ ,  $\text{Al}_2\text{O}_3$ – $\text{Al}$ ,  $\text{SiC}$ – $\text{Si}$ ,  $\text{SiC}$ – $\text{TiSi}_2$ – $\text{Si}$  composites, to name a few. Reactive infiltration works via infiltration of the liquid melts of metal or alloys through capillary suction or applied pressure into the compact green body made up of ceramic particles or fibers often termed as a preform. The liquid phase of metallic melt reacts chemically with ceramic particles/fibers to form a reaction product, usually with a higher melting point that binds the matrix and reinforcement phase together. The process is hence a “transient liquid phase” process.

$\text{Si}$  infiltrated into mixtures of carbonaceous phases and of silicon carbide lead to  $\text{SiC}/\text{SiC}$  composites that are promising candidates for structural components at high temperatures. The significant difficulty in getting the best performance from such  $\text{Si}$ - $\text{C}$ - $\text{SiC}$  composites is the incomplete conversion of  $\text{C}$  to  $\text{SiC}$  and unreacted  $\text{Si}$ . This is due to the very limited width in the stoichiometry of  $\text{SiC}$  (which is very close to a line compound), and it impairs the oxidation resistance and mechanical properties at temperatures above  $1400^\circ\text{C}$ . Infiltration by  $\text{Si}$ -alloys

offers a more promising solution by forming also high melting temperature silicides along with SiC and accommodating larger inequalities between Si and C stoichiometry.

While the stoichiometry imposes a well-balanced ratio of SiC:C in the preform the process of infiltration and reaction sets certain limits to the capillary pore network on the preform: If the characteristic length scale is too fine, the reaction of infiltrating liquid Si with C to form SiC is too quick and leads to significant overheating of the infiltrated body and concomitant cracking due to the highly exothermic nature of the reaction. Furthermore, the growth of SiC can block the capillary network leading to incomplete infiltration. On the other hand, if the characteristic length scale is too large, the conversion reaction will be too slow and incomplete conversion may result. In the case of infiltration with Si-X alloys, obstruction of the infiltration channel may not only come from the formation of the SiC, but also from the formation of solid silicides caused by the depletion in Si of the infiltrating liquid through the reaction to SiC with the preform. In both cases the pore-clogging results in porosity at the center of the part and a gradient in composition. Although there exists a vast amount of research in the field of reactive infiltration of Si and Si alloys in porous carbon, a more fundamental study analyzing these two competing processes, namely reaction and infiltration, is missing in the literature.

The purpose of this thesis is to study the situation, in general, to understand how the processing temperature, preform composition and structure, as well as the structure of the alloy phase diagram, are affecting the fabrication of materials that have at least potentially a higher operating temperature than the processing temperature. Si-Zr alloy was chosen as an example to address the problem and develop an experimental and analytical framework using sessile drop experiments, single microchannel experiments and the infiltration of porous SiC/carbonaceous preforms. The framework of analysis can be further extended to transfer the findings to other Si-X and SiC/C systems.

The thesis is divided into seven chapters. Following the introductory chapter, Chapter 2 is an extensive literature review including information on silicon carbide and the parent class of silicon carbide composites, namely non-oxide ceramic matrix composites as well as thermophysical and physicochemical properties of Si. A small introduction to wettability at high temperature and a thorough literature review of wettability of Si and Si alloys on carbon and silicon carbide are presented.

Chapter 3 details the material properties and experimental methods used in this research. The chapter provides extra details about the experimental setup which was not possible to include in the journal articles that form the later chapters of this thesis.

Chapter 4 presents the experimental results of the wettability of Si and Si-8 at-pct. Zr alloy on glassy carbon and SiC substrates using classical sessile drop experiments. The experiments were performed in argon and vacuum atmosphere. The dependence of evaporation and oxidation of liquid silicon on the pressure in the furnace is analyzed. The experiments helped to confirm Zr as the right choice for an alloying element and to determine the optimal furnace atmosphere during melting.

In Chapter 5, a relation for an adequate pore fraction needed to obtain residual Si and C free composites via reactive Si-X alloy infiltration is presented. An idealizing mathematical model describing the reactive flow of Si-X alloy in a single micron sized capillary channel of carbon as well as in carbonaceous preforms is presented.

Chapter 6 focuses on the reactive flow of Si and Si-8 at-pct. Zr alloy into single capillary channels made up of glassy carbon at temperatures ranging from 1500 °C to 1700°C under a vacuum of  $\sim 5 \times 10^{-2}$  mbar. Laser ablation was used to prepare microchannels in glassy carbon plates. These microchannels have various configurations with a depth ranging from 10  $\mu\text{m}$  to 100  $\mu\text{m}$  and length up to 465 mm. The results shed light on the mechanism of obstruction of pores involved during the infiltration by simplifying the complexity of the pore distribution of a preform.

Chapter 7 presents the results of the infiltration of disk-shaped preforms made of varying sizes and weight percentages of graphite and SiC powder by Si and Si-8 at-pct. Zr alloy. The chapter discusses the experimental process developed for the infiltration of disk-shaped preforms. The effects of the particle size of graphite powder on porosity and porosity distribution of preforms are studied using mercury porosimetry and X-ray computer tomography. The variation and reliability of the porosity measurements are presented. For obtaining 5 mm thick disk-shaped solid Si/C-SiC composites, the optimal particle size of graphite in C-C preforms was determined. The effect of the mass fraction of graphite powder in SiC-C preforms is discussed for the infiltration with Si-Zr alloy.

Finally, the thesis ends with listing the conclusions of the study and a brief outlook on future possibilities considering the current findings.

Additionally, the python codes used to calculate adequate pore fraction and infiltration length plots are displayed in Appendix A.



This page is intentionally left blank.

## 2 Theory and related literature

### 2.1 Ceramic matrix composite

A composite material also referred to as "composite", is primarily made of at least two material phases with different physical and/or chemical properties, which provide the composite with material properties often in between those of the constituting phases. In the majority of the cases a composite consists of two phases namely the matrix phase which is continuous and the distributed phase commonly called the reinforcement phase. The reinforcement phase can be in the form of particles, continuous or short fibers, whiskers or flakes. The composites are classified based on the matrix constituent such as metal matrix composites (MMCs), ceramic matrix composites (CMCs) and organic matrix composites (OMCs). OMCs are generally assumed to include polymer matrix composites (PMCs) and carbon matrix composites also referred as carbon-carbon composites [1, 2].

CMCs are a very important class of high performance ceramic materials which attracted a lot of attention due to their ability to maintain good mechanical properties at elevated temperature. They possess distinctive characteristics such as, thermal and chemical stability, high hardness, high strength at elevated temperatures, low density and high wear resistance. Furthermore, CMCs, especially C and SiC fiber reinforced, show the highest specific strength for temperatures above 900 °C among all available engineering materials (Figure 2.1) [3]. Some of the most important ceramic materials are listed below, few of which are used as matrix phase in CMCs [2]:

- single oxides: alumina ( $\text{Al}_2\text{O}_3$ ), zirconia ( $\text{ZrO}_2$ ), titania ( $\text{TiO}_2$ ), magnesium oxide ( $\text{MgO}$ ), silica ( $\text{SiO}_2$ )
- mixed oxides: mullite ( $3\text{Al}_2\text{O}_3 \cdot 2\text{SiO}_2$ ), spinel ( $\text{MgO} \cdot \text{Al}_2\text{O}_3$ )
- carbides: silicon carbide ( $\text{SiC}$ ), boron carbide ( $\text{B}_4\text{C}$ ), titanium carbide ( $\text{TiC}$ );
- nitrides: boron nitride ( $\text{BN}$ ), silicon nitride ( $\text{Si}_3\text{N}_4$ )
- intermetallics: nickel aluminide ( $\text{NiAl}$ ,  $\text{Ni}_3\text{Al}$ ), titanium aluminide ( $\text{TiAl}$ ,  $\text{Ti}_3\text{Al}$ ), molybdenum disilicide ( $\text{MoSi}_2$ )

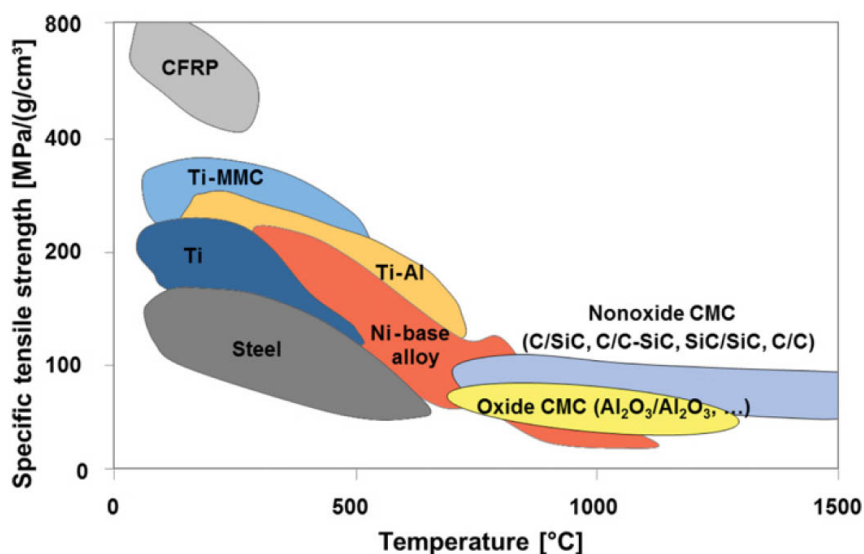


Figure 2.1 – Weight-specific tensile strength of various classes of materials as a function of temperature [3].

- elemental: carbon (C), boron (B).

### 2.1.1 Non-oxide ceramics as the matrix phase

Non-oxide ceramics is the term generally used to collectively refer the group of ceramic materials that do not contain oxygen in their crystal structure. Non-oxide ceramics are comprised of borides, carbides, nitrides, silicides and an exceptional nitride based material containing varying amount of oxygen called sialons [4].

Among the non-oxide ceramics, silicon carbide (SiC) and silicon nitride (Si<sub>3</sub>N<sub>4</sub>) are of great importance. They are perfect candidates for the matrix phase in CMCs because of their unique properties. The presence of strong covalent bonds in their crystal structure gives them high melting points and a substantial improvement in strength. Further, in highly oxidizing environment at elevated temperatures, these compounds form a protective SiO<sub>2</sub> layer to reduce any further degradation in properties by oxidation [5].

## 2.2 Silicon carbide

Silicon carbide (SiC) has been in use as an industrial material since the last century, the synthesis techniques were introduced in 1885 by Cowless and Cowless [6] and in 1893 by Acheson [7, 8]. The most widely used non-oxide ceramic materials are based on silicon carbide. SiC based materials possess many notable properties such as, high strength, high hardness, high wear resistance, high thermal and chemical stability, corrosion resistance, low thermal

expansion coefficient, high thermal conductivity, semi conductivity and good tribological properties [2–5, 9–18]. SiC based ceramic matrix composites, especially those containing carbon or silicon carbide fibers as reinforcements, are promising for a high temperature structural applications, including the after burn section of advanced aero jet engines, gas turbines of electrical power/steam cogeneration, etc. [19]

### 2.2.1 Structure of silicon carbide

In SiC, the fundamental structural unit is a primarily covalently bonded tetrahedron, either  $\text{SiC}_4$  or  $\text{CSi}_4$ . However, approximately 12 % contribution of ionic nature can be found due to the small difference in electronegativity between silicon and carbon (0.7 on Pauling's scale). Silicon carbide crystal structure exhibits remarkable polytypism, meaning that the crystal structure exhibits a large number of one-dimensional ordering sequences without any change in stoichiometry. Generally, it is common to refer to the cubic polytype as  $\beta$ -SiC and all non-cubic structures like hexagonal and rhombohedral as  $\alpha$ -SiC. The polytypes can be classified based on the number of Si-C layers in the unit cell and the crystal system. The most commonly occurring polytypes are 3C-, 4H-, 6H-, and 15R-SiC where C stands for cubic, H for hexagonal and R for rhombohedral (see Figure 2.2 ). 3C-SiC is known as a low-temperature polytype while others are referred to as high-temperature polytypes [20–25]. The 6H polytype can be stabilized by addition of boron while the 4H polytype can be stabilized by aluminum. Nitrogen and aluminum both promote the formation of the 2H polytype. Phosphorous and nitrogen can be used to stabilize  $\beta$ -SiC modifications [26]

### 2.2.2 Types of silicon carbide ceramics

Silicon carbide ceramics come in different varieties whose properties vary accordingly. From a manufacturing point of view, they can be categorized into two types namely self-bonded or second phase bonded silicon carbide. Another popular type of classification is dense or porous silicon carbide. The densification of pure SiC powder is possible only at extremely high pressure and/or temperatures more than 2100 °C due to the very low self-diffusion coefficient of SiC [27, 28]. Therefore, in order to effectively sinter SiC, the use of the sintering aids is essential.

The most common methods to make dense silicon carbide ceramics are pressureless sintering in solid state (SSiC), infiltration of reaction bonded silicon carbide by molten silicon (SiSiC), liquid phase sintered silicon carbide (LPSiC) and hot pressing (HPSiC). All these methods come with their own drawbacks. The SSiC materials are typically densified using sintering additives like C and B [29, 30]. They exhibit fine grained equiaxed microstructure with good high-temperature creep and oxidation resistance [31, 32] but show poor fracture toughness and highly defect-sensitive strength at room temperature [33]. Additionally, due to the higher sintering temperature and prolonged sintering time at these temperatures, abnormal grain growth can occur often resulting in anisotropic  $\alpha$ -SiC phase formation. The SiSiC materials

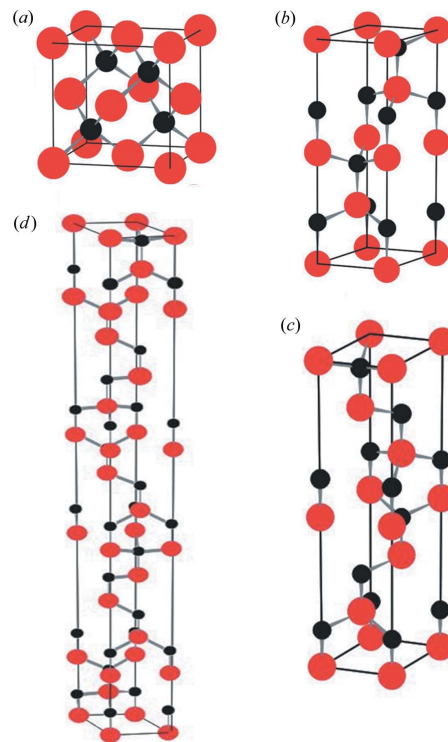


Figure 2.2 – Crystal structures for the four most commonly occurring SiC polytypes: (a) 3C, (b) 4H, (c) 6H and (d) 15R. Si atoms in red and C atoms in black (reproduced from [24]).

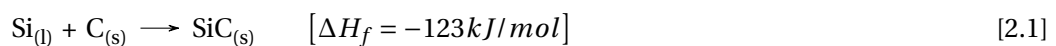
has limited operational temperature due to the lower melting temperature of silicon. Another possibility of achieving SiC densification is using liquid phase forming additives like  $\text{Al}_2\text{O}_3$  [34] and  $\text{Al}_2\text{O}_3 + \text{Y}_2\text{O}_3$  or some other rare earth oxides [35–40]. With this approach the materials can be sintered at relatively low temperature sometimes as low as 1850 °C. The majority of liquid phase sintered materials have equiaxed fine grain microstructure with secondary phase at the triple junction of SiC grains [35–37].

Porous SiC also has shown tremendous potential in industrial application owing to its unique combination of properties such as excellent mechanical strength, good chemical resistance, high thermal conductivity, low thermal expansion coefficient, and high thermal shock resistance [41–45]. In the literature various methods can be found catering to specific applications. The processes can be categorized into partial sintering, replica, sacrificial template, direct foaming, and bonding techniques using alkali, cordierite ( $2\text{MgO} \cdot 2\text{Al}_2\text{O}_3 \cdot 5\text{SiO}_2$ ), mullite ( $3\text{Al}_2\text{O}_3 \cdot 2\text{SiO}_2$ ), silica ( $\text{SiO}_2$ ), Si, SiC, silicon nitride ( $\text{Si}_3\text{N}_4$ ), silicon oxycarbide (SiOC), and frit phases. A detailed review on production processes and properties of open porous SiC ceramic materials can be found in Ref. [46]. As the study is focused mainly on the liquid metal infiltration technique, silicon infiltrated silicon carbide material will be further discussed in detail.

## 2.3 Silicon infiltrated silicon carbide

Silicon infiltrated silicon carbide (SiSiC), developed in 1975 by Hillig et al. [47], is a well known industrial ceramic material due to its remarkable properties such as low porosity, low density, high thermal conductivity, high mechanical strength, excellent chemical, oxidation and thermal shock resistance and high wear and corrosion resistance [48]. The unique combination in properties of Si-SiC composites, make them an ideal candidate for applications like gas turbines (several hot gas path components like 1<sup>st</sup> and 2<sup>nd</sup> stage turbine shrouds and combustor liners [48]), advanced friction system (brake discs, brake pads), highly stressed kiln furniture (beams, rolls, supports), burner parts for direct and indirect combustion (flame tubes, recuperators, jet pipes), heat exchangers, lightweight armor. Over the past couple of decades, enormous interest in Si – SiC ceramics led to development of many variations of these materials – monolithic and particle/fiber reinforced CMCs, which can be obtained from different constituents and processes [49–51]. Essentially, the fabrication of such composites is based on the reactive melt infiltration process (RMI), which in case of silicon infiltration is also called the liquid silicon infiltration process (LSI). The GE global research center has been associated with the development of LSI composites for the past 25 years, which now are even commercially available as HiPerComp™ [48]. Krenkel et al. [51, 52] showed that LSI is one of the novel and cost efficient approaches to manufacturing CMCs with very good tribological and mechanical properties at high temperature. The study explores the feasibility of LSI CMCs as alternative brake pad material for vehicles. Another study involves the feasibility of C/C-SiC composites for space applications and advanced friction systems [50]. Xu et al. [53] reported an economical method to combine chemical vapor infiltration (CVI) and LSI to C/SiC composites. In this method, the carbon fibers were coated with a SiC barrier layer by CVI and then the pre-coated preforms were infiltrated with silicon melt to obtain a final composite. This method reduced the risk of damaging carbon fibers during melt infiltration due to the SiC barrier layer formed by CVD hence resulting in good thermal stability of the mechanical properties and failure behavior.

LSI is considered to be the only process offering the possibility of an economical industrial production of nearly net-shaped and fully dense large complex SiC based components [52, 54]. Therefore, LSI has attracted attention from several industrial sectors. In this method, C or C/SiC microporous preforms are infiltrated by molten Si by capillary forces. The reaction of Si and C results in the transformation of the C preform into a  $\beta$ -SiC body by reactive wetting and infiltration in the final product [55]. The formation of silicon carbide during liquid silicon infiltration is an exothermic reaction (see Reaction [2.1]).



The infiltration temperature is usually about 1500°C. The enthalpy of formation  $\Delta H_f$  is -123 kJ/mol and the heat capacity  $C_p$  is 53 J/mol.K [56]. The sometimes quoted adiabatic temperature

for the SiC formation reaction of about  $\sim 3820^\circ\text{C}$  during Si infiltration is hypothetical, because SiC decomposes at lower temperature already. Parameters like pore size & pore connectivity of the preform, infiltration times & temperatures, wetting behavior and chemical reaction greatly influence the depth of infiltration and final porosity [57, 58]. It appears that to obtain a fully dense composite the porosity of the C based preform has to be higher than a certain threshold value otherwise one ends up with a composite with residual porosity. Moreover, if the porosity is too high one ends up with dense composite but also residual Si.

However, there are some undesirable aspects in the LSI process. The major drawback is the residual unreacted Si in the composite that weakens the mechanical properties at temperatures above  $1400^\circ\text{C}$  [12]. Depending on pore structures and preform reactivity, reaction products could result in a capillary obstruction (due to a solid phase volume increase of up to 58% caused by the reaction between liquid Si and C depending upon the molar volume of the carbonaceous phase) and therefore in incomplete infiltration [59]. In some continuous C fiber based composites where C fibers are used as reinforcement, the reaction with Si during the infiltration process may result in weakening of the CMC [48, 60]. Faster diffusion of C, as compared to Si through solid SiC, aggravates the tendency to obstruct the channels since the solid phase grows into the channel [27]. A common way to overcome the unwanted reaction and the obstruction of the channels is to protect the reinforcement with an inert interphase (SiC or BN). These composites usually consist of 5 to 15 vol % residual Si. This technique is very effective but also expensive in terms of equipment and process time. Furthermore, it does not solve the problem of limited operation temperature, and inhibits also complete conversion.

Another possible solution consists in using metal-Si alloys for the infiltration; the use of alloys can help in reducing the reactivity [61, 62] as well as the amount of residual Si and in lowering the melting temperature [63–65]. To maintain a high operating temperature, the reduced melting point must be designed to be transient, i.e. the preform must react with the melting point depressor or with the silicon in such a way that the resulting alloy has a melting point above the operating temperature. This has been demonstrated to be feasible for Si-Mo alloys infiltrated in Carbon preforms [66]. Among most recent studies, Si-Zr alloys have been used to infiltrate C preforms, obtaining a CMC characterized by high strength, good oxidation resistance and excellent ablation resistance [67]. As this is the main interest of this study, this is discussed in more details in what follows.

## 2.4 Silicon alloys infiltrated silicon carbide

In 1990, Messner and Chiang [66] investigated the infiltration of a carbonaceous preform by silicon-molybdenum alloys to obtain composites free of residual silicon and reduce the associated disadvantages in SiSiC. The selection of the alloying element was based on liquid-phase equilibria and its ability to form stable refractory silicides. The selection of Si-Mo melt was inspired by the very good oxidation resistance of  $\text{MoSi}_2$ . Also  $\text{MoSi}_2$  undergoes a brittle

to ductile transition at ~1000 °C but the melting point is around 2047 °C, which makes the operating range of the composite much wider compared to that for free Si. The infiltration experiments were carried at 4 to 6 at.% of Mo at temperatures in the range of 1450 °C to 1650 °C. During the infiltration of carbonaceous preforms, Si from the alloy reacts with C to form SiC. This reaction is highly exothermic and the local adiabatic reaction temperature can reach ~3000 °C and exceed the decomposition temperature of SiC as shown in Figure 2.3, curve 1. In practice, the maximum temperature is also reduced due to heat dissipation from reaction zone and the trajectories are more like curve 2 in Figure 2.3. This trajectory depends for a given material on the specific reaction rate, sample size and thermal diffusivity of the system. The enrichment of the melt with Mo results in precipitation of refractory molybdenum silicides. They reported both  $\alpha$  and  $\beta$ -SiC along with MoSi<sub>2</sub> and a small amount of unidentified Mo-Si-C ternary phase. They observed some flaws in reacted material such as, partially reacted large carbon inclusions, cracks and veins of solidified melt. The flaws were attributed to thermal stresses generated during reaction and upon cooling. The melt-filled veins are the result of cracks caused due to rapid heat generated by the highly exothermic reaction which are then filled during the infiltration process. The unfilled cracks are from the unrelieved reaction stresses, stresses due to differential thermal expansion due to a gradient in second phase content across the sample, or both. The study also presents a time dependent permeability model for reactive infiltration. The shrinkage of pore radius  $r$  can be linear or parabolic as defined in Equations (2.1) and (2.2).

$$r(t) = r_0 - kt \quad (2.1)$$

$$r(t) = r_0 - k' t^{\frac{1}{2}} \quad (2.2)$$

Where  $k$  and  $k'$  are the linear and parabolic reaction rate constant. The infiltration distance  $l$  with time can be described using Equations (2.3) and (2.4) for  $k$  and  $k'$  respectively, based on Washburn's equation.

$$l^2(t) = \frac{2\beta\Delta P}{\eta} \left[ r_0^4 - 2r_0^3 kt^2 + 2r_0^3 k^2 t^3 - r_0 k^3 t^4 + \frac{(k^4 t^5)}{5} \right] \quad (2.3)$$

$$l^2(t) = \frac{2\beta\Delta P}{\eta} \left[ r_0^4 t - \frac{(8r_0^3 k' t^{\frac{3}{2}})}{3} + 3r_0^3 k'^2 t^2 - \frac{8r_0 k'^3 t^{\frac{5}{2}}}{5} + \frac{k'^4 t^3}{3} \right] \quad (2.4)$$

where, constant  $\beta$  is the geometric factor specific to the chosen capillary model,  $\Delta P$  is the pressure differential and  $\eta$  is the fluid viscosity.

The model showed that the practical infiltration depths of >1 cm are possible before reaction-



choking of pore happens at the preform surface. It is worth noting that the model is only valid when one assumes the viscous forces are rate limiting which is the very basis of Washburn's equation. The microstructure and phase distribution in infiltrated material showed promising high-temperature properties. They concluded that fully dense silicon carbide – molybdenum silicide composites can be formed by Si-Mo alloy metal infiltration and also other alloying elements and that multiple additives may be used [68]. Singh et al. [69, 70] also studied the Si-Mo alloy infiltration for porous carbon preforms and found relatively lower exothermic temperature in case of Si-3.2at.% Mo alloy compared to that of pure Si using differential thermal analysis (DTA). They proposed that this could be the result of better wetting properties of Mo-Si alloys and molybdenum acting as nucleation sites for solution re-precipitation and growth, which is an endothermic process required for crystal growth. They also proposed that the exothermic rise in temperature of the sample is higher for medium pore size ( $\sim 2\text{-}3\ \mu\text{m}$ ) carbon preforms as compared to that of small ( $\sim 0.5\ \mu\text{m}$ ) pore size carbon preforms, due to the faster dissipation of heat. Their modelling and experimental results concluded that for complete infiltration by pure Si the initial pore volume fraction of 0.562 is needed for graphitic carbon and 0.36 for glassy carbon. The required initial pore volume fraction for choke-free infiltration by Si-Mo alloys increases with increasing amount of Mo in the alloy.

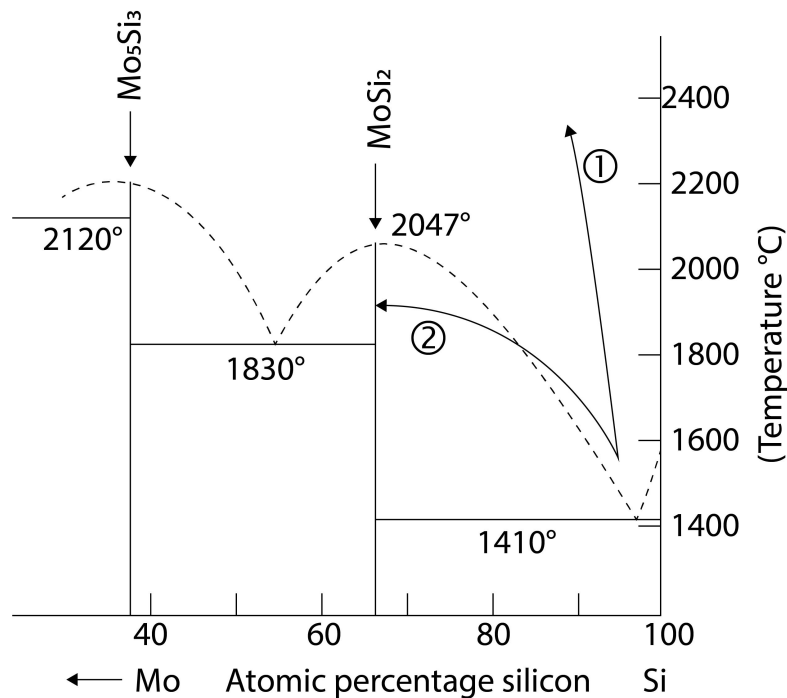


Figure 2.3 – Mo-Si phase diagram [71], showing the change of concentration of Mo in different scenario (1) adiabatic SiC formation (2) in real practice situation with heat dissipation (image reproduced from [66]).

Chakrabarti and Das [72] also reported the reactive infiltration of Si-Mo alloy into carbonaceous preform made from petroleum coke and commercial SiC powders. They used C to SiC weight ratios of 0.5 and 0.6 to prepare the preform by cold pressing into bar shapes. The Mo

concentration was varied from 7 to 29 wt%. These preforms were later infiltrated in a graphite heated furnace under argon atmosphere at a temperature 1.1 – 1.2 times the melting point of the alloy. The composites obtained had densities ranging from 89 % to 95 % of the theoretical densities. The SEM and EDX analysis showed Si,  $\alpha$ -SiC,  $\beta$ -SiC, MoSi<sub>2</sub> and unreacted carbon indicating incomplete reaction. Few intermediate areas containing silicon, aluminum, and iron between MoSi<sub>2</sub> and SiC were observed and attributed to impurities present in the raw material.

Meier and Heinrich [73] investigated the addition of elements like Al, B, Cr and Ti into the MoSi<sub>2</sub>-Si mixture to lower the infiltration temperature. They selected additive elements to lower the melting temperature of the mixture to 1600 °C in order to prevent damage to C-fiber preforms and maintain the reinforcement phase intact. The additives react with carbon from the infiltrated body or silicon to form high-temperature resistant carbides or silicides. They successfully managed to produce SiC-MoSi<sub>2</sub> carbon fiber cofused by infiltration of a MoSi<sub>2</sub>-Si mixture with Al, B, Cr and Ti. The use of the Al can only be justified by its action as melting temperature depressant. They also found that the Al, however used in lower quantities, increases the viscosity of the melt significantly and results in inferior infiltration results even at 1600 °C. They studied various infiltration parameters pertaining to the resulting microstructure and properties. The penetration velocity into the green porous body and the depth of penetration are influenced by the composition of the infiltration mixture, way of powder preparation, infiltration temperature, holding time and pressure. They reported micro cracks due to the very different thermal expansion coefficient of the newly formed phases. The micro cracks reduce the strength at room temperature considerably when compared to SiSiC. The mixture with Ti was the most oxidation resistant material within this group of composites and showed even a better oxidation resistant behavior than SiSiC.

Hao et al. [74] also manufactured similar composites for high temperature structural application by infiltration of the melt of a Si-Mo-X powder mixture (X= Ti, Al, Zr) into porous carbon fiber reinforced carbon matrix composites(C/C). The infiltration temperatures ranged from 1550–2200 °C. Composites infiltrated at higher temperatures are less resistant to ablation, particularly for mixtures containing Al or Ti. With the addition of Ti at higher infiltration temperature denser composites can be produced, the opposite being the case for Al and Zr where higher densities were obtained with lower infiltration temperature. Si-Mo-Ti and Si-Mo-Zr infiltrated composites exhibited better ablation resistance, benefiting mainly from their phase composition and the density, and porosity did not contribute much to the degradation when compared to other composites.

Reitz et al. [75] explored the feasibility of Si-Y alloys to make reactive melt infiltrated SiC composites. They infiltrated porous graphite tubes with eutectic Si-Y alloy for intermittent times from 1 to 180 minutes at 1450 °C. The infiltrated tubes showed silicide phases namely YSi and Y<sub>3</sub>Si<sub>5</sub>.

Singh and Behrendt [76] studied reactive silicon-niobium alloy infiltration into microporous

carbon preforms prepared by polymer precursor pyrolysis. A careful control of pore size & pore volume of porous carbon preforms and of the alloy composition was used to tailor the morphology and quantity of residual phases namely niobium disilicide and silicon in the infiltrated material. The composites obtained by infiltration of Si-5at%Nb alloy in medium pore size preforms showed in average room temperature flexural strength of approximately 290 MPa which is retained to approximately 60% at 1371 °C. They observed that the flexural strength of composites may reduce significantly due to the flaws present as carbon agglomerates. The room temperature fracture toughness of the composites was enhanced by the presence of niobium disilicide phase.

Aoki et al.[77] investigated microstructural and mechanical properties of Si-Hf alloy infiltrated SiC fiber reinforced composites. The manufacturing involved several steps; firstly, the SiC fibers, arranged to form an orthogonal three-dimensional preform, were CVI coated by thin pyrolytic carbon to soften the fibers. Later, a 5–10  $\mu\text{m}$  thick SiC layer was deposited on fibers by CVI in vacuum to protect the surface against molten Si-Hf or Si. Further, the preforms were infiltrated with carbon black added with polyurethane resin followed by drying. The final preforms were infiltrated by Si-8.5 at%Hf at 1375 °C or by Si at 1450 °C. They obtained a highly dense matrix consisting of the reaction-formed SiC and the unreacted Si and HfSi<sub>2</sub> phases with open porosity less than 5% using this technique. The composite, melt-infiltrated with Si-Hf alloy, displayed about 35% higher bending strength than the traditional Si melt-infiltrated composite produced at 1450 °C. The Si-Hf alloy melt-infiltrated composite has been reported to retain its strength in an Ar atmosphere up to 1200 °C. The study showed positive effects on the mechanical properties of composites from low-temperature infiltration processing.

In another study, Aoki and Ogasawara [78] fabricated composites by infiltrating Si-16 at.% Ti alloy melt at 1375 °C under vacuum. The manufacturing process of preforms was similar to that of earlier studies with the Si-Hf alloy mentioned above. They obtained uniform TiSi<sub>2</sub>-Si matrix in the infiltrated composites. Microstructural findings showed the damage to reinforcing fibers and pyrolytic carbon interfaces during the melt infiltration cycle resulting in degradation of properties at higher temperature. It can further be inferred that the TiSi<sub>2</sub>-Si matrix had a lower melting temperature than pure Si.

Whitehead and Page [79] tried a novel approach to make reaction-bonded silicon carbide. They dispersed additives like ZrC, TiC, TaC, B<sub>4</sub>C and TiB<sub>2</sub> in the initial powder mix. The cold-pressed, disk-shaped preforms were infiltrated at 1600 °C by pure Si and were held for 2 h in a vacuum induction furnace. They were able to produce near-net-shaped disks for most cases without any disruption in reaction-bonding process. The added carbides were observed to react with the Si melt to form metal silicides. The original SiC particles did not react with the Si melt but acted as heterogeneous sites for deposition of newly formed SiC during reaction. They found that the reaction kinetics between carbides and Si melt to form silicides is much slower than that of the reaction-bonding process. This is an important factor in retention of the original shape of the green compact. TiB<sub>2</sub> appears to be inert to liquid Si but was wetted by Si. However, the mechanical properties measured via micro-hardness test at room and high

temperature did not show any significant improvement. They attributed this to brittle silicide phase replacing some SiC and the crack formation. They concluded that it would be possible to make residual Si free composites by replacing Si with refractory silicides with precise control of composition of the initial preform.

Wang et al. [67] fabricated carbon fiber reinforced C/C-SiC-ZrC composites by reactive melt infiltration using Si-13 at. pct Zr alloy at 1800 °C. They found that the carbon fiber tows were covered with deposited carbon and SiC followed by a gradient ZrC-SiC matrix. The composites showed very good bending strength due to suppression of crack growth by the gradient matrix. C/C-SiC-ZrC composites exhibited good ablation resistance due to the formation of a protective SiO<sub>2</sub> layer further protecting C fibers from oxygen attack. In another study [80], they infiltrated porous carbon preforms with pure Zr to obtain C/ZrC composites. They were infiltrated at different temperatures ranging from 1900 °C to 2000 °C. As seen in Figure 2.4, the depth of the infiltration increases with the infiltration temperature. The infiltration depth also increases with time until about 30 min but then stays constant due to pore closure phenomenon.

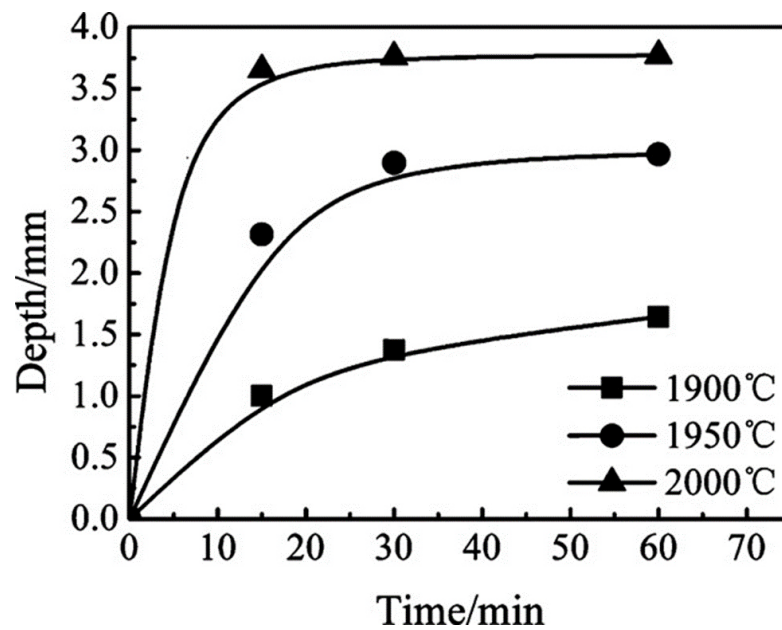


Figure 2.4 – Infiltration depth of Zr as a function of annealing temperature and time (reproduced from [80]).

Tong et al. [65] demonstrated preparation of a high performance low cost C/C-SiC composite by reactive melt infiltration of Si-10at%Zr alloy at 1450 °C. They made a porous C/C preform, by densifying carbon fiber felt using chemical vapor infiltration to deposit pyrolytic carbon. After the infiltration, C, SiC, ZrSi<sub>2</sub> and a small amount of ZrC phases were observed due to in-situ reaction between pyrolytic carbon and Si-Zr alloy. They found no residual silicon with XRD analysis. The infiltrated composites had about 95% of theoretical density. The composites displayed a pseudo ductile fracture behavior with large numbers of fibers pulled out from

the composite on the fracture surface. They reported a flexural strength of 350 MPa at room temperature. The improved oxidation resistance for the C/C-SiC composite is primarily due to the formation of  $\text{ZrO}_2$ ,  $\text{ZrSiO}_4$  and  $\text{SiO}_2$  on the composite surface which ultimately prohibited further oxidation.

In another study [63], Tong et al. also fabricated C/C-ZrC composites by liquid melt infiltration of a Zr-8.8 at. pct Si alloy. The final composites achieved had 5% open porosity with a density of  $2.46 \text{ g/cm}^3$  from a preform with 25 % open porosity and a density of  $1.33 \text{ g/cm}^3$ . The carbon fiber preforms were prepared by three-dimensional needle felting of non-woven carbon fiber cloths which were later infiltrated by pyrolytic carbon via CVI. Preforms were infiltrated at  $1800^\circ\text{C}$  under argon atmosphere with a pressure of 1 atm. They reported carbon, ZrC and  $\text{Zr}_2\text{Si}$  phases in the final composite. A flexural strength of 240 MPa is reported which is low, much lower than for composites infiltrated with Si-10at%Zr alloy. The composites showed excellent ablation resistance compared to C/ZrB<sub>2</sub>-SiC, C/SiC-TaC, C/SiC, C/SiC-ZrB<sub>2</sub>-TaC composites by forming a protective  $\text{ZrO}_2$  barrier layer.

## 2.5 Thermophysical and physicochemical properties of Si

Silicon is a metalloid and second most abundant element in earth's crust accounting for approximately one fourth of the total mass [81]. Silicon crystallizes in a diamond cubic lattice with strong, oriented, covalent bonds at standard conditions. Owing to the high amount of energy required to break the strong covalent bonds and melt the solid, Si has a high melting point of  $1414^\circ\text{C}$ . In fact, based on the bond strength the melting temperature should be even higher. However, the large melting entropy facilitates melting at lower temperature. Si has a density of  $2.329 \text{ g/cm}^3$  at room temperature and shows a density anomaly like water upon melting. The density of Si increases at the melting temperature to  $2.57 \text{ g/cm}^3$  [82, 83], equivalent to approximately 10% reduction in volume. Upon solidification residual Si will hence expand and may help filling pore space left by the reaction of Si and C to SiC. Several values of density of Si at melting temperature can be seen in literature ranging from  $2.53$  to  $2.58 \text{ g/cm}^3$  measured by various techniques like sessile drop [84], Archimedean [85], electromagnetic levitation [86] and high-temperature electrostatic levitator (HTESL) [87]. In one of the recent studies, Rhim and Ohsaka proposed [88] the temperature dependence of the density of liquid Si in  $\text{g/cm}^3$  as shown in the Equation (2.5) using HTESL technique.

$$\rho(T) = 2.58 - 1.59(T - T_m) - 1.15(T - T_m)^2 \text{ g/cm}^3 \quad (2.5)$$

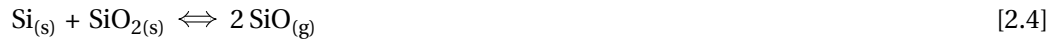
where  $T_m$  is the melting point, 1687 K.

### 2.5.1 Oxidation behavior of Si

Silicon has high affinity towards oxygen. The interesting feature of the interaction between silicon and oxygen is the transition from passive oxidation to active oxidation. In passive oxidation a solid Si oxide is formed on the Si (see Reaction [2.2]) while in active oxidation the Si oxide is in the gaseous state (see Reaction [2.3]).



When a fresh Si surface is in contact with air at room temperature, it is spontaneously covered by a nanometer-thick continuous layer of silica. Upon heating in a furnace, thickening of this oxide layer occurs up to a certain temperature  $T^*$  depending upon the partial pressure of oxygen in the furnace. Up to the temperature  $T^*$ , Si acts as an oxygen getter from the furnace atmosphere. The deoxidation of the oxide layer starts at temperature  $T^*$ . The deoxidation occurs at partial pressure of oxygen exceeding the equilibrium partial pressure at the silicon surface by several orders of magnitude which corresponds to the inverse of Reaction [2.2]. The oxide film dissipates due to the reaction with underlying Si forming volatile silicon monoxide (see Reaction [2.4])[89].



Oxidation of Si occurs even for temperatures above  $T^*$ , but without the formation of any solid oxide film as seen in reaction Reaction [2.3]. In Figure 2.5, the schematic representation of various configurations of oxidation state of the Si surface at a constant temperature  $T$  is shown based on the partial pressure of oxygen in the furnace  $P_{\text{O}_2}^f$  [90]. The three phase equilibria of Si, silica and gas is represented in Figure 2.5 (a). In this configuration, at the critical partial pressure of oxygen  $P_{\text{O}_2}^{f*}$ , the transition from oxidized to oxide layer-free Si surface can be considered as a broken oxide layer where Si, silica and gas exists in a three-phase equilibrium at the surface. This kind of configuration can be obtained for Si with a thick oxide layer which is then cracked by heating under the effect of thermomechanical stresses. Another way to achieve the three-phase equilibrium is by forming a continuous thin layer of silica with thickness of tens of nm or less. Here the high temperature diffusion of oxygen through the layer can be reasonably assumed faster than the rate of chemical reaction forming silica [91].

Depending on the flow of oxygen from the surrounding atmosphere,  $J_{\text{O}}^+$  which is proportional to  $P_{\text{O}_2}^f$ , and the oxygen flow leaving the surface in the form of SiO,  $J_{\text{O}}^-$  which is proportional to equilibrium pressure of SiO,  $P_{\text{SiO}}^s$  (the superscript  $s$  is to indicate the values at the surface

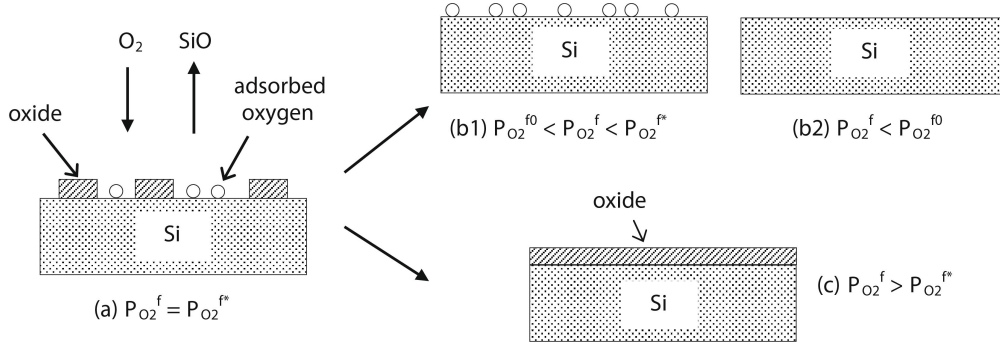


Figure 2.5 – Schematic representation of the passive-to-active transition of Si at constant temperature  $T$ . (a) the Si/silica/gas three-phase equilibrium at  $P_{O_2}^f = P_{O_2}^{f*}$  (b1), the Si surface is skin free but contains adsorbed oxygen at  $P_{O_2}^{f0} < P_{O_2}^f < P_{O_2}^{f*}$  (b2) a clean, adsorption-free surface is obtained at  $P_{O_2}^f < P_{O_2}^{f*}$  (c) Si is oxidized at  $P_{O_2}^f > P_{O_2}^{f*}$  (reproduced from [90]).

of Si), the configuration will change to either of Figure 2.5 (b) or (c). Deoxidation happens when  $J_O^- > J_O^+$ . This condition is met for  $P_{O_2}^f < n \cdot P_{SiO}^s$ , where the value of  $n$  depends on the atmosphere of furnace which is 0.4 for vacuum and 0.8 for neutral gas [92]. Once the temperature is fixed the thermodynamic variance of equilibrium is equal to unity, meaning that the partial pressure of oxygen at the Si surface,  $P_{O_2}^s$  and  $P_{SiO}^s$ , are well defined implying the corresponding value of  $P_{O_2}^{f*} = n \cdot P_{SiO}^s$ . The dependence of  $P_{O_2}^{f*}$  and  $P_{O_2}^s$  on the temperature is plotted in Figure 2.6 for inert gas taking  $n=1$  [56, 90]. According to Figure 2.6, considering the  $P_{O_2}^f \approx 10^{-5}$  atm if inert gas like Ar is used in the furnace atmosphere, the  $T^*$  is close to 1300 K where Si is still in solid state. For  $T < T^*$ , passive oxidation (see Reaction [2.2]) occurs where the silica film is thickened with time [89]. For  $T > T^*$ , active oxidation (see Reaction [2.3]) occurs where transformation of incident oxygen happens into the gaseous SiO without forming any solid film.

Usually, when Si is introduced in the furnace at room temperature under a high  $P_{O_2}^f$  value, the value of  $T^*$  increases and it also promotes strong thickening of oxide film from room temperature to  $T^*$ . These conditions can cause the delay in passive to active transition of oxidation or in some cases even subdue the phenomenon. Therefore, Maillart et al. [93] suggests to introduce Si directly at the experimental temperature to avoid the formation of solid oxide film and obtain a skin free Si surface at  $T > T^*$ . It is worth noting that it is possible to obtain a skin free Si surface at  $P_{O_2}^f$  much higher than  $P_{O_2}^s$  due to the reduction of silica (see Reaction [2.4]) film by underlying Si as seen in Figure 2.6.

If the Reaction [2.3] is assumed to have achieved steady state with  $J_O^- = J_O^+$ , the equilibrium partial pressure of oxygen on a skin free Si surface can be calculated using Equation (2.6) [92].

$$P_{O_2}^s = \left[ \left( \frac{2D_{O_2}}{D_{SiO}} \right) \left( \frac{P_{O_2}^f}{K} \right) \right]^2 \cong \left( \frac{2P_{O_2}^f}{K} \right) \quad (2.6)$$

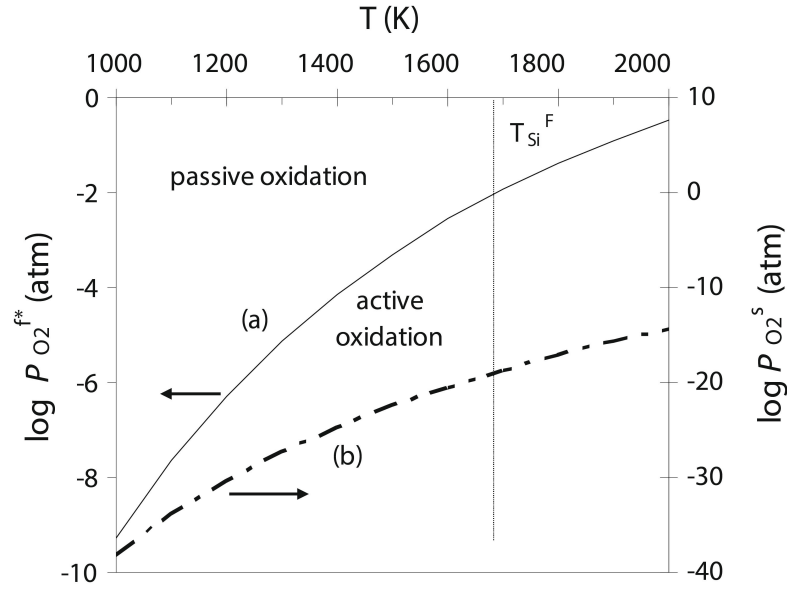


Figure 2.6 – The curve (a) represents the variation of the critical partial pressure of oxygen in the furnace ( $P_{O_2}^{f*}$ ) with temperature. The region above the curve defines the passive oxidation state while the one below defines the active oxidation state. The curve (b) represents the variation of the critical partial pressure of oxygen at the Si surface corresponding to Si/silica/gas three phase equilibrium.  $T_{Si}^F$  is the melting point of Si (reproduced from [90]).

where,  $K$  is the equilibrium constant of Reaction [2.3] and  $D_{O_2}$  and  $D_{SiO}$  are the diffusion coefficient of  $O_2$  and SiO species in the neutral gas, respectively. Figure 2.7 shows the variation of  $P_{O_2}^S$  and  $P_{O_2}^f$  at 1700 K and 1800 K. The maximum value of  $P_{O_2}^f$  for which the Si/silica/gas three phase equilibrium can exist is around  $10^{-2}$  atm. The effective oxygen pressure at the surface of Si is as low as  $10^{-20}$  atm for the values of partial pressure of oxygen in the range of  $10^{-4} - 10^{-5}$  atm.

### 2.5.2 Surface tension of Si

The surface tension of Si has been studied well before the invention of silicon infiltration to form silicon carbide composites owing to its importance in single crystal manufacturing [94]. Keck et al. [94] measured the surface tension of Si using the drop weight (DW) method. They melted the tip of the suspended high-purity polycrystalline Si rod of approximately 5 mm in inert argon atmosphere to form the molten droplet. The surface tension  $\gamma$  was then calculated using Equation (2.7), where  $r$  is the radius of the rod,  $W$  is the weight of the droplet and  $\phi$  is a geometric correction factor.

$$\gamma = \frac{\phi g W}{2\pi r} \quad [\text{N/m}] \quad (2.7)$$

The earlier review of the reported surface tension values was done by Keene [95]. The reported



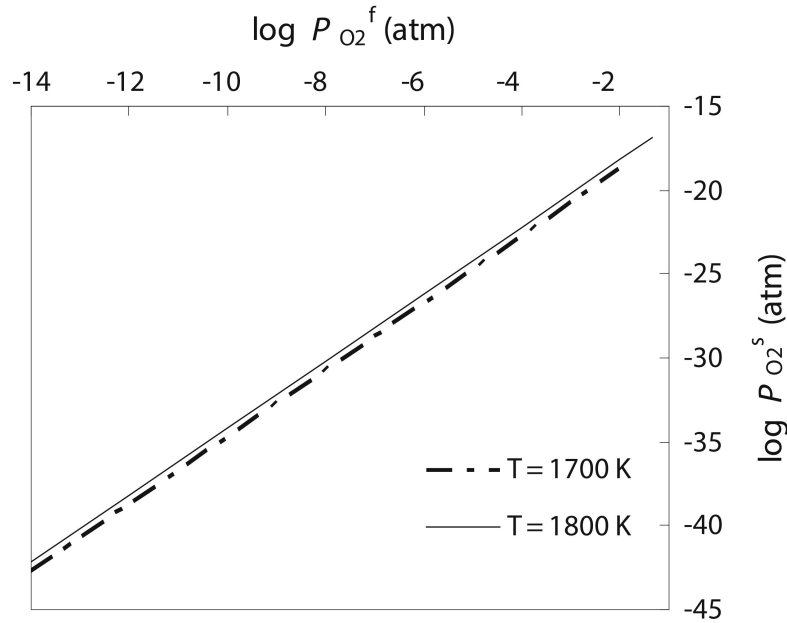


Figure 2.7 – Variation in the equilibrium partial pressure of oxygen at the skin free surface of Si,  $P_{O_2}^S$  as a function of the partial pressure of oxygen in the furnace  $P_{O_2}^f$  (reproduced from [90]).

values were mostly based on sessile drop (SD) experiments and are summarized in Table 2.1. According to Keene, lower surface tension and its temperature coefficient are the effect of oxygen contamination.

Table 2.1 – summary of the surface tension values of Si reviewed by Keene [95].

Reference	$\gamma$ mN/m	$(d\gamma/dT)$ mN/mK	Method	Comment
Keck[94]	720		DW	
Dzhimekv[96]	750		SD (in He)	at 1550 °C
Levin [97]	737	-0.104	SD	
Kingery [98]	860		SD (H <sub>2</sub> )	740 in He
Tavadze[99]	735	-0.149		
Elyutin [100]	833	-0.0836	SD	
Naidich [101]	746	-0.152	SD (vac)	
Lukin [102]	727	-0.152	SD (vac)	
Hardy [103]	885	-0.28	SD	

A later review by Mills et al. [104] provided more recent results of surface tension of Si, measured by various techniques like the sessile drop method, the maximum bubble pressure method, the dynamic hanging drop method (DHD), the ring method (RD), surface laser-light scattering (SSLS) and the oscillating drop (OD) method using electromagnetic levitation, which are summarized in Table 2.2.

Table 2.2 – Surface tension of molten silicon measured by different authors.

Reference	Method	Contact Material	Temp. range °C	$P_{O_2}$ Pa	$\gamma$ mN/m	$(d\gamma/dT)$ mN/mK
Kimura [105]	RD	SiC, SiB <sub>2</sub>	1430-1650	Ar	734	-0.07
Huang [106]	SD	BN	1415-1515	0-50	825	-0.1
Chung [107]	DHD	SiC	1430-1495	Pure Ar	819	-0.308
Przyborowski [108]	OD	None (EML)	1000-1500	$< 2 \times 10^{16}$ ( <i>atm cm</i> <sup>-3</sup> )	784	-0.65
Kawasaki [109]	SSLS	SiC	1415-1500	$1.6 \times 10^{18}$ ( <i>atm cm</i> <sup>-3</sup> )	801, (810)	-0.24
Rhim [87]	OD	None (ESL)	1180-1510	Vac $< 10^{-6}$	875	-0.22
Mukai, Hibiya [110]	BD, SD	BN	1420-1500	$5 \times 10^{-16} - 10^{-13}$	816	-0.80

The temperature dependence of the surface tension of molten Si studied by Zhou et al. [111] using an upgraded electrostatic levitator at a vacuum of  $\sim 7 \times 10^{-6}$  mbar showed that it can be expressed by single fitting Equation (2.8).

$$\gamma(T) = 721.13 - 0.0615 \times (T - T_m) \quad mN/m \quad (1459K < T < 1845K) \quad (2.8)$$

The authors attributed their much lower value of the surface tension to the differences in the partial pressure of oxygen.

Mukai et al. [110] measured the effect of partial pressure of oxygen on the surface tension of molten Si in the temperature range of 1693 to 1873 K and  $P_{O_2}$  in the range of  $10^{-25}$  to  $10^{-14}$  MPa using the sessile drop method on a high purity BN substrate. In Figure 2.8, it can be observed that the change in surface tension is very low in the range of  $P_{O_2} \leq 10^{-22}$  MPa. As the partial pressure increases from  $10^{-22}$  to  $10^{-20}$  MPa, the surface tension decreases remarkably and increases slightly with further increase in partial pressure.

### 2.5.3 Viscosity of Si

Due to the high melting temperature of Si, the viscosity measurements of the molten Si are usually done using an oscillating viscometer. In a typical oscillating viscometer [112], a body, typically hollow or solid cylinder, a solid disc, or a sphere is suspended on a suspension wire to form a torsion pendulum. In vacuum, this pendulum can oscillate indefinitely once it's made to oscillate in horizontal plane with the torsion wire as axis of rotation. However, when oscillating in the fluid, for the same pendulum the amplitude of oscillation will continuously decrease and will eventually come to halt. The time period of oscillation will remain the

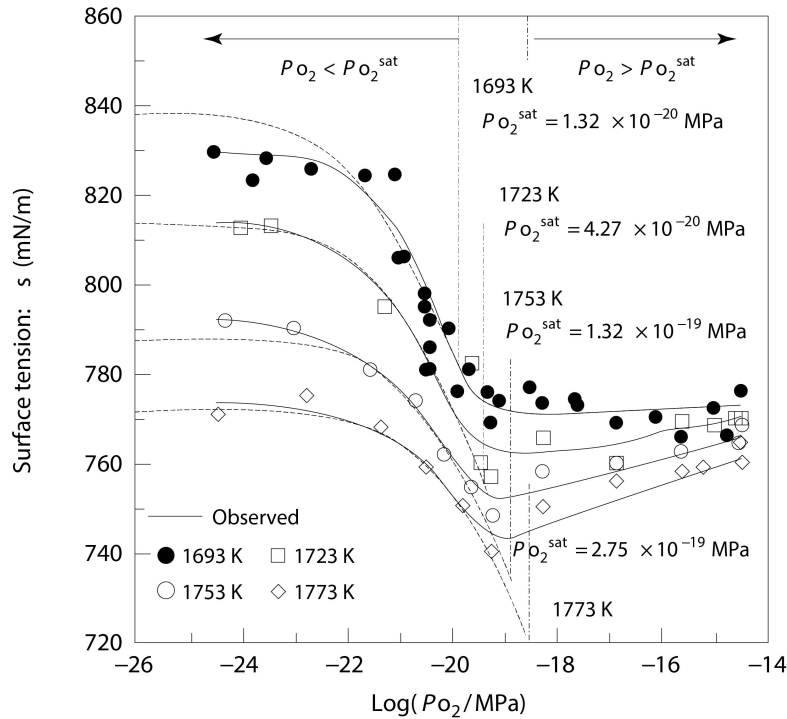


Figure 2.8 – Surface tension of molten Si as a function of partial pressure of oxygen at various temperature [110].

same during motion but will be slightly higher than that obtained in the vacuum. The viscous forces exerted by the fluid are responsible for the decrease in oscillation amplitude and are a function of the viscosity of the surrounding fluid and the geometry of the oscillating body. This arrangement is referred to as an absolute oscillating viscometer since it measures the viscosity of the fluid in terms of dimensions of oscillating body, measured time period and decrement in amplitude without reference to the viscosity of any other fluid. A schematic representation of a state of the art oscillating viscometer is shown in Figure 2.9.

Silicon being the most important semiconductor material, its viscosity has been studied by various researchers extensively [84, 113–115]. In the literature it is observed that the reported values show variations based on the crucible material used for the experiments. The literature values showed big discrepancy where the crucible material used were alumina ( $\text{Al}_2\text{O}_3$ ) [84], pyrolytic boron nitride (PBN) [114], SiC and PBN [115]. A more extensive study with various crucible materials such as silicon carbide (SiC), graphite (C), highly sintered alumina ( $\text{Al}_2\text{O}_3$ ), silicon nitride ( $\text{Si}_3\text{N}_4$ ), hot pressed boron nitride (BN), quartz ( $\text{SiO}_2$ ) and 8 mol% yttria stabilized zirconia (8 mol%-YSZ) was done by Sato et al. [113]. The results of their studies along with the few mentioned above are shown in Figure 2.10. The viscosity of Si shows a good Arrhenius behavior with temperature.

The temperature dependence of the viscosity in mPa s of molten Si is defined in the Equa-

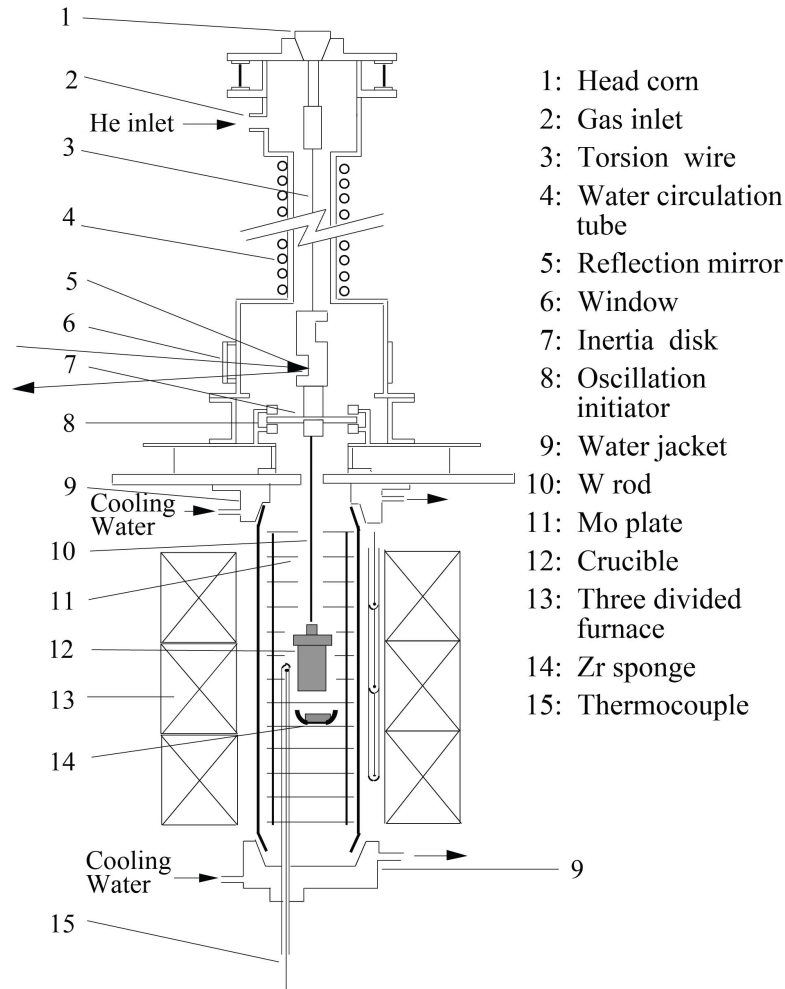


Figure 2.9 – Schematic representation of the oscillating viscometer (reproduced from [113]).

tion (2.9) with activation energy  $E_\eta = 15.7 \text{ kJ/mol}$  [113].

$$\log \eta = -0.727 + 819/T \quad (2.9)$$

The molten Si has a unusually low viscosity and low activation energy for viscous flow. Usually a metal with a higher melting point shows higher viscosity and activation energy. Iron has a viscosity of  $5.9 \text{ mPa s}$  at  $1811 \text{ K}$ , whereas Si has one order lower viscosity of  $0.575 \text{ mPa s}$  at the melting point of  $1683 \text{ K}$  [113].

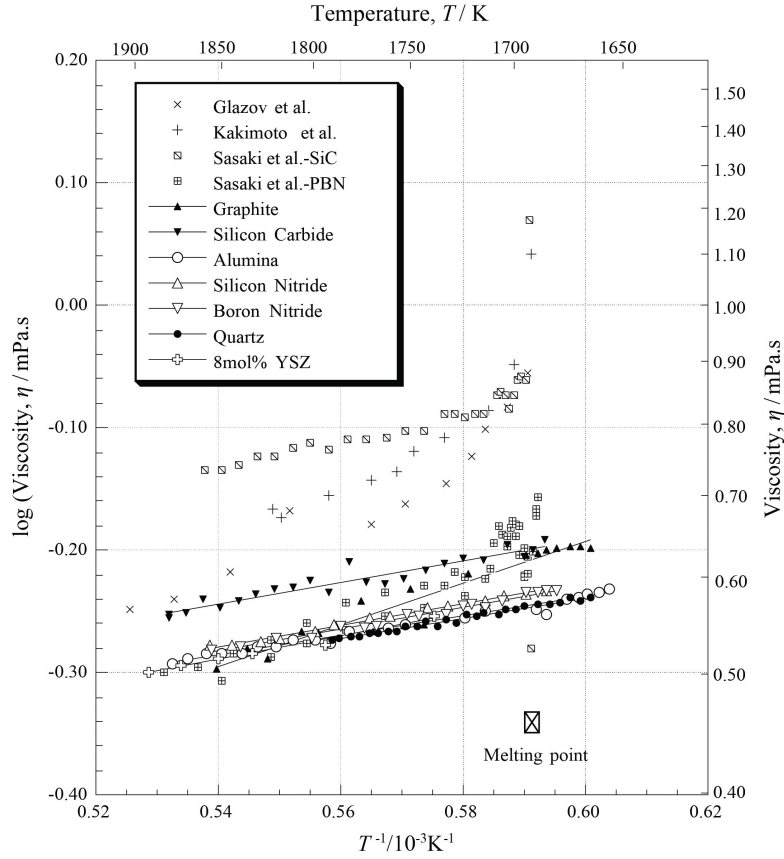


Figure 2.10 – Viscosities of molten silicon at different temperature obtained for various materials of crucibles (reproduced from [113]).

## 2.6 Wetting at high temperature

Wetting by liquids of a solid surface is usually characterized by its contact angle  $\theta$  as defined in Figure 2.11. The result of the minimal energy state is given by the Young (or Young-Dupré) equation (see Equation (2.10)), where  $\gamma_{SV}$  is the surface energy between solid and gas phases,  $\gamma_{SL}$  is the surface energy between solid and liquid phases, and  $\gamma_{LV}$  is the surface energy of the liquid–gas surface. [116–118].

$$\cos \theta = \frac{\gamma_{SV} - \gamma_{SL}}{\gamma_{LV}} \quad (2.10)$$

In general, the system is defined as non-wetting when the contact angle is more than  $90^\circ$  while a wetting system has a contact angle less than  $90^\circ$ .

### 2.6.1 Sessile drop technique

Sessile drop experiments are relatively simple and widely used technique to have a quantitative measure of wetting behavior of chemically inert as well as reactive systems. The experiments

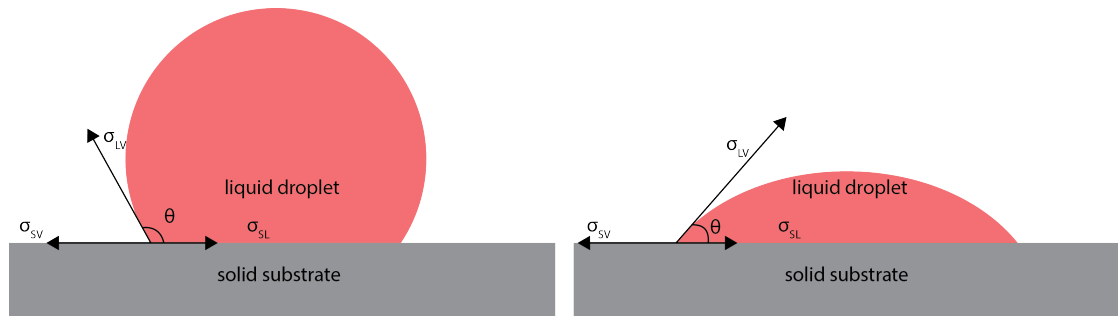


Figure 2.11 – Schematic of liquid droplet on solid substrate showing a non-wetting system on the left and a wetting system on the right.

usually involve putting a liquid droplet with volume ranging from 0.005 to 5 ml [119] on a horizontal solid substrate. The droplet can be formed by melting the metal on substrate as illustrated in Figure 2.12 or by dispensing a pre-molten liquid droplet using special techniques. The contact angle and its evolution over time is the most important quantity obtained by sessile drop experiments. A larger droplet can also be used to measure the liquid surface energy ( $\sigma_{LV}$ ) provided the density of the liquid is known. The drop profile is observed by some sort of goniometer and the contact angle is usually measured with still, cine, video or x-ray camera. These experiments are performed in either inert atmosphere or in vacuum. The droplet sometimes needs illumination to obtain a good contrast but at higher temperatures the self-illumination of the droplet is sufficient to get a good quality image. The liquid front moves over the substrate surface to reach the equilibrium configuration.

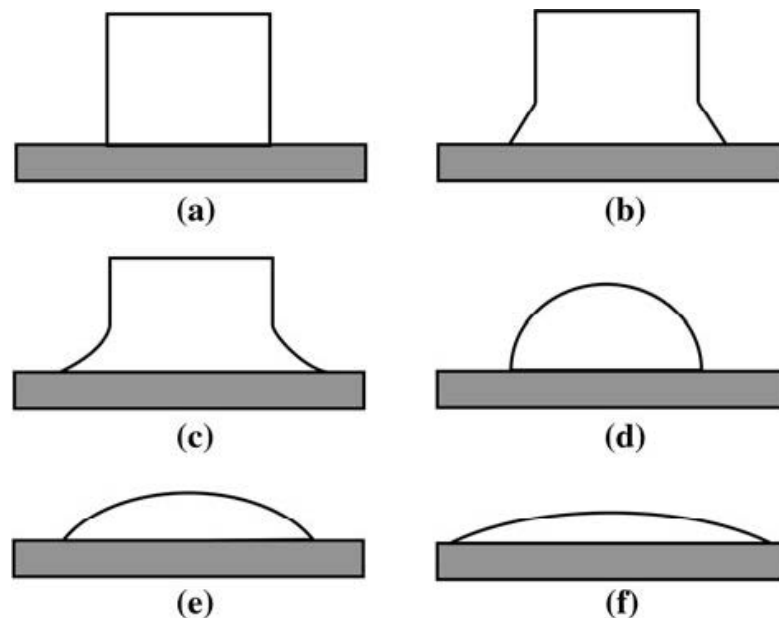


Figure 2.12 – Schematic representation of the melting process of silicon and its spreading on the graphite substrate. (a) before melting, (b) start of melting, (c) during melting, (d) complete melting, (e) during spreading, and (f) stabilization (reproduced from [120]).

A sessile drop experiments can be conducted in various forms as shown schematically in Figure 2.13 [119]. In the classical sessile drop technique as shown in Figure 2.13(a), the sessile material is placed onto the substrate and heated above its melting temperature. While conceptually alloys can also be formed in-situ (Figure 2.13(b)) it is preferable to provide the alloy in its homogenized, prefabricated form. The in-situ alloying is of interest if the reactive species would otherwise react with the substrate in solid state. In the dispensed drop technique the metal or alloy is melted in an inert ceramic tube and dispensed on the substrate through a small hole by applying back pressure via inert gas or a plunger as seen in Figure 2.13(c). This technique helps in getting rid of oxide films by disrupting it during dispensing. Another interesting technique is melting the material to form a droplet on an inert substrate and then later transfer it to the reactive substrate by raising and lowering the substrate as shown in Figure 2.13(d). The configuration in Figure 2.13(e) can be used to determine advancing and receding contact angle by studying the hysteresis effect during raising and lowering of the substrate. With lower melting temperature liquids, the tilted substrate can be used to measure the advancing and receding contact angle as shown in Figure 2.13(f). For a small droplet when the effect of gravity is negligible, the drop profile is a spherical cap, the contact angle can be calculated by using Equation (2.11), where,  $\theta_{\text{calc}}$  is calculated contact angle,  $H$  is the height of the droplet and  $D$  is the diameter of the droplet in plane of contact with substrate.

$$\theta_{\text{calc}} = \arctan\left(\frac{2H}{D}\right) \quad (2.11)$$

The texture and roughness of the substrate also affects the wetting characteristic by liquids. From energy considerations one finds that for non-wetting systems a rough surface increases the contact angle and for wetting systems usually decreases the contact angle. However, the equilibrium thus determined may not be reached due to intermediate metastable situations during spreading. The wetting at high temperature study is of high importance in various industrial practices such as brazing, soldering, coating, and composites manufacturing by infiltration [121–125]. Several researchers have focused on studying the wetting of various metals and alloys on ceramic substrates to make composite materials [69, 123, 126–130].

### 2.6.1.1 Other parameters obtained from sessile drop experiments

The surface tension of high melting point liquids can easily be calculated using the sessile drop method, which otherwise would need a more complicated and expensive setup. Kingery et al. [98] demonstrated that the value of surface tension of higher melting point elements like silicon, iron and nickel can be evaluated with accuracy of  $\pm 2\text{-}3\%$ .

The effects of temperature on liquid surface energies can also be measured using sessile drop experiments. However, the reliability is not good since it needs several hundred degrees of rise in temperature to measure the change in droplet shape reliably.

The profile measurements of sessile drops can be used to calculate the density of the liquid

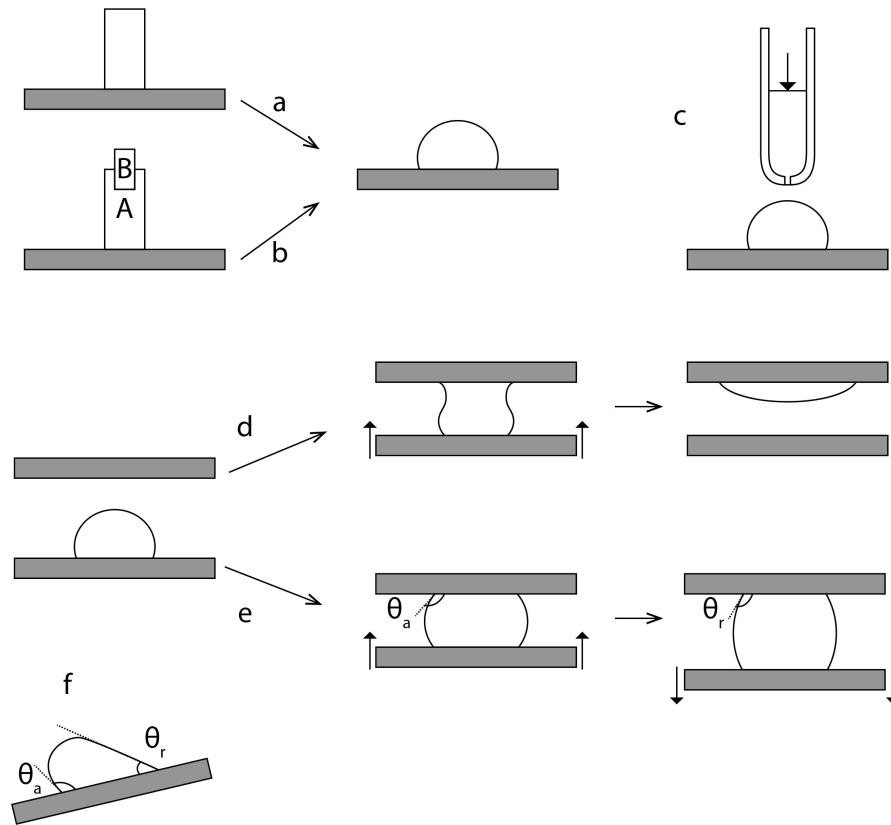


Figure 2.13 – Methods of conducting sessile drop experiments: (a) classical technique, (b) in situ alloy formation, (c) dispensed drop, (d) transferred drop, (e) transferred drop, (f) tilted plate (figure reproduced from [119]).

by measuring the volume and using known mass of material provided that the losses due to evaporation are negligible. Sessile drop experiments are also used to derive the quantities describing spreading and penetration phenomenon like adhesion and work of immersion.

### 2.6.2 Reactive wetting of carbon by Si

Wettability of Si with carbon has been studied for a couple of decades in order to produce low-cost solar cells where graphite or SiC are mainly used as die material [131]. Several researchers have studied the wettability of Si with various types of carbon and graphite materials [120, 132–139]. As discussed before, the wettability of liquids is usually quantified using the contact angle  $\theta$  and is often measured using sessile drop experiments. It has been observed that the wetting of carbon by Si is reaction controlled also referred as reactive wetting. Initially the carbon is not wetted by Si with initial contact angles in the range from  $120^\circ$  to  $146^\circ$  [132, 134]. As soon as the liquid Si comes in contact with C, it starts to react to form  $\beta$ -SiC. The contact angle further reduces with time as the droplet spreads on the substrate. The final contact angle is referred to as the equilibrium contact angle. The wetting behavior depends on the type of substrates such as glassy or vitreous carbon, pyrolytic graphite, and natural graphite. It also



depends on the surface roughness and porosity of the material. The equilibrium contact angle decreases with increasing surface roughness, in some cases it decreases down to 0° which is probably due to Si infiltration into the porous graphite substrate [120]. The equilibrium contact angles reported by few authors for liquid Si on glassy carbon and graphite substrates are summarized in Table 2.3

Table 2.3 – The equilibrium contact angles of liquid Si on glassy carbon and graphite substrates.

Author	Glassy/ vitreous carbon	Graphite
Li and Hausner [134, 135]	10° – 40° (Ra < 0.005 μm)	35° (Ra = 0.005 μm) 3° (Ra = 3.18 μm)
Dezellus et al. [132]	36° (Ra = 5 nm)	35° – 40° (Ra = 2–4 nm)
Whalen and Anderson[137]	40° – 50°	5° – 15° (pyrolytic graphite)
Naidich et al. [118]		15°
Ciftja et al. [120]		30° (Ra < 0.1 μm)

Voytovych et al. studied the reaction of Si with graphite and vitreous carbon from the melting temperature to 1600 °C in an inert He atmosphere using sessile drop technique and proposed a three stage reaction mechanism resulting in formation of SiC at the interface [136]. They also observed two distinct types of SiC morphologies in agreement with Ciftja et al. [120]; one which exists at the interface and consist of very fine SiC particles and the second with much larger and compact crystals growing from the interface into the liquid Si (see Figure 2.14). They discussed the mechanism of permeable SiC layer formation at the interface by nucleation and growth followed by growth of the reaction layer by diffusion of C through permeable SiC. The SiC layer thickness was 15-25 μm for polycrystalline graphite and approximately 10 μm for vitreous carbon at 1600 °C for a holding time of 20 min. Another important finding was that the layer is impervious to liquid silicon, making time practically a redundant factor once the layer thickness has reached a certain value. Further thickening, which proceeds very slowly by grain boundary diffusion of C through SiC, is almost negligible. They derived a relation between reaction layer thickness and time from Fick's Law and the Gibbs–Helmholtz equation, which is represented by the Equation (2.12)

$$e^2(t) = \left( D_C^{gb} \frac{2\delta}{d} \ln \frac{1}{a_{(C)}^*} \right) t \quad (2.12)$$

Where,  $e$  is SiC layer thickness,  $t$  is time,  $D_C^{gb}$  is grain boundary diffusion coefficient of C through SiC,  $d$  is the average size of SiC grains,  $\delta$  the thickness of the grain boundary and  $a_{(C)}^*$  the activity of carbon in the liquid in equilibrium with SiC. They also reported the reaction layer thickness for Si–Al (25 at.% Si) on vitreous carbon to be 5-6 μm at 1000 °C for 60 min holding time. Arjan et al. [120] also did similar experiments with graphite substrates of different surface roughness. These experiments show the complexity of wetting affected not only by the type of carbon but also by the surface roughness. The wetting behavior was completely

different for rough and smooth surfaces. As reported by different authors, there is also a large variance in reported contact angle [132, 135, 137]. Different techniques for wettability studies have been reviewed by Komolafe and Medraj [140]. In their opinion, the level of understanding of non-reactive wetting is very good as compared to the complex reactive wetting systems. The early stage of reactive wetting is generally very quick in the beginning and does not depend on any reaction. At the later stages, the kinetics is rather controlled by the nature of the reaction. The reaction may involve dissolution, intermetallic formation, or combination of both. The microstructural changes might also happen in fraction of seconds. Therefore, it is rather difficult to find a single model that can describe the kinetics of all the stages involved in reactive wetting.

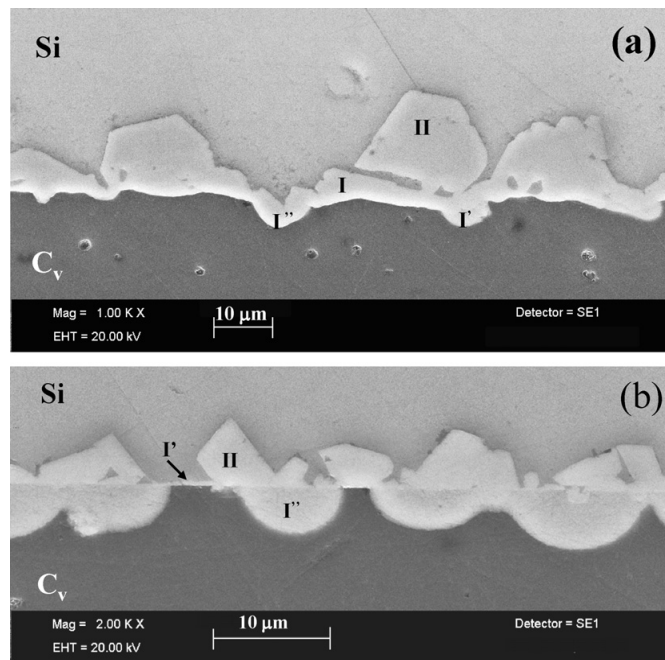


Figure 2.14 – SEM micrograph of the reacted interface for a silicon/vitreous carbon couple after 10 min at 1430 °C: (a) at the centre of the interface (equiaxed zone) and (b) in the periphery (columnar zone) [136].

Similar reaction mechanism to form SiC during the silicon infiltration process was studied by Margiotta et al. [55] using optical microscopy. They proposed a six-step process during LSI that consists of: (i) rapid liquid silicon infiltration, (ii) rapid carbon dissolution by liquid silicon, (iii) rapid silicon carbide formation, (iv) completion of a continuous silicon carbide layer at all silicon–carbon interfaces, (v) (slow) carbon diffusion through the continuous silicon carbide layer to react with liquid silicon, (vi) formation of cracks within the silicon carbide structure that were filled with liquid silicon.

In the most recent studies, Hofbauer et al. [141] proposed a slightly different reaction mechanism during infiltration, which considers the reaction by vapor phase of Si during infiltration. They infiltrated capillaries with 0.1 to 0.3 mm gap made up of vitreous carbon by silicon

at temperatures ranging from 1500 °C to 1900 °C at different argon pressure ranging from 1 mbar and 500 mbar. They divided the reactive wetting and infiltration into ten steps shown schematically in Figure 2.15.

1. Evaporation and diffusion of silicon: Silicon atoms with kinetic energy greater than the energy of evaporation exit the liquid phase and diffuse in the gas above the meniscus. Si atoms reach the capillary wall by a random walk and strike the solid surface.
2. Si adsorption and nucleation on the C substrate: surface defects or impurities provide energetically favorable sites for adsorption. If the impinging Si atoms find suitable sites with ample resting time, clusters with other Si atoms can be formed and reaction with the C substrate can form SiC. This process is called chemoepitaxy or chemisorption.
3. Crystal growth by transversal movement of the two-dimensional gas of the impinging Si atoms to the edges of the SiC islands: the chemisorption-built SiC nuclei grow in thin circular shape on the carbon surface as single crystals. Gas-phase atoms adsorbed on the surface move up to the edges of the island and react with the C substrate to form SiC
4. Island growth (Volmer-Weber growth): The higher rates of transversal movement along the surfaces and grain boundaries compared to the volume diffusion of C or Si atoms through the SiC layer results in a flat-oriented island growth also known as Volmer-Weber growth.
5. Coalescence of the SiC islands to form a continuous SiC layer: Further growth and coalescence of the SiC islands occurs until the C substrate is completely covered with SiC - marked as SiC I in Figure 2.15. The rims of the SiC islands form the boundaries between grains.
6. Partial flaking of SiC crystals: additional Si atoms are assumed to be introduced into the grain boundaries, where they form new SiC and generate compressive stress in the SiC layers. These stresses can lead to a detachment of SiC crystals due to the low adhesive forces between the SiC crystals and the carbon substrate. The disconnected crystals slip into the silicon melt, where they are being dissolved at the Si / SiC interface and re-precipitated. The flaking mechanism results in a reduction of SiC coverage near the three phase boundary.
7. The remaining SiC crystals act as a diffusion barrier: the large flat crystals of type SiC I protect the substrate from the silicon melt attack. There are many grain boundaries between these large crystals which provide a diffusion path for rapid growth of SiC layers. The exposed surfaces of the substrate are slowly transformed into SiC, and this is why the three-phase line lags behind the boundary between zones I and II.
8. Carbon diffusion through the SiC layer: C atoms diffuse through the pore surfaces of the SiC layer and along the SiC grain boundaries and react with Si at the Si / SiC interface to form large SiC crystals shown in Figure 2.15 as SiC II.

9. Pore formation in the SiC III layer: the voids formed in the carbon substrate after the diffusion of carbon atoms from the substrate through the SiC layer are partially compensated by the counter-diffusion of Si atoms from the melt into the pores where they react to SiC with residual carbon. The pore formation in SiC III is unavoidable due to lesser molar volume of SiC as compared to the reactants Si and C. SiC II however has no pores since there is always the possibility of inflow of molten Si when cavities are formed by Si diffusing away.
10. Si diffusion through the SiC layer: Silicon diffuses to the C / SiC interface from the melt along the grain boundaries and at the pore surfaces and reacts with C to form SiC III. Inside SiC III pores, Si can form SiC with C atoms diffusing in the opposite direction and thus subsequently filling the pores.

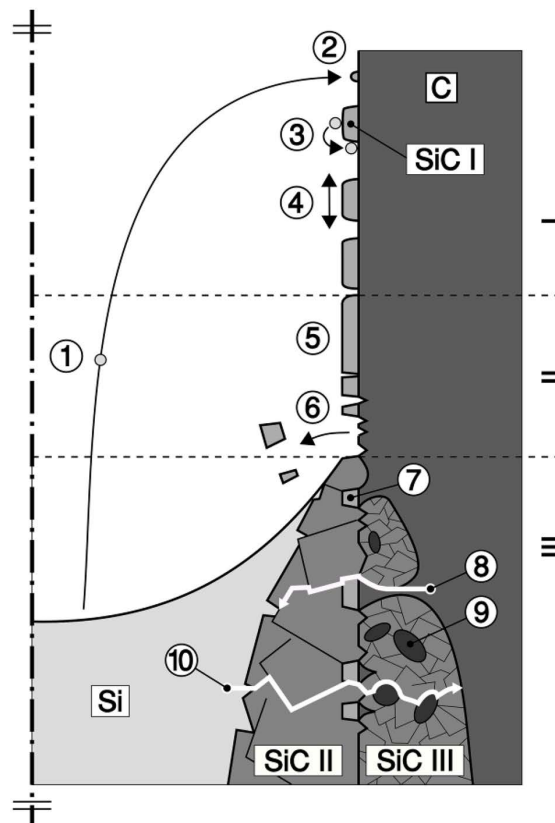


Figure 2.15 – Mechanisms at the infiltration front in carbon channel divided in zones I to III. - 1: Si evaporation and diffusion, 2: Si adsorption and nucleation on the C substrate, 3: crystal growth by transversal movement of the two dimensional gas of the impinging Si atoms to the edges of the SiC islands, 4: island growth (Volmer-Weber growth), 5: coalescence of the islands to a continuous SiC layer, 6: partial flaking of the SiC crystals, 7: remaining SiC layer acts as a diffusion barrier, 8: Carbon diffusion along the SiC grain boundaries, 9: pore formation in the SiC layer, 10: silicon diffusion along the SiC grain boundaries (reproduced from [141]).

### 2.6.3 Wetting of SiC by Si

Liquid Si is essentially nonreactive with SiC. Both hot pressed and self-bonded SiC shows good wetting by Si [137]. In literature, contact angles from 30° to 54° are reported for Si on various SiC substrates such as polycrystalline, monocrystalline,  $\alpha$  – SiC and  $\beta$  – SiC [129, 130, 134, 137, 138, 142–148]. Yupko et al. found that the surface roughness of SiC plays a minor role in wetting [148].

Nonetheless, during the interaction between Si and SiC, a slight dissolution of SiC in Si occurs, the mole fraction of carbon dissolved in Si in equilibrium with SiC close to melting point of Si is about  $2.9 \times 10^{-4}$ . The SiC at room temperature is usually instantaneously covered with nanometer-thick oxide layer. Similar to solid Si, depending on the partial pressure of oxygen at a given temperature, SiC also displays a passive to active oxidation transition. The passive oxidation reaction is as shown in Reaction [2.5]. And the reduction of the SiO<sub>2</sub> passive layer by the underlying SiC results in deoxidation of SiC as shown in Reaction [2.6] [149].



Both Si and SiC surfaces become skin free in a commercially pure Ar atmosphere ( $P_{\text{O}_2} \approx 10^{-5}$  atm) above 1100 °C [13, 92]. Therefore, at the melting point of Si both Si and SiC are deoxidized resulting in an instantaneous equilibrium contact angle [92]. Impurities of water vapor in the furnace atmosphere strongly increase the growth rate of the silica layer on SiC, thereby delaying the passive-to-active oxidation transition [13]. In high vacuum, depending on time and temperature a nanometer to tens of nanometer thick graphite layer is formed due to loss of Si from SiC surface by evaporation [90].

Roger et al. [150] studied the interaction of liquid silicon on surfaces of  $\alpha$  – SiC and  $\beta$  – SiC at 1450 and 1600 °C. They observed that large faceted SiC crystals are formed on the surface of molten Si and on the substrate. These grains are mainly formed by a temperature dependent dissolution and growth mechanism of the SiC substrate. In Figure 2.16, various stages involved in the formation of SiC crystals on the surface of molten Si and at the surface of substrate are shown. The solubility of carbon in molten silicon decreases with temperature, the liquid is then supersaturated in colder areas, which is responsible for the growth of large SiC crystals in the coldest regions. All the experiments were carried out in a inductively heated graphite susceptor, in that case the furnace atmosphere can also act as a source of carbon.

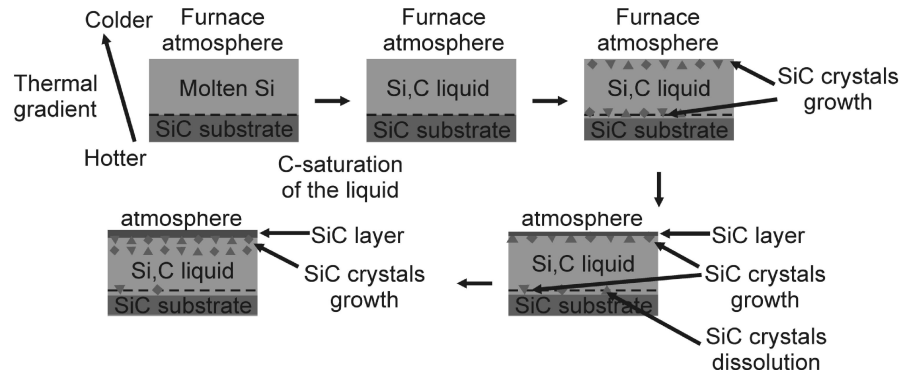


Figure 2.16 – The stages of the interaction between molten Si on SiC. The furnace's atmosphere is a source of carbon (figure reproduced from [150]).

#### 2.6.4 Kinetic aspect of reactive infiltration

Einset [151] reported capillary infiltration rates of silicon into a porous graphite medium manufactured by tape casting and pyrolysis. The article proposes that the rate of infiltration of Si in porous media made up of particles of C and SiC can be predicted by mercury porosimetry and organic liquid infiltration rate measurement combined with a simple, single-pore model based on Washburn's analysis. In this model, the infiltrated distance  $x$  is parabolic in time and given as:

$$\frac{x^2}{t} = \frac{\gamma \cos(\theta)}{2\mu} r \quad (2.13)$$

where,  $\mu$  is the fluid's viscosity,  $\gamma$  is the surface tension,  $r$  is the pore radius and  $\theta$  is the wetting angle. However, the real porous medium cannot be modeled just with simple Washburn analysis since it is a network of interconnected capillaries with varying diameter rather than a single capillary of uniform cross section. Einset proposed an effective pore diameter using the Hagen-Poiseuille equation and Dullien's model [152] given as:

$$D_{\text{eff}} = \frac{1}{3} \left[ \sum_k D_k \right]^2 \left[ \sum_k D_k \sum_j \left( \frac{D_k}{D_j} \right)^3 \right]^{-1} \quad (2.14)$$

where the summations are over the number of segments of the repeating pore unit.

Nevertheless, the model has several assumptions and the measurement of effective pore diameter is very sensitive [151, 153]. Einset also found that the infiltration of Si is analogous to that of infiltration of organic liquids like acetone, methanol, toluene and cyclohexane. This is surprising since Si reacts with the preform while the organic liquids are non-reactive. This highlight that the liquid ingress in his preforms was not controlled by the reaction rate limiting step. The rate of infiltration of Si was measured by tracking the infiltration front using the change in temperature due to the exothermic reaction. The square of the infiltration distance

was plotted against time and the experimental data was fit to the equation  $x^2 = Kt$  where infiltration rate constant is  $K = 3.5 \times 10^{-5} \text{ m}^2/\text{s}$ .

Sergi et al. [154] did Si infiltration in millimeter size drilled capillaries in solid C preforms. The experiment helped them to validate a Lattice-Boltzmann model for capillary infiltration. The reaction mechanism of formation of SiC is also observed to be controlled by diffusion of C through newly formed SiC. The thickness of the reaction-formed SiC layer Figure 2.17 was between 6 to 25  $\mu\text{m}$ . The pore closure phenomenon could not be observed since the capillary size was much larger than the SiC layer thickness

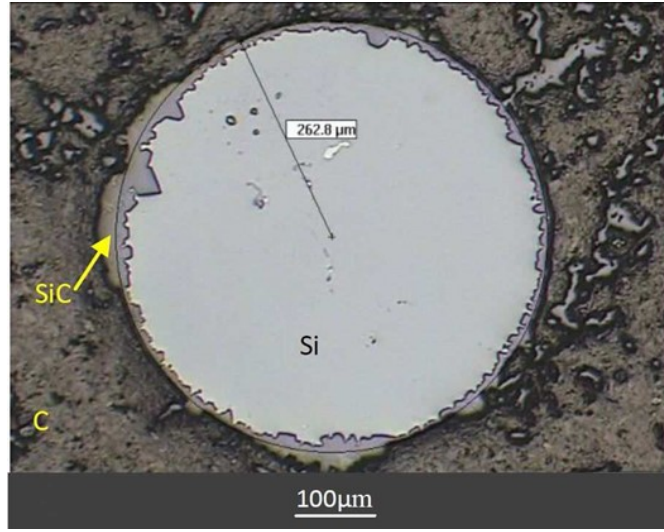


Figure 2.17 – Cross-section of infiltrated channel of diameter 0.5 mm with a dwell time of 24 h at 1450°C. The circle represented with a solid line indicates the initial diameter. The process of C dissolution leads to an increase of the diameter by  $9.2 \pm 4 \mu\text{m}$  on average (before  $516 \pm 3 \mu\text{m}$ ) [154].

Reitz et al. [75] studied the flow behavior of pure Si and eutectic Si- 16at%Y alloy in porous graphite tubes having an inner diameter of 1.5 mm and a porosity of 18% with wall thickness of 1 mm at 1450 °C. The maximum heights reached are similar: ~70 mm for Si, and ~60 mm for Si-Y. The climbing rates were however notably different: ~2.4 mm / min for Si and ~14 mm / min for the alloy. The infiltration depth in the porous wall varied from 100 to 300  $\mu\text{m}$  for both pure Si and Si-Y alloy. They described this system, on the premise that throughout the infiltration phase the contact angle is favorable and consistent and that the flow rate is regulated by the drag, using Poiseuille's law as seen Equation (2.15).

$$\frac{dh}{dt} = \frac{d_k^2}{32\eta h} \left( \frac{4\gamma \cos\theta}{d_k} - \rho gh \right) \quad (2.15)$$

wherein  $dh/dt$  is the vertical flow rate,  $d_k$  is the capillary diameter,  $\eta$  is the viscosity of the liquid,  $\gamma$  is the liquid/gas interfacial energy,  $\theta$  is the contact angle between the liquid and the solid,  $\rho$  is the density of the liquid, and  $g$  is the gravitational constant. Reaction of both

pure Si and Si-Y alloy at the tube wall and within the infiltrated graphite results in a bimodal SiC layer. The thickness of the SiC layers increases with time until 30 minutes. This SiC layer then maintains a constant thickness of  $50\ \mu\text{m}$  while the grains coarsen for next 150 minutes as seen in Figure 2.18. The total duration of the experiment is 180 minutes. They observed formation of high melting point silicides, YSi in the pores and  $\text{Y}_3\text{Si}_5$  forms within the bulk metal in the tube. The depth of infiltration into the porous graphite with micrometer-sized channels is controlled by choking due to reaction formed SiC. As the choking occurs within seconds, further reaction happens without continued ingress of the alloy.

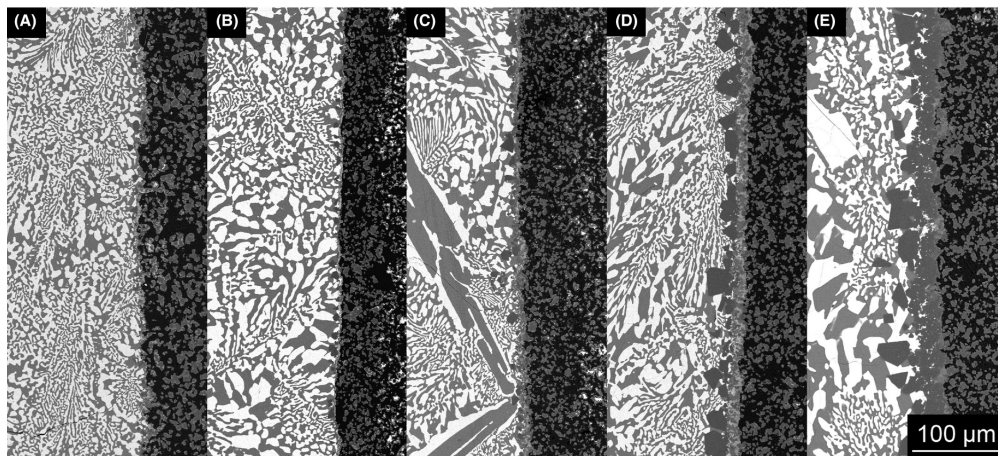


Figure 2.18 – Growth of SiC layer at the graphite wall in a Si-Y alloy infiltrated sample after (A) 1 minute, (B) 5 minutes, (C) 10 minutes, (D) 30 minutes, and (E) 180 minutes of reaction time. (figure reproduced from [75]).

Hofbauer et al. [141] conducted in-situ observation of infiltration of gap capillaries, made from glassy carbon, at different temperature and argon pressure in a special thermo-optical measuring furnace. They observed constant infiltration rates which are in contradiction to the rates predicted by the Washburn equation by previous authors [151, 153]. In Washburn's model, the rate of ingress slows down due to the viscous drag. Furthermore, the increasing hydrostatic pressure causes an additional slowing down. Washburn's model is based on a good wetting by liquid meaning that the contact angle is less than  $90^\circ$ . However, various authors have reported reactive wetting behavior of carbon [132, 155] where, initially carbon is not wetted by silicon until it reacts instantaneously to form SiC. The wetting angle decreases slowly and reaches a steady value between  $9^\circ$  and  $44^\circ$ , which brings us to the conclusion that wetting of carbon by silicon is reaction limited and the rate-determining process, in the present case. They also reported a strong pressure dependence of the infiltration rate, which cannot be explained by the reaction of silicon melt with carbon. They confirmed by their gap capillary experiments that the rate of evaporation increases with increasing saturation vapor pressure and decreases with increasing square root of temperature. They concluded that the Si evaporation plays a dominant role in the kinetics of Si infiltration into carbon preforms and the infiltration rate depends on the temperature and the pressure as well as the surface roughness of the wetting substrate.



## 2.7 The Si-Zr alloy system

The Si-Zr binary system got attention initially due to magnetic ferro-silicon alloys and inoculants used in steel making. In the advent of ultra-high temperature ceramics the system is getting more attention in recent years due to their considerable stability and oxidation resistance [156–159]. Following equilibrium phases can be found using the phase diagram calculated by Chen et al. [156]: Si,  $\text{Si}_2\text{Zr}$ ,  $\alpha\text{-SiZr}$ ,  $\beta\text{-SiZr}$ ,  $\alpha\text{-Si}_4\text{Zr}_5$ ,  $\beta\text{-Si}_4\text{Zr}_5$ ,  $\text{Si}_2\text{Zr}_3$ ,  $\text{Si}_3\text{Zr}_5$ ,  $\text{SiZr}_2$ ,  $\text{SiZr}_3$ ,  $\alpha\text{-Zr}$  and  $\beta\text{-Zr}$ . The occurrence of few other intermetallic phases such as  $\text{Si}_5\text{Zr}_6$  and  $\text{SiZr}_4$  was also proven, however, there exist some ambiguities with regard to their proper stoichiometry [158]. The binary phase diagram of Si-Zr system calculated using THERMOCALC is shown in Figure 2.19 for which the thermodynamic database file (tdb) was provided by Chen, H. M. (School of Material Science and Engineering, Central South University, China), the author of most recent assessment of the Si-Zr phase diagram. Figure 2.20 shows calculated phase diagram of the Si – Zr binary system with experimental data.

Zirconium, referred to as  $\alpha\text{-Zr}$ , has a hexagonal close packed structure (hcp, A3) at normal pressure and room temperature, which at 863 °C changes to  $\beta\text{-Zr}$ , a body centered cubic modification of Zr. Si exhibits cubic diamond type structure at the same condition. Further details regarding crystal structure and lattice parameters of phases occurring in Si-Zr binary phase diagram are listed in [158].

In Table 2.4 the invariant reactions occurring in Si-Zr binary system are listed with corresponding temperature and composition. However, there are slight discrepancies in liquid composition reported by different authors. The one in particular worth noticing is a deviation in the Si – rich eutectic composition, which fluctuates from 6.70 at.% Zr [157], through 8.19 at.% Zr [156], up to 10 at.% Zr [158].

Table 2.4 – Invariant reactions in the Si – Zr system [156, 158].

Reaction	Type	Liquid composition % at. Zr	Temperature °C
$\text{L} \leftrightarrow \text{Si} + \text{Si}_2\text{Zr}$	Eutectic	8.19	1345.70
$\text{L} + \beta\text{-SiZr} \leftrightarrow \text{Si}_2\text{Zr}$	Peritectic	19.70	1620.00
$\text{L} + \beta\text{-Si}_4\text{Zr}_5 \leftrightarrow \beta\text{-SiZr}$	Peritectic	47.20	2207.60
$\text{L} + \beta\text{-Si}_4\text{Zr}_5 \leftrightarrow \text{Si}_2\text{Zr}_3$	Peritectic	63.10	2212.40
$\text{L} + \text{Si}_2\text{Zr}_3 \leftrightarrow \text{Si}_3\text{Zr}_5$	Peritectic	67.80	2176.30
$\text{L} + \text{Si}_3\text{Zr}_5 \leftrightarrow \text{SiZr}_2$	Peritectic	80.60	1923.98
$\text{L} + \text{SiZr}_2 \leftrightarrow \text{SiZr}_3$	Peritectic	89.60	1651.50
$\text{L} \leftrightarrow \text{bcc-Zr} + \text{SiZr}_3$	Eutectic	92.00	1570.96
$\text{bcc-Zr} \leftrightarrow \text{hcp-Zr} + \text{SiZr}_3$	Degenerated	–	866.00
$\text{Si}_3\text{Zr}_5 \leftrightarrow \text{Si}_2\text{Zr}_3 + \text{SiZr}_2$	Eutectoid	–	1745.30
$\text{L} \leftrightarrow \beta\text{-Si}_4\text{Zr}_5$	Congruent	55.60	2252.00
$\alpha\text{-SiZr} \leftrightarrow \beta\text{-SiZr}$	Polymorphic	–	1461.19
$\alpha\text{-Si}_4\text{Zr}_5 \leftrightarrow \beta\text{-Si}_4\text{Zr}_5$	Polymorphic	–	1859.50

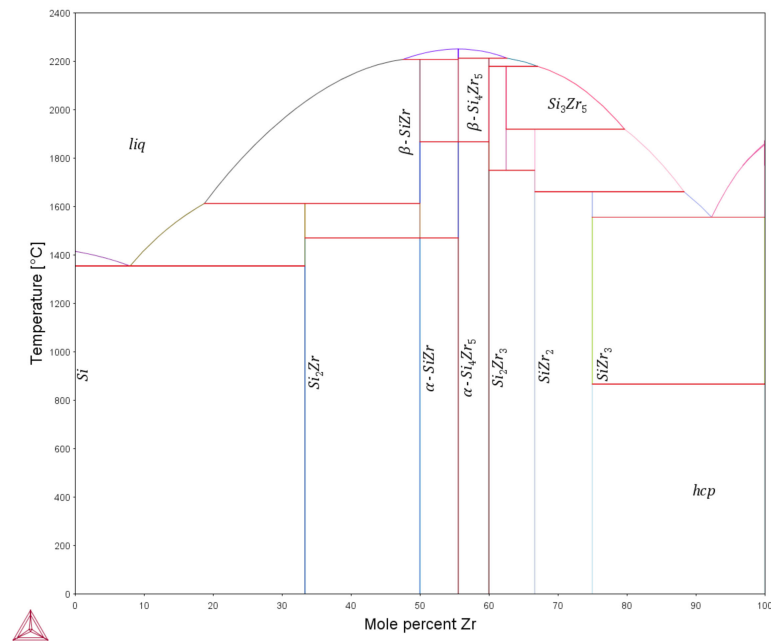


Figure 2.19 – Calculated binary phase diagram of Si and Zr using THERMOCALC. (Thermodynamic database file provided by Chen, H. M., School of Material Science and Engineering, Central South University, China.)

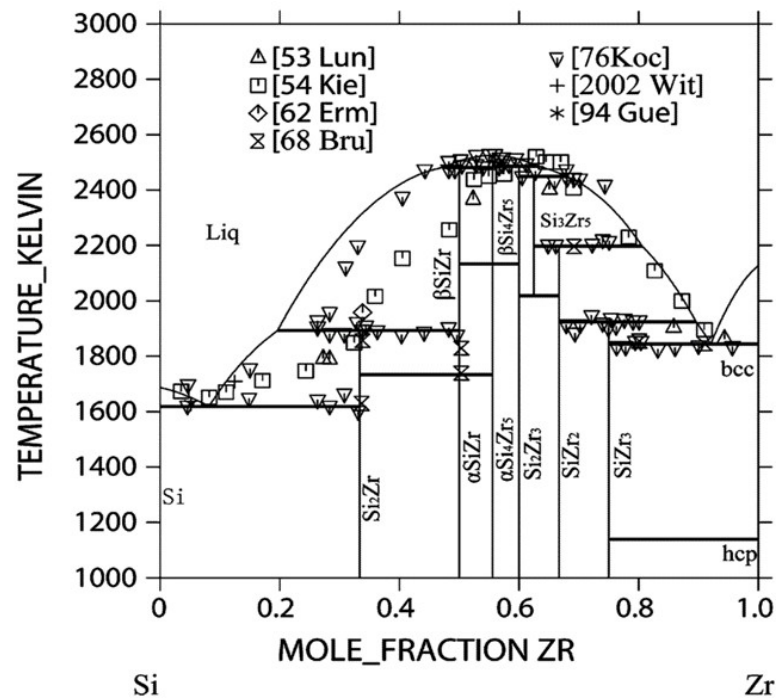


Figure 2.20 – Calculated phase diagram of the Si – Zr binary system with experimental data (reproduced from [156]).

## 2.8 The C-Si-Zr ternary system

Chen et al. [160] have done a thermodynamic assessment of the C-Si-Zr system using ThermoCalc. The isothermal section at 1473 K of calculated ternary phase diagram of C-Si-Zr is shown in Figure 2.21. They found only possible ternary compound as  $\text{Zr}_5\text{Si}_3\text{C}_x$  which was also experimentally reported by Wang et. al [161]. It is worth noting that the first two silicides (in terms of increasing Zr content) are in equilibrium with SiC and that only at higher Zr concentration, by and large above 50 at.% the ZrC phase becomes stable.

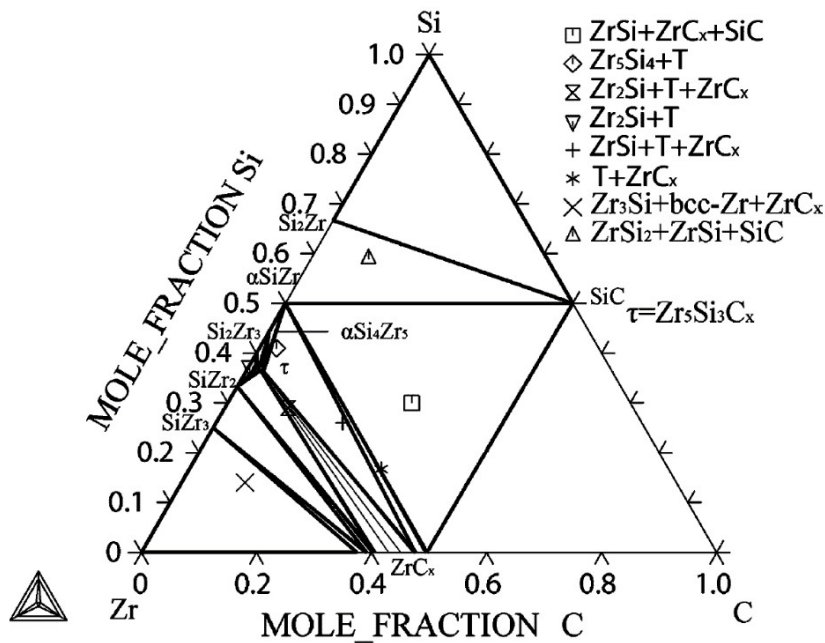


Figure 2.21 – Calculated isothermal section of C–Si–Zr at 1473K with experimental data [161] (reproduced from [160]).

## 2.9 Conceptual considerations

There is a tremendous interest in research related to the reactive infiltration of Si and its alloys to manufacture SiC composites. Based on the available literature, the following points need to be considered while studying the fabrication of fully dense SiC composites via reactive infiltration of Si or Si-alloys into porous carbonaceous preforms.

### 2.9.1 Preform composition

SiC exists in many polytypes (refer to subsection 2.2.1), however, it is the only stoichiometric compound observed in the equilibrium phase diagram of Si and C. Therefore, a full conversion of the porous carbonaceous preform into a dense SiC by reactive infiltration of liquid Si need

precisely the same number of moles of Si as C in the preform. Furthermore, the reaction formed solid SiC has to occupy the volume of solid C or the pores. This introduces another constraint on the amount and the distribution of porosity. Additionally, the size of the C particle has to be such to allow conversion to SiC by reaction on reasonable time scale. The theoretical volume fraction of the pores in a preform to completely convert it into SiC by reaction with liquid Si can be calculated by the extra volume of pores needed for the formation of SiC. The carbonaceous preform can be made up of graphite and/or amorphous carbon or their mixture with density ranging between 2.2 to 1.5 g/cm<sup>3</sup> respectively. Using the densities and molar mass of the reactants and products from the Table 2.5, one gets the increase in solid phase volume fraction due to the formation of solid SiC from 36 % to 57 % for amorphous carbon and graphite respectively, as has been also indicated by Singh et al. [69, 70]

Table 2.5 – Molar volume of Si, C and SiC calculated from their molecular weight and approximate densities from literature.

	C <sub>solid</sub>	+	Si <sub>liquid</sub>	→	SiC <sub>solid</sub>
Molecular weight	12		28		40
Density (g/cm <sup>3</sup> )	1.5 to 2.2		2.5		3.2
Molar volume (cm <sup>3</sup> )	8 to 5.4		11.2		12.5

Most of the times the preforms for SiSiC composites are made up of mixture of graphite, SiC powder and organic binder which is pyrolysed to form the amorphous carbon. The SiC addition may be beneficial in lowering the exothermic reaction temperature (Reaction [2.1]) as well as using denser green preforms. Some of the reported preform compositions and their properties after infiltration are summarized in Table 2.6. One can see from this that the preform characteristics affect greatly the final outcome of the composite for a given infiltrant.

### 2.9.2 The use of Si alloys as infiltrants

The precision of stoichiometric composition needed to manufacture SiSiC without residual Si or unreacted C makes it an almost impossible task. However, in certain applications like brake pads or disks the residual graphite does not harm much. Also, in case of the net shape parts which need no further machining the oxidation resistance is provided by the SiC layer on the surface that provides oxidation resistance by formation of a SiO<sub>2</sub> layer. In that case, one would consider to take an excess amount of C in the preform and process it for excessively long time to force the last bit of Si to react with C to form SiC. Still, we did not see any claim in the literature to where one has obtained SiSiC with no residual Si[48, 164]. This of course has to do with the failure in achieving the exact amount of porosity and stoichiometry of Si and C keeping in mind the diffusion length scale of C and Si in SiC and large difference in the molar volume of the reactants and products.

At this point, it becomes apparent how Si-X alloys may provide a useful alternative by capturing the residual Si in the form of silicides with high melting points. Indeed, by formation of silicides

of variable stoichiometry some latitude can be gained in the volume fraction of pores. The following aspects must be taken into account when selecting the alloying element:

- i) The alloying element must form silicides with higher melting temperature than that of pure Si.
- ii) The activity of the alloying element should be such that the formation of SiC over the formation of the alloying element's carbide is favored. The formation of the carbide of the alloying element will promote the residual Si in the pores.
- iii) The initial concentration of the alloying element should be such that when the reaction between the infiltrant and the preform is complete, the effective concentration of the alloying element in the remaining infiltrant in the pores should be beyond the composition where the first silicide has formed (Figure 2.22).
- iv) The alloying element should not significantly lower the melting point of the  $\text{SiO}_2$  layer formed under oxidizing conditions. The depression in melting point of  $\text{SiO}_2$  might result in poor ablation resistance due to lower viscosity of protective oxide layer.
- v) It might be helpful to chose the concentration of the alloying element near eutectic temperature as it may facilitate the infiltration at lower temperature.

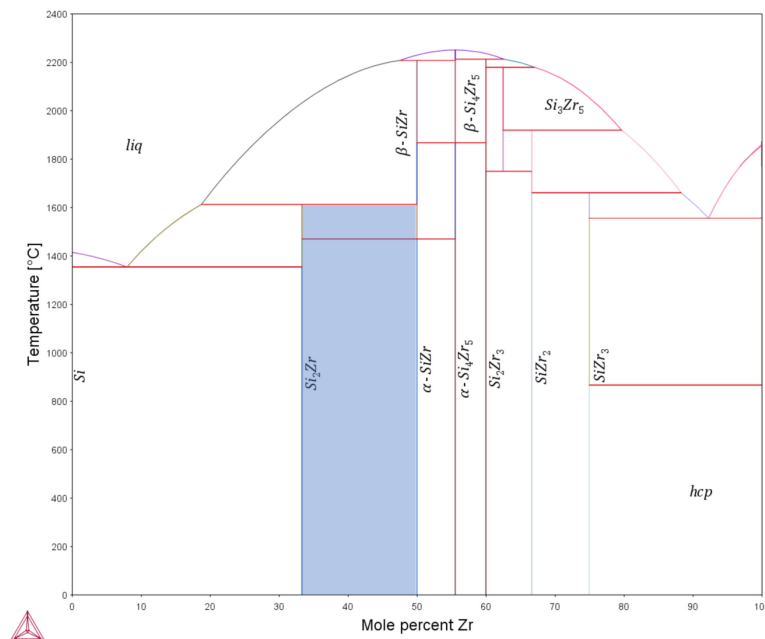


Figure 2.22 – Example of the desired resultant composition (highlighted in light blue color in Si-Zr equilibrium phase diagram ) of the infiltrant after the reaction with preform, which is beyond the composition where the first silicide is formed.

### 2.9.3 Kinetic considerations

There is an apparent contradiction in the literature concerning the kinetics of the reactive infiltration process. Some of the researchers have reported that the infiltration rate follows a parabolic law [57, 154, 165] while others have reported infiltration depth as a linear function of time [62, 75, 141]. It would appear that the two claims are not so contradictory, but complementary. If we consider a pore represented by a carbon capillary of radius  $R$  being infiltrated by liquid Si, in order to obtain the infiltration, the inner surface of the C capillary must have reaction formed SiC layer and at the same time the capillary forces must be large enough to suck in the Si. One could come to think that either of the two things could be rate limiting. In Figure 2.23, two limiting cases where the Si ingress is controlled via triple line velocity characterized by a contact angle larger than equilibrium contact angle and the second one where the Si ingress is limited by the viscous forces.

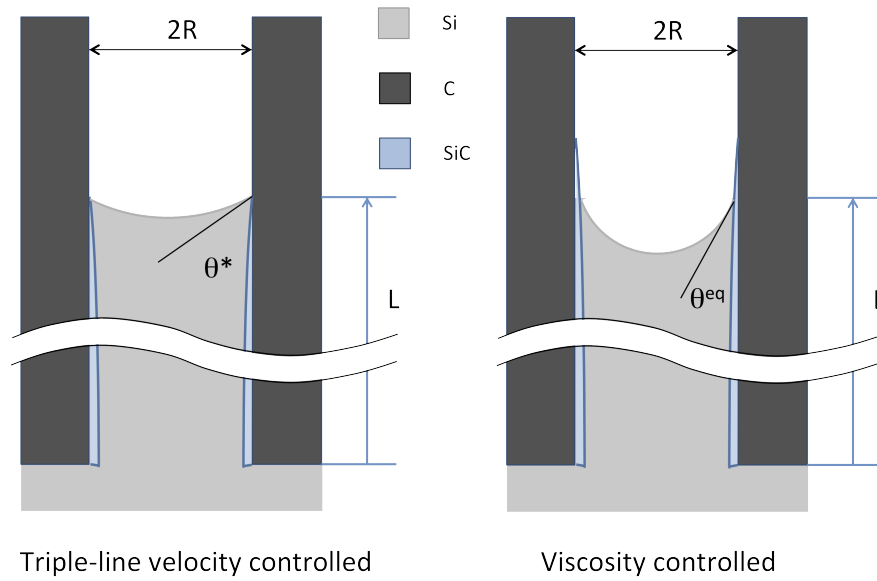


Figure 2.23 – Schematic of two limiting cases of Si ingress in C capillary with radius  $R$  are triple line controlled characterize by contact angle greater than equilibrium contact angle (left) and viscosity controlled ingress characterized by reaction front being always ahead of the meniscus of Si (right).

For a capillary with radius  $R$  where the liquid Si has infiltrated to depth  $L$ , the pressure difference by viscous force ( $\delta P_{vis}$ ), gravitational force  $\delta P_{grav}$  and capillary force  $\delta P_{cap}$  are given as follows:

$$\Delta P_{vis} = \frac{8\eta L}{R^2} \frac{dL}{dt} \quad (2.16)$$

$$\Delta P_{grav} = \rho g L \quad (2.17)$$

$$\Delta P_{cap} = \frac{2\gamma \cos \theta^*}{R} \quad (2.18)$$

where,  $\eta, \rho, \gamma$ , and  $\theta$  are viscosity, density and contact angle of Si at the given temperature, respectively.

If the actual contact angle,  $\theta^*$  is larger than the equilibrium contact angle,  $\theta^{eq}$ , the triple line will advance at a speed equal to the reaction rate. Once the contact angle has reached  $\theta^{eq}$ , the further advancement is still possible at the speed given by the viscous forces as long as the metallostatic pressure does not balance out the capillary forces as described Equation (2.19).

$$\frac{dL}{dt} = \frac{R^2}{8\eta L} \Delta P = \frac{R^2}{8\eta L} \left( \frac{2\gamma \cos \theta^{eq}}{R} - \rho g L \right) \quad (2.19)$$

If  $\nu_0$  is the reaction controlled, temperature dependent speed of triple line, the condition to have the same ingress rate given by the reaction and viscous drag is given by Equation (2.20).

$$\begin{aligned} \nu_0 &= \frac{R^2}{8\eta L} \left( \frac{2\gamma \cos \theta^{eq}}{R} - \rho g L \right) \\ 8\eta L \nu_0 &= 2R\gamma \cos \theta^{eq} - R^2 \rho g L \end{aligned} \quad (2.20)$$

which gives,

$$L = \frac{2R\gamma \cos \theta^{eq}}{R^2 \rho g + 8\eta \nu_0} \quad (2.21)$$

Figure 2.24 shows the resulting graph from Equation (2.21). The parameter space gets divided into two regions: at lower capillary heights and larger pore radius, the ingress of Si is reaction controlled (left side of the curve represented by the blue line), while at higher capillary heights and smaller pore radius the ingress is viscous drag controlled (to the bottom right of blue curve). The upper branch of the curve which is directed towards larger radii and short infiltration length reflects the limitation by metallostatic pressure. This means that the capillary force is not sufficient to pull the liquid up higher than to a certain equilibrium height. When approaching that value, the available pressure difference (denoted by the terms in bracket of Equation (2.19) ) to overcome the viscous forces becomes very small. In real preforms, the pore size radius must be replaced by equivalent pore size radius.

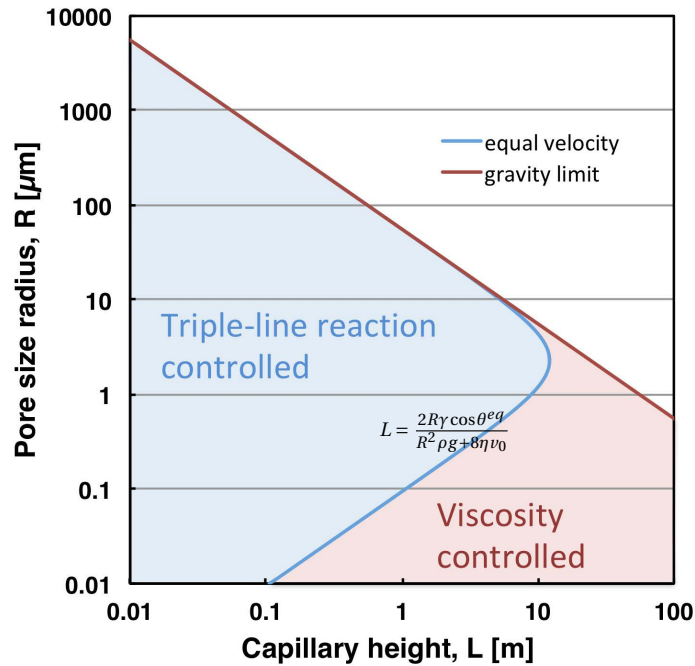


Figure 2.24 – Separation of the parameter space  $R, L$  into triple-line reaction controlled (blue) and viscosity controlled combinations (red). The gravity limit indicates the possible filling height at which metallostatic forces equilibrate the capillary forces, which of course depends on the density, the surface tension and the contact angle.

## 2.10 Research objectives

As can be seen from the literature review, in recent years scientific research on silicon infiltrated silicon carbide has been quite intense, however, research has focused mainly on functional and applied aspects and ignored more fundamental features of reactive wetting and capillary infiltration in reactive systems. In addition, reaction phenomena are quite complex, defined by several different stages and by microstructural changes occurring within fractions of a second; the reaction may take the form of dissolution, intermetallic formation or a combination of both processes, depending on the different components present in the system. These phenomena, together with the characteristics of preform porosity, eventually influence capillary flow and therefore microstructural features of the final infiltrated material, such as residual silicon and porosity.

We have found that different researchers have used several types of C-C or C-SiC preforms. It should be noticed, however, that there is a threshold value for both the upper and lower porosity levels to obtain "absolute dense" composites without residual Si, C or porosity. One of the objectives of the thesis is to lay down a way that is generally applicable to the determination of acceptable porosity values of the preform as a function of the concentration of alloys.

The gradient structure of the silicide phase observed in composites infiltrated by Si-X alloys is



another significant observation in the literature. In unassisted, capillary force-driven infiltration, there is continuous enrichment of the alloying element at the front of the infiltration as the Si in alloy reacts with C and proceeds further. Silicides with a melting temperature much higher than the alloy or pure Si could result in solid phase precipitation at the front of the infiltration. In order to understand the reactive Si-X alloy infiltration of porous carbonaceous preforms, the phenomenon of precipitation of solid silicides, apart from the well-reported "pore clogging" by reaction formed SiC layer, needs to be investigated to make the "fully dense" composites without residual Si, C or porosity.

The present study is focused on infiltration of transition metal-Si alloys into porous carbon preform as this route offers the possibility of the most economical route to form composites without unreacted silicon and with improved high-temperature performance. The aim of the present research is to study and understand the fundamental principles of reactive wetting and infiltration kinetics of Si-X alloy infiltrated silicon carbide composites.

While many of the concepts developed in this thesis are generally applicable to Si-X systems, the experimental work has been limited to the Si-Zr system. As can be seen from Figure 2.19 and Figure 2.21, the Si-Zr system fulfills the points i), ii), iii), and v) of the list of requirements given in subsection 2.9.2. The compliance of the point iv) of that list is illustrated by the quasi-binary cut through the ternary Si-Zr-O system reproduced in Figure 2.25.

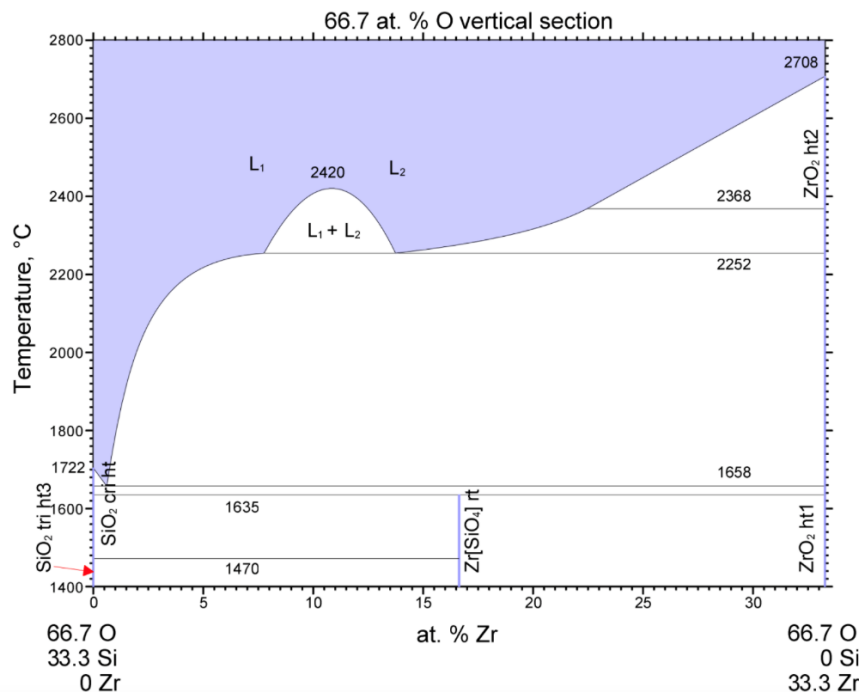


Figure 2.25 – The quasi-binary cut through the ternary Si-Zr-O system to illustrate that the Zr does not lower the melting temperature of  $\text{SiO}_2$  significantly resulting in poor ablation properties.

Table 2.6 – Typical characteristics of the preforms reported by various researchers and their properties after infiltration by a mentioned infiltrant.

Reference	Preform characteristic	Infiltrant	Properties after infiltration
Calderon et al. [162]	various type of C  porosity 15 % to 44 %	Si	dense beta SiC matrix, C, residual porosity optimal porosity >36 %
Liensdorf [163]	wood based preform porosity >60 %	Si	fully dense 81 % SiC, 18 % Si & 1 %C density 3 g cm <sup>-3</sup>
Margiotta et al.[55]	C preform preform ~43 %		
Tong et al. [64]	C preform porosity 21 % to 56%	Si-10 at. % Zr	open porosities <7% phase - SiC, Si <sub>2</sub> Zr, residual C & Si optimal porosity 31 % to 46 %
Tong et al. [65]	C fiber preform porosity 25.83% density 1.32 g/cm <sup>3</sup>	Si-10 at. % Zr	open porosity 5 % density 2.07 g/cm <sup>3</sup> SiC, ZrSi <sub>2</sub> , ZrC and C
Aoki et al. [77]	SiC fiber, C coating  density ~2 g cm <sup>-3</sup>	Si-8.5 at.%Hf	residual 2.7-3.8 vol% Si
Aoki and Ogasawara [78]	SiC fiber, C coating  porosity 30-33%	Si-16at.%Ti	open porosity <1%  density 2.6-2.7 g cm <sup>-3</sup>
Messner and Chiang [66]	density ~0.80 g cm <sup>-3</sup>	Si-4 to 8 mol% Mo	residual Si <5 %
Singh and Behrendt [69]	C preform  porosity >37 %	Si-1.7 and 3.2 at.% Mo	low residual C and Si

This page is intentionally left blank.

## 3 Materials and methods

This chapter enlists all the raw materials and experimental setups used in the current study, including the characterization tools as well as the analysis methods.

### 3.1 Materials

#### 3.1.1 Glassy carbon plate

Glassy carbon plates of commercial grade SIGRADUR-G were used in sessile drop and microchannel experiments. They were sourced from HTW, Germany. SIGRADUR-G grade has a density  $1.42 \text{ g/cm}^3$  and 0% open porosity. Glassy carbon plates were chosen over dense graphite plates because of their negligible porosity and 0% open porosity. In sessile drop experiments, the plates were used as substrates with dimensions  $15 \text{ mm} \times 15 \text{ mm} \times 3 \text{ mm}$ . On the other hand, in microchannel experiments, they were used to make micron-sized capillary channels by laser ablation, and had dimensions  $25 \text{ mm} \times 100 \text{ mm}$  or  $50 \text{ mm} \times 3 \text{ mm}$ .

#### 3.1.2 Silicon

Electronic grade pure Si, procured from Institute for Nonferrous Metallurgy and Purest Materials, TU Bergakademie Freiberg, Germany, was used in sessile drop experiments. The Si chips used for preform infiltration and microchannel experiments had 99.99% purity, and were generously supplied by Sicerma GmbH, Germany.

#### 3.1.3 Si-Zr alloy

The near eutectic Si-Zr alloy with composition of 8 at. pct Zr was manufactured in small quantity by induction melting of Si and Zr chips in desired proportion at the Mechanical Metallurgy Laboratory, EPFL, Switzerland. The Si-8 at. pct Zr alloy was used for sessile drop experiments. However, the induction melting in a relatively small graphite crucible was not a

good technique to produce the large quantities needed for infiltration experiments.

Si-8 at. pct Zr alloy was procured in large quantities for infiltration experiments from Chengdu Huarui Industrial Co Ltd.(CHDR metals), China. The alloy composition provided by the supplier is shown Table 3.1. The XRD analysis of the alloy from CHDR metals also confirmed some impurities in the form of Al, as seen in Figure 3.1. The alloy was available as shards ranging from few mm in equivalent diameter to small chunks of up to 3 cm in equivalent diameter.

Table 3.1 – Composition of Si-8 at. pct Zr alloy % provided by CHDR metal, China.

	Zr	Fe	Al	Ca	Ni	Cr	Cu	Si
wt %	21.15	0.26	0.10	0.08	0.004	0.006	0.003	bal.
at %	7.64	0.15	0.12	0.07	0.00	0.00	0.00	bal.

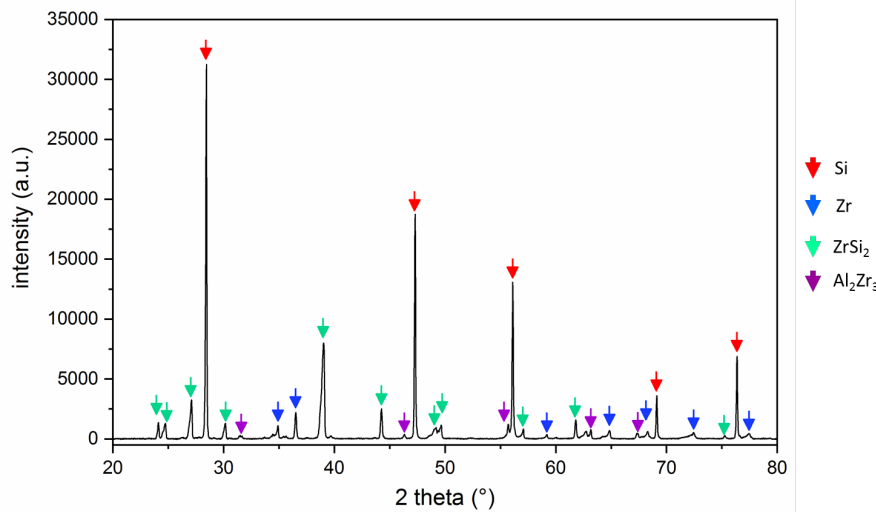


Figure 3.1 – The composition of the Si-8 at. pct Zr alloy analyzed with XRD.

### 3.1.4 Graphite and SiC powders

Graphite powder of commercial grades Ecophit GFG5, TIMREX KS10, TIMREX KS25, TIMREX KS44 and TIMREX KS75, characterized by their  $d_{90}$  particle size of 5, 10, 25, 44 and 75  $\mu\text{m}$ , were used to make porous carbonaceous preform with and without SiC powder. For this study, the Ecophit grade was sourced from SGL, Germany, and the TIMREX graphite powders was provided by Imerys Graphite & Carbon Switzerland Ltd. Typically, the graphite powders has an ash content of  $\sim 0.06\%$  and moisture content of  $\sim 0.1\%$ . The rest of the impurities provided by Imerys in their test report are summarized in Table 3.2. The graphite powder has a flaky shape, see (Figure 3.2) (a).

Alpha silicon carbide ( $\alpha$ - SiC) powder of grade F800 was procured from Tracomme AG, Switzer-

Table 3.2 – Typical impurity levels in the TIMREX grade graphite powders.

Ash %	Moisture %	Al	As	Ca	Co	Cr	Cu	Fe	Mo	Ni	Pb	Sb	Si	Ti	V	S
										ppm						
0.06	0.1	13	<0.5	90	<1	<1	<1	50	<1	2	<2	<0.1	90	7	3	50

land. The F800 grade has particle size  $d_{90}$  of approximately 14  $\mu\text{m}$ . The powder has an angular shape, see (Figure 3.2) (b), and looks green in color.

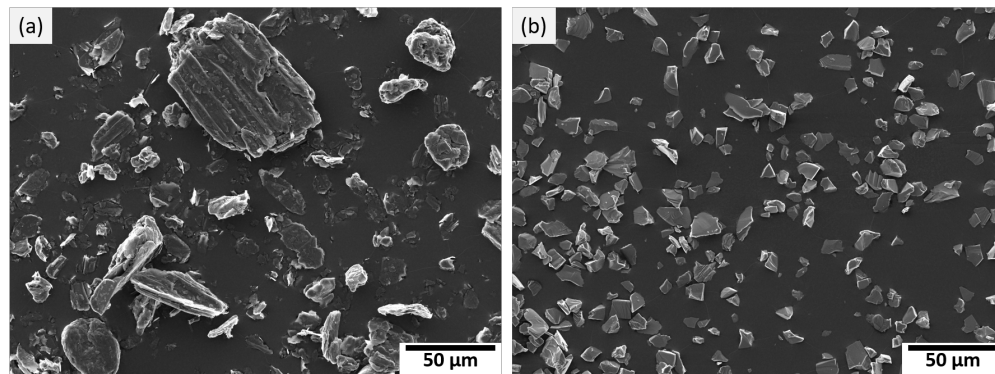


Figure 3.2 – SEM image of (a) TIMREX KS44 graphite particle showing flaky shape particles and (b) SiC F800 showing angular shape particles.

### 3.1.5 Binder and pore forming agent

Bakelite PF GA T 10 R, a phenolic resin from HEXION, USA was used as an organic binder to make the preforms, by cold or warm pressing the powder mix. The binder must later be pyrolysed to form amorphous carbon in the preform. Corn starch sourced from Sigma-Aldrich, Germany was used as pore former in some of the preforms. During the pyrolysis, the gases produced by the decomposition of the corn starch help in creating a more open pore structure in the preform.

### 3.1.6 Crucibles

Graphite was chosen as the material for the crucible because other high temperature materials, like alumina and zirconia, can act as a source of undesirable oxygen. As Si is very sensitive to oxidation, contamination with oxygen creates problems in melting Si chips used for infiltration. The graphite crucibles were made by machining dense graphite block by STEINEMANN CARBON AG, Switzerland.

To protect the graphite crucible from reacting with molten Si, they were coated with boron nitride (BN). BN is very stable at high temperatures and is not wetted by Si. The BN coating was applied by a 3M<sup>®</sup> BN spray sourced from Tracomme AG, Switzerland. Rods and

machined clamps of various size made from dense graphite were also procured from STEINE-MANN CARBON AG, Switzerland, and were used in single microchannel capillary infiltration experiments.

Graphite foil having thickness of 0.5 mm was sourced from SGL, Germany, and used as a wicking material to transport the molten Si and Si-Zr alloy to the porous preforms. The graphite foil was also used to prepare the single-use crucibles coated with BN to melt Si and Si-Zr alloy in the infiltration experiments. The graphite foil was rolled to make a cylinder of the crucible and the edges were glued by phenolic resin mixed in ethanol. The bottom was made from a circular piece of graphite foil bent at the edges to make a lid shape, which was then glued with phenolic resin. The formed graphite crucible was subsequently pyrolysed at 1000 °C in a vacuum tube furnace. Later, the inside of the crucible was coated with BN spray and dried in an oven at 110 °C, for a minimum duration of 1 hour.

## 3.2 Experimental methods

### 3.2.1 Sessile drop experiment

Sessile drop experiments were carried out to analyse the wetting behavior of Si and a near eutectic Si-Zr alloy on glassy carbon and polycrystalline SiC substrates measuring 10 mm × 10 mm × 3 mm. The substrates were polished using SiC paper with the following grit sizes: 800, 1200, 2000 and 4000. Further reduction of surface roughness was achieved with semi-automatic polishing using 1 µm diamond suspensions, and the final polishing with acidic aluminum oxide suspension was performed using a TEGRAMIN (Struers, Germany) grinding and polishing machine. The surface roughness was measured using a NanoFocus µsurf explorer confocal microscope (NanoFocus AG, Germany) and the µSoft Analysis XT software. The substrates were also cleaned with isopropyl alcohol (99.99%) just before being put into the furnace. The electronic grade pure Si and Si-8 at. pct Zr alloy pieces with mass in the range of 50 – 80 mg were kept on the substrate. The Si and Si-Zr alloy pieces were carefully cleaned using a HNO<sub>3</sub> (65%), HF (40%) and CH<sub>3</sub>COOH (100%) solution in 5 : 3 : 3 ratio, to remove the oxide layer, followed by rinsing with water and then drying in a vacuum oven. Care was taken to expose the substrate as well as the Si and Si-Zr alloy pieces to the atmosphere for the least possible time before putting them in the furnace.

A custom made alumina tube furnace (Gero GmbH Neuhausen, Germany) was used to heat the samples above their melting temperature under a controlled atmosphere. The furnace can be operated at a maximum temperature of 1600 °C, both under vacuum and an inert gas (Ar or N<sub>2</sub>) atmosphere. The samples were placed at the end of the alumina tube with smaller diameter and exactly half the length of the furnace so that the samples are placed exactly at the middle of the furnace tube to ensure the samples are closest possible to the thermocouple. The furnace was sealed with glass plates on both end of the tubes. The illumination bulb and the image capturing device were placed on either end of the tube to adjust the desired lighting

to capture a still image of the droplet. The setup was developed by Institute for Nonferrous Metallurgy and Purest Materials, TU Bergakademie Freiberg, Freiberg, Germany and was used in similar experiments previously. In our experiments, as the substrate and the molten droplet were self-illuminating in red color at 1500 °C, no external illumination was needed to capture the images with good contrast for measuring the droplet dimensions from which the contact angle was extracted by

$$\theta_{\text{cal}} = 2 \arctan \frac{2h}{d} \quad (3.1)$$

using the measured values of height,  $h$ , and diameter,  $d$ , of the droplet from the captured profile. The equation is based on the assumption that the droplet is a cap of an ideal sphere, i.e. its shape is unaffected by gravity. The contact angles of Si and Si-Zr alloy on glassy carbon and SiC substrates were observed at 1500 °C for an hour to measure the equilibrium contact angle as well the reaction at the interface of the molten droplet and the substrate. The furnace along with the image capture system and its major components is shown in Figure 3.3

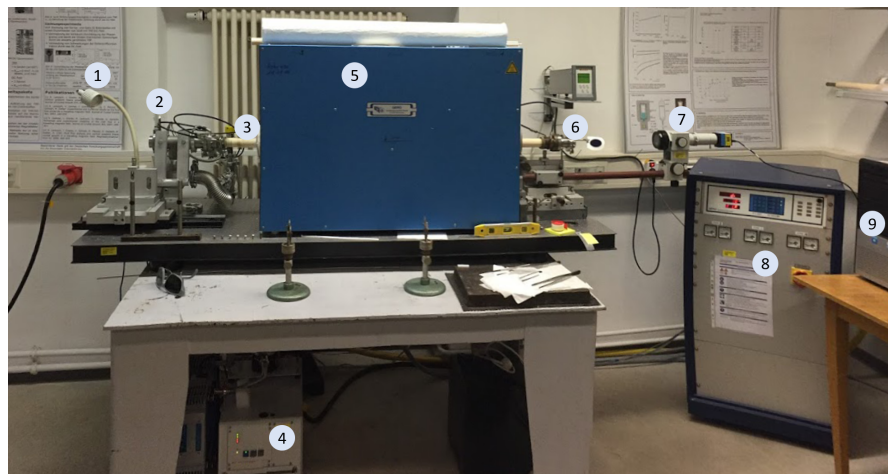


Figure 3.3 – A custom made alumina tube furnace used for sessile drop experiments showing its major component 1:lights for back illumination, 2: glass sealing window and valves for vacuum and air, 3: alumina tube, 4: turbo molecular pump, 5: insulation, 6: glass sealing window and ND filter, 7: digital camera, 8: furnace controller 9: computer to record images.

Two sets of measurements of contact angles were carried out; one under vacuum of  $5 \times 10^{-5}$  mbar, using a turbomolecular pump (BOC Edwards, Munich, Germany), and the second under a static argon atmosphere (99.999%, sourced from Linde) at 500 – 600 mbar. The Ar gas was passed through an Oxisorb<sup>®</sup> cartridge from Messer Group GmbH (Krefeld, Germany) before introducing the argon into the furnace, which should have provided a final purity of better than 5 ppb O<sub>2</sub> within the argon. However, as the tubes are made up of alumina there is a possibility of introduction of oxygen in the furnace atmosphere. The oxygen partial pressure in the alumina tube furnace is about  $10^{-18}$  mbar at 1500 °C according to the Ellingham-diagram.



To be on the safe side, a small piece of Ti sponge was placed next to the substrate as an oxygen getter material at high temperatures, since Ti has higher affinity towards oxygen than Si. The furnace was repeatedly flushed with argon and again pumped to high vacuum at least three times before starting the actual experiments and ramping up the temperature. The furnace was heated to 1500 °C with a heating rate of 350 °C/h and was held at this temperature for 1 hour for experiments carried out under vacuum. On the other hand, for the experiments carried out in static Ar environment, the furnace was heated to 1400 ° at a rate of 350 °C/h, later at 100 °C/h until it reached 1500 ° and was held at this temperature for 1 hour. Later, the furnace was switched-off and left to cool down overnight.

The samples with the solidified droplet on the surface were then cut in the middle and the cross-section was mounted in epoxy resin (SpeciFix Resin, Struers, Germany) to prepare the samples for SEM and EDX analysis. Automatic grinding of the samples was initially conducted using a 40 µm diamond pad. Further, automatic polishing was carried out using diamond suspensions of 6, 3 and 1 µm, and final polishing with a suspension of acidic aluminum oxide, again using the Struers TEGRAMIN grinding and polishing machine. The mount was then placed onto a aluminum sample holder using double-sided conductive carbon tape. As the resin is non-conductive, a quick dry conductive silver paint is used to make the contact between the C / SiC substrate and the aluminum sample holder by painting a thick line from the edge of the substrate to the Al holder. This is necessary to avoid the charge build-up on the sample surface in the SEM. The reaction layer at the interface of Si / Si-Zr alloy and C / SiC substrate after the solidification was analysed using a Tescan VEGA3 SBU electron microscope (EO Elektronen-Optik-Service GmbH, Germany) and elemental analysis was done using a BR AXS Quantax 200 EDX system (Bruker Nano GmbH, Berlin, Germany).

### 3.2.2 Single capillary microchannel infiltration experiment

Reactive melt infiltration of Si and Si alloys is a competition between capillary forces and reaction of Si with C. To understand the effect of capillary rise and reaction rate simultaneously, we designed experiments to infiltrate single micron-sized glassy carbon capillaries with Si and near eutectic Si-Zr alloy.

#### 3.2.2.1 Fabrication of microchannel capillaries

Manufacturing micron-sized capillaries with an infiltrable length of a few hundred mm to observe the "pore closure" effect due to reaction was a tricky task. The aspect ratio required for the capillary with equivalent diameter of a few micrometers and length of a few hundred mm was almost impossible to manufacture with glassy carbon by any conventional manufacturing technique. Hence, the microchannels were manufactured by engraving a 10 – 100 µm deep and 1 – 4 mm wide groove on a highly polished glassy carbon plate and then clamping it with another flat plate without groove. The glassy carbon plates were cleaned in an ultrasonic bath for 5 minutes and then washed with isopropyl alcohol before clamping them together. The

grooves were made in various geometries in terms of aspect ratios, and were either straight or tortuous. Threaded graphite clamps and bolts were used to securely clamp the glassy carbon plates at high temperature. In Figure 3.4, on the left a glassy carbon plate with laser ablated microchannels with straight, curved and rectangular microchannels can be seen, and on the right side are two glassy carbon plates with grooved channels clamped together to make a capillary channel.

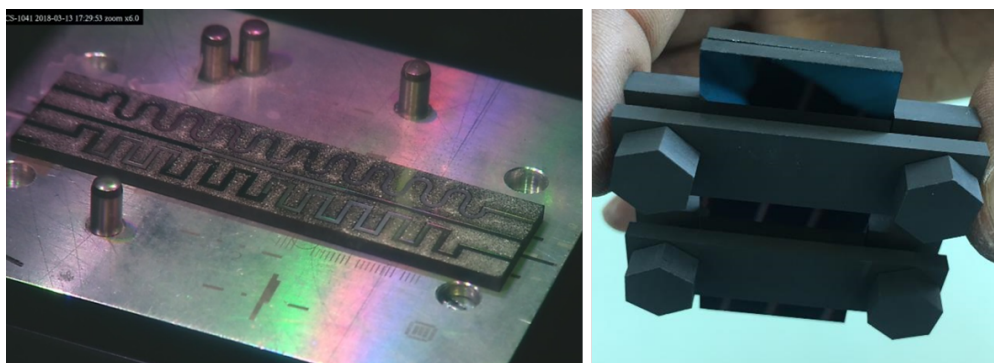


Figure 3.4 – A glassy carbon plate with three laser ablated microchannels with different shapes, and on right are two glassy carbon plates clamped together to make a capillary channel.

Microchannels ranging from 0.01–0.1 mm in depth and up to 460 mm in length were manufactured using laser ablation. Various configurations of the microchannel structures are shown in Figure 3.5. In some cases up to 4 different channels were engraved with a distance in between them to do more experiments with the same external experimental conditions. A pulsed laser (SuperRapid laser from Lumera GmbH) was used for machining the channels. The short pulse laser works at a wavelength of 355 nm (frequency tripled), and has a nominal pulse length of 10 ps. The laser pulses were guided toward the sample through a galvano scan head (ScanLab GmbH). A 160 kHz pulse repetition rate and a pulse energy of about 14  $\mu\text{J}$  (2.2 W average power) were used for ablation. A hatched pattern was used to write the structure to attain a smooth surface. A total of six hatch directions were applied at 0°, 90°, 30°, 120°, 60° and 150°. By changing the pulse energy and the number of repetitions, the necessary depth was achieved. Since the pattern was larger than the maximum possible writing area of the machine, stitching was added to the scan head. A graded transition zone was used to reduce the edges between the stitching areas. The roughness of both the polished and the laser ablated surface was measured with a Leica DCM8 confocal microscope to observe the resulting surface roughness.

### 3.2.2.2 Experimental setup

The experimental setup to conduct the infiltrations of the laser ablated capillary channel of glassy carbon is shown in Figure 3.6. Two graphite rods were used to keep the glassy carbon plates with the microchannel upright. A single-use crucible made of graphite foil with its inside coated with BN was used to place the pieces of Si or Si/Zr alloy such that it levels a

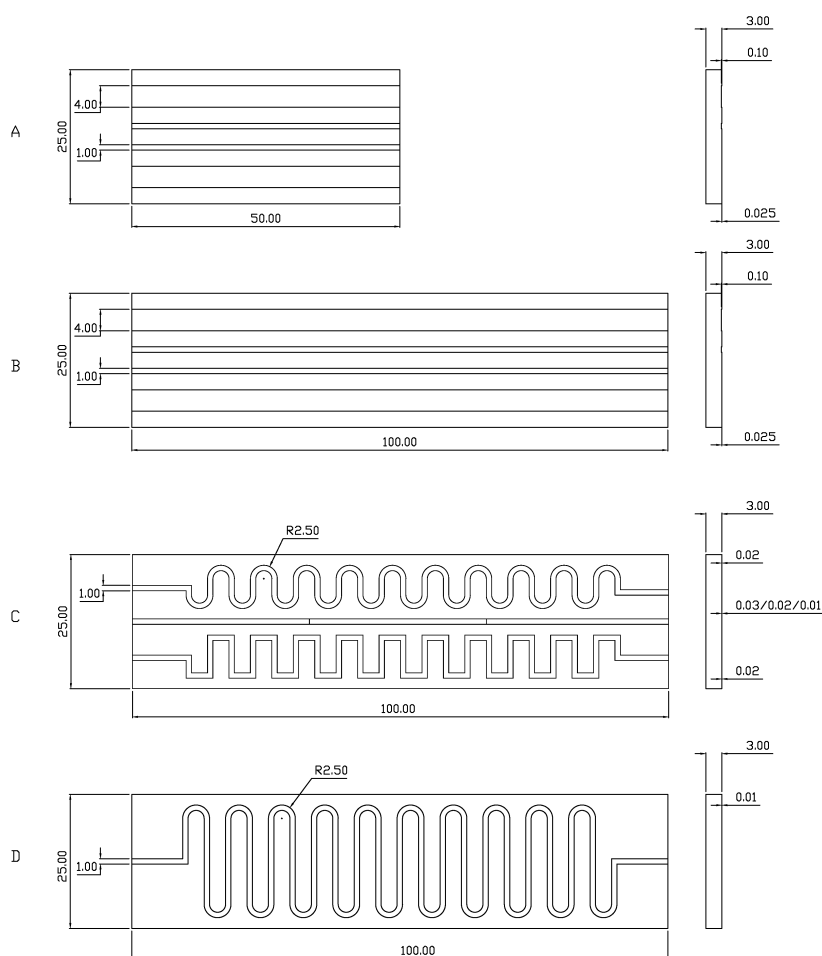


Figure 3.5 – Various configurations of microchannels to achieve different depth, length and tortuosity of the channels.

little above the bottom end of the glassy carbon plates to ensure the contact of Si/ Si-Zr alloy after melting with the entrance of the microchannels. Pure Si and near eutectic Si-Zr alloy were used to generate melts to infiltrate the capillaries. The microchannels supported by two graphite rods together with the graphite foil crucible were then put in a bigger graphite crucible lined with graphite foil and a thick graphite cloth at the bottom to protect from the spillage of molten Si or Si-Zr alloy. The bigger graphite crucible is then put in to the graphite furnace (FCT, Germany), which can be operated under vacuum or Ar environment up to 2100 °C.

The furnace was flushed with Ar and pumped to primary vacuum twice before starting the experiment. The experiments were performed under vacuum of approximately  $10^{-2}$  mbar. The experiment could not be performed under Ar atmosphere in the graphite furnace available at the laboratory because of the oxidation of Si resulting in unsuccessful infiltration. A typical heating cycle involved heating the furnace to 200 °C at a heating rate of 60 °C/h and holding

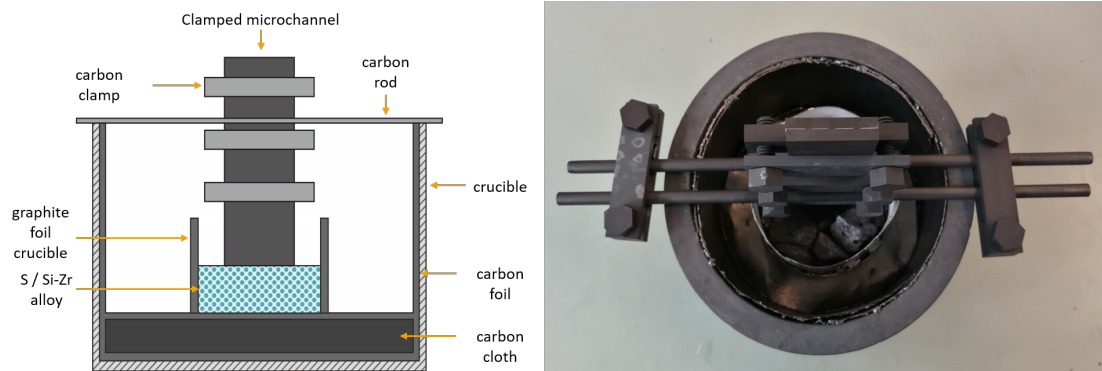


Figure 3.6 – Experimental setup used to keep the glassy carbon microchannel upright and infiltrate with Si / near eutectic Si-Zr alloy.

for 30 minutes to remove the moisture. Later, the furnace is heated at a heating rate of  $300^{\circ}\text{C}/\text{h}$  to the desired infiltration temperature from  $1500^{\circ}\text{C}$  to  $1700^{\circ}\text{C}$ . After reaching the infiltration temperature, the heating was stopped and the furnace was left to cool down at the maximum possible rate by its water cooled jacket.

### 3.2.2.3 Analysis of the microchannels

Due to the closed furnace without any observation window and the nature of experiments at high temperature and vacuum, it was not possible to perform any in-situ measurements to track the capillary flow of the melt in the microchannel. After cooling down the furnace, the infiltrated microchannels were taken out and the extra metal stuck at the bottom of the glassy carbon plates was carefully cut using a diamond saw without damaging the glassy carbon plates. The graphite clamps were also removed by taping the glassy carbon plates with transparent Tesa<sup>®</sup> tape to ensure that they don't come apart during handling. Later, the microchannel was observed using non-destructive X-ray radiography with RX solution EasyTom XL, France, to see the extent of the infiltration. The region of the channels filled with Si or Si-Zr alloy is darker in appearance than the empty region in the channel. The samples were then cut using a diamond blade saw at the desired location to observe the cross-sections. The cut samples were mounted in a cylindrical shape die using epoxy resin (SpeciFix Resin, Struers, Germany) to facilitate the grinding and polishing. The automated polishing was then carried out using the 6, 3 and  $1\text{ }\mu\text{m}$  diamond suspension and the final polishing with the suspension of acidic aluminum oxide using the Struers TEGRAMIN grinding and polishing machine. Further analysis of the reaction layer and phases of the alloy were carried out using a Tescan VEGA3 SBU electron microscope (EO Elektronen-Optik-Service GmbH, Germany) and elemental analysis was done using a BR AXS Quantax 200 EDX system (Bruker Nano GmbH, Berlin, Germany).

### 3.2.3 Preform infiltration experiments

The preform infiltration experiments were designed to study the effect of various parameters like temperature, reactivity of carbon, porosity and pore size distribution, mass fraction of graphite and SiC powder in the reactive infiltration of carbonaceous preform by near eutectic Si-Zr alloy. Disk-shaped porous carbonaceous preform were produced by uni-axial cold or warm compaction of the mixture as differently sized graphite powder or their mixture with SiC powder.

#### 3.2.3.1 Powder mixing and characterization

The first step in making the preform is to mix the powders. To make the powder mixture, the graphite powder, SiC powder, bakelite as an organic binder and, optionally, corn starch as pore former were weighed in desired mass fraction and put together in a plastic bottle with alumina balls. A roller mill was used to homogeneously mix the powder mixture by rolling it for approximately 12 hours. The homogeneous powder mixture was then finely sieved using a mechanical shaker (ASM 200, Siebtechnik GmbH, Germany) to remove the alumina balls and big clumps, if any.

For carbon only C-C preforms, 86 wt. % of graphite powder, 10 wt. % of bakelite and 4 wt. % of corn starch with graphite powder of various particle sizes with  $d_{90}$  ranging from 5 to 75  $\mu\text{m}$  was used to make the powder mix. The preforms were prepared to study the effect of graphite particle size and porosity.

SiC-C preforms were prepared for the analysis of the effect of graphite mass fraction by mixing SiC powder of grade F800 and graphite powder of grade TIMREX KS25 or TIMREX KS44 in varying proportions (0 to 30 wt %) with bakelite as binder (10 wt %).

The density of the powder mixtures was measured using Helium pycnometry (AccuPyc II 1340, Micromeritics, United States). The particle size distribution analysis of the graphite powders, SiC powder and the SiC-C powder mixtures was done using laser diffraction particle size analyzer (LS 13 320 Beckman Coulter, United States). The sample for particle size analysis was prepared by taking a small amount of powder mixture that was added to isopropanol and then stirred using an ultrasonic stirrer. The sample was then analysed using the universal liquid module of laser diffraction particle size analyzer.

#### 3.2.3.2 Fabrication of preforms

The disk shaped C-C preforms with 50 mm diameter and thickness of approximately 5 mm were made from graphite powder mixtures weighing about 12.7 g. The C-C preforms were compacted using a uni-axial hydraulic press and a cylindrical tool steel die of 50 mm and held for 2 minutes under the applied force of either 90 kN or 110 kN at room temperature. The SiC-C preforms were difficult to handle without breakage when pressed at room temperature. Hence,

a hot mounting press (Buehler SimpliMet 1000, USA) generally used to mount metallography specimens was used to manufacture SiC-C preforms. The hot pressed preforms have much better green strength compared to the preforms pressed at room temperature. The typical compaction process included heating up to 150 °C in 5 min and keeping it for 2 minutes under 28 MPa pressure, and afterwards cooling to room temperature in 3 minutes.

The green preforms were later pyrolysed under inert atmosphere of flowing Ar in an alumina tube furnace at 1000 °C or 1400 °C to carbonize the organic binder and the corn starch used in some preforms. A typical pyrolysis cycle consisted of heating the preforms from room temperature to 500 °C at a rate of 60 °C/h and of 200 °C/h up to 1000 °C or 1400 °C, holding for 15 minutes, followed by free cooling.

### 3.2.3.3 Preform characterization

The dimensions of the pyrolysed preforms were measured with a digital vernier caliper with least count of 0.01 mm along with the weight to calculate the apparent density.

Further, the porosity and pore size distribution were measured by mercury intrusion porosimetry (PASCAL 140/400, Thermo Finnigan, Germany). A piece of pyrolysed preform weighing between 0.5 g to 0.7 g was taken from the disks and kept for an hour in the oven at 110 °C to remove the moisture. The skeletal density of the powder mix measured by helium pycnometry was used for density calculations in mercury intrusion porosimetry.

The porosity analysis of the SiC-C preforms was also done with X-ray computer tomography using a RX solution EasyTom XL, France. The samples for X-ray CT were made by cutting the preform into smaller pieces by a diamond saw and then manually grinding it on a SiC paper of 800 grit to get the final dimension to approximately 1 mm × 1 mm × 10 mm. The thinner sample helps to get it closer to the X-source to get a higher magnification and resolution. The voxel size was about 0.55 µm. The CT data was processed by Fiji [166] and Avizo® software to partition the particles and porosity based on the contrast generated by difference in the atomic mass of the elements in the powder mix. The pores voxel were assumed disconnected if they do not share a common face.

### 3.2.3.4 Infiltration setup

The infiltration of the preforms was done in a graphite heated furnace from FCT Systems, Germany under vacuum of approximately  $10^{-2}$  mbar. The infiltration setup involved a single-use graphite foil crucible coated with BN and a graphite foil cylinder to support the preform and act as a wick to transport the molten Si-Zr alloy placed at the bottom without touching the preform directly (Figure 3.7). Alternatively, the graphite crucible was coated with BN and then was lined with graphite foil, which was also coated with BN, as shown in Figure 3.8, was used as multi-use crucible at the expense of graphite foil lining. The crucible was then put on the graphite cloth to protect from any spillage of alloy in a much bigger graphite crucible lined

with graphite foil to absorb the Si vapors.

The infiltration heating cycle started with preheating the furnace up to 200 °C at a heating rate of 60 °C / h and holding at this temperature for 30 min, and subsequent heating until the infiltration temperature reached 1500 °C at a heating rate of 520 °C / h and holding for 1 h, and then cooling down by switching-off the heating of the furnace. For some experiments the infiltration temperature was raised to 1700 °C.

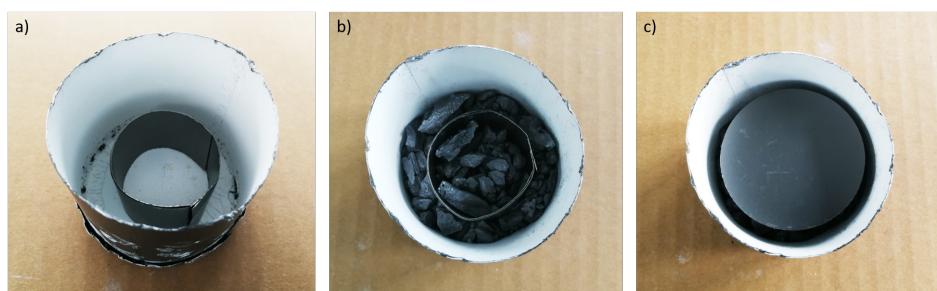


Figure 3.7 – Crucible setup for the infiltration process; a) graphite foil crucible coated with a BN from inside and a graphite foil cylinder as a wick in the center, b) Si-Zr alloy shards placed into the crucibles, c) placing preform disc on a graphite foil wick.

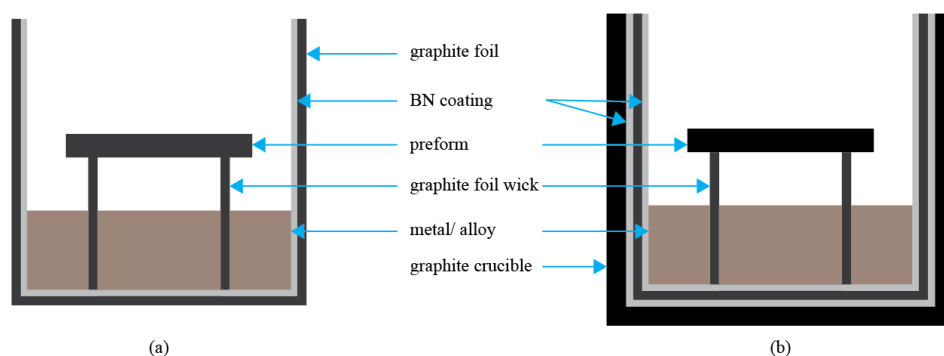


Figure 3.8 – Schematics of two alternative crucible setup for the preform infiltration experiments; (a) single use graphite foil (b) multi use graphite crucible coated with BN and graphite foil lining.

### 3.2.3.5 Analysis of infiltrated sample

The infiltrated sample was taken out from the crucible and the excess alloy, if any, sticking with the wick was cut and/or ground out carefully. The dimensions and the weight of the infiltrated preforms were measured to calculate the density after infiltration. A small piece of the infiltrated disc was then cut using a diamond saw and mounted in cold setting epoxy resin (SpeciFix Resin, Struers, Germany) to observe the cross-section. Automatic grinding of the samples was initially performed using a 40 µm diamond pad. Later, automatic polishing was done using diamond suspensions of 6, 3 and 1 µm, and final polishing with a suspension of acidic aluminum oxide with Struers TEGRAMIN grinding and polishing machine. The extent

of infiltration and reaction of graphite particles with Si-Zr alloy was studied using SEM (Tescan VEAG3 scanning electron microscope) and EDX (Bruker AXS Quantax 200 EDX system). Pore phase fraction was determined using grayscale thresholding by using ImageJ [166] software. X-ray diffraction (XRD) using the PANalytical X'Pert PROh-2h (PANalytical, Netherlands) scan system equipped with a Johansson monochromator (Cu  $K\alpha_1$  radiation=1.5406 Å) and a X'Celerator linear detector. Phase compositions of the spectra were analyzed by using HighScore Plus Software.



This page is intentionally left blank.

## 4 Wetting behavior of Si and Si-Zr alloy on C and SiC

### 4.1 Disclaimer

The part of this chapter is published in Journal of European cermaic society in Apr 2019 as "M. Naikade, B. Fankhanel, L. Weber, A. Ortona, M. Stelter, and T. Graule, "Studying the wettability of Si and eutectic Si-Zr alloy on carbon and silicon carbide by sessile drop experiments", *Journal of the European Ceramic Society*, vol. 39, no. 4, pp. 735–742, 2019, ISSN: 0955-2219. DOI: 10.1016/j.jeurceramsoc.2018.11.049". Specific details and explanation for greater clarification are included.

### 4.2 Abstract

The contact angles of two different systems, molten silicon and a eutectic Si-8 at. pct Zr alloy and their evolution over time on vitreous carbon and polycrystalline silicon carbide (SiC) substrates were investigated at 1500 °C under vacuum, as well as in argon using the sessile drop technique. The contact angle and microstructure of the liquid droplet/solid substrate interface were studied to understand fundamental features of reactive wetting as it pertains to the infiltration process of silicon and silicon alloys into carbon or C/SiC preforms. Both pure Si and the eutectic alloy showed good wettability on vitreous carbon and SiC characterized by equilibrium contact angles between 29° and 39°. The eutectic alloy showed a higher initial contact angle and slower spreading as compared to that of pure Si. On vitreous carbon both silicon and the eutectic alloy formed SiC at the interface, while no reaction was observed on the SiC substrates.

### 4.3 Introduction

Silicon infiltrated silicon carbide (Si-SiC) manufactured by means of the so-called liquid silicon infiltration process (LSI) has drawn considerable attention from different industrial sectors, due to the possibility of an industrial scale production of nearly net-shaped large complex

components with very low porosity [52]. The first step in LSI consists of producing a carbon-based microporous medium known as a preform (which may already contain  $\alpha$ -SiC particles), which is easy to mold into the desired final shape. Later, in the furnace, the liquid silicon is pulled into the preform by capillary forces and reacts exothermally with the carbon preform to form a  $\beta$ -SiC body via reactive wetting and diffusion controlled conversion [55]. However, there are still some undesired aspects of LSI. Firstly, the presence of residual unreacted silicon in the composite impairs the mechanical properties above 1300 °C [12]. Secondly, if carbon fibers are used as reinforcement, their reaction with silicon may result in the weakening of the composite [48, 60]. Finally, depending on the pore characteristics and the preform's reactivity, the solid phase reaction products could cause capillary obstruction and incomplete infiltration [59]. As a result of the diffusion of carbon through solid SiC being faster than that of silicon, the growth of the solid phase occurs into the capillary channel, therefore potentially obstructing liquid transport [27, 28, 168]. Additionally, the unreacted silicon expands during solidification and may create internal stresses and/or cracks.

One way of avoiding the unwanted reaction and obstruction of channels is to protect the reinforcement with an inert interphase, such as SiC or BN. Although being effective, this technique is expensive in terms of equipment and process time. Furthermore, it fails to solve the problem of the limited operation temperature due to residual silicon. Another solution is to use metal – silicon alloys, as they have shown to reduce reactivity [61, 62] and lower the amount of residual silicon, as well as the infiltration temperature [63]. The alloying element must be chosen based on the liquid-phase equilibria and its ability to form refractory silicides, which have a higher melting temperature than pure silicon. This has been shown to be feasible for Si-Mo alloys infiltrated into carbon preforms [66, 68]. Apart from increasing the melting point, the refractory silicides were found to improve mechanical properties and oxidation resistance at high temperatures [73]. Among most recent studies [63, 67], one example of refractory silicides used was Si-Zr alloys. Si-Zr alloys have been used to infiltrate carbon preforms as to obtain a ceramic matrix composite (CMC) characterized by high strength, good oxidation resistance, and excellent ablation resistance. Several studies focussing on different aspects of metal-silicon alloy infiltrated CMCs can be found in literature [62, 63, 66–68, 73, 169–171], however, these works have mainly focussed on practical and applied aspects. More fundamental features of reactive wetting and capillary infiltration in reactive systems have been overlooked or not analysed in depth. Several groups have studied the wetting properties of silicon and silicon alloys on various types of graphite materials and SiC [90, 120, 126, 129, 132, 133, 135–138, 150, 172–174]. To our knowledge, there hasn't been any study yet featuring the fundamental wetting properties of any composition of Si-Zr alloy on carbon or SiC substrates. The present work aims at filling this gap by performing classical sessile drop experiments to study the spreading of pure silicon and Si-Zr alloy at 1500 °C on vitreous carbon and polycrystalline SiC substrates and study the effect of reactive wetting.

#### 4.4 Experimental procedure

The experiments were performed in an alumina tube furnace (Gero GmbH Neuhausen, Germany) under a controlled atmosphere. The furnace can be operated at a maximum temperature of 1600 °C, both under vacuum and an inert gas (Ar or N<sub>2</sub>) atmosphere. The vitreous carbon (Sigma-Aldrich Chemie GmbH, Germany) and polycrystalline SiC (3M Technical Ceramics, Germany) substrates measuring 15 mm x 15 mm x 3 mm were manually polished using SiC paper with the following grit sizes: 800, 1200, 2000 and 4000. Next, semi-automatic polishing using 1 μm diamond suspensions and final polishing with an acidic aluminum oxide suspension were performed. The surface roughness was measured by means of a NanoFocus μsurf explorer confocal microscope (NanoFocus AG, Germany) using μSoft Analysis XT software. The pieces of pure silicon and Si-8 at. pct Zr alloy (henceforth: Si<sub>0.92</sub>Zr<sub>0.08</sub>) were carefully cleaned using a HNO<sub>3</sub> (65%), HF (40%) and CH<sub>3</sub>COOH (100%) solution in the ratio of 5:3:3, to remove the oxide layer, followed by rinsing with water then drying in a vacuum oven. The silicon and Si<sub>0.92</sub>Zr<sub>0.08</sub> alloy pieces with the weight in the range of 50–80 mg were put on the substrates and placed into the alumina tube, as shown in Figure 4.1. The small alumina tube, in which the samples were placed, was approximately half the length of the furnace, ensuring that the sample was near to the thermocouple situated in the middle of the furnace. The tube furnace had glass caps on both sides, while the light source and digital camera were placed on opposite sides. The image acquisition was carried out by means of a computerized digital image analyzer. The values of the height and the diameter of the droplets were taken directly from the images of the droplets during the experiments.

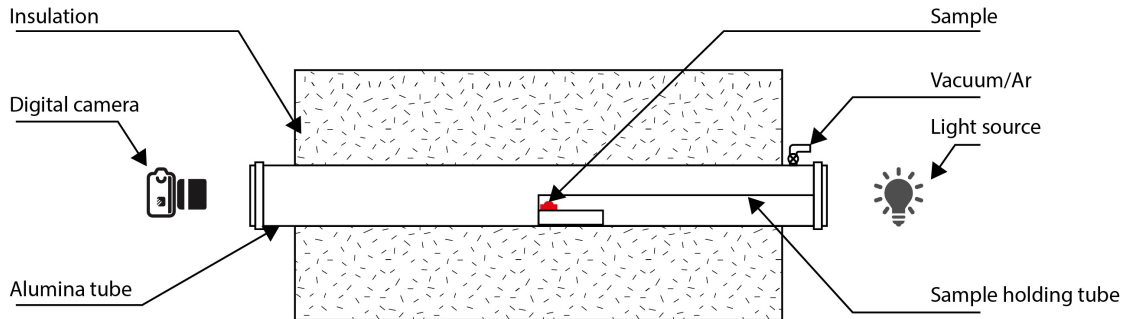


Figure 4.1 – Schematic of metal droplet on substrate placed in a tube furnace with both sides covered by glass to observe and measure the contact angle using a digital camera.

The contact angles of silicon and Si<sub>0.92</sub>Zr<sub>0.08</sub> alloy on vitreous carbon and sintered silicon carbide (SiC) were determined at 1500 °C for 1 h. The measurements of the contact angles were started immediately after the formation of a liquid droplet after complete melting of the sample. For the calculations, it was assumed that the droplets took the form of a spherical cap, due to their tiny volume. The contact angles  $\theta_{\text{cal}}$  were deduced from binary pictures using Equation 4.1 where  $h$  is the measured height and  $d$  is the measured diameter of the droplet.

$$\theta_{\text{cal}} = 2 \arctan \frac{2h}{d} \quad (4.1)$$

The first set of experiments were performed under vacuum at  $5 \times 10^{-5}$  mbar, using a turbo-molecular pump (BOC Edwards, Munich, Germany), while the second set of experiments were performed under a static argon atmosphere (99.999 %, sourced from Linde) at 500-600 mbar. Furthermore, an Oxisorb<sup>®</sup> cartridge from Messer Group GmbH (Krefeld, Germany) was used before introducing the argon into the furnace, which should have provided a final purity of less than 5 ppb O<sub>2</sub> within the argon. To ensure the cleanliness in the alumina tube, the furnace was repeatedly flushed with argon and pumped to high vacuum for at least 3 times before beginning the experiments. For the experiments carried out under vacuum, the furnace was heated to 1500 °C with a heating rate of 350 °C/h and was held at 1500 °C for 1 h. For the experiments in argon, the furnace was heated to 1400 °C with a rate of 350 °C/h, later at 100 °C/h until reaching 1500 °C and was held at 1500 °C for 1 h. Additionally, a few pieces of titanium sponge were placed near the substrate to act as an oxygen getter and reduce the oxygen partial pressure in furnace below the level caused by impurities in argon. The cross-sections of the solidified droplets and substrates were later studied using a SEM (Tescan VEGA3 SBU, EO Elektronen-Optik-Service GmbH, Germany) and EDX (BR AXS Quantax 200 EDX, Bruker Nano GmbH, Berlin, Germany) to analyze the morphology and composition of the reaction layer between the droplet and the substrate.

## 4.5 Results

### 4.5.1 Surface roughness

The surface roughness values determined in accordance with ISO 4287 for R<sub>a</sub> and ISO 25178 for S<sub>a</sub> values are summarized in Table 4.1.

Table 4.1 – Surface roughness of substrates measured by NanoFocus confocal microscope using  $\mu$ Soft Analysis XT software.

Substrate	Ra(nm)	Sa( $\mu$ m)
Vitreous carbon	5.5 - 6.8	0.04 - 0.07
SiC	8.8 - 10.1	0.10 - 0.17

### 4.5.2 Contact angles under vacuum

The contact angles of pure silicon and the Si<sub>0.92</sub>Zr<sub>0.08</sub> alloy measured under vacuum at  $5 \times 10^{-5}$  mbar on vitreous carbon and SiC substrates are shown in Figure 4.2. The time on X-axis begins with the initial formation of the liquid droplet from a solid piece, as observed by the camera. The contact angle measured immediately after formation of the liquid droplet will be further referred to as the initial contact angle. The increase in pressure with increasing temperature is expected, however, it was observed that the pressure in the tube furnace kept rising with time, even though the temperature was constant at 1500 °C. Moreover, the height of the droplet kept reducing, whereas the diameter of the droplet remained unchanged. These two observations

were interpreted as the vaporization of the droplet during the experiment, which apart from the initial contact angle, makes the measured contact angles incorrect. The accuracy of the contact angle measurement is estimated to be  $\pm 2^\circ$ . The estimation is based on the uncertainty of diameter and height measurement. The accuracy of the measurement was determined by repeating the calculation of one contact angle more than 20 times. The initial contact angles measured immediately after formation of the droplet are summarized in Table 4.2 for pure silicon with their respective melting temperatures. The  $\text{Si}_{0.92}\text{Zr}_{0.08}$  alloy showed a slightly different behavior compared to pure Si. The initial contact angle on vitreous carbon and SiC was  $51^\circ$  and  $52^\circ$ , respectively, followed by slow spreading of the droplet for 120 s until it reached the final contact angle of  $43^\circ$  and  $44^\circ$  (Table 4.2). Since the spreading time is relatively short for the considerable effect of evaporation and change in diameter and height of droplet was clearly noticeable. The temperature change is also nominal for 120 s. The measured contact angle at this time is referred to as the final contact angle after the droplet is formed. The equilibrium contact angle at  $1500^\circ\text{C}$  could not be measured due to the decrease in droplet height due to evaporation.

Table 4.2 – The initial and final contact angle of silicon and  $\text{Si}_{0.92}\text{Zr}_{0.08}$  on vitreous carbon and SiC substrates and respective temperatures measured under vacuum.

Sample	Substrate	Melting temperature ( $^\circ\text{C}$ )	Contact angle ( $^\circ$ )	
			Initial	Final
Silicon	Vitreous carbon	1452	45	-
	SiC	1446	42	-
$\text{Si}_{0.92}\text{Zr}_{0.08}$	Vitreous carbon	1404	51	43
	SiC	1399	52	44

#### 4.5.3 Contact angles under an argon atmosphere

The contact angles of silicon and  $\text{Si}_{0.92}\text{Zr}_{0.08}$  alloy measured under an argon atmosphere at 500 mbar on vitreous carbon and SiC substrates are shown in Figure 4.3. The partial pressure of Ar changed to  $\sim 600$  mbar upon heating to  $1500^\circ\text{C}$  and raised further by 5-8 mbar during the 1h holding time at  $1500^\circ\text{C}$ . The initial contact angle of silicon on vitreous carbon and SiC was  $41^\circ$  and  $42^\circ$ , respectively which decreases within 60 s to the final contact angles of  $35^\circ$  and  $40^\circ$ , respectively. The latter is not a significant decrease considering its still in the range of experimental accuracy. Once the temperature reached  $1500^\circ\text{C}$ , the contact angle on vitreous carbon steadied at  $36^\circ$  and to  $38^\circ$  on SiC. The virtually constant contact angle therefore considered as equilibrium contact angle at  $1500^\circ\text{C}$ .

The  $\text{Si}_{0.92}\text{Zr}_{0.08}$  alloy showed a very different behavior under Ar compared to that under vacuum. The initial contact angle on vitreous carbon was  $46^\circ$  at  $1404^\circ\text{C}$  and stayed almost constant for 28 min, then suddenly dropped to  $29^\circ$  at  $1452^\circ\text{C}$  and then stayed nearly constant throughout the experiment at  $1500^\circ\text{C}$ . In contrast,  $\text{Si}_{0.92}\text{Zr}_{0.08}$  alloy on SiC had an initial

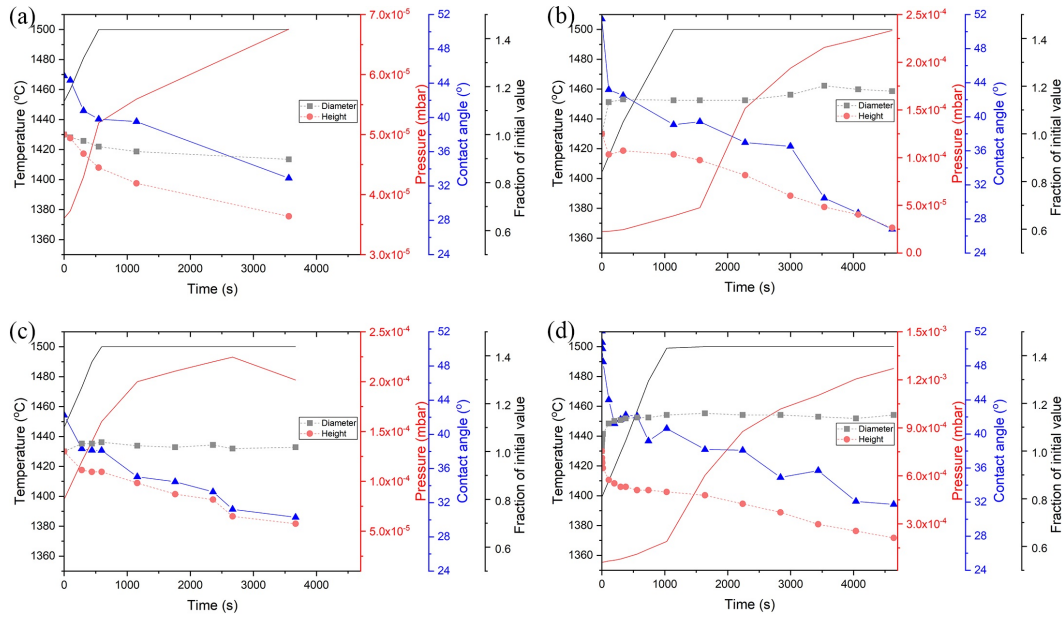


Figure 4.2 – Development of the contact angle, diameter and height of the droplet of (a) silicon on vitreous carbon (b)  $\text{Si}_{0.92}\text{Zr}_{0.08}$  alloy on vitreous carbon (c) silicon on SiC (d)  $\text{Si}_{0.92}\text{Zr}_{0.08}$  alloy on SiC with changing temperature and vacuum pressure.

contact angle of 52° at 1400 °C, which decreased rapidly to 46° in 2 min and kept decreasing slowly to 39° until the temperature reached 1500 °C and then remained almost constant for the time of hold at that temperature. The initial, final and equilibrium contact angle for pure silicon and  $\text{Si}_{0.92}\text{Zr}_{0.08}$  alloy are summarized in Table 4.3.

Table 4.3 – Initial, final and equilibrium contact angle of pure silicon and  $\text{Si}_{0.92}\text{Zr}_{0.08}$  on vitreous carbon and SiC substrates and respective temperatures measured under an argon atmosphere.

Sample	Substrate	Melting Temperature (°C)	Contact angle (°)		
			Initial	Final	Equilibrium (at 1500 °C)
Silicon	Vitreous carbon	1435	41	35	36
	SiC	1432	42	40	38
$\text{Si}_{0.92}\text{Zr}_{0.08}$	Vitreous carbon	1404	46	44	29
	SiC	1400	52	46	39

#### 4.5.4 SEM and EDX analysis

The experimental systems can be classified into two categories, namely reactive systems, where the metal or alloy can react with the substrates to form reaction products at the interface, and non-reactive systems where the metal or alloy cannot react with substrates to form any reaction product. Figure 4.4 (a) and (b) show the SEM images of the cross section of solidified

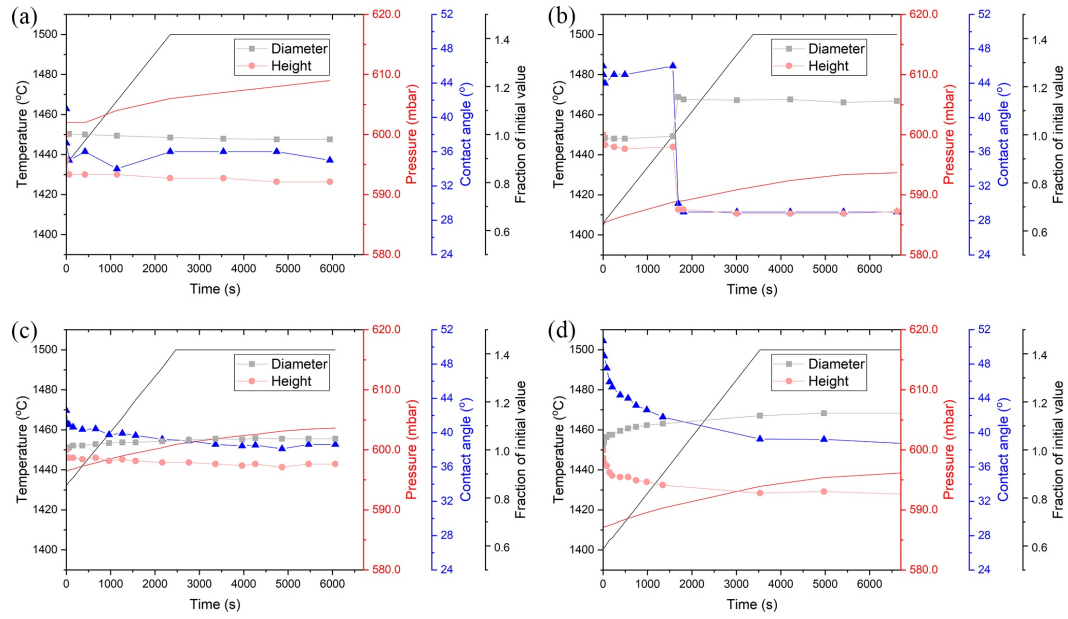


Figure 4.3 – Development of the contact angle, diameter and height of the droplet of (a) silicon on vitreous carbon (b)  $\text{Si}_{0.92}\text{Zr}_{0.08}$  alloy on vitreous carbon (c) silicon on SiC (d)  $\text{Si}_{0.92}\text{Zr}_{0.08}$  alloy on SiC with changing temperature and Ar pressure.

silicon droplet on vitreous carbon. The reaction layer is composed of SiC, as analyzed by EDX (Figure 4.6 (a), (b)), and has an average thickness of  $\sim 5\mu\text{m}$ . As for the non-reactive system, as was previously mentioned, no reaction layer appeared between pure silicon and the SiC substrate, as seen in Figure 4.5 (a) and (b). There is, however, a slight erosion of the SiC substrate at the silicon and SiC interface.

The solidified droplet of the  $\text{Si}_{0.92}\text{Zr}_{0.08}$  alloy on vitreous carbon is characterized by a typical eutectic microstructure with needle-shaped Si-Zr phase within the Si matrix (Figure 4.4 (c), (d)). The reaction layer at the interface is primarily composed of SiC as seen by EDX analysis in Figure 4.6 (c), (d). On the SiC substrate, the  $\text{Si}_{0.92}\text{Zr}_{0.08}$  alloy did not exhibit any continuous reaction layer (Figure 4.5 (c), (d)), as was expected (Figure 4.7 (c), (d)).

## 4.6 Discussion

### 4.6.1 Si evaporation in vacuum

The measurements of the contact angles of the pure silicon droplet on vitreous carbon conducted under vacuum were affected by vaporization of the liquid droplet. This resulted in an apparent decrease in the contact angle from  $40^\circ$  to  $33^\circ$  within 50 min, as seen on Figure 4.10 (captured at  $1500^\circ\text{C}$ , 50 min interval). It was observed that the droplet's height decreased while the diameter remained constant, which is a clear indicator of liquid volume reduction. Additionally, the vacuum pressure continued to increase during the measurements



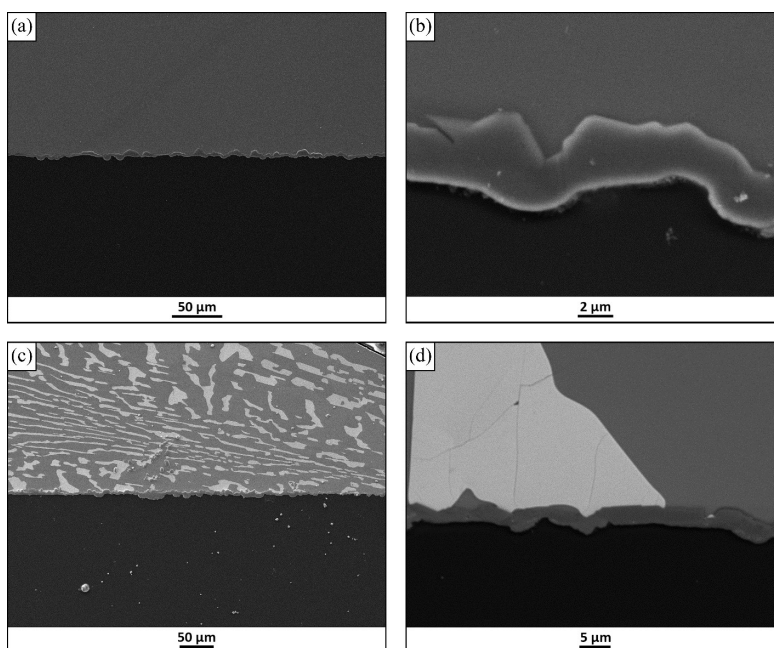


Figure 4.4 – SEM images of the cross section of (a), (b) the solidified silicon droplet (gray) on vitreous carbon (black) with the visible SiC reaction layer formed at the pure silicon-carbon interface, (c), (d) the solidified Si<sub>0.92</sub>Zr<sub>0.08</sub> droplet on vitreous carbon (black), exhibiting needle-shaped Si-Zr phase in silicon and the SiC reaction layer formed at the interface.

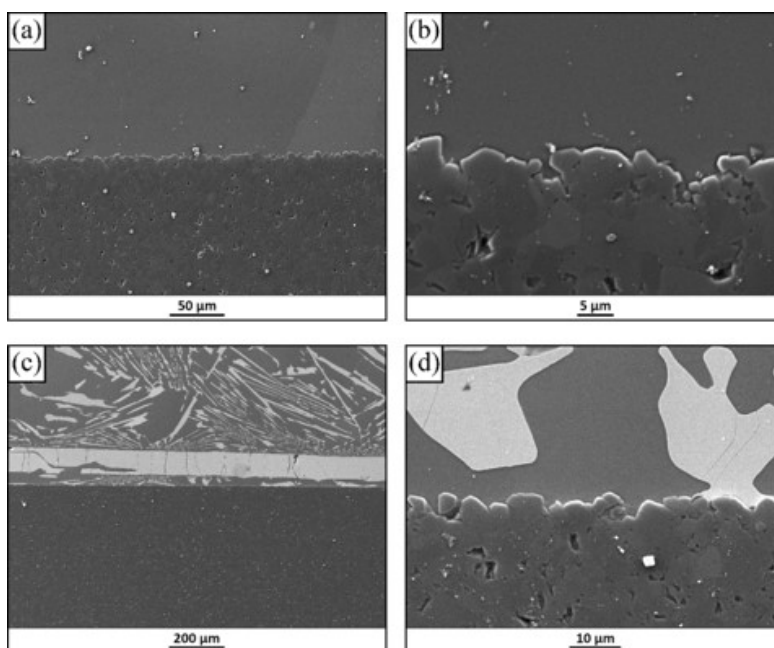


Figure 4.5 – SEM images of the cross section of (a), (b) solidified silicon droplet on the SiC substrate showing no reaction layer and slight erosion at interface, (c), (d) the solidified Si<sub>0.92</sub>Zr<sub>0.08</sub> alloy on the SiC substrate exhibiting needle-shaped Si-Zr phase and slight erosion at the interface.

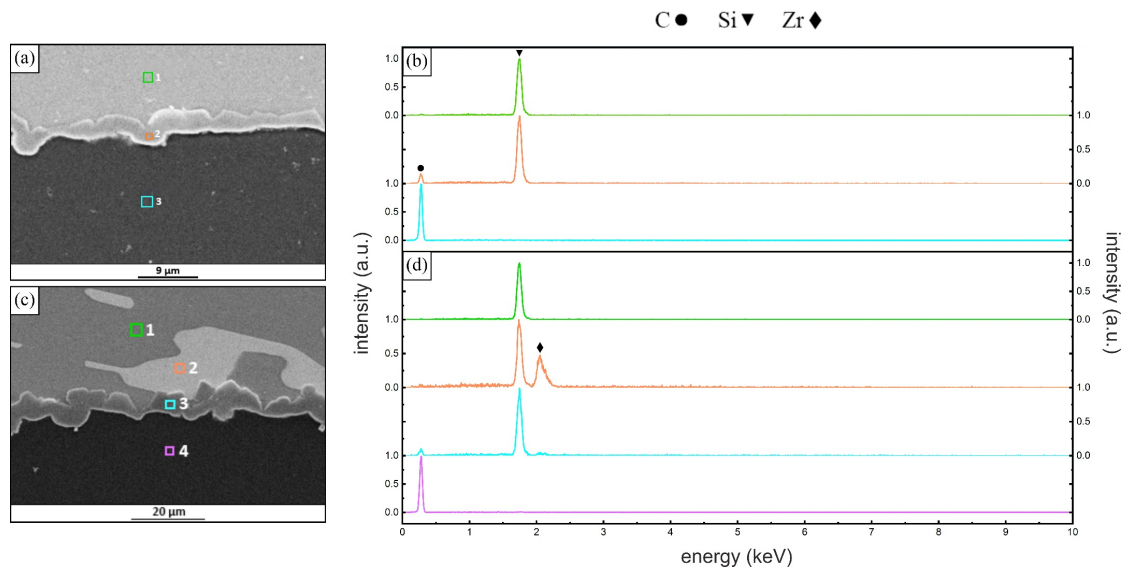


Figure 4.6 – EDX analysis of the interface of (a), (b) solidified silicon droplet on the vitreous carbon substrate showing a SiC layer at the Si/C interface, (c), (d) solidified  $\text{Si}_{0.92}\text{Zr}_{0.08}$  droplet on the vitreous carbon substrate showing a SiC layer at the C/Si-Zr eutectic phase interface.

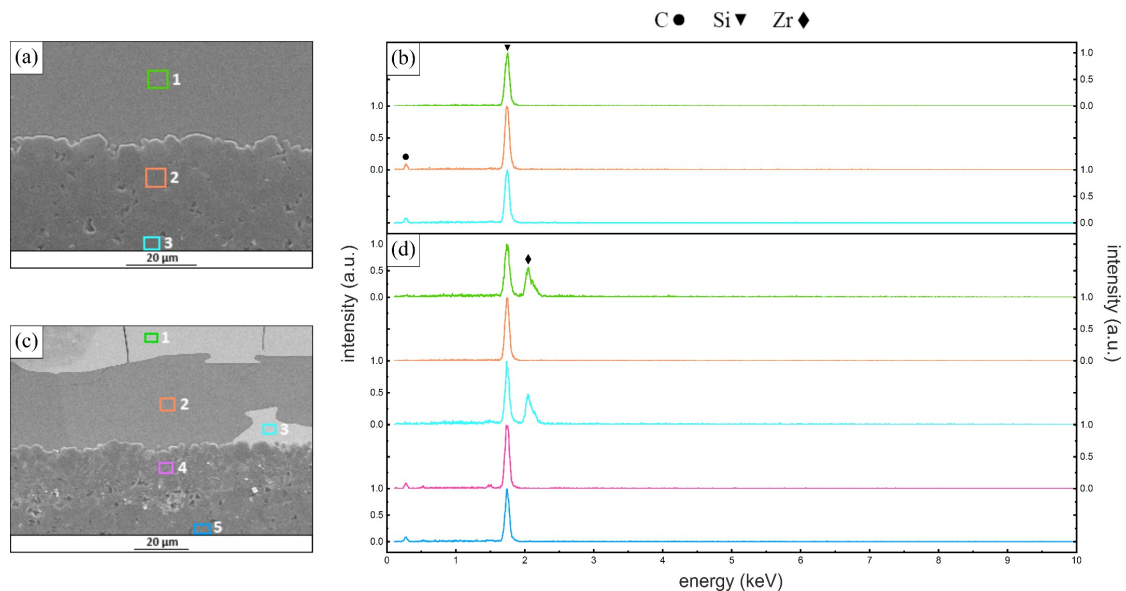


Figure 4.7 – EDX analysis of the interface of (a), (b) solidified silicon droplet on the SiC substrate showing no reaction layer at the Si/SiC interface, (c), (d) solidified  $\text{Si}_{0.92}\text{Zr}_{0.08}$  droplet on the SiC substrate showing no reaction layer at the SiC/Si-Zr eutectic phase interface.

even at constant temperature of 1500 °C, possibly due to vaporization (Figure 4.2). Nevertheless, the initial contact angle can still be considered to be a valid measurement as no significant evaporation was registered at the moment when the liquid droplet formed. It is worth mentioning that the formation of silicon vapor has significant implications during the liquid metal infiltration of porous carbon preforms. If the silicon vapors are in contact with carbon preform long time before the liquid silicon infiltration process begins, silicon vapors could infiltrate the pores and react with the carbon to form a thin layer of SiC. This may result in the formation of a diffusion barrier slowing down further conversion of carbon into SiC by liquid silicon.

Another interesting observation of the solidified droplet on the surface of substrate showed the condensation of Si vapor near the outer edge of the solidified metal droplet. In Figure 4.8 near the edge of the solidified droplet of Si-Zr alloy on the surface of C and SiC substrate a small layer of condensed Si can be seen. In case of C substrate, Si reacts to form thin SiC layer, however in case of SiC it remains unreacted. The condensation of the Si can be due to the selective evaporation of Si from the surface of liquid droplet and adsorption on the C or SiC substrate. There is also possibility of few Si atoms sublimating from the surface of solidified droplet and condensing on the slightly cooler substrate next to the edge of droplet.

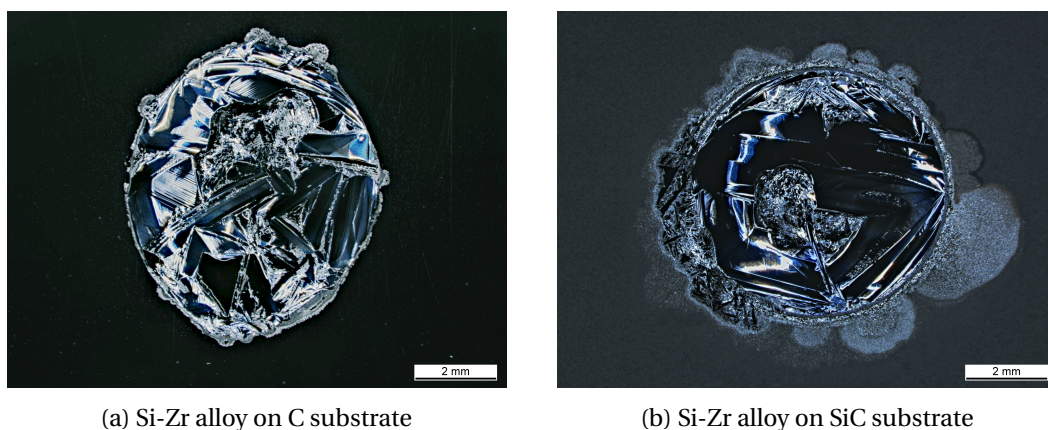


Figure 4.8 – Solidified droplet of Si-Zr alloy on (a) C substrate (b) SiC substrate showing condensed Si near the outside edge of the droplet.

#### 4.6.2 Formation SiC layer before formation of droplet

Dezellus et. al observed the contact angle of silicon on vitreous carbon by the dispensed drop method [132]. The initial contact angle was about 150° at 1430 °C which is much higher than contact angle observed in this study by using the classical sessile drop technique. There is an inherent problem with the classical sessile drop technique where the metal is melted on the substrate directly, significant part of the wetting process is absent or concealed by the melting process. Therefore the initial contact angle reported here are not corresponding to the non-reacted carbon substrate but rather most likely to be on reaction formed SiC layer

during the melting process.

The thin SiC layer can also be formed before melting by the sublimation of Si atoms from the surface of the metal sample and condensing on the substrate which further reacts with carbon to form SiC. Another possible mechanism is solid state diffusion of Si through the surface of substrate which is in immediate contact with the bottom of metal sample. The Figure 4.9 shows schematically the sublimation process of Si atoms from the surface and the solid state diffusion through the surface of substrate in contact with metal sample to form a very thin SiC layer. The subsequent melting and spreading happens on this thin SiC layer instead of carbon.

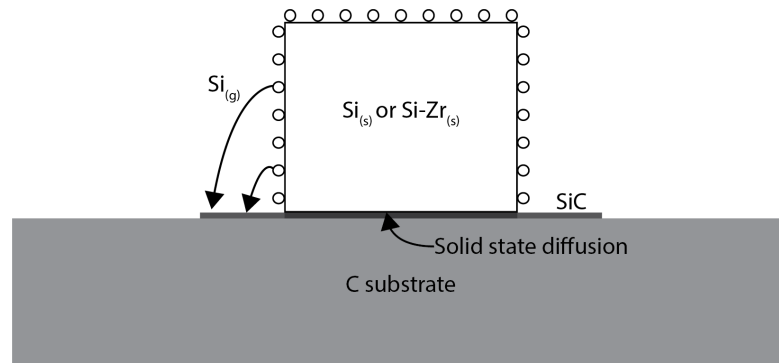


Figure 4.9 – Schematic of condensation of Si from the surface of metal sample on the C substrate to form thin SiC layer and solid state diffusion through the surface of substrate where metal sample is in contact.

The melting temperature and formation of the droplet of the  $\text{Si}_{0.92}\text{Zr}_{0.08}$  alloy occur at 30 °C lower than that of pure Si, which is favorable to lower the infiltration temperature. The initial slow spreading of the  $\text{Si}_{0.92}\text{Zr}_{0.08}$  alloy droplet was observed on both the vitreous carbon and SiC substrates. The higher initial contact angle of the  $\text{Si}_{0.92}\text{Zr}_{0.08}$  alloy compared to that of pure silicon may affect the infiltration kinetics adversely. The higher the contact angle, the more unfavorable the wetting becomes.

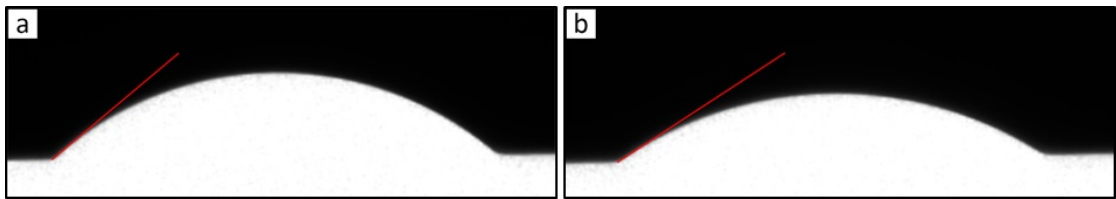


Figure 4.10 – Silicon droplet on vitreous carbon at 1500 °C, (a) contact angle 40°, (b) pseudo decrease in contact angle to 33° due to evaporation.

#### 4.6.3 Oxidation at liquid surface in Ar atmosphere

The contact angles measured under the argon atmosphere were more reliable due to negligible evaporation of liquid droplet evident through the negligible change in the volume of the

droplet with the time, measured using the height and the diameter of the droplet. The pressure in the tube remained nearly constant during the holding time. Therefore, the contact angles measured can be considered valid even after the initial contact angle as opposed to the ones measured under vacuum. However, the measurement of contact angle is very sensitive to residual oxygen in the tube, as a result of impurities in Ar. The smallest amount of oxygen could form a thin solid oxide layer, resulting in a non-spherical droplet, as seen in Figure 4.11. The titanium sponge placed near the sample helped to eliminate the solid oxide film formation of the liquid sample droplet by preferential oxidation.

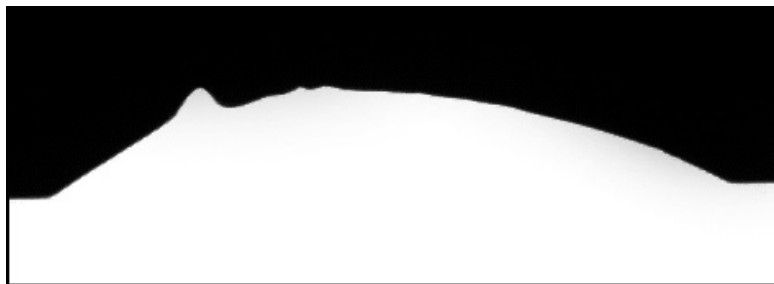


Figure 4.11 – Silicon droplet layer on SiC at 1500 °C with a non-spherical surface due to formation of a solid oxide layer on the surface.

#### 4.6.4 Equilibrium contact angle

The contact angle showed a typical trend, i.e. that the contact angle decreased with the increase in temperature from the melting point to 1500 °C and then reaching its equilibrium value shortly after reaching a constant temperature of 1500 °C. The measured initial contact angle of pure silicon on vitreous carbon and SiC substrates are in good agreement with previous work of Whalen et al. [137]. However, those authors did not consider the effect of evaporation due to high vacuum. Moreover, the contact angle varies significantly, depending on the type of graphite substrates, porosity and roughness [120]. The reasons for choosing the vitreous carbon substrate instead of graphite are its fully dense structure and isotropy. In some graphite substrates the liquid melt seeps through the pores by capillary forces, resulting in false contact angle measurements due to reduction in net volume of the droplet on the surface. The vitreous carbon substrates used in the experiments were fully dense preventing infiltration of silicon into porosity (Figure 4.4). The  $\text{Si}_{0.92}\text{Zr}_{0.08}$  alloy was characterized by a relatively slow initial droplet spreading when compared to the almost instantaneous spreading of pure Si, where, additionally, the initial contact angle was much higher. The slower initial spreading may be caused by the homogenization process occurring during the transition from the solid eutectic phase to liquid phase or the time required for the Si from the  $\text{Si}_{0.92}\text{Zr}_{0.08}$  alloy to form the SiC reaction layer at the interface due to lower activity of Si in the alloy than in the pure Si. This could also help to explain the sudden drop of contact angle of the  $\text{Si}_{0.92}\text{Zr}_{0.08}$  alloy on vitreous carbon substrate from 46° to 30° (Figure 4.3 (b)), although a more in-depth study is needed to understand this phenomenon. Even though the initial contact angle exhibits good wettability on both the vitreous carbon and SiC substrates, the kinetics of wetting will strongly affect the

reactive infiltration process.

#### 4.6.5 Reaction mechanism at interface

The SEM images showed the formation of a distinct SiC layer along both of the vitreous carbon/pure silicon and vitreous carbon/Si<sub>0.92</sub>Zr<sub>0.08</sub> alloy interfaces (Figure 4.4). The formation and growth of the SiC layer occurs in three stages, as explained by Voytovych et al. [136]; (i) a permeable micron thick layer of SiC is formed by means of nucleation and growth (ii) rapid growth of the reaction layer occurs via diffusion of carbon in liquid state silicon and a threshold layer thickness of  $\sim 10 \mu\text{m}$  is reached (iii) the reaction layer becomes impervious to liquid silicon, resulting in negligible growth via grain boundary diffusion of carbon where only coarsening of the reaction layer's microstructure occurs thereafter. The value of the reaction layer thickness depends on the type of carbon and its reactivity. The similarity between the contact angle of silicon on vitreous carbon and SiC substrates can be explained by the rapid formation of the solid SiC layer at the interface that controls the spreading. This results in further spreading of the liquid on the micron-thick SiC layer rather than directly on the vitreous carbon. Interestingly enough, the spreading on SiC substrate is slower than on the vitreous carbon. It might indeed be that the larger surface roughness of the SiC substrate slows down the triple line. Another possible explanation could have been the contamination by oxygen of Si<sub>0.92</sub>Zr<sub>0.08</sub> alloy or the surface of SiC substrate. In long duration experiments at 1500 °C, the alumina tube might act as oxygen source. However, we did not see any indication of oxide film formation on droplet which causes non uniform surface of droplet, where pieces of titanium sponge used as oxygen getter were absent (Figure 4.11). Also, there is no change in contact angle during 1h holding time at 1500 °C. In the case of the Si<sub>0.92</sub>Zr<sub>0.08</sub> alloy, a similar reaction layer is observed. It is however worthwhile noting that the final contact angle of the Si<sub>0.92</sub>Zr<sub>0.08</sub> alloy on the SiC substrate is larger than the one on vitreous carbon, albeit both contact angles are for the contact of the liquid with SiC. These differences might again be caused by the difference in surface roughness between the SiC reaction layer and the SiC substrate.

The SiC substrates did not form a reaction layer at the interface with either pure silicon or the Si<sub>0.92</sub>Zr<sub>0.08</sub> alloy, as seen in Figure 4.5. This is in agreement with the thermodynamic assessment of Si-C-Zr system done by Chen et al. [160]. A few SiC grains can be seen to have become dislodged from the substrate. The surface roughness at the interface also seems to have increased when compared to the measured surface roughness ( $R_a = 8.8 - 10.1 \text{ nm}$  Table 4.1) of the polished substrates before the experiment. This can be interpreted as a slight erosion of the SiC substrates' interface, caused by the dissolution of SiC in the molten droplet.

#### 4.7 Conclusion

The contact angles measured under vacuum are affected by evaporation from the surface of the liquid droplet, resulting in a pseudo decrease in the contact angle over time. The Si<sub>0.92</sub>Zr<sub>0.08</sub> alloy showed good wettability on both the vitreous carbon (equilibrium contact

angle 29° at 1500 °C) and the polycrystalline SiC substrates (equilibrium contact angle 39° at 1500 °C). However, the  $\text{Si}_{0.92}\text{Zr}_{0.08}$  alloy droplet was characterized by a higher initial contact angle and slow spreading when compared to the instantaneous spreading of the pure silicon droplet on the substrates. The formation of the continuous reaction layer of SiC was confirmed along both of the vitreous carbon/pure silicon and vitreous carbon/  $\text{Si}_{0.92}\text{Zr}_{0.08}$  alloy interfaces. The SiC reaction layer growth was limited to a maximum value of  $\sim 5 \mu\text{m}$  in both cases, due to a newly formed SiC diffusion barrier layer, which prohibits the further reaction of liquid Si with the carbon substrate.

## 4.8 Outlook

As discussed and observed during the experiments, the inherent problems with the sessile drop techniques are solid state reaction at the interface, reaction happening before complete wetting of the solid metal to form a droplet, reaction between substrate and gas phase of metal. Therefore, it was not possible to accurately determine the initial wetting behavior of liquid silicon and Si-Zr alloy on the carbon and SiC substrates. Another method of measuring contact angle by dispensing a premolten droplet on the substrate will help in avoiding most of the drawbacks mentioned earlier. The initial spreading seems to happen in fraction of seconds so a use of a high speed camera to capture this phenomenon would definitely give valuable insights in the reactive spreading of Si and Si-Zr alloy on carbon. By incorporating dispensed drop technique with high speed camera to capture the spreading one could understand the reactive wetting to better extent.

## 4.9 Acknowledgment

The authors are grateful to Swiss National Science Foundation (SNSF) for funding the project (Grant number 200021\_163017) and the JECS Trust for funding the visit of Manoj Naikade to Institute for Nonferrous Metallurgy and Purest Materials, TU Bergakademie Freiberg, Freiberg, Germany (Contract No. 2016117).



## 5 Analytical modelling pertaining to LSI issues

### 5.1 Ideal preform porosity to obtain fully dense composites

In the literature, the LSI process is often advertised as leading to (near) net shape, pore-free SiC material. However, it is often overlooked that the stoichiometric nature of the SiC imposes nearly perfect adequacy between available Si and available carbon. The former is essentially controlled by the pore volume fraction architected into the preform and the latter is given by the free carbon concentration per volume in the preform.

A major difficulty in such calculations is that the reaction of liquid silicon with the carbonaceous preform material is not volume conservative. This can be seen by looking at the molar volume of liquid silicon at its melting temperature in the  $10.8 \text{ cm}^3$  ballpark while SiC has a molar volume of the compound, i.e. for 1 mol of Si and 1 mol C, of  $12.5 \text{ cm}^3$  roughly. While there is some latitude in the molar volume of the carbonaceous material, ranging from  $3.4 \text{ cm}^3$  for diamond to about  $8 \text{ cm}^3$  for glassy carbon, the sum of the molar volumes of liquid Si and the carbonaceous material will always be larger than that of SiC. In an LSI process, in which the liquid silicon is initially brought into the pore space of the preform and then let to react, this will inevitably lead to either porosity after reaction or a global shrinkage of the infiltrated form. In such an event, hoping for “pore-free, net shape material” is optimistic, to say the least.

The alternative picture of the LSI process is that the reduction in volume due to reaction is constantly compensated by free liquid Si that enters the preform. While this view is conceptually appealing, it is based on the, again optimistic, assumption that as reaction proceeds, none of the parts of the preform are separated from the external liquid silicon reservoir. The interest of achieving such a processing route would be of course, that the resulting material is indeed pore free. As mentioned in the literature review, typical pore volume fractions thus calculated in the literature are in the 55 to 58 vol.-pct ballpark for graphite and somewhat below 40 vol.-pct for glassy carbon. It can be quite challenging to make self-standing handleable preforms at that level of porosity based on particles. Furthermore, full carbonaceous preforms may overheat due to the exothermic reaction and lose their integrity. Hence, it is a quite often followed path



to provide already some SiC particles in the preform to i) reduce the level of necessary porosity, and ii) add some thermal mass to the system to keep the temperature variations due to the local reaction small.

One of the advantages of the infiltration with liquid silicon alloys is exactly that the fully-fed condition until the end can be somewhat alleviated because the last volume of liquid that is sealed in the pore by clogging of bottle-necks by the reaction is enriched in the alloying element and will eventually convert into a combination of silicides. Some variability in the completeness of the reaction conversion can be compensated by a variability in volume fraction of the silicides in the mixture of silicides that is being formed. Such buffering capacity is also vital in real preforms to compensate for slight variability in the volume fraction of reactive carbonaceous material and porosity on a length scale of the reaction process throughout the preform, i.e., on the level of a few tens of micrometers.

In what follows, the appropriate average pore volume fraction in the preform will be calculated for the ideal case in which liquid silicon alloy is fed continuously until the end of the Si + C conversion reaction. We further aim that there is no residual carbon, no residual porosity and no change in the external dimensions of the preform, i.e. that the whole process is volume conservative. The parameters that will enter the discussion are:

- The volume fraction of silicon carbide particles included in the preform,  $V_{SiC}$
- The volume fraction of pore space in the preform,  $V_p$
- The volume fractions of the various sources of carbon in the preform, in the present case graphite,  $V_{gr}$ , and pyrolyzed phenolic resin,  $V_{pc}$
- The molar concentration of silicon in the infiltrating metal,  $c_{Si}$

We start with the case for infiltration with pure liquid silicon. The goals outlined above will be attained if the sum of the volume fractions occupied by the various forms of carbonaceous material and the pore volume fraction in a preform will correspond to the SiC volume fraction formed by the reaction:

$$V_{gr} + V_{pc} + V_p = \left( \frac{V_{gr}}{V_m^{gr}} + \frac{V_{pc}}{V_m^{pc}} \right) V_m^{SiC} \quad (5.1)$$

where  $V_m^{gr}$ ,  $V_m^{pc}$ , and  $V_m^{SiC}$  are the molar volumes of graphite, pyrolysed phenolic resin, and SiC, respectively. Rearranging leads to:

$$V_p = V_{gr} \left( \frac{V_m^{SiC}}{V_m^{gr}} - 1 \right) + V_{pc} \left( \frac{V_m^{SiC}}{V_m^{pc}} - 1 \right) \quad (5.2)$$

Of course, the result will depend on the type and relative propensity of the carbonaceous phases provided in the preform. Now, we consider the case of an alloy with a concentration

of  $1 - c_{Si}$  in potentially silicide forming species. The silicides are taken to have the general stoichiometry  $Si_nX$ . It can easily be seen that the guiding equation formulated above for pure Si will be modified such that the volumes held in the preform by the various forms of carbonaceous materials and pores must not only accommodate the SiC after reaction but also the silicide phase formed. Hence,

$$V_p = V_{gr} \left( \frac{V_m^{SiC}}{V_m^{gr}} - 1 \right) + V_{pc} \left( \frac{V_m^{SiC}}{V_m^{pc}} - 1 \right) + V_{Si_nX} \quad (5.3)$$

In order to be able to determine the volume fractions of the silicides we have to observe that the number of moles of silicon per volume of preform going into reaction-formed SiC,  $C_{Si,SiC}$ , is

$$\left( \frac{V_{gr}}{V_m^{gr}} + \frac{V_{pc}}{V_m^{pc}} \right) = C_{Si,SiC} \quad (5.4)$$

To this adds the number of moles of silicon per volume entering into the silicide,  $C_{Si,Si_nX}$ , whence the amount of alloying element X per volume available for the formation of silicide,  $C_{X,Si_nX}$ , is found as

$$C_{X,Si_nX} = \frac{1 - c_{Si}}{c_{Si}} (C_{Si,SiC} + C_{Si,Si_nX}) \quad (5.5)$$

The number of moles per volume of the preform of element X and the number of moles of silicon entering into the silicide are of course linked by the stoichiometry as

$$C_{Si,Si_nX} = n C_{X,Si_nX} \quad (5.6)$$

Inserting and rearranging leads to

$$C_{X,Si_nX} = \frac{\frac{1 - c_{Si}}{c_{Si}} C_{Si,SiC}}{\left( 1 - \frac{n(1 - c_{Si})}{c_{Si}} \right)} \quad (5.7)$$

The volume fraction of silicide at the end of the reaction is then found as

$$V_{Si_nX} = C_{X,Si_nX} V_m^{Si_nX} = \frac{\frac{1 - c_{Si}}{c_{Si}} C_{Si,SiC}}{\left( 1 - \frac{n(1 - c_{Si})}{c_{Si}} \right)} V_m^{Si_nX} = \frac{\frac{1 - c_{Si}}{c_{Si}} \left( \frac{V_{gr}}{V_m^{gr}} + \frac{V_{pc}}{V_m^{pc}} \right)}{\left( \frac{(n+1)c_{Si} - n}{c_{Si}} \right)} V_m^{Si_nX} \quad (5.8)$$

We can insert this expression in the above expression for  $V_p$ , yielding:

$$V_p = V_{gr} \left( \frac{V_m^{SiC}}{V_m^{gr}} - 1 \right) + V_{pc} \left( \frac{V_m^{SiC}}{V_m^{pc}} - 1 \right) + \frac{\frac{1 - c_{Si}}{c_{Si}} \left( \frac{V_{gr}}{V_m^{gr}} + \frac{V_{pc}}{V_m^{pc}} \right)}{\left( \frac{(n+1)c_{Si} - n}{c_{Si}} \right)} V_m^{Si_nX} \quad (5.9)$$

Dividing on both sides by  $V_p$  leads to an explicit equation involving the ratios of  $V_{gr}/V_p$  and

$V_{pc}/V_p$  that must be obeyed:

$$1 = \frac{V_{gr}}{V_p} \left( \frac{V_m^{SiC}}{V_m^{gr}} - 1 \right) + \frac{V_{pc}}{V_p} \left( \frac{V_m^{SiC}}{V_m^{pc}} - 1 \right) + \frac{\frac{1-c_{Si}}{c_{Si}} \left( \frac{V_{gr}}{V_p} \frac{1}{V_m^{gr}} + \frac{V_{pc}}{V_p} \frac{1}{V_m^{pc}} \right)}{\left( \frac{(n+1)c_{Si}-n}{c_{Si}} \right)} V_m^{Si_nX} \quad (5.10)$$

We note that the volume fraction of SiC already present in the preform has no effect on the result, as expected. It is just an additional volume that does not intervene in the conversion. The typical preform fabrication process consists in mixing the solid (or liquid) constituents of the preform in certain mass ratios and the pore volume fraction will be a result of the compaction process of the constituents. These mass ratios of the constituents can be converted into volume fraction ratios in the solid phase of the preform:

$$\frac{M_{SiC}}{m_{SiC}} V_m^{SiC} : \frac{M_{gr}}{m_{gr}} V_m^{gr} : \frac{M_{pc}}{m_{pc}} V_m^{pc} = \frac{M_{SiC}}{\rho_{SiC}} : \frac{M_{gr}}{\rho_{gr}} : \frac{M_{pc}}{\rho_{pc}} = V_{SiC} : V_{gr} : V_{pc} \quad (5.11)$$

We can thus express the volume fraction of carbonaceous material in terms of the volume fraction of graphite as:

$$V_{pc} = \frac{M_{pc} \rho_{gr}}{M_{gr} \rho_{pc}} V_{gr} \quad (5.12)$$

and, obviously,

$$\frac{V_{pc}}{V_p} = \frac{M_{pc} \rho_{gr}}{M_{gr} \rho_{pc}} \frac{V_{gr}}{V_p} \quad (5.13)$$

Inserting this into the equation above, we find for the ratio of graphite volume fraction and pore volume fraction:

$$1 = \frac{V_{gr}}{V_p} \left( \left( \left( \frac{V_m^{SiC}}{V_m^{gr}} - 1 \right) + \frac{M_{pc} \rho_{gr}}{M_{gr} \rho_{pc}} \left( \frac{V_m^{SiC}}{V_m^{pc}} - 1 \right) \right) + \frac{\frac{1-c_{Si}}{c_{Si}} \left( \frac{1}{V_m^{gr}} + \frac{M_{pc} \rho_{gr}}{M_{gr} \rho_{pc}} \frac{1}{V_m^{pc}} \right)}{\left( \frac{(n+1)c_{Si}-n}{c_{Si}} \right)} V_m^{Si_nX} \right) \quad (5.14)$$

Solving for  $V_{gr}/V_p$ , leads to

$$\frac{V_{gr}}{V_p} = \frac{1}{\left( \left( \frac{V_m^{SiC}}{V_m^{gr}} - 1 \right) + \frac{M_{pc} \rho_{gr}}{M_{gr} \rho_{pc}} \left( \frac{V_m^{SiC}}{V_m^{pc}} - 1 \right) + \frac{\frac{1-c_{Si}}{c_{Si}} \left( \frac{1}{V_m^{gr}} + \frac{M_{pc} \rho_{gr}}{M_{gr} \rho_{pc}} \frac{1}{V_m^{pc}} \right)}{\left( \frac{(n+1)c_{Si}-n}{c_{Si}} \right)} V_m^{Si_nX} \right)} = A \quad (5.15)$$

Of course, the sum of the volume fractions of all elements forming the preform, i.e. SiC, graphite, pyrolyzed phenolic resin, and pores, must equal to 1:

$$V_p + V_{SiC} + V_{gr} + V_{pc} = 1 \quad (5.16)$$

Rearranging and expressing the volume fraction of SiC and pyrolyzed phenolic resin in the

preform by the volume fraction of graphite leads to:

$$\frac{V_{gr}}{V_p} \underbrace{\left( 1 + \frac{M_{SiC}\rho_{gr}}{M_{gr}\rho_{SiC}} + \frac{M_{pc}\rho_{gr}}{M_{gr}\rho_{pc}} \right)}_B = \frac{(1 - V_p)}{V_p} \quad (5.17)$$

We hence find that the pore volume fraction that leads to complete conversion and no volume change in LSI can be written as

$$AB = \frac{(1 - V_p)}{V_p} \quad (5.18)$$

whence:

$$V_p = \frac{1}{(1 + AB)} \quad (5.19)$$

While the formalism can be applied to any sort of Si-X alloy with X a silicide former, we would like to concentrate on the Si-X system used in this thesis, i.e. Si-Zr, in order to be able to get some numerical values. The silicides in this system are of stoichiometry  $Si_2Zr$  and  $SiZr$ , i.e. the calculations are to be done for  $n = 2$  and  $n = 1$ .

We can now calculate the adequate porosity for a given composition of the preform in terms of the mass ratio of the constituents and see how this value evolves for the liquid metal composition  $c_{Si}$  as well as the type of silicide formed. We do this here as an example for a preform based on 70 g of SiC, 20 g of graphite and 6 g of carbon coming from the pyrolysis of 10 g of phenolic resin. The resulting ideal pore volume fraction as a function of the composition of the infiltrant are shown for the silicides  $Si_2Zr$  and  $SiZr$ .

The calculated results stand by and large to reason: as the potential for silicide formation is increased the larger the pore space for infiltration gets. The more Si can be captured by a given silicide the more additional pore space can be admitted. This is the reason why the line for  $SiZr$  passes below the line of  $Si_2Zr$ .

The curves indicative for the formation of the silicides (shown in Figure 5.1) subdivide the parameter space of pore volume fraction and infiltrant composition in three distinct regions: i) above the blue curve, there will be free silicon available, even if all carbon is converted; ii) in the space below the red curve there will most likely be free carbon around even when the reaction is finished; and iii) between the red and the blue curve there is the “sweet spot” of processing, i.e., the  $c_{Zr} - V_p$  combination space that allows a material after the reaction has ended that has potentially no pores, and where only SiC and silicides are present. The red line is, however, not a hard limit: if the silicide former is at the same time also a strong carbide former, some of the free carbon can also be bonded in carbides of the infiltrant's alloying element. This, however, depends significantly on the relative stability of the silicides, the X-carbide and SiC. Of course, if ternary phases are present, those may affect the result as well. It is, however, quite common that SiC is stable with the first two stable silicides in many Si-X

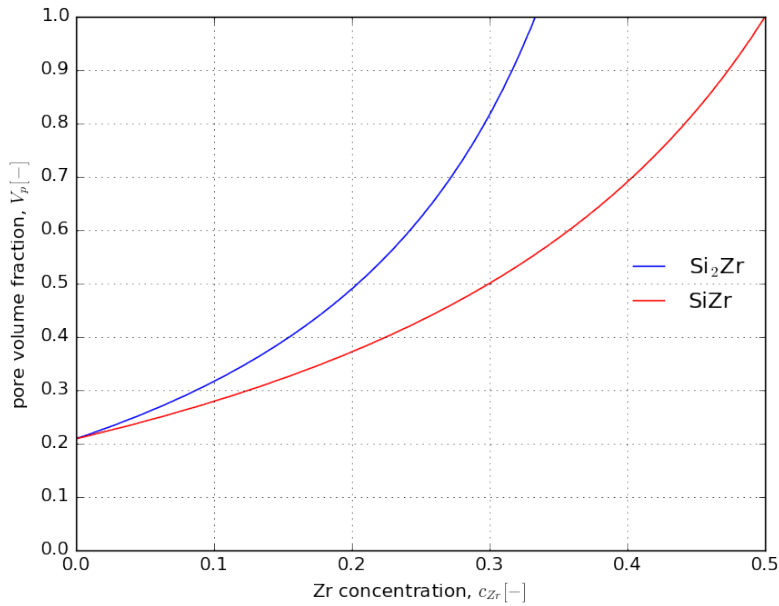


Figure 5.1 – Evolution of the ideal pore volume fraction with infiltrant concentration in silicide forming element, in the case shown for a preform made of 70 g SiC powder, 20 g graphite and initially 10 g of phenolic resin that after pyrolysis results in 6 g of amorphous carbon.

systems. The “sweet spot” calculation may hence also be applicable to other Si-X systems used in LSI, provided that the adequate values for the molar volumes of the silicides are used.

A last remark is concerned with Si-X systems forming silicides of stoichiometries that can not be written with integer values for  $n$ . In the derivation, there is no need that the  $n$  be an integer. For a  $\text{Mo}_5\text{Si}_3$  silicide, one could well take  $n = 0.6$  but would need to calculate the molar volume of  $\text{Mo}_5\text{Si}_3$  for one mole of Mo-atoms to stay consistent.

## 5.2 Detailed calculation of the phases present

As we mentioned above, the curves indicative for the formation of the silicides subdivide the parameter space: pore volume fraction vs. infiltrant composition in three distinct regions: above the blue curve there will be free silicon at the end of the reaction, in the space below the red curve residual free carbon is expected and between the lines there will be a mixture of silicides present.

In order to assess the success of an infiltration apparent density is a common tool to qualify the composite. It is hence important to have an idea about the expected density in the event that the resulting material consists not only of SiC but also of silicides. We formulate in what follows a general approach how the volume fractions of the phases present after full conversion and the resulting density can be estimated. We first consider the space above the blue curve the

pore space is larger than would be needed to fully convert the carbonaceous phases into SiC and hence we have to be concerned with the formation of SiC, Si, and the first stable silicide of stoichiometry  $\text{Si}_n\text{X}$ .

We start with a preform that is composed of volume fractions of SiC, graphite, pyrolysed carbon, and pores in volume fractions of  $V_{\text{SiC}}$ ,  $V_{\text{gr}}$ ,  $V_{\text{pc}}$ , and  $V_p$ . We consider the case where the carbonaceous phases will get fully converted, and the resulting composite has the same volume as the apparent volume of the preform. The liquid is supposed to have access to the pore space everywhere until the end of the reaction. The small shrinkage of the liquid corresponding to the composition of the silicide is neglected. Furthermore, the partial molar volumes of silicon and the silicide former, X, are considered identical and hence the molar volume of the liquid alloy is independent of composition. We look at a volume of the preform of unity such that volume and volume fraction can be used interchangeably. The volume fractions of the phases constituting the unreacted preform can be found based on their mass fractions in the solid and the pore volume fraction,  $V_p$ , that can be either measured by, e.g., mercury porosimetry, or inferred from the apparent density of the preform. The relevant relations are:

$$V_p = \left( 1 - \frac{\rho_{app}}{\frac{M_{\text{SiC}} + M_{\text{gr}} + M_{\text{pc}}}{\frac{M_{\text{SiC}}}{\rho_{\text{SiC}}} + \frac{M_{\text{gr}}}{\rho_{\text{gr}}} + \frac{M_{\text{pc}}}{\rho_{\text{pc}}}}} \right) \quad (5.20)$$

$$V_{\text{SiC}} = \frac{\frac{M_{\text{SiC}}}{\rho_{\text{SiC}}} \rho_{app}}{M_{\text{SiC}} + M_{\text{gr}} + M_{\text{pc}}} \quad (5.21)$$

$$V_{\text{gr}} = \frac{\frac{M_{\text{gr}}}{\rho_{\text{gr}}} \rho_{app}}{M_{\text{SiC}} + M_{\text{gr}} + M_{\text{pc}}} \quad (5.22)$$

$$V_{\text{pc}} = \frac{\frac{M_{\text{pc}}}{\rho_{\text{pc}}} \rho_{app}}{M_{\text{SiC}} + M_{\text{gr}} + M_{\text{pc}}} \quad (5.23)$$

In such circumstances, we can compare the situation in the beginning with volume fractions  $V_{\text{SiC}}$ ,  $V_{\text{gr}}$ ,  $V_{\text{pc}}$ , and  $V_p$ , with that in the end with  $V_{\text{SiC}}$ ,  $V_{\text{SiC},\text{react}}$ ,  $V_{\text{Si}_n\text{X}}$ , and  $V_{\text{Si},\text{free}}$ . It must hold:

$$V_p + V_{\text{gr}} + V_{\text{pc}} = V_{\text{SiC},\text{react}} + V_{\text{Si}_n\text{X}} + V_{\text{Si},\text{free}} \quad (5.24)$$

The reacted volume fraction of SiC must be linked to the volume fractions of the carbonaceous phases by:

$$V_{SiC, react} = \left( \frac{V_{gr}}{V_m^{gr}} + \frac{V_{pc}}{V_m^{pc}} \right) V_m^{SiC} \quad (5.25)$$

For the volume fraction of the first silicide,  $V_{Si_nX}$ , we can write with the number of mol of the silicide former,  $N_X$ ,

$$V_{Si_nX} = N_X V_m^{Si_nX} \quad (5.26)$$

The total number of mol per volume of Si,  $N_{Si}$ , having entered the preform by infiltration is linked to  $N_X$  by

$$N_{Si} = N_X \frac{c_{Si}}{(1 - c_{Si})} \quad (5.27)$$

Of these, the number of mol per volume,  $N_{Si, Si_nX}$ , entering eventually in the solid silicide is

$$N_{Si, Si_nX} = n N_X \quad (5.28)$$

On the other hand, those entering in carbide formation,  $N_{Si, SiC react}$ , is given by

$$N_{Si, SiC react} = \left( \frac{V_{gr}}{V_m^{gr}} + \frac{V_{pc}}{V_m^{pc}} \right) = N_{Si} - N_{Si, Si_nX} - N_{Si, free} = N_X \left( \frac{c_{Si}}{(1 - c_{Si})} - n \right) - N_{Si, free} \quad (5.29)$$

From the starting equation we find

$$V_{Si_nX} + V_{Si, free} = V_p + V_{gr} + V_{pc} - V_{SiC, react} = V_p + V_{gr} \left( 1 - \frac{V_m^{SiC}}{V_m^{gr}} \right) + V_{pc} \left( 1 - \frac{V_m^{SiC}}{V_m^{pc}} \right) \quad (5.30)$$

With  $N_{Si, free} V_m^{liquid} = V_{Si, free}$  we find:

$$\begin{aligned} V_{Si, free} &= \left( N_X \left( \frac{c_{Si}}{(1 - c_{Si})} - n \right) - \left( \frac{V_{gr}}{V_m^{gr}} + \frac{V_{pc}}{V_m^{pc}} \right) \right) V_m^{liquid} \\ &= \left( \frac{V_{Si_nX}}{V_m^{Si_nX}} \left( \frac{(n+1)c_{Si} - n}{(1 - c_{Si})} \right) - \left( \frac{V_{gr}}{V_m^{gr}} + \frac{V_{pc}}{V_m^{pc}} \right) \right) V_m^{liquid} \end{aligned} \quad (5.31)$$

which allows us to substitute  $V_{Si, free}$  in the previous equation. Isolating  $V_{Si_nX}$  leads to

$$V_{Si_nX} = \frac{V_p + V_{gr} \left( 1 - \frac{V_m^{SiC}}{V_m^{gr}} + \frac{V_m^{liquid}}{V_m^{gr}} \right) + V_{pc} \left( 1 - \frac{V_m^{SiC}}{V_m^{pc}} + \frac{V_m^{liquid}}{V_m^{pc}} \right)}{\left( 1 + \frac{V_m^{liquid}}{V_m^{Si_nX}} \left( \frac{(n+1)c_{Si} - n}{(1 - c_{Si})} \right) \right)} \quad (5.32)$$

The volume fraction of free silicon becomes then

$$V_{Si, free} = \left( \frac{V_{Si_n X}}{V_m^{Si_n X}} \left( \frac{(n+1) c_{Si} - n}{(1 - c_{Si})} \right) - \left( \frac{V_{gr}}{V_m^{gr}} + \frac{V_{pc}}{V_m^{pc}} \right) \right) V_m^{liquid} \quad (5.33)$$

For the domain where free carbon is expected, i.e. below the red curve, we proceed analogously. The preform will react with the entering liquid Si-X alloy of with a concentration of  $c_{Si}$  in the alloy. The final situation is that all silicon that has entered the preform has either reacted with the carbonaceous phases or is captured in the next stable silicide of the stoichiometry  $Si_m X$ .

The final situation will be that the initial volume fraction of the pores, and a fraction of the volume fraction of the carbonaceous phases will be replaced by freshly reacted SiC and  $Si_m X$ . Hence,

$$V_p + \Delta V_{gr} + \Delta V_{pc} = V_{Si_m X} + V_{SiC, react} \quad (5.34)$$

Similarly to above it can be shown that the fraction,  $N_{Si}$ ,  $SiC_{react}$ , of silicon atoms being available for reaction with carbonaceous phases is linked to the total number of silicon atoms per volume,  $N_{Si}$ , entered by infiltration by

$$N_{Si, SiC react} = N_{Si} \left( \frac{(m+1) c_{Si} - m}{c_{Si}} \right) \quad (5.35)$$

Combined with  $N_{Si} = N_{Si, SiC react} + N_{Si, Si_m X}$  one finds

$$N_{Si, Si_m X} = N_{Si, SiC react} \frac{m(1 - c_{Si})}{(m+1) c_{Si} - m} \quad (5.36)$$

The volume fraction of the  $Si_m X$  phase can be expressed now as a function of the fraction of silicon atoms having entered the preform by infiltration, and reacted to fresh SiC,  $N_{Si, SiC react}$ , as

$$V_{Si_m X} = N_{Si, Si_m X} V_m^{Si_m X} = N_{Si, SiC react} \frac{m(1 - c_{Si})}{(m+1) c_{Si} - m} V_m^{Si_m X} \quad (5.37)$$

Similarly, the volume fraction of freshly reacted SiC becomes

$$V_{SiC, react} = N_{Si, SiC react} V_m^{SiC} \quad (5.38)$$

The fractions the volumes of the carbonaceous phases,  $\Delta V_{gr}$  and  $\Delta V_{pc}$  for graphite and pyrolytic carbon, respectively, that react with the silicon are consumed proportional to their atomic concentration in the preform:

$$\Delta V_{gr} = \frac{V_{gr}}{\frac{V_{gr}}{V_m^{gr}} + \frac{V_{pc}}{V_m^{pc}}} N_{Si, SiC react} \quad (5.39)$$



and

$$\Delta V_{pc} = \frac{V_{pc}}{\frac{V_{gr}}{V_m^{gr}} + \frac{V_{pc}}{V_m^{pc}}} N_{Si, SiC \text{ react}} \quad (5.40)$$

Expressing all volume fractions, i.e.  $\Delta V_{gr}$ ,  $\Delta V_{pc}$ ,  $V_{Si_m X}$ , and  $V_{SiC, react}$ , as a function of  $N_{Si, SiC \text{ react}}$  one finds

$$N_{Si, SiC \text{ react}} = \frac{V_p}{\left( \frac{m(1-c_{Si})}{(m+1)c_{Si}-m} V_m^{Si_m X} + V_m^{SiC} + \frac{V_{gr}+V_{pc}}{\frac{V_{gr}}{V_m^{gr}} + \frac{V_{pc}}{V_m^{pc}}} \right)} \quad (5.41)$$

Inserting in the expressions above allows finding the respective volume fractions. We note that for the Si-Zr system, the free silicon volume fraction gets negative when the initial pore volume fraction reaches the blue curve in Figure 5.1 from above and so do the volume fractions of the carbonaceous phases if one passes the red line in Figure 5.1 from below.

The interest of the calculations presented above is i) to be able to make a quantitative prediction of what phases and how much of them should be present for a given preform infiltrated with a given alloy when full reaction conversion is reached; and ii) to assess the observed density after infiltration against a qualified expectation. Both will be used in the chapter on preform infiltration.

### 5.3 Modelling pore clogging in a single carbon microchannel

The pore clogging in Si alloy infiltration can be anticipated to happen by two effects. First, by formation of solid SiC in the pore space upon reaction of carbon with liquid silicon, and second, by the precipitation of solid silicides at the infiltration front due to continuous consumption of silicon at the infiltration front by the initial wettable SiC formation and concomitant enrichment of the silicide former. We present here a basic mathematical model to obtain the conditions under which the pore clogging can happen by precipitation of silicides. We make the following simplifying assumptions:

1. The infiltration rate is controlled by the rate of reaction at the triple line and takes a characteristic value for a given temperature.
2. The change in composition of the liquid at the triple line has no influence neither on the growth rate of the SiC layer nor on the triple line velocity (at least as long as the infiltrant is liquid at the triple line).
3. The reaction of some of the silicon in the liquid with the carbon wall does neither lead to changes in the channel geometry nor to reduction of the liquid volume but simply to consumption of Si atoms.

4. The enthalpy of reaction is neglected and the whole process happens at an imposed temperature,  $T$ .
5. The pore closure due to excessive growth of SiC is not considered here.

The assumptions are valid as long as the channels are relatively wide compared to the thickness of the SiC layer, and if reaction is relatively slow. We use Si-Zr alloy as an example infiltrant but the model is also applicable to other alloying element which can form silicides.

### 5.3.1 Development of the model

Consider a rectangular channel of carbon with cross-section  $we$ , where  $w$  stands for the width and  $e$  for the thickness such that  $w \gg e$  as shown in Figure 5.2. The microchannel is infiltrated to a length  $L$  and the quantity of silicon atoms,  $n_{Si}$ , that have been consumed so far by the formation of SiC correspond to a volume of length,  $\lambda$ , taking into account the initial concentration of Si,  $c_{Si}$ , and the molar volume. The quantity of zirconium atoms,  $n_{Zr}$ , in that same volume are rejected into the liquid behind and diluted in a volume of length,  $\delta$ , that corresponds to the diffusion length. With the help of the observation from references [57,

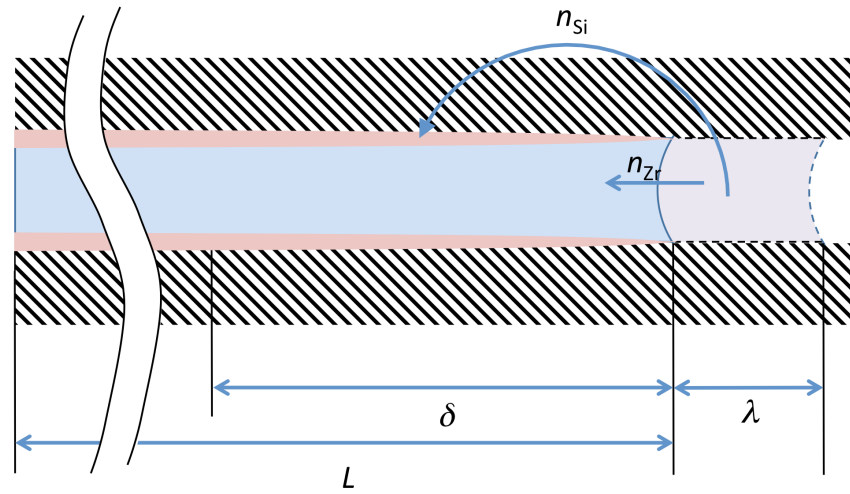


Figure 5.2 – Schematic of the carbon microchannel with rectangular cross section  $we$  filled with the liquid Si-Zr alloy to a length  $L$ . The quantity of silicon atoms,  $n_{Si}$ , that have been consumed so far by the formation of SiC corresponds to a volume of length,  $\lambda$ , taking into account the initial concentration of Si,  $c_{Si}$ , and the molar volume. The quantity of zirconium atoms,  $n_{Zr}$ , in that same volume are rejected into the liquid behind and diluted in a volume of length,  $\delta$ , that corresponds to the diffusion length.

136, 141, 151], the thickness of the reaction formed SiC layer,  $d_{SiC,0}$ , can be assumed to evolve according to Equation (5.42),

$$d_{SiC} = d_{SiC,0} \exp[-Q_{SiC}/RT] t^{1/n} \quad (5.42)$$

with  $d_{SiC,0}$  the prefactor,  $Q_{SiC}$  the activation energy of the SiC growth,  $t$  is the time since the beginning of the growth, and  $R$  and  $T$  are the gas constant and the temperature, respectively. For the derivation, we keep  $n$  as a parameter since there are in the literature various descriptors for the growth kinetics of the SiC layer, with  $n$  sometimes equal to 2 and sometimes equal to 4. We further assume, as stated in the simplifying assumptions, that the velocity of ingress,  $v$ , is a fixed value for a given temperature, and can be expressed as a function of temperature as

$$v = v_{tr} = v_0 \exp[-Q_{triple}/RT] \quad (5.43)$$

with  $v_0$  the prefactor and  $Q_{triple}$  the activation energy of the triple line reaction, while  $R$  and  $T$  are as usual the gas constant and the temperature, respectively. The diffusion length,  $\delta$ , is given as a function of the time,  $t$ , and the diffusion coefficient,  $D_{Si/Zr}$  as

$$\delta = \sqrt{D_{Si/Zr} t} \quad (5.44)$$

The diffusion coefficient can again be written as a function of temperature,  $T$ , in terms of a prefactor  $D_{Si/Zr,0}$  and an activation energy,  $Q_{diff}$ , as

$$D_{Si/Zr} = D_{Si/Zr,0} \exp[-Q_{diff}/RT] \quad (5.45)$$

The quantity of silicon atoms, that has been consumed when the triple line arrives at a position  $L$  in the channel is given by

$$n_{Si}^{SiC} = \frac{2(e+w)Ld_{SiC,0} \exp[-Q_{SiC}/RT] t^{1/n}}{V_m^{SiC}} \quad (5.46)$$

From this we can deduce the equivalent length,  $\lambda$ , of alloy that is consumed in the formation of SiC as

$$\lambda = \frac{2(e+w)Ld_{SiC,0} \exp[-Q_{SiC}/RT] t^{1/n}}{ew} \frac{V_m^{liquid}}{V_m^{SiC}} \frac{1}{c_{Si,0}} \quad (5.47)$$

and the reduced length,  $\lambda_{Zr}$ , that corresponds to the length filled by all the zirconium atoms left behind becomes:

$$\lambda_{Zr} = \frac{2(e+w)Ld_{SiC,0} \exp[-Q_{SiC}/RT] t^{1/n}}{ew} \frac{V_m^{liquid}}{V_m^{SiC}} \frac{(1-c_{Si,0})}{c_{Si,0}} \quad (5.48)$$

under the assumption that the partial molar volumes of silicon and zirconium atoms are identical. The zirconium atoms contained in that volume are then mixed with the atoms contained in a volume given by  $ew(\delta - \lambda_{Zr})$  with initial composition  $c_{Si,0}$ . The total volume of these two volumes is then again  $ew\delta$ . The silicon concentration in that volume,  $c_{Si}$ , can be calculated as

$$c_{Si} = \frac{\delta - \lambda_{Zr}}{\delta} c_{Si,0} \quad (5.49)$$

There is a critical value of zirconium enrichment and, hence, silicon concentration,  $c_{Si}^{crit}$ , at which the formation of zirconium silicide will block the flow of liquid and stop the infiltration. The accumulated virtual pure zirconium length,  $\lambda_{Zr}$ , takes the value

$$\lambda_{Zr} = \frac{\delta (c_{Si,0} - c_{Si}^{crit})}{c_{Si,0}} \quad (5.50)$$

whence

$$\frac{\delta (c_{Si,0} - c_{Si}^{crit})}{(1 - c_{Si,0})} = \frac{2(e + w) L d_{SiC,0} \exp[-Q_{SiC}/RT] t^{1/n} V_m^{liquid}}{e w V_m^{SiC}} \quad (5.51)$$

With  $e \ll w$  we can write

$$\frac{(c_{Si,0} - c_{Si}^{crit})}{(1 - c_{Si,0})} \frac{V_m^{SiC}}{V_m^{liquid}} = \frac{2L d_{SiC,0} \exp[-Q_{SiC}/RT] t^{1/n}}{e \delta} \quad (5.52)$$

The time over which the growth of the SiC layer affects the Si concentration of the volume under consideration of length,  $\delta$ , from the infiltration front is  $t = \delta/v$ . Inserting this in the equation above we find:

$$\frac{(c_{Si,0} - c_{Si}^{crit})}{(1 - c_{Si,0})} \frac{V_m^{SiC}}{V_m^{liquid}} = \frac{2L d_{SiC,0} \exp[-Q_{SiC}/RT] \left(\frac{\delta}{v}\right)^{1/n}}{e \delta} = \frac{2L d_{SiC,0} \exp[-Q_{SiC}/RT]}{e \delta^{\frac{n-1}{n}} v^{\frac{1}{n}}} \quad (5.53)$$

The diffusion length,  $\delta$ , itself is linked to the total time the infiltration has taken place, the latter being given by  $L/v$ , by:

$$\delta = \sqrt{D_{diff} \frac{L}{v}} \quad (5.54)$$

Inserting this value of  $\delta$  in the above equation, we find:

$$\begin{aligned} \frac{(c_{Si,0} - c_{Si}^{crit})}{(1 - c_{Si,0})} \frac{V_m^{SiC}}{V_m^{liquid}} &= \frac{2L d_{SiC,0} \exp[-Q_{SiC}/RT]}{e (D_{diff} L)^{\frac{n-1}{2n}} v^{\frac{1}{n} - \frac{n-1}{2n}}} \\ &= \frac{2L d_{SiC,0} \exp[-Q_{SiC}/RT]}{e (D_{diff} L)^{\frac{n-1}{2n}} v^{\frac{3-n}{2n}}} \\ &= \frac{2L^{\frac{n+1}{2n}} d_{SiC,0} \exp[-Q_{SiC}/RT]}{e D_{diff}^{\frac{n-1}{2n}} v^{\frac{3-n}{2n}}} \\ &= \frac{2L^{\frac{n+1}{2n}} d_{SiC,0} \exp[-Q_{SiC}/RT]}{e D_{diff,0}^{\frac{n-1}{2n}} \exp[-(n-1)Q_{diff}/2nRT] v_0^{\frac{3-n}{2n}} \exp[-(3-n)Q_{triple}/2nRT]} \end{aligned} \quad (5.55)$$

Isolating the length of infiltration,  $L$ , at which the critical concentration is obtained at the infiltration front leads to

$$L = \left[ \frac{(c_{Si,0} - c_{Si}^{crit})}{(1 - c_{Si,0})} \frac{V_m^{SiC}}{V_m^{liquid}} \frac{e}{2} \frac{D_{diff,0}^{\frac{n-1}{2n}}}{v_0^{\frac{n-3}{2n}} d_{SiC,0}} \exp \left[ \frac{2nQ_{SiC} - (n-1)Q_{diff} - (3-n)Q_{triple}}{2nRT} \right] \right]^{\frac{2n}{n+1}} \quad (5.56)$$

This is a closed expression (Equation (5.56)) for the length,  $L$ , over which the infiltration should be able to take place before blocking by the formation of silicide is observed. All important system parameters, i.e. channel dimension, growth and diffusion kinetics and infiltration rate enter into the equation, as well as the initial concentration of the alloy.

### 5.3.2 Implications of the model

In Figure 5.3 (a), an example of the effect of temperature on infiltration length of a carbon microchannel with a rectangular cross section and of thickness of  $10\mu\text{m}$ , infiltrated by Si-8 at. pct Zr alloy, is plotted using Equation (5.56). The values for the parameters used in the model are taken from the references [132, 175–177]. The value  $d_{SiC,0}$  was calculated from the experimental observations of Voytovych et al.[176]. The value of  $c_{Si}^{crit}$  was taken as per the Si-Zr phase diagram considering the concentration of Zr is such that 80 % of the phase fraction at given temperature is solid using lever rule, which corresponds to approximately 27.8 at. pct Zr below peritectic temperature of  $1620^\circ\text{C}$ , and increases to 43.6 at. pct Zr above  $1620^\circ\text{C}$ . The calculation used a value of  $n = 2$ .

$$\begin{aligned} V_m^{SiC} &= 1.25 \times 10^{-5} \text{ m}^3/\text{mol} \\ V_m^{liquid} &= 1.31 \times 10^{-5} \text{ m}^3/\text{mol} \\ D_{diff,0} &= 15 \times 10^{-9} \text{ m}^2/\text{s} \\ v_0 &= 2 \times 10^{-4} \text{ m/s at } 1500^\circ\text{C} \\ d_{SiC,0} &= 9 \times 10^{-6} \text{ m} \\ Q_{SiC} &= 200 \times 10^3 \text{ J/mol} \\ Q_{diff} &= 28 \times 10^3 \text{ J/mol} \\ Q_{triple} &= 185 \times 10^3 \text{ J/mol} \end{aligned}$$

The triple line velocity indicated here is significantly larger, by a factor of 5, roughly, than the observed triple line velocities in sessile drop spreading experiments. While the latter could be considered as a good approximative indicator for the spreading rate on inner surfaces of preforms or microchannel experiments, the observed infiltration distances in pure Si experiments set a lower limit to triple line velocity. It is roughly that lower limit that has been chosen here. On the other hand, the thermal activation energy of the triple line velocity,  $Q_{triple}$ , has been derived from observed spreading rates in sessile drop experiments at different temperatures [176]. From Figure 5.3 (a), one could conclude that the infiltration length

decreases with increase in process temperature for a near eutectic concentration of alloy. The sudden change in infiltration length for the process temperature above the peritectic temperature is due to the fact that the solid fraction is much lower above the peritectic temperature for a given composition.

The Figure 5.3 (b) shows the infiltration length as a function of initial Zr concentration for a 10  $\mu\text{m}$  carbon microchannel at 1500  $^{\circ}\text{C}$ . One can clearly see that with increasing Zr concentration the infiltration length reduces and for a certain threshold value ( $\sim 33$  at. % Zr in this case) where the alloy itself is solid at the infiltration temperature resulting in no infiltration. Another important thing to notice is the very high infiltration length as the Zr concentration closes to zero. This is due to the fact that in developing the leading equation reflected in the graph we did only consider the clogging by silicide formation at the infiltration front and not clogging at the rear of the infiltration by reaction formed SiC.

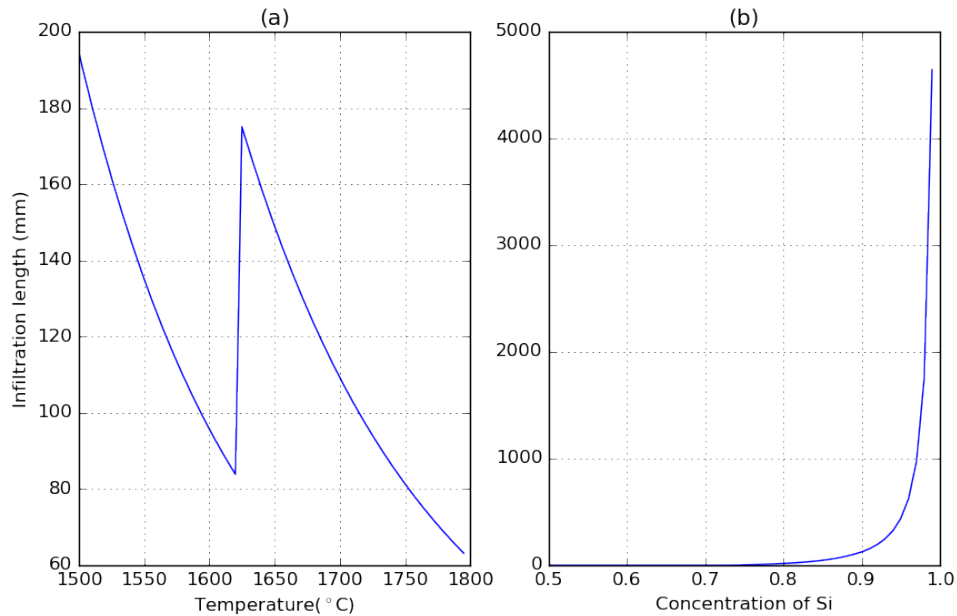


Figure 5.3 – Infiltration length calculated using Equation (5.56) for a carbon microchannel with a rectangular cross section and of thickness of 10  $\mu\text{m}$  (a) with increasing temperature, infiltrated by Si-8 at. pct Zr alloy (b) infiltration length as function of initial Si fraction at 1500  $^{\circ}\text{C}$ .

## 5.4 Extension of the model to preform infiltration

The simple straight rectangular capillary is a good descriptor of the single microchannel experiments but not for a preform as used in typical infiltration experiments. Those preforms deviate in two points from the simple microchannel: i) the geometry is no longer a straight

infiltration capillary of fixed cross-section, and ii) parts of the surface of the channels are provided by existing SiC in the preform. To account for these features we have to adapt the model. This is outlined in the following.

#### 5.4.1 Accounting for arbitrary capillary shape

An arbitrary pore channel cross section leads to two changes in the equations developed above: i) the surface-to-volume ratio changes, which has an effect on the amount of Si consumed and hence the concentration of the alloying element close to the infiltration front, and ii) the velocity of the triple line is now no longer only parallel to the infiltration direction that is on first order perpendicular to the outer surface but locally meanders around that infiltration direction vector. The situation is schematically depicted in Figure 5.4 The changing of the surface-to-

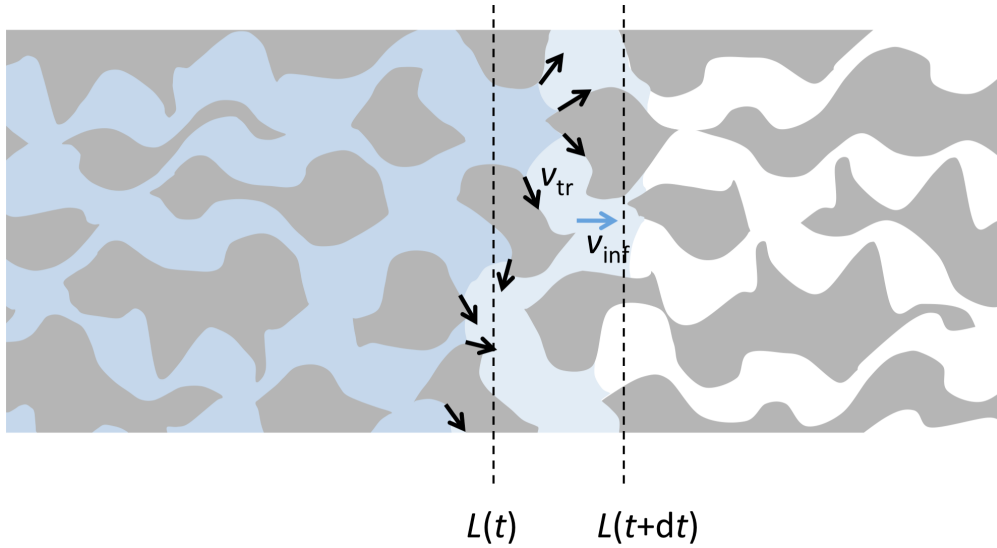


Figure 5.4 – Schematic representation of the infiltration in a real preform. The infiltration velocity,  $v_{inf}$ , is no longer equal to the triple line velocity as in the microchannel model.

volume ratio from bottle-necks to larger spaces can be accounted for by a characteristic capillary radius,  $R^*$ , that is chosen such that its specific surface is equal to that of a preform under consideration. The deviation of the triple line velocity vector,  $v_{tr}$ , with regard to the infiltration direction is taken care of by the vector average of the triple line velocity vector,  $v_{inf} = v_{tr} = v_{tr} \cos \alpha$ , where  $\alpha$  is the angle between the local triple line velocity and the macroscopic infiltration direction. We hence write:

$$v_{inf} = v_{tr} \langle \cos \alpha \rangle = \xi v_{tr} = \xi v_0 \exp^{-Q_{triple}/RT} \quad (5.57)$$

Note that the factor  $\xi$  accounts for the local surface inclination coming from both, the local change in channel cross-section and the tortuosity of the infiltration path.

### 5.4.2 Accounting for the presence of SiC particles

The SiC particles present in the preform will change the surface available for reaction. The fraction of the preform surface that has to react in order to allow advancing of the infiltration front is given by a factor,  $\phi$ . In first approximation, one could assume that  $\phi$  is equal to one minus the volume fraction of SiC,  $V_{p,SiC}$ , in the solid of the preform. It is, however, expected that this is a lower limit given the fact that the graphite and SiC particles are mixed with the phenolic resin and hence both the SiC particles and the graphite particles are at least in part covered with a thin film of pyrolytic carbon. Therefore, the factor  $\phi$  is most likely contained by  $1 - V_{p,SiC} \leq \phi \leq 1$ . The rate of infiltration is not expected to change since the parts of the surface composed of carbonaceous material will only allow the advancing of the infiltration front at the rate that the interface between liquid and preform is converted into wetted SiC. We consider here that  $\langle \cos \alpha \rangle$  is the same for the surfaces formed by SiC as for those formed by carbonaceous material.

### 5.4.3 Changes to the guiding equations

The changes to the guiding equations of the infiltration model of the microchannel are outlined in the following. The infiltration velocity,  $v_{inf} = dL/dt$ , becomes now a fraction of the triple line velocity,  $v_{tr}$ , but remains proportional to it, as outlined above. The quantity of silicon atoms, that has been consumed when the triple line arrives at a position  $L$  in the preform is now given by

$$n_{Si}^{SiC} = \frac{2\pi R^* \phi L d_{SiC,0} \exp[-Q_{SiC}/RT] t^{1/n}}{V_m^{SiC}} \quad (5.58)$$

where the factor,  $\phi$ , accounts for the reduced consumption of Si due to the presence of SiC particles and persists in the development as presented for the microchannel. The geometrical change from  $2(e + w)$  for the surface and  $ew$  for the cross section (both for a unity of length) to the corresponding values of  $2\pi R^*$  and  $\pi R^{*2}$ , respectively, of the equivalent capillary as defined above, leads to a replacement of the term  $2/e$  by  $2/R^*$ . If all these changes are introduced, the guiding equation determining the infiltration length becomes:

$$L = \left[ \frac{(c_{Si,0} - c_{Si}^{crit})}{(1 - c_{Si,0})} \frac{V_m^{SiC}}{V_m^{liquid}} \frac{R^*}{2\phi} \frac{D_{diff,0}^{\frac{n-1}{2n}}}{\xi^{\frac{n-3}{2n}} v_0^{\frac{n-3}{2n}} d_{SiC,0}} \exp \left[ \frac{2nQ_{SiC} - (n-1)Q_{diff} - (3-n)Q_{triple}}{2nRT} \right] \right]^{\frac{2n}{n+1}} \quad (5.59)$$

### 5.4.4 The equivalent pore radius of the preform

The equivalent radius for the porous preform can be determined as follows: Be  $a_i$  the specific surface area per weight in  $m^2 g^{-1}$  of the particle type  $i$ . The specific surface area per volume,



$\alpha_i$ , is then:

$$\alpha_i = a_i \rho_i \quad (5.60)$$

with  $\rho_i$  the density of particle type  $i$  in  $\text{gm}^{-3}$ . The inner surface per volume of the preform is the sum of the products of volume fraction of the particles of type  $i$  times their specific surface area per volume, and it must be equal to the volume fraction of equivalent cylindrical channels with radius  $R^*$  times their specific surface area. For the latter we find:

$$\alpha_{eq. cyl.} = \frac{2\pi R^*}{\pi R^{*2}} = \frac{2}{R^*} \quad (5.61)$$

As said before, that must be equal to the specific surface area of the particles:

$$V_p \alpha_{eq. cyl.} = \frac{2V_p}{R^*} = V_{gr} \alpha_{gr} + V_{SiC} \alpha_{SiC} \quad (5.62)$$

whence

$$R^* = \frac{2V_p}{V_{gr} \alpha_{gr} + V_{SiC} \alpha_{SiC}} \quad (5.63)$$

Hence, for every preform,  $R^*$  can be calculated based on the particles that are included in the preform. For simplicity's sake we neglect the pyrolysed carbon from the bakelite.

#### 5.4.5 Implication of the model to preform infiltration

In Figure 5.5 (a), the infiltration length is plotted with increasing infiltration temperature for a SiC-C preform with  $R^* = 0.5 \mu\text{m}$ , infiltrated by Si-8 at. pct Zr alloy, using Equation (5.59). The value of  $\phi = 0.5$  and  $\xi = 1/3$  were used for the calculations. The rest of the parameters are same as mentioned before in the infiltration length calculation for microchannel. As expected this also shows the similar trend of decreasing infiltration depth with increasing temperature and sudden increase in the infiltration depth at peritectic temperature. In Figure 5.5 (b), the infiltration length for a SiC-C preform with  $R^* = 0.5 \mu\text{m}$  as a function of initial Zr concentration in the alloy is also plotted using the Equation (5.59) for a processing temperature of  $1500^\circ\text{C}$ . Also, a similar trend can be observed where the infiltration depth is decreasing with increasing initial Zr concentration in the alloy. The values of the infiltration length where initial Zr concentration is very low have to be taken with a grain of salt: it could very well be that the infiltration is stopped earlier by the clogging of the entrance channels due to the formation of SiC, which was however not considered here. Overall, the model for adequate pore fraction combined with the model for pore clogging in preforms by silicide formation at the infiltration front highlights the concurring interest in the choice of the right alloy composition: on the one hand, larger silicide former contents in the alloy increase the latitude in adequate porosity levels in the preform, as illustrated in Figure 5.1 by the increasing distance between the red and the blue line as the concentration of the silicide forming alloying element increases. On the

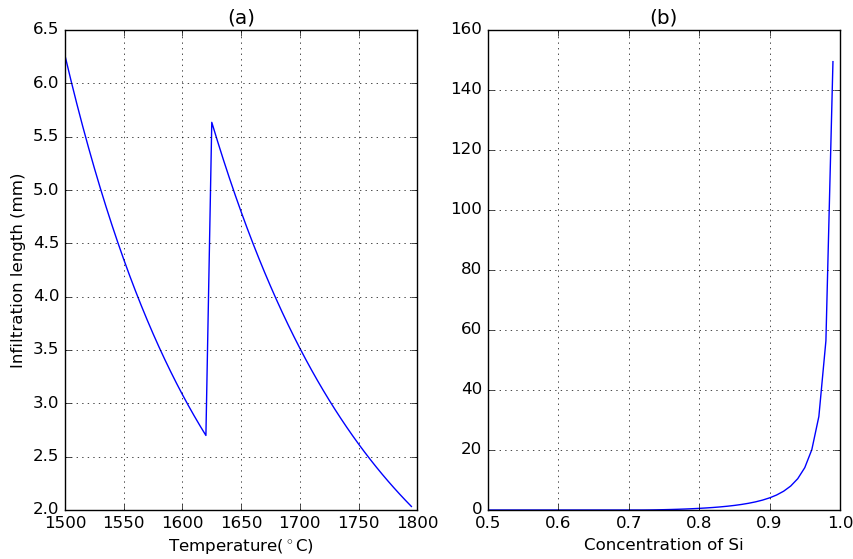


Figure 5.5 – Infiltration length calculated using Equation (5.59) for a SiC-C preform having  $R^* = 0.5 \mu\text{m}$  (a) with increasing temperature, infiltrated by Si-8 at. pct Zr alloy (b) with increasing Si fraction infiltrated at  $1500^\circ\text{C}$ .

other hand, increasing the concentration of the silicide forming element in the infiltrating alloy reduces the expected infiltration length due to solid silicide precipitation at the infiltration front, as shown in Figure 5.5.

The parameters to play with are then the particle size of the constituents of the preform and the volume fraction of carbonaceous material in the preform. Both are likely to affect the equivalent radius  $R^*$  and the coverage parameter  $\phi$ . Combinations with large particles and low carbonaceous phase content (and concomitantly, low pore volume fraction in the preform) seem the most promising that could also accommodate larger silicide former concentrations in the infiltrant. At the same time, such a parameter set would also reduce the risk of clogging due to reactive SiC formation. The limit in this direction is set by the length scale over which reaction conversion can be obtained.

## 5.5 Differential model for non-isothermal infiltration experiments

In the current study and in many practical infiltration settings the infiltration is not isothermal but starts as soon as the liquid silicon or silicon alloy is in contact with the preform. Many of the intervening quantities in the isothermal model are however temperature dependent and will change with the changes in temperature during infiltration. In all generality, closed form expression for the infiltration will no longer be available. We develop for the non-isothermal case hence a differential scheme that can be numerically integrated.

### 5.5.1 Formulation of the model

We start with the number of Si atoms,  $n_{Si}^{SiC}$ , that have been consumed for the formation of wettable SiC from the volume element extending by the diffusion length,  $\delta$ , from the infiltration front back into the liquid at time  $t$ . Similarly, to Equation (5.46), we find:

$$n_{Si}^{SiC}(t) = \frac{2(e+w)L(t)\theta_{SiC,0}\exp[-Q_{SiC}/RT(t)]\left(\frac{\delta(t)}{v(t)}\right)^{1/n}}{V_m^{SiC}} \quad (5.64)$$

The same quantity a moment  $dt$  later,  $n_{Si}^{SiC}(t+dt)$ , is

$$n_{Si}^{SiC}(t+dt) = \frac{2(e+w)L(t+dt)\theta_{SiC,0}\exp[-Q_{SiC}/RT(t+dt)]\left(\frac{\delta(t+dt)}{v(t+dt)}\right)^{1/n}}{V_m^{SiC}} \quad (5.65)$$

We assume that the only rapidly changing entity is the infiltration length,  $L$ , and hence write

$$n_{Si}^{SiC}(t+dt) - n_{Si}^{SiC}(t) = \frac{2(e+w)(L(t+dt) - L(t))d_{SiC,0}\exp[-Q_{SiC}/RT(t)]\left(\frac{\delta(t)}{v(t)}\right)^{1/n}}{V_m^{SiC}} \quad (5.66)$$

and with  $L(t+dt) - L(t) = v(t)dt$

$$\frac{dn_{Si}^{SiC}(t)}{dt} = \frac{2(e+w)v(t)d_{SiC,0}\exp[-Q_{SiC}/RT(t)]\left(\frac{\delta(t)}{v(t)}\right)^{1/n}}{V_m^{SiC}} \quad (5.67)$$

The equivalent channel length of liquid,  $\lambda$ , as used previously, becomes:

$$\lambda(t) = \int_0^t \frac{dn_{Si}^{SiC}(t)}{dt} dt \frac{V_m^{liquid}}{ew} \frac{1}{c_{Si,0}} \quad (5.68)$$

and for  $\lambda_{Zr}$  as well as the silicon concentration in the volume element within  $\delta$  of the infiltration front we find analogously to above

$$\lambda_{Zr}(t) = \int_0^t \frac{dn_{Si}^{SiC}(t)}{dt} dt \frac{V_m^{liquid}}{ew} \frac{(1 - c_{Si,0})}{c_{Si,0}} \quad (5.69)$$

and

$$c_{Si}(t) = \frac{\delta(t) - \lambda_{Zr}(t)}{\delta(t)} c_{Si,0} \quad (5.70)$$

The diffusion length,  $\delta$ , is simply related to the time,  $t$ , since the infiltration started

$$\delta(t) \approx \sqrt{D_{Si/Zr,0} \exp[-Q_{diff}/RT(t)] t} \quad (5.71)$$

accepting some approximation, given that the temperature itself is also a function of time. The triple line velocity,  $v(t)$ , will also vary due to the variation of temperature with time:

$$v(t) = v_0 \exp[-Q_{triple}/RT(t)] \quad (5.72)$$

Lastly, the actual position of the triple line,  $L(t)$ , can be found by integration of the triple line velocity:

$$L(t) = \int_0^t v(t) dt \quad (5.73)$$

The time temperature history,  $T(t)$ , can be arbitrarily set. Typically, the infiltration will start when  $T$  reaches the melting temperature of the alloy. At that point,  $t = 0$ . Once the silicon concentration reaches its critical value, where silicide formation will stop the further advancing of the triple line, the triple line velocity will go to zero. That is, however, not necessarily the end of the infiltration process: as time goes on, the diffusion length will increase. Since at the same time the value of  $\lambda_{Zr}$  stagnates according to Equation (5.69), diffusion will eventually increase the Si concentration at the infiltration front again and allow further ingress, but at a slower rate. The condition for the triple line velocity becomes then

$$v(t) = \begin{cases} v_0 \exp[-Q_{triple}/RT(t)] & \text{for } c_{Si} < c_{Si}^{crit} \\ 0 & \text{else} \end{cases} \quad (5.74)$$

The result of the numerical integration of such a non-isothermal infiltration is shown in Figure 5.6, for an infiltration run with a continuous heating ramp of 1500 °C/h up to 1500 °C, 1 minute hold and natural cool down after the furnace had been switched off. Several domains can be recognized in the modelled curve: in the blue region in Figure 5.6, the infiltrated length increases more than proportionally with time due to the fact that the infiltration velocity is increasing with temperature. At the transition between the blue and the green domain, the clogging condition  $c_{Si} < c_{Si,crit}$  is reached and the triple line advances only because the diffusion brings constantly silicon to the triple line (or in other words Zr is transported away from the triple line). There is a dynamic equilibrium between enrichment in Zr due to advancing of the triple line and reduction of Zr due to diffusion. Once the maximum temperature is reached, the furnace is shut off, the dynamic equilibrium persists until the solidification temperature is reached where all infiltration comes to a halt.

It is instructive to model the same process for the case that the temperature is raised to 1700 °C as shown in Figure 5.7. There are similar domains observed as at 1500 °C. The notable difference comes when the temperature reaches 1893 K (1620 °C), the peritectic temperature of formation of  $ZrSi_2$ . At that temperature, the critical silicon concentration takes a jump. In the present modelling the critical Si concentration has been 0.73 for temperatures below 1893 K and 0.57 for temperatures above. Compared to the infiltration with maximum temperature 1500 °C, the infiltration length reaches higher values due to the combination of the longer time at high temperature, which increases the diffusion length, and the lower critical silicon

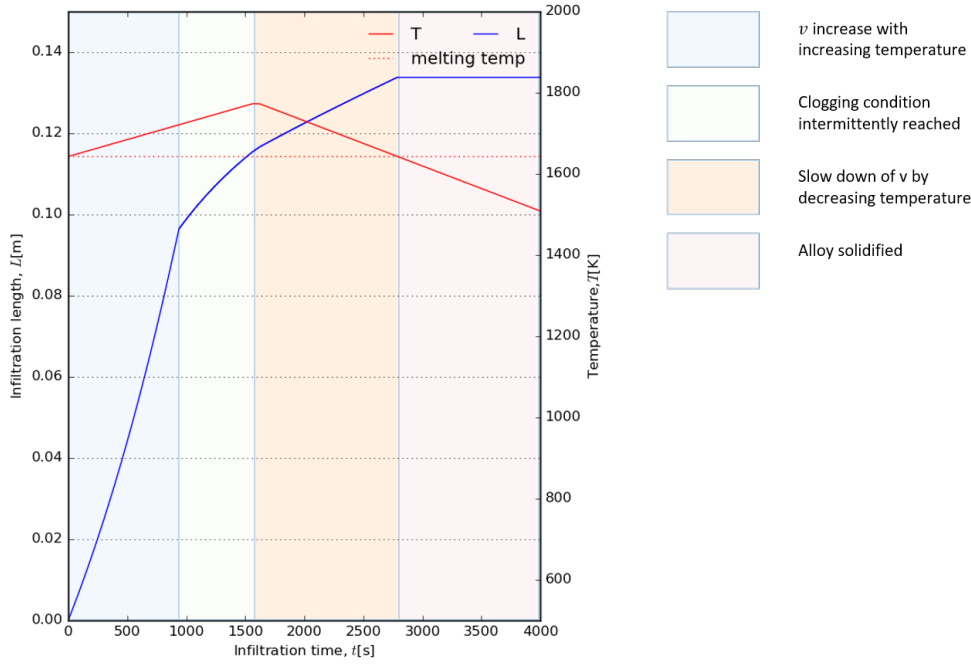


Figure 5.6 – Evolution of infiltration length,  $L$ , and temperature in a non-isothermal infiltration experiment of a Si-8 at.-pct Zr alloy into a microchannel of 10  $\mu\text{m}$  thickness. At the beginning the infiltration accelerates since the reaction at the triple line is thermally activated. The change in slope in the green region comes by since the clogging condition  $c_{\text{Si}} < c_{\text{Si,crit}}$  is reached but continuously alleviated by the diffusion of Si to the triple line. After having reached the maximum temperature, the triple line velocity stagnates, yet remains controlled by the Si diffusion regime. In the red domain the triple line is stalled due to solidification of the alloy.

concentration at the maximum temperature of the process. The chosen critical composition in the present case corresponds to 80 % of solid phase at the eutectic temperature and the peritectic temperature, respectively for temperatures below and above the peritectic temperature. Alternatively, the critical composition could be chosen as that corresponding to an arbitrary fraction of solid at each temperature. The critical silicon concentration in the liquid would also then take a jump at the peritectic temperature except for the case when the solid fraction is chosen as very close to 0. It is instructive to compare the non-isothermal model to the isothermal model with the explicit expression of  $L$  as a function of the processing parameters. It turns out that the isothermal model predicts only the infiltration length achieved in the blue regime, i.e. the one until the critical composition is reached for the first time. The closed form, and the lack of consideration that the flow condition recovers thanks to diffusion once the triple line has come to a halt, are the main cause for this.

We can of course model the isothermal case by the differential approach of the non-isothermal model by taking a starting temperature identical to the isothermal temperature and choosing a heating ramp of 0 K/h. The results of this are shown in Figure 5.8. It can be seen that the

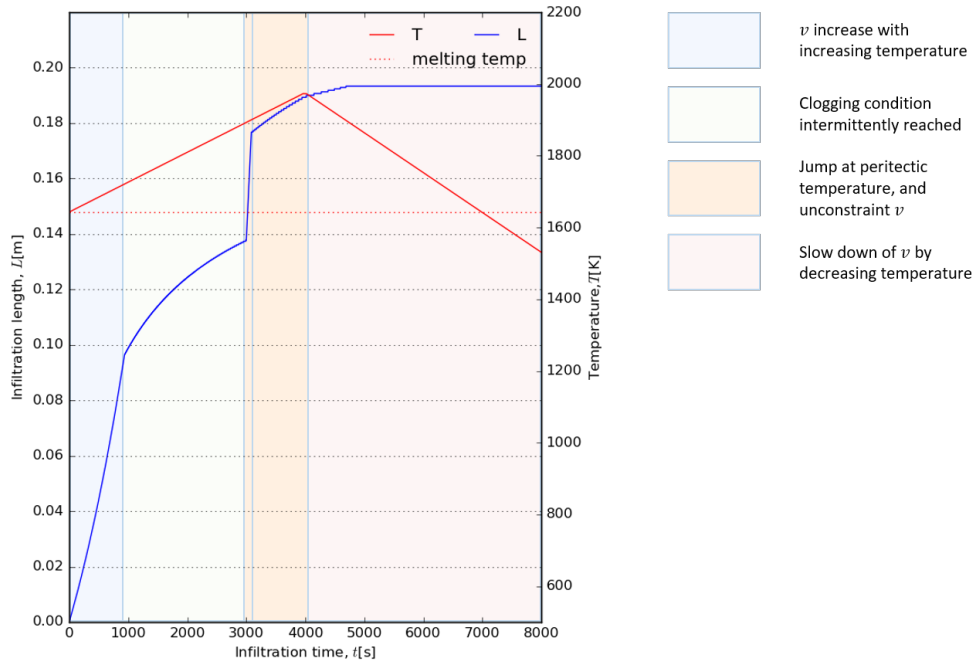


Figure 5.7 – Evolution of infiltration length,  $L$ , and temperature in a non-isothermal infiltration experiment of a Si-8 at.-pct Zr alloy into a microchannel of  $10\text{ }\mu\text{m}$  thickness. As in the example at  $1500^\circ\text{C}$  the infiltration accelerates in the beginning due to thermal activation. The change in slope in the green region comes by since the clogging condition  $c_{\text{Si}} < c_{\text{Si,crit}}$  is reached but continuously alleviated by the diffusion of Si to the triple line. At the peritectic temperature, the critical silicon concentration takes a jump and the triple line is again at its unconstrained speed. After having reached the maximum temperature, the triple line velocity stagnates, yet remains controlled by the Si diffusion regime.

infiltration length goes, under the influence of diffusion, way above the value evaluated with the explicit scheme.

The non-isothermal model developed for the single microchannel infiltration can naturally also be extended to be used for the preform infiltration experiments along the lines outlined above for the isothermal case.

### 5.5.2 Limits of the differential model

The diffusion mediated ingress appearing in the differential model has to be taken with a grain of salt: In the formulation of the model, it has been assumed that silicon is only consumed while the triple line is advancing, leading us to the statement that  $\lambda_{\text{Zr}}$  stagnates when the triple line is at rest. When the triple line comes to a halt, however, there is still some silicon consumed by the continuing of the reaction to SiC, albeit at a (rapidly) decreasing rate as the arrest time increases. This will lead to a slower advancing rate in the diffusion controlled regime than obtained by the current formulation and most likely results in a terminal arrest of

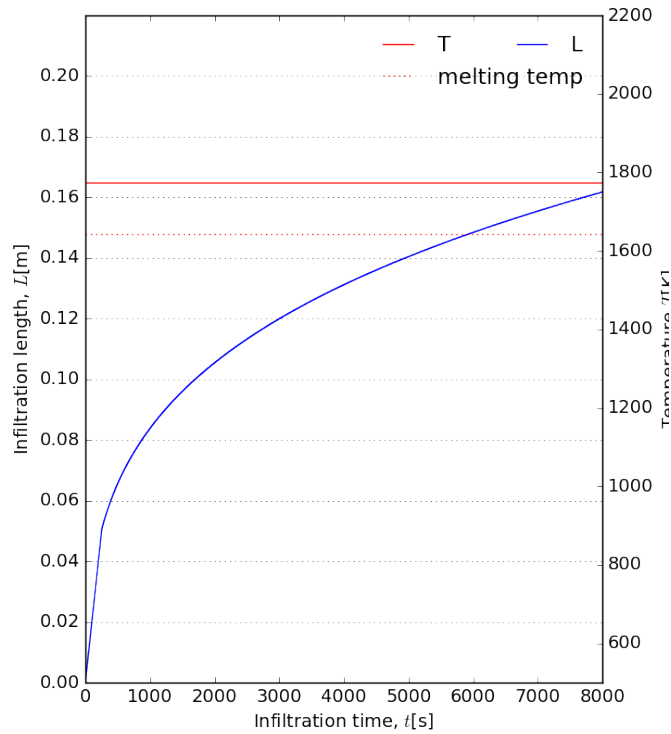


Figure 5.8 – Evolution of infiltration length,  $L$ , with the differential scheme developed for the non-isothermal case applied to the isothermal case by setting the heating rate to 0 and the starting temperature to the isothermal temperature.

the infiltration front and not to a "creeping" advancement of the infiltration front above all limits for long enough times. Including this in the numerical scheme would, however, require a complicated case distinction of silicon consumption between the situation where the triple line moves or is at rest and also a change in formulation at restart of the movement of the triple line. We limit ourselves here to state that the infiltration length shown in Figure 5.6 obtained by diffusion mediated ingress is an overestimation and that the real infiltration length expected is somewhere in between the length achieved when the triple line comes first to a halt and the diffusion mediated infiltration length calculated for a given processing time at high temperatures.

A second limitation is that the diffusion length is constantly updated to the new temperature in the non-isothermal model. Upon increasing the temperature this will always lead to an overestimation of the actual diffusion length because diffusion did not operate all along at the (high) current temperature but evolved somewhat more slowly, which made us call Equation (5.71) an approximation. The second effect of this updated diffusion length is that as temperature decreases in the non-isothermal model, the diffusion length calculation is subjected to a competition between increase in time (leading to a longer diffusion length)

and reduction in diffusion coefficient by reduced thermal activation (leading to a shorter diffusion length). If the net outcome of this competition is a shortening of the diffusion length, this will decrease artificially the concentration of silicon at the infiltration front by virtue of Equation (5.70). This leads to the situation that the silicon concentration is increasingly above the critical concentration and continues to increase as temperature decreases. This is the reason why the infiltration length comes to a halt in the modelling shown in Figure 5.7 albeit the solidification temperature is not yet reached.



This page is intentionally left blank.

## **6 Kinetics of reactive flow of Si and Si-Zr alloy in carbon capillaries**

### **6.1 Disclaimer**

The present Chapter is written in paper style to be submitted to the Journal of the European Ceramic Society. Only the mathematical model for the channel infiltration is not presented in full length here since it has been developed in detail in chapter 5 of this thesis and presenting it once again here in detail would have been redundant. We nevertheless use the results of the modelling in the discussion as if the model had been given in the paper.

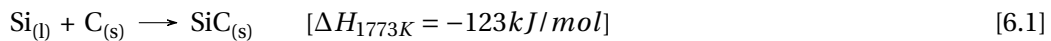
### **6.2 Abstract**

In this work, the mechanisms leading to the pore closure in Reactive Melt Infiltration (RMI) of carbon by pure silicon and a near eutectic Si-8 at-pct Zr alloy at 1500 °C and 1700 °C under vacuum were studied. Various geometrical configurations of microchannels were fabricated via laser ablation of glassy carbon plates. The micron size capillary channels allowed simplifying the complicated porosity distribution in the infiltration of powder or fibres based porous preform while keeping the physical dimensions in the range of where the physical phenomenon of pore closure takes place. The extent of infiltration was analysed by means of X-ray radiography. For RMI of pure Si, the widely accepted decrease in capillary radius by the formation of a solid state SiC layer by the reaction of liquid Si and C was observed, but did not lead to closure and it is hence not the infiltration limiting step in channels as small as 10 µm. However, in the case of the Si-Zr alloy infiltration, another mechanism of pore closure was observed, namely the precipitation of zirconium silicides at the infiltration front, due to Zr enrichment in the alloy by the continuous consumption of Si for the formation of SiC.

### **6.3 Introduction**

Silicon infiltrated silicon carbide (Si-SiC), since its development in 1975 by Hillig et al.[47], has gained popularity as an industrial ceramic material, known for its remarkable properties, such

as low porosity, low density, high thermal conductivity, high mechanical strength, excellent chemical, oxidation and thermal shock resistance and high wear and corrosion resistance [9, 52]. Increasing interest led to the development of many variants, such as monolithic and particle or fibre reinforced ceramic matrix composites (CMC). Although they can be obtained from different constituents and processes [50, 51, 178, 179], the fabrication concept is based on the reactive melt infiltration (RMI) process, also known as liquid silicon infiltration (LSI) in the case of Si infiltration. The general idea consists of infiltrating a porous carbonaceous preform by liquid Si to attain a fully dense Si-SiC composite. The liquid Si is pulled into the porous preform, driven by capillary forces where a chemical reaction occurs between the liquid Si and solid C, resulting in a solid SiC matrix, according to the following reaction [56]:



where *l* is liquid, *s* is solid and  $\Delta H$  is enthalpy of formation

This reaction is highly exothermic, potentially causing an increase in local temperature by several hundred degrees. This, in turn, results in the occurrence of thermal stresses within the material, which could potentially lead to material failure [132, 180]. Additionally, depending on the pore characteristics and the reactivity of the preform, capillary blockage and, as a consequence, incomplete infiltration may take place [59]. The diffusion of C through solid SiC is faster than that of Si; therefore, the growth of solid state reaction product proceeds also into the pore space, potentially blocking further transport of liquid Si [27, 28, 168]. Moreover, the remaining unreacted Si expands during solidification, inducing additional stress concentrations [181]. Various approaches have been made to overcome these issues, such as including inert interphase such as SiC or BN, by chemical vapor deposition (CVD) of carbon fibres followed by infiltration. These techniques, however, being effective, remain expensive in terms of processing and equipment. Furthermore, they hamper the conversion reaction and, hence, do not solve the problem of limited operation temperature, restricted by residual Si. An alternative approach is to use metal – silicon alloys, as they not only lower the amount of residual Si by the formation of high temperature silicides but also lower the infiltration temperature [61, 62, 66, 68]. The alloying element is selected based on liquid-phase equilibria and the ability to form refractory silicides with higher melting temperatures than pure Si. This has been demonstrated using Si-Mo, Si-Zr, Si-Co and Si-Hf alloys [64, 69, 73, 77, 182, 183]. Several researchers have also studied the wetting behaviour of Si and Si alloys on various types of graphite and SiC [90, 120, 132, 133, 135, 136, 138, 150, 167, 184], increasing the understanding of the physical principles behind Si and metal – Si alloys infiltration. However, certain phenomena occurring at the micron scale remain unclear. Classical sessile drop experiments [155, 167], millimetre sized capillaries [154] or direct observations of preform infiltration [57, 151, 185] are commonly used to characterise the reactive infiltration process; however, the differences in experimental macroscopic scale may overlook certain effects, which could only be observed at the micron scale.

In this study, the process of Si-SiC composite formation by RMI was idealized by infiltration experiments of carbon capillary microchannels with pure Si and near eutectic Si-8 at-pct Zr alloy at 1500 °C and 1700 °C. By infiltrating microchannels of various designs, produced using laser ablation, it was possible to simplify the complicated porosity distribution in porous preforms while maintaining the physical dimensions in the range at which the physical phenomenon of pore closure takes place. The experimental products were analysed using X-ray radiography and scanning electron microscopy (SEM), the characterization of which allows further enhancing our understanding of the capillary closure phenomenon during RMI of Si and Si-Zr alloy.

## 6.4 Materials and Methods

### 6.4.1 Material

Vitreous carbon plates (SIGRADUR-G, HTW, Germany), also referred to as glassy carbon, were selected as the source of carbon due to their dense structure compared to graphite plates, which tend to have significant porosity. For RMI, pure Si (Sicorma GmbH, Germany) and near eutectic Si-8 at-pct Zr alloy (Chengdu Huarui Industrial Co Ltd., China) were used.

### 6.4.2 Fabrication of microchannels

Microchannels, with a depth ranging from 0.01 mm to 0.1 mm and length of up to 460 mm, were fabricated using laser ablation. For machining the channels, a pulsed laser (SuperRapid laser from Lumera GmbH) was used. The short pulse laser operates at a wavelength of 355 nm (frequency tripled) and has a nominal pulse length of 10 ps. The laser pulses were directed towards the sample via a galvano scan head (ScanLab GmbH). For ablation, a pulse repetition rate of 160 kHz and pulse energy of about 14  $\mu$ J (2.2 W average power) was used. The structure was written with a hatched pattern. A total of six hatch directions (0°, 90°, 30°, 120°, 60°, 150°) were applied to achieve a smooth surface. The required depth was achieved by adjusting the pulse energy and the number of repetitions. Since the pattern was larger than the writing area of the scan head stitching was applied. A graded transition zone was used to minimize edges between the stitching areas.

Various configurations of channels were produced to study different aspects of reactive infiltration, summarised in Table 6.1 and depicted in Figure 6.1.

### 6.4.3 Infiltration setup

Two vitreous carbon plates, one flat and unmachined and one with laser ablated microchannels were clamped together using graphite clamps and bolts sourced from Steinemann Carbon AG, Switzerland (2 clamps for 50 mm-long and 3 for 100 mm-long samples), as schematically shown in Figure 6.2. The carbon plates were cleaned in an ultrasonic bath for 5 minutes in

Table 6.1 – Summary of dimensions of microchannels in various configurations.

configuration	channel number	shape	width (mm)	depth (mm)	length* (mm)
A	1	straight	1	0.1	50
	2	straight	4	0.1	50
	3	straight	1	0.025	50
	4	straight	4	0.025	50
B	1	straight	1	0.1	100
	2	straight	4	0.1	100
	3	straight	1	0.025	100
	4	straight	4	0.025	100
C	1	straight	1	0.03 / 0.02 / 0.01	100/3
	2	rectangular bend	1	0.02	241
	3	curved bend	1	0.02	207
D	1	curved bend	1	0.01	465

\* along the center-line of the channel

isopropyl alcohol and then dried using a clean compressed gas canister (Druckluft 67, Kontakt Chemie, Belgium) just before clamping them together. Utmost care was taken to avoid any dust entrapment in the channels.

Approximately 80 g of pure silicon or the eutectic Si-8 at-pct Zr alloy was placed in a crucible made up of graphite foil (SGL, Germany) coated with a boron nitride spray (3M, Germany). The graphite foil crucible was next placed into a larger graphite crucible. The clamped infiltration form was situated slightly above the bottom of the graphite foil crucible by two graphite rods, as shown in Figure 6.3. Finally, the whole setup was put in a graphite heated vacuum furnace (FCT, Germany). The furnace was heated to 1500 °C or 1700 °C at the rate of 300 °C/h under a vacuum of  $\sim 5 \times 10^{-2}$  mbar. After reaching the final temperature, the heating was turned off and the furnace was let cool down.

#### 6.4.4 Analyses

The surface roughness after polishing and after laser ablation was measured using a Leica DCM8 confocal microscope. The infiltrated microchannel samples were imaged via X-ray radiography using an RX solution EasyTom XL, France. The infiltrated fragment of the microchannels typically shows up darker than the rest of the carbon plate and empty channel. Based on the radiographs, the samples were cut using a diamond saw to observe infiltration cross-sections selectively. The samples were then mounted in resin and polished using an automatic polishing machine (TEGRAMIN, Struers GmbH, Switzerland) and 15, 9, 6 and 1  $\mu\text{m}$  diamond suspensions and including a final polishing step with 0.5  $\mu\text{m}$  alumina suspension. The reaction layer and interphase were analysed using a scanning electron microscope and EDX (Tescan VEAG3 with Bruker AXS Quantax 200 EDX system).

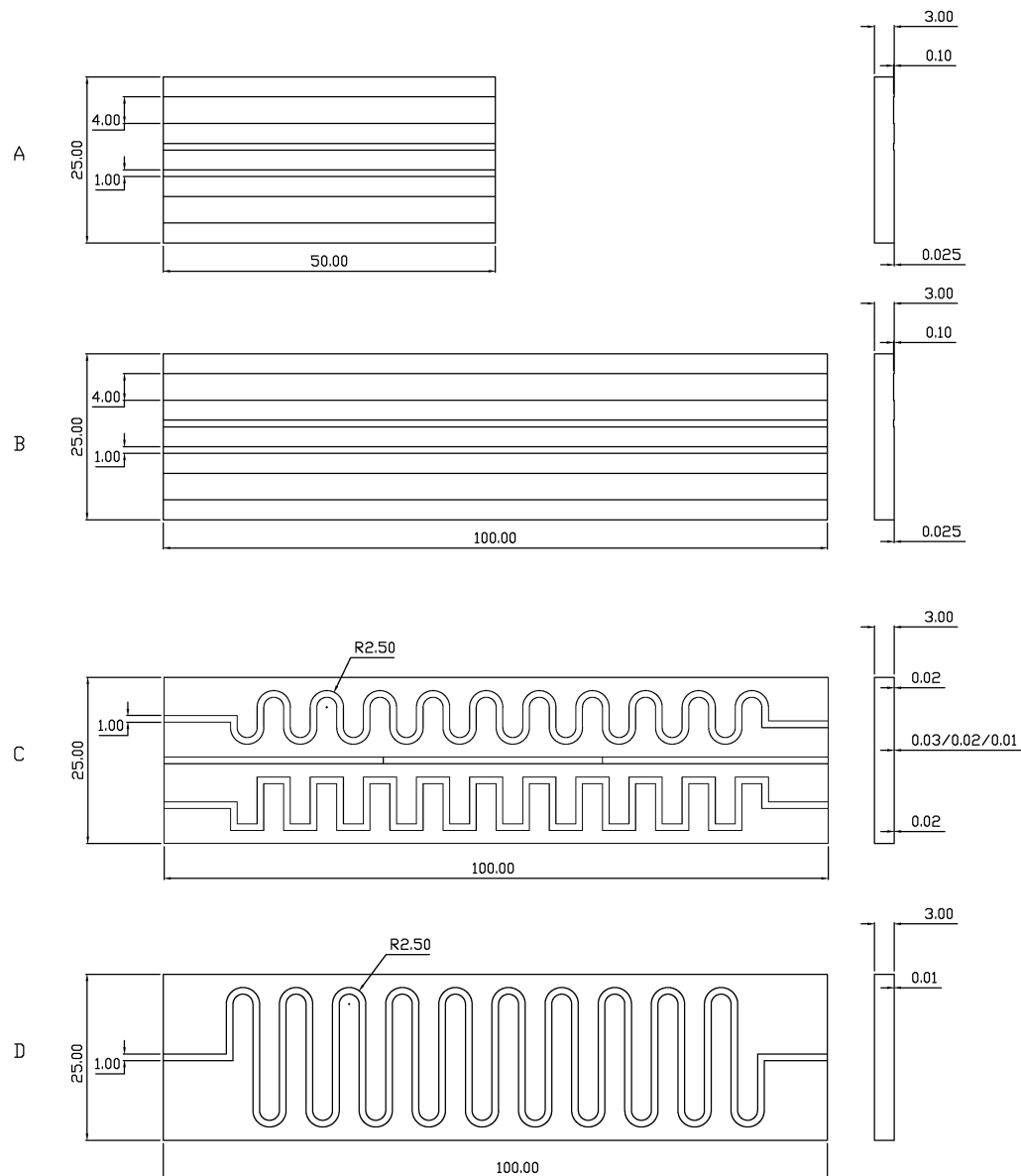


Figure 6.1 – Various configurations of microchannels with their dimensions used in this research. Length indications are in mm.

## 6.5 Results and discussion

### 6.5.1 Surface roughness

The surface roughness values determined using confocal microscopy by Leica DCM8 microscope in accordance with ISO 4287 for  $R_a$  and ISO 25178 for  $S_a$  values are summarized in Table 6.2.

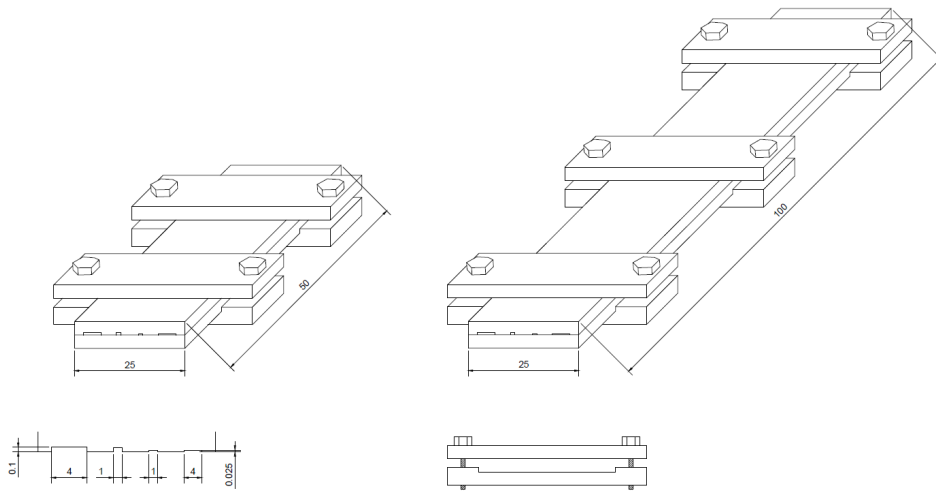


Figure 6.2 – Schematic of capillary microchannel assembly by clamping vitreous carbon plate with laser ablated groove together with another vitreous carbon plate. Length indications are in mm.

## 6.5.2 Microchannel characterization

### 6.5.2.1 Configuration A

Microchannel configuration A was designed to study the effect of the aspect ratio of the channels and the effect of side edges. Pure Si was used to infiltrate the microchannels at 1500 °C. The X-ray radiograph taken after the infiltration showed complete infiltration of all 4

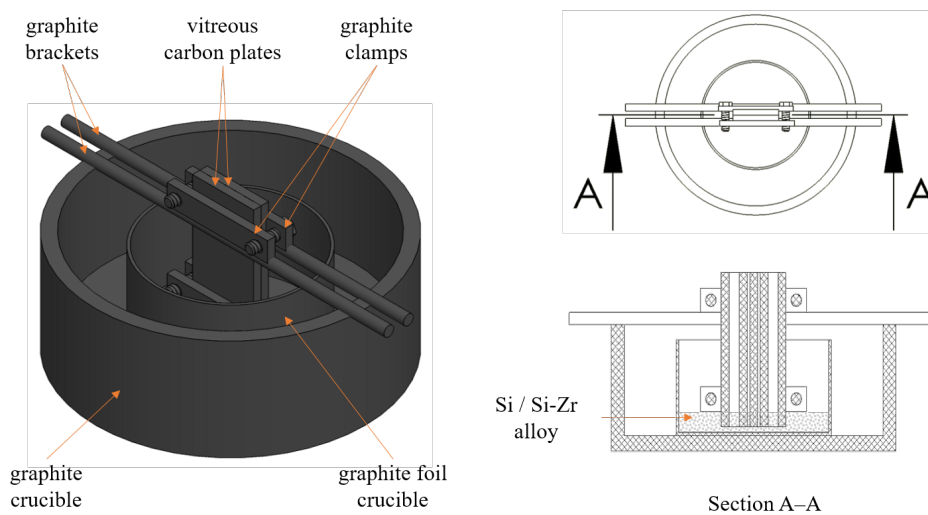


Figure 6.3 – Experimental setup of infiltration showing microchannel made by clamping vitreous carbon plates being kept upright by graphite brackets in the graphite crucible. The melting Si or Si-Zr alloy was kept in the BN coated graphite foil crucible in the center.

Table 6.2 – Surface roughness of the polished surface and laser ablated surface of glassy carbon plate (measured on 20  $\mu\text{m}$  deep channel) measured by Leica DCM8.

Surface	$R_a$ (nm)	$S_a$ (nm)
As polished	$3.4 \pm 0.2$	$5.4 \pm 0.6$
Laser ablated	$49.3 \pm 2.5$	$185.0 \pm 21$

channels (Figure 6.4). In the X-ray radiograph, the channels filled with Si appears darker than the unfilled channels. The four microchannels had width-to-depth aspect ratios varying from 10 to 160, as shown in Table 6.3.

Table 6.3 – Aspect ratio of laser ablated microchannels in vitreous carbon.

Width (mm)	Depth (mm)	Aspect ratio
1	0.1	10
4	0.1	40
1	0.025	40
4	0.025	160

SEM analysis of each Si infiltrated microchannel was carried out at the height of 15 mm, 25 mm and 35 mm from the bottom. Multiple images from each microchannel were combined to measure the average thickness of the reaction layer. For this purpose, the grid was put onto every image to ensure equal distances between the consecutive measurements. In Figure 6.5 (a), an example of an SEM image made by the panoramic stitching of several high resolution pictures from the cross section of the 1 mm by 0.1mm microchannel is shown with the typical grid used to measure the reaction layer thickness at a fixed interval. The black part in the image is carbon, and the light part is the channel filled with solidified Si. The darker gray phase at the microchannel walls is the SiC reaction layer. The measurements of reaction layer thickness were carried out every 25  $\mu\text{m}$ . Afterward, they were divided into three groups, namely the left edge, middle and right edge, to investigate the potential effect of the edges on the formation of the reactive layer. Moreover, the opposite walls of the channels were analyzed separately since the reactivity of the polished and the laser ablated surface might be different. Henceforth, the designation ‘bottom’ refers to the microchannel wall influenced by the laser ablation process, whereas ‘top’ is the opposite, not influenced, as-polished surface. In Figure 6.5 (b), the average thickness of the reaction layer of four microchannels with aspect ratios from 10 to 160 are plotted for three groups left edge (L), middle (M) and right edge (R). The systematic layer thickness measurement did not show any trend from the left edge to the right edge. Also, the thickness of the reaction layer did not show any significant change along the length of infiltration. Therefore, the assumption of two infinite parallel plates separated by a micron size gap forming a microchannel along the length can be considered valid. However, a significant difference in reaction layer thickness was found between each channel’s top and bottom walls. One possible reason behind this behavior is a strong correlation between



surface roughness and reactivity as has been observed by others previously [119, 186] .

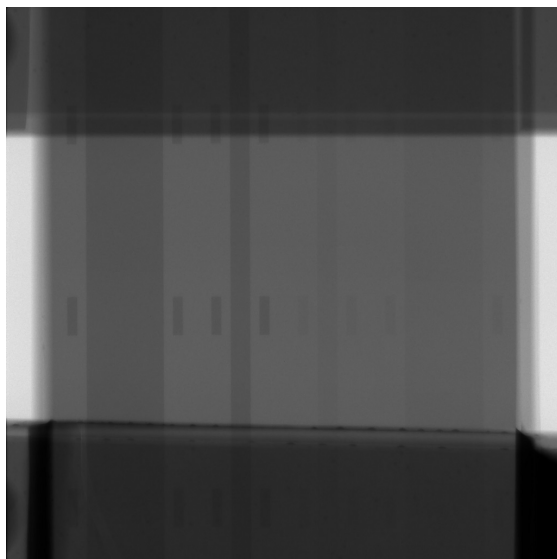


Figure 6.4 – Radiograph of microchannels in configuration A showing complete infiltration of all the channels.

#### 6.5.2.2 Configuration B

The dimensions of microchannels in configuration B was similar to configuration A except that the length was 100 mm instead of 50 mm. The small grooves, as seen in the radiograph (Figure 6.6 ) were markers to observe the direction of formation of the reaction layers by measuring the distance between the outer edge of the microchannel and the marker. The sealing between the two plates was, however, insufficient to allow for this kind of observation since the alloy seeped through the tiniest gaps possible to fill the gaps. The microchannels were infiltrated by near eutectic Si-8 at-pct Zr alloy at 1500 °C. The radiograph showed complete infiltration along the whole length (Figure 6.6 ). It can be seen from the radiograph that the zirconium-rich phase from the eutectic alloy is increasing as the infiltration proceeds. As the infiltration by alloy proceeds, the Si concentration of the alloy decreases due to reaction with carbon to form SiC. The reaction layer, in this case, was also found to be mainly SiC with some traces of trapped Zr as observed with SEM (Figure 6.7). The SEM images of the 0.02 x 1 microchannel taken at 0, 20, 40, and 60 mm (Figure 6.7) from the microchannel entrance shows the correlation between the increase in the concentration of  $\text{ZrSi}_2$  phase and the infiltration length to the corresponding region of the radiograph in Figure 6.6.

#### 6.5.2.3 Configuration C

Configuration C was designed to study the effect of tortuosity and change in the capillary thickness. The microchannel with rectangular bends would provide a more tortuous path

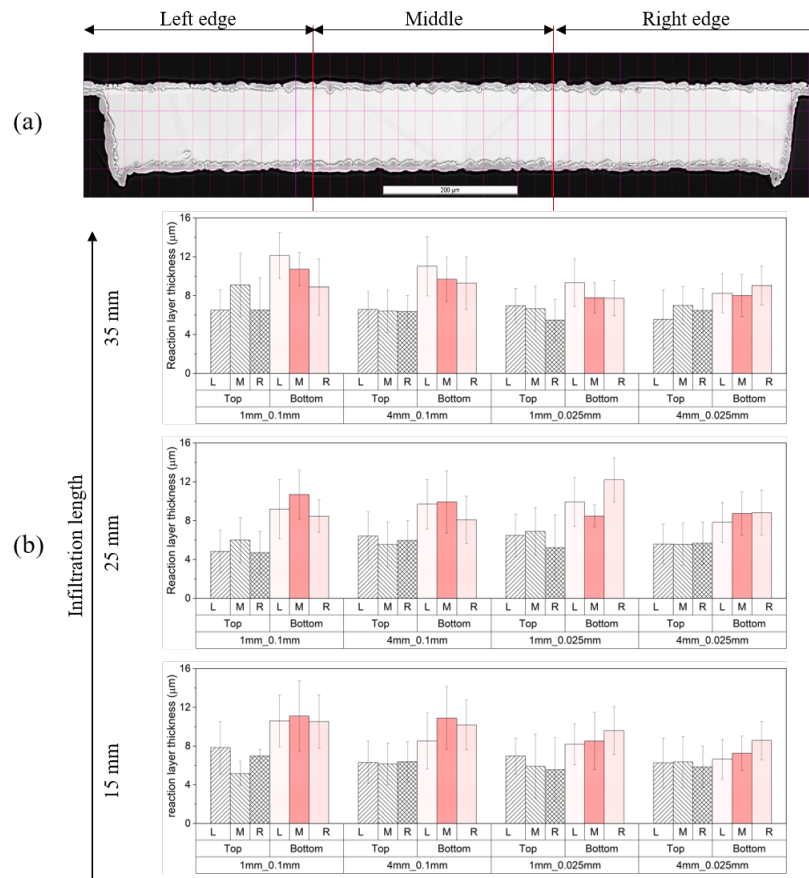


Figure 6.5 – (a) SEM image showing a cross-section of 1 mm by 0.1mm microchannel infiltrated at 1500 °C in the sample with a grid for reaction layer's thickness measurements (b) Reaction layer thickness along the infiltration length at 15, 25 and 35 mm from the bottom for all 4 channels divided into the left edge (L), middle (M) and right edge (R) and top and bottom laser ablated plate infiltrated by pure Si.

with abruptly reducing velocity than the one with semi-circular bends. Both the channels had a depth of 0.02 mm, while the middle channel was straight and was divided into three equal parts with thickness 0.03 mm near the entrance, 0.02 mm in the center part and 0.01 mm towards the end of the channel. The tortuous shape was also a means to increase the possible infiltration length of the channel.

The radiograph (Figure 6.8(a)) shows that all three microchannels were completely infiltrated by Si-8 at-pct Zr alloy at 1500°C. Some coarse Zr-rich primary phases can be seen in both the rectangular bend and the curved bend channels. As can be seen in the close-up image to the right, the Zr-rich phase is also present further in the direction of the infiltration front. It simply gets more finely dispersed. This can be interpreted as facilitated nucleation of the Zr-rich phase by larger oversaturation of zirconium, i.e., higher Zr-content. In the middle straight channel, the initial two sections with 0.03 mm and 0.02 mm depth had a fine eutectic structure. The top one-third section of approximately 33 mm with 0.01 mm depth showed a longer

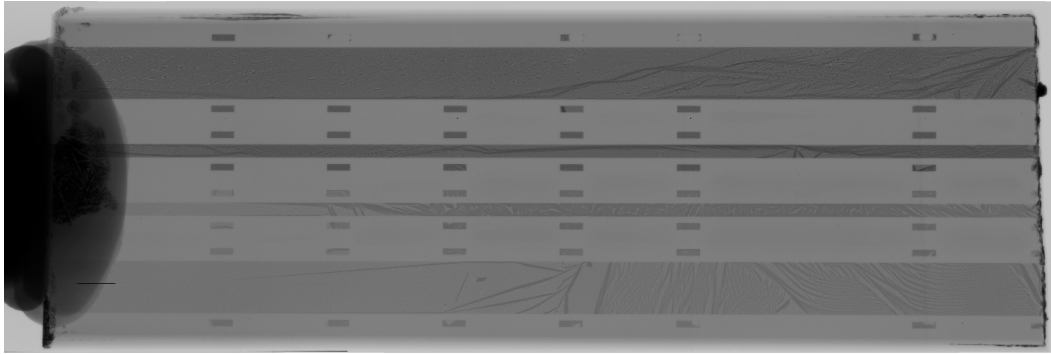


Figure 6.6 – Radiograph of microchannels of configuration B after infiltration by near eutectic Si-8 at-pct Zr alloy.

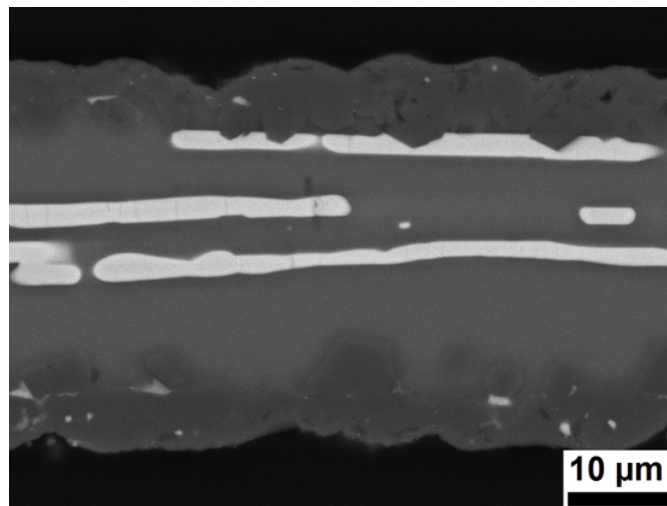


Figure 6.7 – SEM image of cross section of 1 mm x 0.025 mm microchannel at 20 mm from the bottom. The lighter part in the middle is Zr rich phase while the reaction layer is mainly SiC with some trapped Zr.

needle-like structure of Zr rich phase, which was extracted for phase fraction analysis using the grayscale thresholding technique (Figure 6.8 (b)). The grayscale threshold was adjusted manually to separate Zr rich dark grey regions (presumably the  $\text{ZrSi}_2$  primary phase) using the grayscale threshold function of Fiji [166] software. The fraction of the black region was then plotted against the length of infiltration. The tendency of a slight increase in Zr rich phase fraction can be observed; however, there was still complete infiltration of the microchannel.

#### 6.5.2.4 Configuration D

The configuration D was designed with semi-circular bends to observe the effect of tortuosity in microchannels with a depth of 0.01 mm. The microchannel had a total length of 465 mm. The sample D1 and D2 were infiltrated using Si-8 at-pct Zr alloy at 1500 °C. In Figure 6.9, the

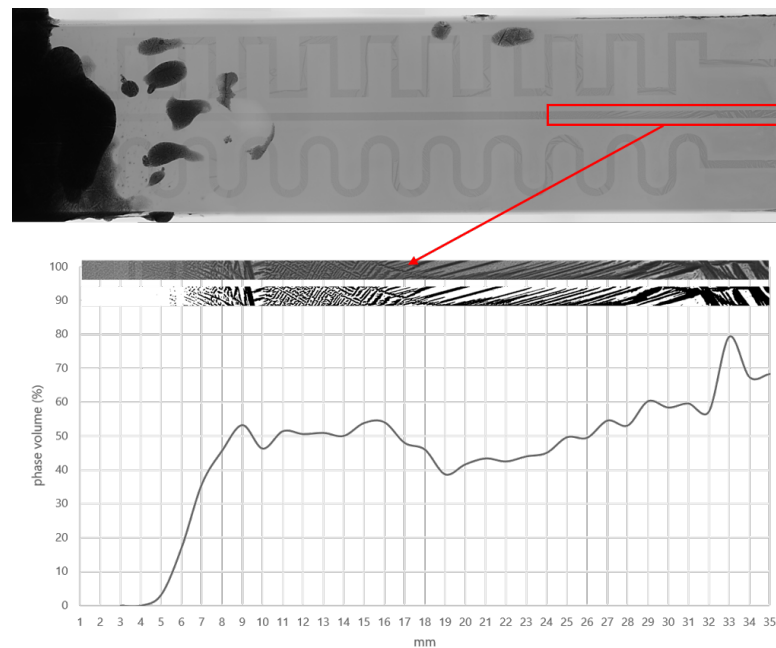


Figure 6.8 – (a) Radiograph of microchannels of configuration – C after infiltration by near eutectic Si-8 at-pct Zr alloy (b) Phase fraction analysis of 0.01 mm section of the gradient channel. The black fraction represents the Zr-rich phase.

so-called pore closure phenomenon was observed, where the infiltration of alloy stopped in the microchannel approximately at 166 mm and 120 mm from the entrance in sample D1 and D2, respectively. A similar effect of the increase in Zr-rich phase fraction along the length of microchannel was observed. The radiograph of sample D3 after infiltration by pure Si at 1500 °C showed complete infiltration (Figure 6.10 ). As the microchannels are very thin compared to the total thickness of 6 mm glassy carbon plate assembly, the contrast obtained in the radiograph due to the small difference in attenuation of SiC/Si in the microchannel compared to the glassy carbon plate is much lower than for the Si-Zr alloy. The results show that the infiltration of pure Si is dominated by triple line velocity and not affected by reduction in channel cross section due to the formation of the SiC layer even at 0.01 mm microchannels. In contrast, during the infiltration of Si-8 at-pct Zr alloy, the concentration of Si at the infiltration front keeps decreasing as infiltration proceeds along the microchannel due to the reaction of Si from liquid alloy with C from glassy carbon plate to form solid SiC layer at the interface. The enrichment of the infiltration front in Zr results in precipitation of Zr silicides, possibly causing the (intermittent) closure of the microchannel at the front.

The sample D4 was infiltrated by Si-8 at-pct Zr alloy at 1700 °C. In the radiograph (Figure 6.11 ) after infiltration, the microchannel closure was observed at 322 mm. The higher infiltration temperature retards the precipitation of primary Zr-rich solid phases to higher Zr-concentrations.

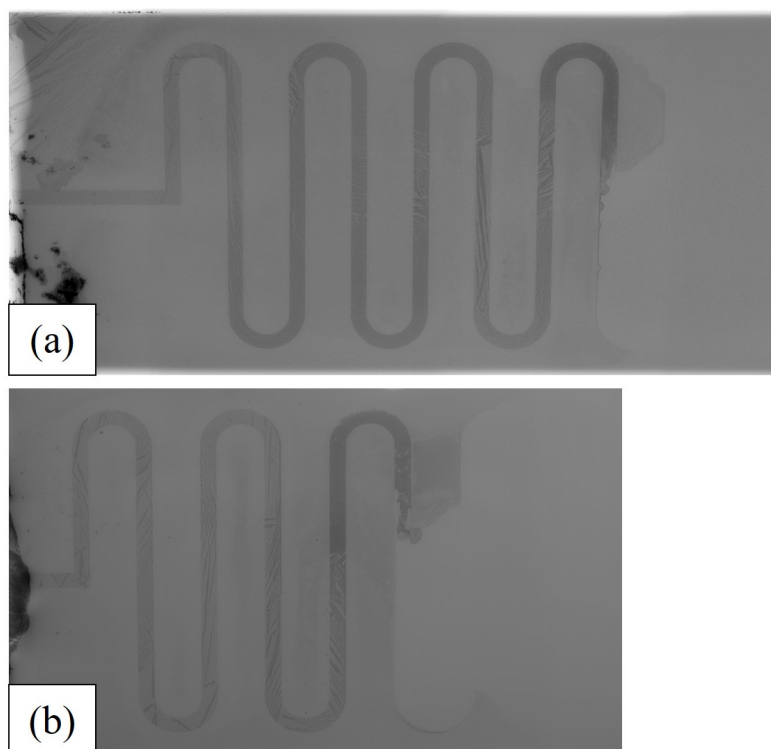


Figure 6.9 – Radiographs of two samples D1 and D2 after infiltration by Si-8 at-pct Zr alloy at 1500 °C.

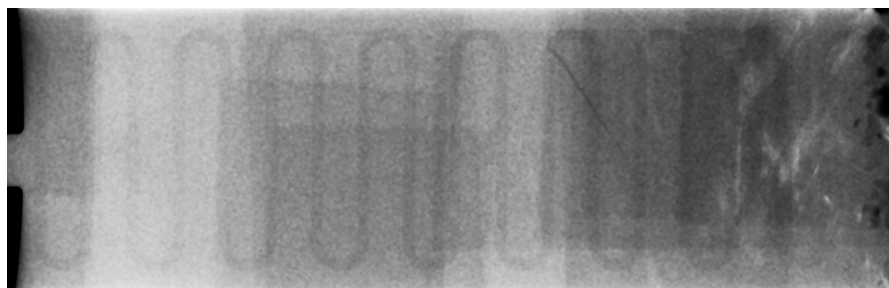


Figure 6.10 – Radiograph of sample D3 showing complete infiltration by pure Si at 1500 °C.

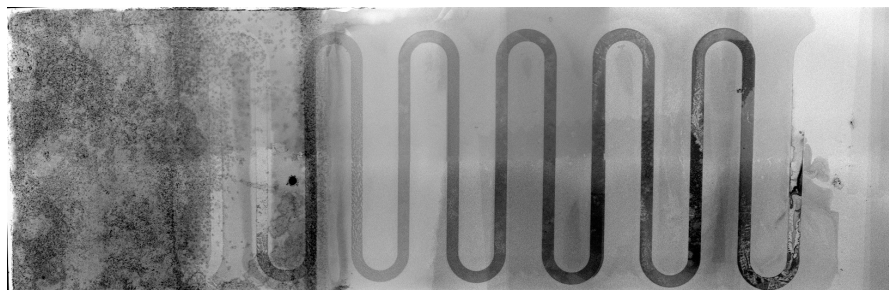


Figure 6.11 – Radiograph of sample D4 infiltrated by Si-8 at-pct Zr alloy at 1700 °C showed closure of the microchannel at 322 mm.

### 6.5.3 The morphology of reaction layer between silicon and vitreous carbon

Several authors have carried out experimental studies on the reaction mechanism occurring at the Si/vitreous carbon interface [120, 133, 136, 187]. A general finding described the reaction formed layer as a bi-layer. We also observed a similar bi-layer in our experiments with both pure Si and Si-Zr alloy infiltrated microchannels, as seen in Figure 6.5 (a) and Figure 6.7. The bi-layer can be clearly distinguished and observed in the BSE image (Figure 6.12) of the cross section of 0.1 mm deep microchannel from configuration A. Initially, the layer I is formed at the interface by carbon dissolution followed by micron-sized SiC grain precipitation. The SiC particles of layer I subsequently dissolve and re-precipitate as faceted crystals forming layer II. The results, being in line with the research of Voytovych et al. [136] and Deike et al. [187], lead to the general picture that this complex zone consists of a thin, continuous SiC layer (I), approximately 1-2  $\mu\text{m}$  thick, separating so-called 'pockets' (I') from layer II. In layer II two different types of grains can be observed – faceted SiC crystals (denoted as IIa) and columnar SiC crystals (denoted as IIb). The single crystals can reach far into the Si. Some of them seems to be detached from the layer and being completely surrounded by the Si phase.

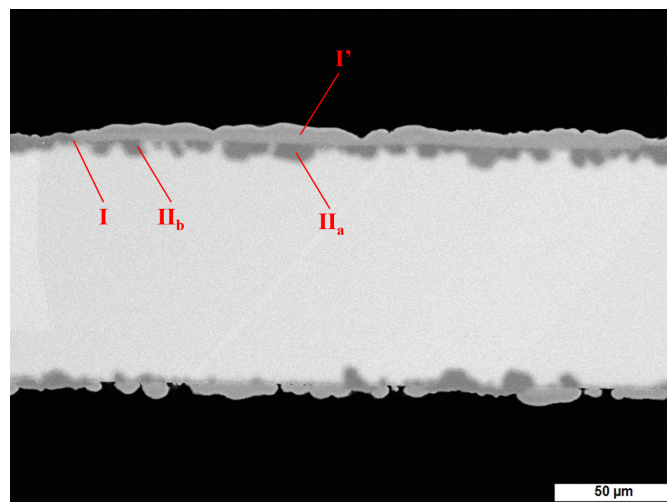


Figure 6.12 – BSE image of Si infiltrated 1mm by 0.1mm microchannel sample of configuration –A taken at 15mm from bottom.

Despite the fact that the reaction layer thickness was observed to be nearly constant with increasing infiltration distance in the sample of configuration A, the morphology of SiC changes substantially, as shown in Figure 6.13. These observations seem to be in agreement with the findings of Voytovych et al. [136] and Deike et al. [187]. They reported that for a long – term experiment, at times  $t$  longer than a certain critical time  $t^*$ , homogenization of the reaction zone occurs due to grain coarsening which then leads to disappearance of layer I.

The EDX point analysis across the reaction formed SiC layer at the interface between molten silicon, and the vitreous carbon microchannel of configuration A illustrates the changes in concentration of silicon as seen in Figure 6.14. The zones A,B and C in the Figure 6.14



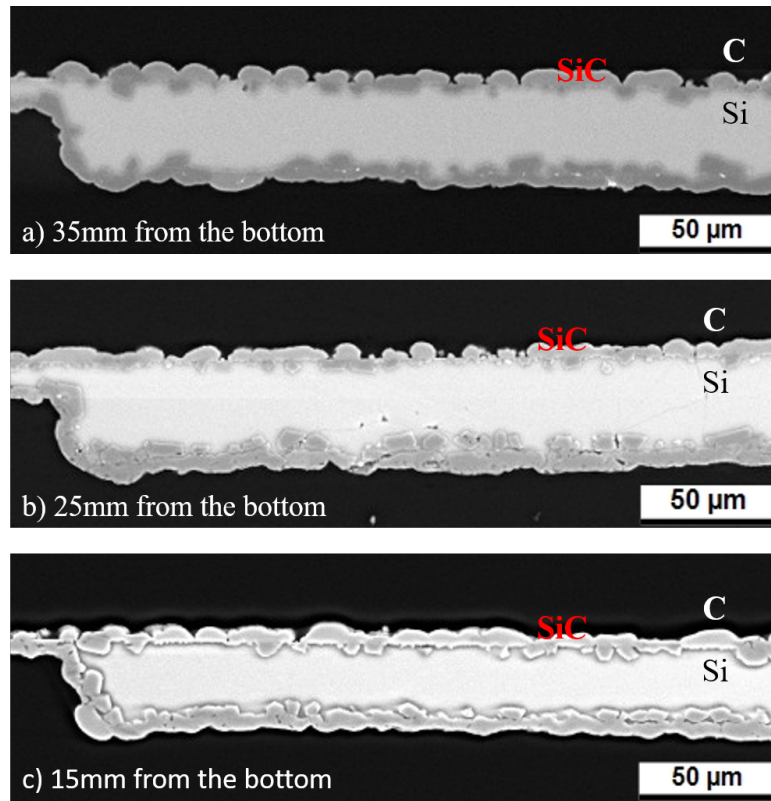


Figure 6.13 – SEM analysis of the reacted interface between silicon and vitreous carbon at 1500 °C, 1 mm x 0.025 mm microchannel sample of configuration A.

represent Si, SiC and vitreous carbon, respectively. The point in region C with a yellow marker shows a higher silicon concentration than expected. This was attributed to the larger spot size of the electron beam generating a signal from both SiC and C simultaneously at the interface. The silicon concentration drops from region A to B by approximately 22%, which gives the concentration ratio of Si,  $B/A \approx 0.75$  which is in good agreement with the results from Voytovych et al. [136] and Deike et al. [187]. The concentration of silicon over zone B is nearly constant. The results show that the homogenization of the reaction zone occurs for long-term experiments, which leads to the depletion of layer I.

The mechanism of reaction formation of SiC layer at the interface of liquid Si and vitreous carbon was observed to be similar as in our previous studies [167] and the description of Voytovych et al. [136]. The formation of reaction layer between liquid Si and vitreous carbon occurs in three stages:

- at short times  $t < 1\text{min}$ , nucleation and growth processes lead to the formation of an equiaxed, micron – thick layer of SiC;
- at intermediate times  $1\text{ min} < t < t^* \approx 20\text{ min}$  thickening of the SiC layer occurs up to approximately  $10\mu\text{m}$ ;

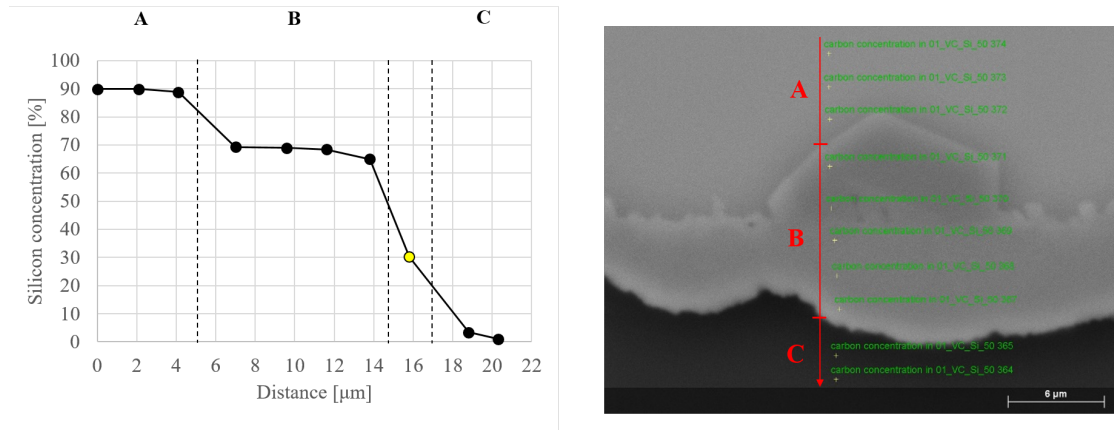


Figure 6.14 – Silicon concentration profile across the reaction zone formed between silicon and vitreous carbon.

- at long times  $t > t^* \approx 20$  min the growth rate of the SiC layer becomes negligible and, due to the homogenization, the layer previously observed as a complex one is replaced by a single SiC layer.

The reaction zone between vitreous carbon and silicon has a relatively small thickness. This illustrates the low diffusion coefficient of Si and C in SiC. According to Gern et al. [188], the SiC layer is formed as soon as the first contact between C and molten Si occurs. Thus, further thickening of the layer is controlled by the diffusion of Si and C in SiC. Eveno et al. [27] and Hon et al. [28, 189] showed that the diffusion of C in SiC is much faster than the diffusion of Si. They also showed that both Si and C are more prone to diffuse via grain boundaries rather than by bulk lattice diffusion.

According to the comprehensive study done by Voytovych et al. [136] on the kinetics of reaction layer growth, the growth of SiC at  $t < t^*$  and  $t > t^*$  occurs by two different mechanisms. At short times  $t < t^*$ , during the growth of SiC crystals at the liquid Si/C interface, micrometer-sized holes are formed between SiC crystals, which enable direct communication between the carbon substrate and the bulk liquid through layer I. The thickening of the reaction layer throughout these times occurs by liquid state diffusion. However, at long times  $t > t^*$ , the layer I becomes impervious for the liquid Si, thus further thickening occurs by grain boundary diffusion. The reaction layer's growth rate becomes negligibly small; therefore, only the homogenization of the reaction layer is observed.

#### 6.5.4 Interpretation of pore closure in Si vs Si-Zr alloy infiltration

Several researchers have proposed the pore occlusion model in LSI with the help of classical sessile drop experiments [136, 155, 167], infiltration of C-C preform [57, 184], infiltration of millimetre and sub-millimetre sized graphite capillaries [133, 141, 154]. Fundamentally,



they all agree on the role of the solid-state reaction formed SiC in reducing the diameter of infiltration capillary. However, to the best of our knowledge, no consideration in the literature is given for the effect of the enrichment of the alloying element at the infiltration front as the Si in alloy reacts with the C from the capillary channel to form SiC.

For the sake of convenience, if we ignore the influence of the thickness of the reaction formed SiC layer in the inner wall of the tube, the infiltration length ( $L$ ), reached by the alloy in the rectangular capillary channel with the thickness ( $e$ ), in this case, the separation of the two glassy carbon plates due to the laser ablated groove, as derived in section 5.3, can be written as follows:

$$L = \left[ \frac{(c_{Si,0} - c_{Si}^{crit})}{(1 - c_{Si,0})} \frac{V_m^{SiC}}{V_m^{liquid}} \frac{e}{2} \frac{D_{diff,0}^{\frac{n-1}{2n}}}{v_0^{\frac{n-3}{2n}} \theta_{SiC,0}} \exp \left[ \frac{2nQ_{SiC} - (n-1)Q_{diff} - (3-n)Q_{triple}}{2nRT} \right] \right]^{\frac{2n}{n+1}} \quad (6.1)$$

where,  $c_{Si,0}$  is the initial concentration of Si in the alloy,  $c_{Si}^{crit}$  is the critical concentration of Si below which the precipitation of solid silicide phase occurs as per phase diagram at the given temperature,  $V_m^{SiC}$  is the molar volume of the SiC,  $V_m^{liquid}$  is the molar volume of the liquid alloy,  $D_{diff,0}$  is the diffusion coefficient for Si in liquid Si-Zr alloy,  $v_0$  is the prefactor for the triple line velocity at the given temperature,  $\theta_{SiC,0}$  is the prefactor for the growth of SiC layer with time,  $R$  is the universal gas constant,  $T$  is the processing temperature,  $n$  is the parameter defining the order of growth kinetics and  $Q_{SiC}$ ,  $Q_{diff}$ , and  $Q_{triple}$  are the activation energies for SiC formation, diffusion of Si in the alloy and triple line, respectively. The typical values for various parameters from the literature ([132, 175–177]) are mentioned below.

$$\begin{aligned} V_m^{SiC} &= 1.25 \times 10^{-5} \text{ m}^3/\text{mol} \\ V_m^{liquid} &= 1.31 \times 10^{-5} \text{ m}^3/\text{mol} \\ D_{diff,0} &= 15 \times 10^{-9} \text{ m}^2/\text{s} \\ v_0 &= 2 \times 10^{-4} \text{ m/s at } 1500^\circ\text{C} \\ \theta_{SiC,0} &= 9 \times 10^{-6} \text{ m} \\ Q_{SiC} &= 200 \times 10^3 \text{ J/mol} \\ Q_{diff} &= 28 \times 10^3 \text{ J/mol} \\ Q_{triple} &= 185 \times 10^3 \text{ J/mol} \end{aligned}$$

The triple line velocity indicated here is significantly larger, by a factor of 5, roughly, than the observed triple line velocities in sessile drop spreading experiments. While the latter could be considered a good approximative indicator for the spreading rate on the microchannel's inner surfaces, the observed infiltration distances in pure Si experiments set a lower limit to triple line velocity. It is roughly this lower limit that has been chosen here. On the other hand, the thermal activation energy of the triple line velocity,  $Q_{triple}$ , is derived from observed spreading rates in sessile drop experiments at different temperatures [176]

The value of  $c_{Si}^{crit}$  in case of Si-Zr changes at peritectic temperature (1620 °C), below the peritectic temperature an approximate value of 0.72 is used while above the peritectic temperature 0.56 is used for the calculation; which was calculated by using the lever rule for a composition containing 80 % solid phase fraction at a given temperature. Using the parameters mentioned above and Equation 2, we can calculate infiltration length  $L$  with a varying initial concentration of Si,  $c_{Si,0}$ , for the values of  $e = 10 \mu\text{m}$  and  $e = 15 \mu\text{m}$  as shown in Figure 6.15

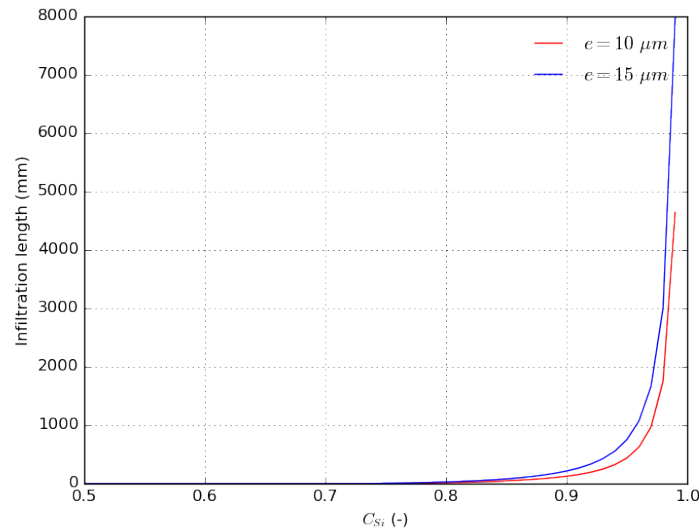


Figure 6.15 – Infiltration length as a function of the initial concentration of Si in the alloy for microchannels with depth  $e = 10 \mu\text{m}$  and  $e = 15 \mu\text{m}$ .

Due to the assumption to neglect the effect of channel closure due to the reaction formed SiC, the infiltration length values are unrealistic when the initial concentration of Si is close to 1 or  $c_{Zr,0} \approx 0$ .

Similarly, in Figure 6.16, the effect of the temperature on the infiltration length is plotted for an initial atomic concentration of Si  $c_{Si,0} = 0.92$  for the microchannel depth  $e = 10 \mu\text{m}$  and  $e = 15 \mu\text{m}$ .

In our experiment of pure Si infiltration with 0.01 mm ( $e$ ) channel (sample D3), we observed a complete infiltration of the channel of 465 mm length (Figure 6.10). In the SEM image of a cross section of the channel at 5 mm from the exit end of the channel, we can see that the actual value of  $e$  is around 0.015 mm, mostly due to geometrical misfit during the clamping of two plates and the cross section might not be at perfectly perpendicular plane (Figure 6.17). The average SiC reaction layer thickness is around 5  $\mu\text{m}$ . From this, we can conclude that the infiltration velocity for 0.01 mm capillary is fast enough to avoid the pore closure phenomenon for an infiltration distance of around 460 mm. However, much slower infiltration rates are observed during the infiltration of actual preforms due to higher tortuosity and non-uniform pores along the infiltration path [152]. Therefore, to observe the pore closure effect for

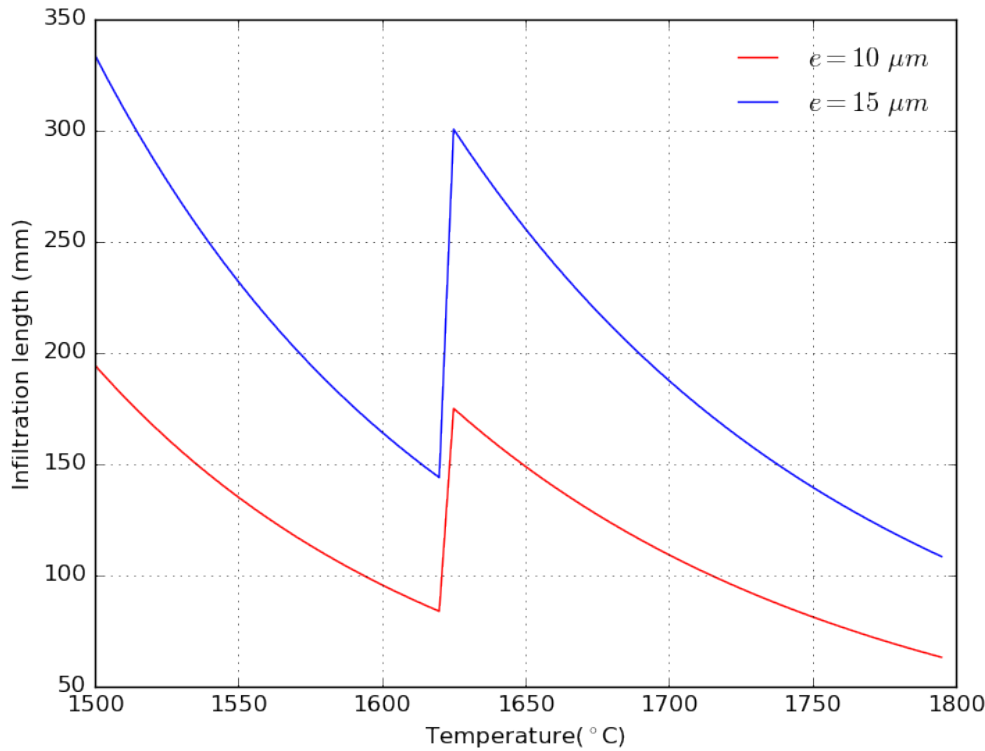


Figure 6.16 – The infiltration length achieved with increasing temperature for the microchannel depth  $e = 10 \mu m$  and  $e = 15 \mu m$  infiltrated with an Si-Zr alloy with an initial atomic concentration of Si  $c_{Si,0} = 0.92$ .

infiltration by pure Si, a much lower microchannel depth is needed for the length of capillaries used in this study.

In the case of infiltration of sample D1 and D2 by Si-8 at-pct Zr alloy at 1500 °C, termination of the capillary rise was observed at approximately 166 mm and 120 mm, respectively. The variation in infiltration length might result from slightly different resulting depths due to the geometrical misfit of glassy carbon plates' straightness. This can also be seen in the calculated infiltration lengths for  $e = 10 \mu m$  and  $e = 15 \mu m$  in Figure 6.15 and Figure 6.16, where the infiltration length is longer for a higher value of  $e$ . However, the mechanism of obstruction is far different from that of pure Si. As the infiltration front moves along the capillary channel, the reaction of Si from the alloy with C forms SiC. The diffusive flux of Si is not high enough to compensate for the loss of Si due to reaction, enriching the Zr content of the liquid volume gradually at the front. This shifts the equilibria to the right side in the phase diagram as shown by the solid arrow in Figure 6.18, where the temperature of infiltration is well below the solidus line to precipitate the zirconium silicides at the infiltration front. The reduced permeability due to further precipitation of zirconium silicides blocks the flow of liquid alloy, resulting in capillary choke-off. In the BSE images of the cross section of the sample D1 taken near the

channel entrance, the SiC reaction layer can be observed at the entrance, while in the middle, solidified Si and  $\text{ZrSi}_2$  can be seen. However, at the clogging location, the channel can be observed to be filled with zirconium silicides without any Si, which indicates the blockage of the channel is caused by the precipitation of  $\text{ZrSi}_2$  and not only due to the formation of the SiC layer (Figure 6.19) at the entrance. The topmost portion of the clogged channel from sample D2 showed SiC at the reaction interface on the C microchannel channel's inner walls and  $\text{ZrSi}_2$  in the middle, as seen in Figure 6.20.

By increasing the infiltration temperature to  $1700^\circ\text{C}$ , a higher infiltration length of 322 mm was observed in sample D4 (Figure 6.11). When we compare this to the calculated infiltration length value in Figure 6.16 for  $1500^\circ\text{C}$  and  $1700^\circ\text{C}$ , we see that one should get a lower infiltration length for a higher infiltration temperature in the isothermal analysis. This discrepancy can be attributed to two things. First, the experiments' setup does not allow controlling when the liquid should be in contact with the entrance of the microchannel. The infiltration starts as soon as the alloy is molten, somewhere around  $1400^\circ\text{C}$  [167]. As the temperature continues to increase, near the peritectic temperature of the alloy,  $1620^\circ\text{C}$ , there is a sudden increase in the infiltration length, and then again, it decreases with temperature. Since the furnace temperature increases as the infiltration front is progressing, the sudden decrease in solid volume fraction at the front can result in an overall increase in the infiltration length achieved. Numerical calculations using the non-isothermal model from chapter 5 further highlight that the intermittent choke-off by Zr-enrichment is reached before reaching the maximum infiltration temperature. Therefore the triple line advances thanks to continuous alleviation of the choke-off concentration by diffusion. With the higher maximum temperature this diffusion mediated regime continues for a longer time and hence results in higher infiltration depth. A second factor that may have attributed to the observed higher infiltration length is a slight difference in value of  $e$  with increasing temperature, due the change in the gap between the glassy carbon plates held together by graphite fittings having different coefficient of thermal expansion. The EDX analysis of the top portion of the microchannel where clogging was observed, showed that the channel has  $\text{ZrSi}_2$  and  $\text{ZrSi}$  in the center of the channel and SiC at the inner walls, as seen in Figure 6.21. It was also observed that some of the  $\text{ZrSi}_2$  penetrated through the reaction layer to form tiny island like structures near the junction of two big SiC grains of the reaction layer. From the EDX analysis, it is evident that at  $1700^\circ\text{C}$ , as the Zr concentration increases, the alloy composition shifts towards the right in the phase diagram, as shown by the dotted arrow in Figure 6.18. At  $1700^\circ\text{C}$ , the volume fraction of the solid primary phase decreases much more slowly and also sets in at higher Zr-concentrations.

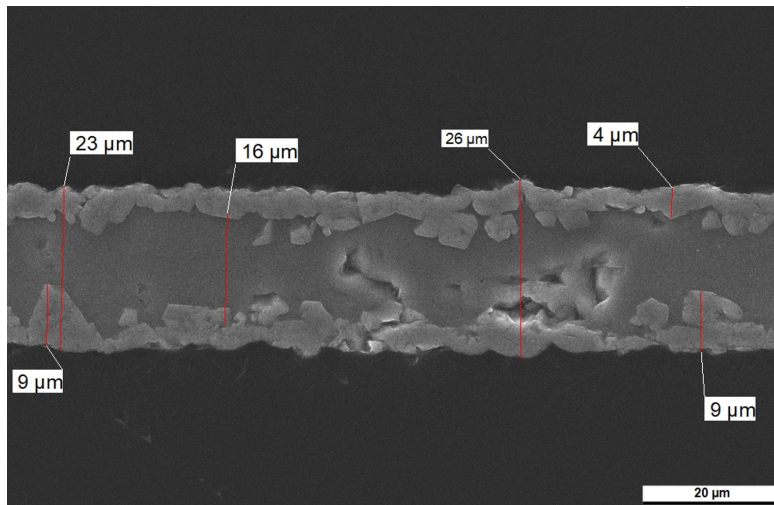


Figure 6.17 – SEM image of cross section taken at 5 mm from the exit end of 0.01 mm deep microchannel infiltrated with pure Si.

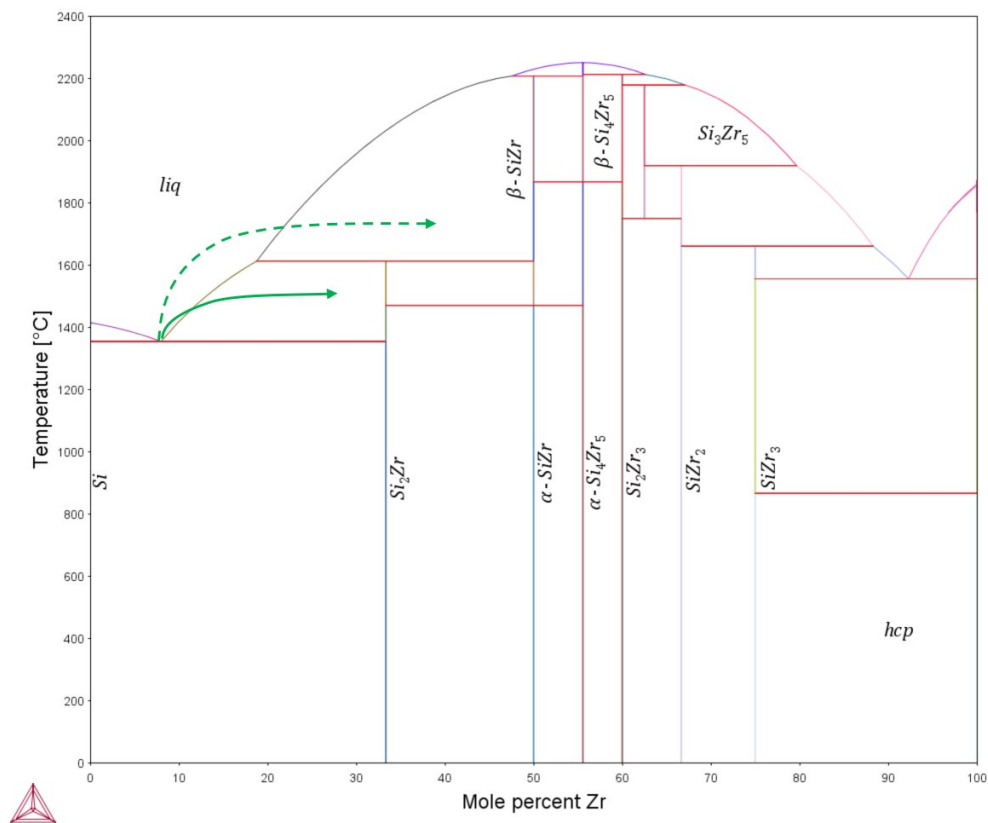


Figure 6.18 – Si-Zr phase diagram reproduced in Thermocalc using data from [156] showing the alloy composition shift as the alloy flows through microchannel at 1500 °C by a solid arrow and at 1700 °C by a dotted arrow.

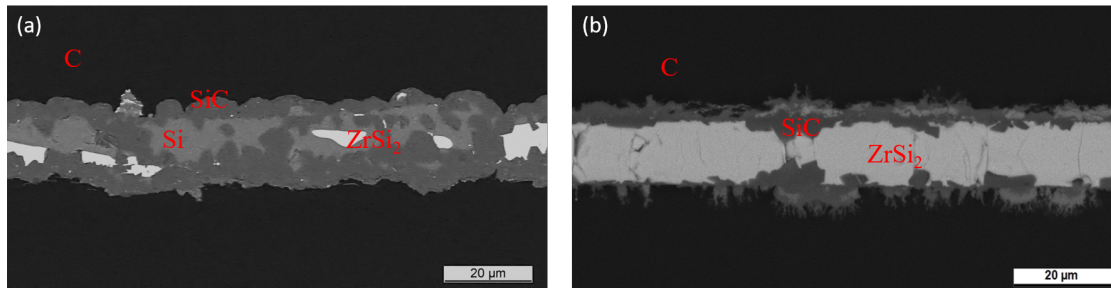


Figure 6.19 – BSE image of the cross section of sample D1, infiltrated at 1500 °C (a) the region near the inlet of the microchannel showing SiC reaction layer and in the middle Si and ZrSi<sub>2</sub> (b) the clogging region showing SiC at the interface and solidified ZrSi<sub>2</sub> in the channel.

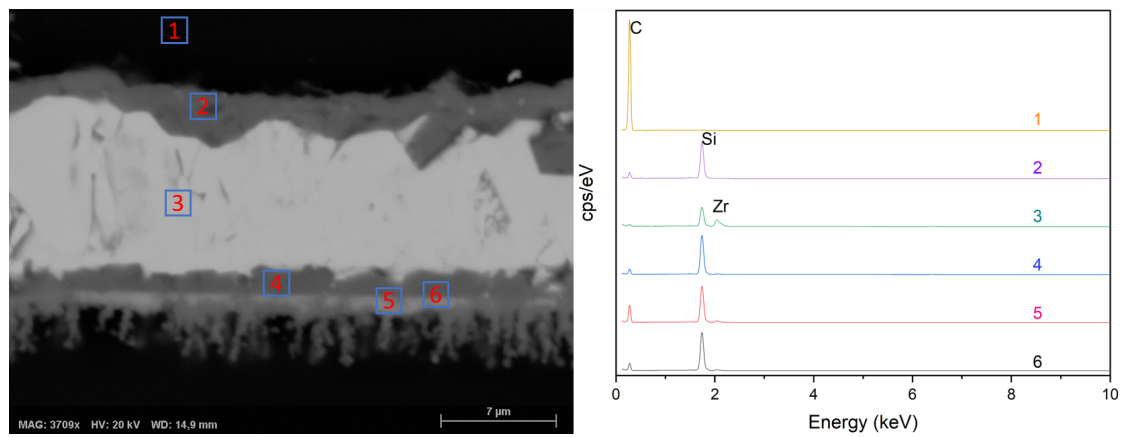


Figure 6.20 – BSE image of the cross section of sample D2, infiltrated at 1500 °C at the end of clogging region with EDX analysis at various points with different contrast.

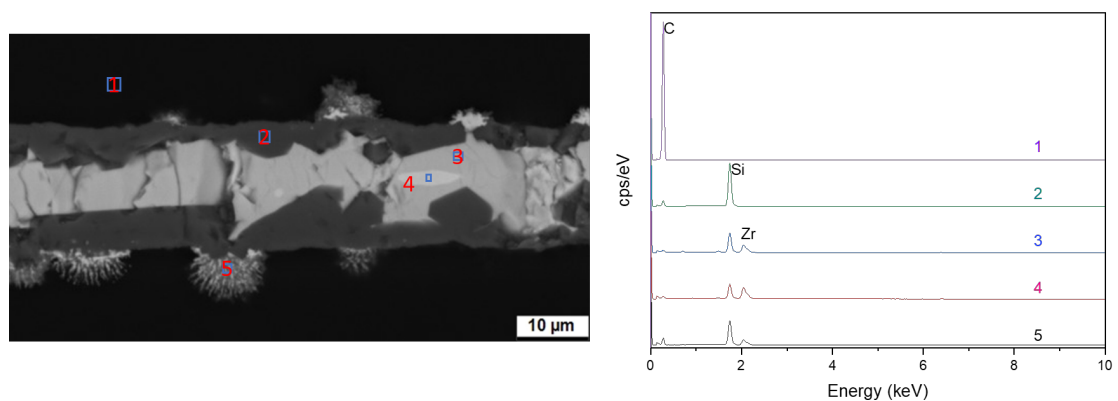


Figure 6.21 – BSE image of the cross section of sample D4, infiltrated at 1700 °C at the end of clogging region with EDX analysis at various points with different contrast.

## 6.6 Conclusion

With the innovative approach of laser ablated microchannels made from glassy carbon plates, the microscopic effects accompanying reactive melt infiltration can be observed experimentally. The extent of infiltration in the microchannels can be observed non-destructively using radiography. Both Si and Si-Zr alloy formed SiC at the inner walls of C microchannels. Two distinct mechanisms for pore-blocking were proposed in reactive melt infiltration of C for pure Si and Si-Zr alloy. In the case of the flow of pure Si in the microchannel, the microchannel's dimensions and tortuosity were not sufficiently small and sufficiently developed, respectively, to observe the blockage by the rapid formation of SiC at the ingress point experimentally. The infiltration velocity of Si in C is found to be too high compared to the rate of growth of the reaction layer, even for 0.01 mm deep microchannel to observe this phenomenon.

Another pore blockage mechanism was observed when it comes to infiltration by Si-Zr alloy in glassy carbon microchannels. As the alloy is rising in the capillary, Zr concentration increases gradually at the infiltration front due to the reaction of Si with C to form SiC. The enrichment of Zr in alloy volume results in the potential precipitation of zirconium silicides. The reduced permeability due to precipitated solid zirconium silicides further slows down the liquid alloy flow and finally blocks the capillary. The effect of an increase in infiltration temperature will depend on whether the experiment is conducted isothermally or in a gradual heating regime. In the isothermal case the more rapid formation of SiC is likely to actually reduce the ingress length despite the higher solubility of Zr in the liquid. In a gradually heating regime, the infiltration length may be expected to be larger the higher the final temperature is, in particular if the experiments are conducted above the peritectic temperature of  $\text{ZrSi}_2$  formation. The sudden decrease in solid fraction above the peritectic temperature for the atomic concentrations of Zr above 0.33, leads to significantly longer infiltration length for both the isothermal and gradually heating process regimes. It is also in that temperature range, i.e. above the peritectic temperature, in which the both  $\text{ZrSi}_2$  and  $\text{ZrSi}$  precipitate eventually leading to higher operating temperature than with free silicon. The ability to obtain high-temperature silicides by transient liquid-phase infiltration Si-Zr alloy into porous C makes it a suitable candidate to manufacture SiC composites, which can be used at higher operating temperatures than the melting point of pure Si. The phenomena described here are not limited to LSI with Si-Zr alloys but should, *mutatis mutandis*, also be transferable to LSI with other alloying systems.

## 7 Reactive infiltration of C/C and SiC/C preforms

### 7.1 Disclaimer

The present chapter is written in paper style to be submitted to the Journal of the European Ceramic Society. Only the mathematical model for the channel infiltration is not presented in full length here, as it was developed in detail in chapter 5 of this thesis and presenting it once again would be redundant. We nevertheless use the results of the modelling in the discussion as if the model was given in the paper.

### 7.2 Abstract

Porous carbonaceous preforms made from graphite powder, as well as a mix of graphite and silicon carbide (SiC) powder, with varying graphite powder mass fractions and particle sizes were infiltrated at 1500 °C and 1700 °C by Si-8 at. pct Zr alloy to produce dense Si-Zr-SiC composites. The experiments were performed in a graphite chamber vacuum furnace under a vacuum of approximately  $10^{-2}$  mbar. The graphitic preforms could only be infiltrated completely and with minimal defects when the  $d_{90}$  particle size was equal or larger than 75  $\mu\text{m}$ . The complete conversion of graphite to SiC by reaction of Si with C was, however, not possible in these preforms. The major defects were residual porosity cracks induced by thermal stresses and the expansion of residual Si upon solidification. The most desirable results were obtained for preforms composed of a mixture of graphite and SiC powders, with preforms containing 15-20 % mass fraction of graphite and infiltrated at 1500 °C. The infiltrated composites with negligible porosity and least residual unreacted graphite particles were characterised by a density of approximately 3.4 g/cm<sup>3</sup>.

### 7.3 Introduction

Silicon carbide (SiC) is one of the most important and industrially used non-oxide ceramic materials for high temperature applications, due to its ability to have exceptional mechanical



strength and chemical stability at high temperatures. Based on the manufacturing method used, the properties and processing time can vary greatly. The most common methods for obtaining dense silicon carbide ceramics are pressureless sintering in solid state (SSiC), infiltration of reaction bonded silicon carbide by molten silicon (SiSiC), liquid phase sintered silicon carbide (LPSiC) and hot pressing (HPSiC). Silicon infiltrated silicon carbide (SiSiC), developed in 1975 by Hillig et al. [47], is a well known industrial ceramic material due to its remarkable properties, such as low porosity, low density, high thermal conductivity, high mechanical strength, excellent chemical, oxidation and thermal shock resistance and high wear and corrosion resistance [48]. Additionally, it represents a very cost-effective method to manufacture large and complex parts. SiSiC, also known as liquid silicon infiltration (LSI), involves infiltrating a porous carbonaceous preform by molten Si, which exothermically reacts with C to form SiC, resulting ideally in a dense composite. Over the past couple of decades Si – SiC ceramics have generated tremendous interest, which has led to the development of many variations of these materials – monolithic and particle/fiber reinforced CMCs, which can be obtained from different constituents and processes [49–51]. However, LSI has its disadvantages, the foremost being the presence of residual Si, rendering the composite unusable for use near or above the melting temperature of Si.

Messner et al. [66] has shown that Si-alloy infiltration can be used to overcome the limitation of residual Si by replacing the residual Si with refractory silicides, characterised by higher melting temperatures. The alloying element is selected in such a way, that when Si from the alloy reacts with C to form SiC, the concentration of the alloying element increases and results in the formation of a refractory silicide with a higher melting temperature. Several researchers have studied the process and properties of the Si-alloy infiltration with alloying elements, like Mo, Ti, Y, Zr, Co and Hf to produce dense SiC composites [72, 75, 77, 182, 183].

The reactive infiltration of porous carbonaceous preforms with Si or Si alloys is a fairly complex process and is affected by various parameters, e.g. pore volume fraction, the size, shape and distribution of pores, the reactivity of carbon depending on the type of carbonaceous phase used, as well as the particle size and shape. The preforms are usually made from a mixture of C, SiC, organic binder and pore forming materials (e.g. starch). The mass fraction of each constituent plays an important role in the nature of produced preforms and, consequently, in the reactive infiltration process itself. Most of the physical phenomena involved in the reactive infiltration process are temperature dependent. Additionally, the atmosphere inside the furnace can significantly affect the process, as the melting of the metal or alloy can be disrupted by oxidation [105].

In this study, a comprehensive experimental analysis of the effects of various key parameters involved in the reactive infiltration of C-C and SiC-C preforms by near eutectic Si-Zr alloy was performed.

## 7.4 Materials and methods

### 7.4.1 Materials

Graphite powders of grade Ecophit GFG5, TIMREX KS10, TIMREX KS25, TIMREX KS44 and TIMREX KS75, characterised by particle sizes,  $d_{90}$ , in the range of 5, 10, 25, 44 and 75  $\mu\text{m}$ , respectively, were used in the experiments. Ecophit grade was sourced from SGL carbon, Germany, while TIMREX grades were sourced from Imerys Graphite & Carbon Switzerland Ltd. Silicon carbide powder of grade F800 (green) was sourced from Tracomme AG, Switzerland. A phenolic resin, Bakelite PF GA T 10 R from HEXION was used as the organic binder. Corn Starch (Sigma-Aldrich, Germany) was used in the SiC-free preforms as the pore former. Graphite foil and custom size graphite crucibles were sourced from SGL carbon, Germany and STEINEMANN CARBON AG, Switzerland, respectively. Si with 99.99% purity (Sicerma GmbH, Germany) and near eutectic Si-8 at. pct Zr alloy (Chengdu Huarui Industrial Co Ltd., China) were used for the infiltration of carbonaceous porous preforms.

### 7.4.2 Manufacturing of porous preforms

#### 7.4.2.1 Powder mixing

The graphite powder, SiC powder, Bakelite (binder) and optionally corn starch (pore former) were weighed and put in a desired proportion in a plastic bottle together with alumina balls. The bottle was then kept on a roller mill for approximately 12 hours to obtain a homogeneously mixed powder. The homogeneous mixture was next sieved to remove the alumina balls using a mechanical shaker (ASM 200, Siebtechnik GmbH, Germany).

The C-C preforms were prepared for studying the effect of graphite particle size on the infiltration process, by mixing 86 wt. % of graphite powder, 10 wt. % of bakelite and 4 wt. % of corn starch with graphite powder of various particle size with  $d_{90}$  ranging from 5 to 75  $\mu\text{m}$ .

Table 7.1 – Summary of powder mix used to produce C-C preforms to determine the effect of graphite particle size.

Mix name	Graphite powder grade 86 wt %	$d_{90}$ from supplier $\mu\text{m}$	specific surface area (BET) $\text{m}^2/\text{g}$
C_C_01	Ecophit GFG5	5	35
C_C_02	TIMREX KS10	10	16
C_C_03	TIMREX KS25	25	12
C_C_04	TIMREX KS44	44	9
C_C_05	TIMREX KS75	75	6.5

The SiC-C preforms were prepared for studying the effect of graphite mass fraction by mixing SiC powder of grade F800 and graphite powder of TIMREX KS25 or TIMREX KS44 grade in

varying proportion along with bakelite as binder. The details of the powder mix for C-C and SiC-C preforms are summarized in Table 7.1 and Table 7.2, respectively.

Table 7.2 – Summary of powder mix used to make the SiC-C preforms to determine the effect of mass fraction of graphite and SiC powder.

Mix name	SiC F800 wt %	TIMREX KS25 wt %	TIMREX KS44 wt %	Bakelite wt %
SiC_C_01	90	0		10
SiC_C_02	85	5		10
SiC_C_03	80	10		10
SiC_C_04	75	15		10
SiC_C_05	70	20		10
SiC_C_06	65	25		10
SiC_C_07	60	30		10
SiC_C_08	70		20	10
SiC_C_09	65		25	10
SiC_C_10	60		30	10

#### 7.4.2.2 Cold pressing of preforms

For the forming process, 12.7 g of powder was weighed out for each preform to obtain preforms with a diameter of 50 mm and an approximate thickness of 4 mm. The C-C preforms without SiC powder (Table 7.1) were cold pressed in a cylindrical tool steel die of 50 mm using uni-axial hydraulic press and held for 2 min under an applied force ranging from 90 kN to 110 kN, corresponding to 46 and 56 MPa, respectively.

#### 7.4.2.3 Hot pressing of preforms

For the SiC-C preforms made of a mixture of SiC and graphite powder (Table 7.2), hot pressing was chosen to obtain better green strength. A uni-axial hot mounting press ((Buehler SimpliMet 1000, USA)) with a 40 mm die was used for hot pressing the powder mix. The typical compaction cycle included heating up to 150 °C in 5 minutes, holding for 2 min under 28 MPa pressure and subsequently cooling to room temperature in 3 min. The obtained thickness for the preforms were approximately 5 mm.

#### 7.4.2.4 Pyrolysis of preforms

The compacted C-C and SiC-C preforms were next pyrolyzed to carbonize the bakelite used as the binder material. Pyrolysis was performed in an alumina tube furnace under an inert atmosphere of flowing argon. For C-C preforms, two temperatures were used, 1000 °C or 1400 °C. The SiC-C preforms were pyrolyzed consistently at 1000 °C. The process proceeded by applying a heating rate of 60 °C/h from room temperature to 500 °C and of 200 °C/h up to 1000

°C or 1400 °C, holding for 15 min, followed by free cooling as show in Figure 7.1.

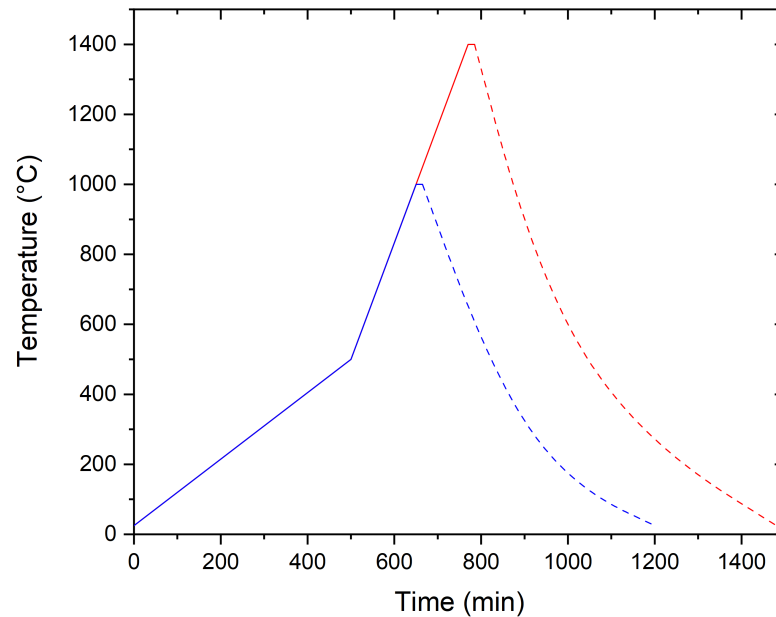


Figure 7.1 – Heating programs used for pyrolysis of the preforms.

### 7.4.3 Infiltration setup

#### 7.4.3.1 Furnace equipment

The reactive melt infiltration experiments were performed in a graphite heated vacuum furnace (FCT Sysyems, Germany), in which the atmosphere can be controlled to be either vacuum or inert gas like argon or nitrogen. The furnace has a maximum operating temperature of 2400 °C. The experiments were conducted under a vacuum of approximately  $10^{-2}$  mbar. A typical infiltration process involves pre-heating up to 200 °C at a heating rate of 60 °C/h and holding for 30 min at 200 °C and later heating until reaching the infiltration temperature of 1500 °C at a heating rate of 520 °C/h and holding for 1 h and subsequently cooling down by switching off the furnace heating, as shown in Figure 7.2.

#### 7.4.3.2 Graphite foil crucibles

A graphite foil with a thickness of 0.5 mm was formed to make a cylinder, which was next glued using a mixture of bakelite resin and isopropyl alcohol with 50-50 wt%. A circular piece of graphite foil molded into a shape of a lid was glued to the bottom of this cylinder and cured at 120 °C. Later, the cured crucible was pyrolysed at 1000 °C to transform the resin into carbon. The inner walls of the crucibles were sprayed with BN (sourced from 3M <sup>TM</sup>) to reduce the direct reaction by molten Si and Si-Zr alloy with the crucible. The advantage of such a setup is its cost-effectiveness and suitability for single use. Alternatively, a graphite foil was used to

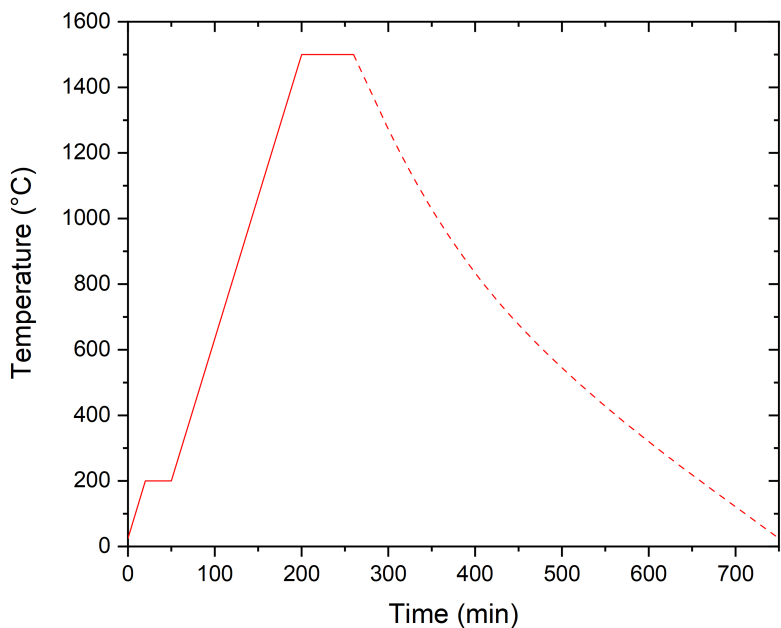


Figure 7.2 – Schematic of heating program used for the reactive melt infiltration process.

cover the inner wall of a graphite crucible, which was already coated with BN. Subsequently, the inner wall of the graphite foil is again sprayed with BN and dried at 120 °C. This setup was quicker compared to using pyrolyzed graphite foil crucibles. In Figure 7.3, the infiltration setup with single use crucibles made up of graphite foil and graphite crucible lined with graphite foil and coated with BN are shown. The inner walls of both types of crucible setup were coated with BN.

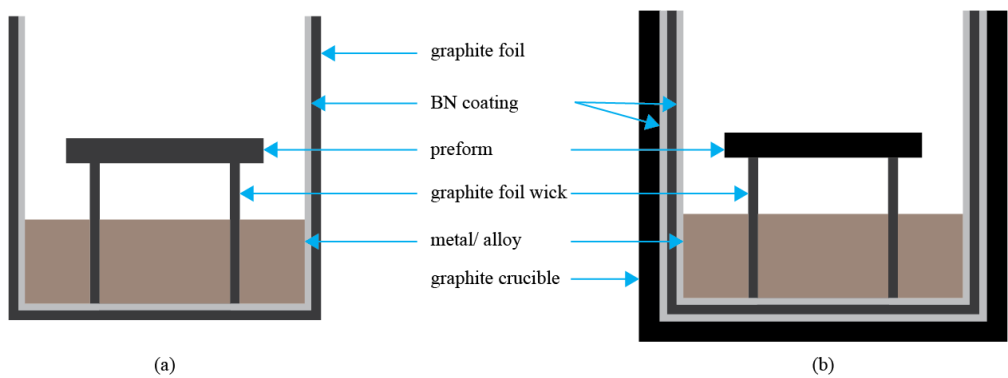


Figure 7.3 – Schematic of preform infiltration setup using (a) graphite foil crucible (b) graphite crucible with graphite foil lining having inner walls coated with BN.

#### 7.4.4 Analyses

The particle size distribution of the graphite powders, SiC powder and their mixtures were measured using a laser diffraction particle size analyzer (LS 13 320 Beckman Coulter, United States).

A helium pycnometer (AccuPyc II 1340, Micromeritics, United States) was used to measure the density of the graphite powders, SiC powder and their mixtures. The porosity and the pore size distribution of the pyrolysed preforms were measured using mercury intrusion porosimetry (PASCAL 140/400, Thermo Finnigan, Germany). The skeletal densities from Helium pycnometry were used for porosity calculations using Hg porosimetry.

X-ray tomography (RX solution EasyTom XL, France) was also used to analyse the porosity of the pyrolyzed preforms. The samples for tomography were cut using a diamond saw and then manually ground to the approximate dimension of 1 mm x 1 mm x 5 mm on 800 grit SiC polishing paper.

The cross-section of the infiltrated preforms were cut using a diamond saw and cold mounted in epoxy resin (SpeciFix Resin, Struers, Germany). Initially, automatic grinding of the samples was carried out using a 40  $\mu\text{m}$  diamond pad. Thereafter, automatic polishing was performed using 6, 3 and 1  $\mu\text{m}$  diamond suspensions and final polishing with an acidic aluminum oxide suspension. SEM and EDX analysis of the polished samples was done using the Tescan VEGA3 scanning electron microscope with Bruker AXS Quantax 200 EDX system.

### 7.5 Results

#### 7.5.1 Particle size and density of powders

The graphite powder particles are flaky in shape, while the SiC F800 powder is angular in shape, as can be seen in the SEM images in Figure 7.4. The particle size and distribution of SiC F800

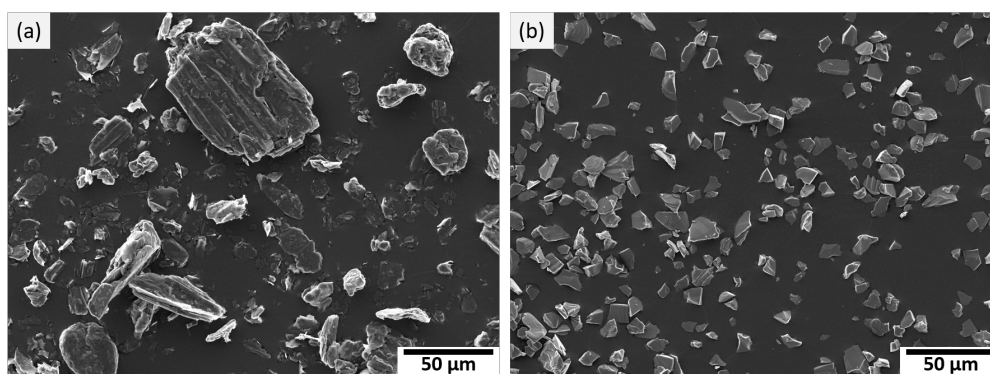


Figure 7.4 – SEM images of the TIMREX KS 44 graphite powder (left) and SiC F800 powder (right) showing their flaky and angular shape, respectively.

and TIMREX KS 25 graphite powder mixtures after mixing as described in Section 7.4.2.1 are shown in Figure 7.5 and the dependence of the graphite fraction on the characteristic particle size, namely  $d_{10}$ ,  $d_{50}$  and  $d_{90}$ , are shown in Table 7.3. The  $d_{90}$  values of TIMREX KS 25 and SiC F800 powders were found to be  $\sim 30 \mu\text{m}$  and  $\sim 16 \mu\text{m}$ , respectively. The  $d_{90}$  value of the powder mixtures are increasing from  $\sim 16 \mu\text{m}$  to  $\sim 27 \mu\text{m}$  as the graphite content increases from 0 to 30 wt. %. The modal particle diameters of SiC F800 and TIMREX KS 25 are approximately  $10 \mu\text{m}$  and  $20 \mu\text{m}$ , respectively. The SiC F800 powder has narrower particle size distribution than the TIMREX KS 25. As the graphite powder content increases the particle size distribution becomes wider and the modal particle diameter slightly increases.

Figure 7.6 shows the particle size and distribution of SiC F800 and TIMREX KS 44 graphite powder mixtures. TIMREX KS 44 has a  $d_{90}$  value of  $\sim 49 \mu\text{m}$ . The  $d_{90}$  value of the SiC F800 and TIMREX KS 44 graphite powder mixtures are increasing from  $\sim 39 \mu\text{m}$  to  $\sim 42 \mu\text{m}$  as the graphite content increases from 20 to 30 wt. %. The dependence of the characteristic particle size, namely  $d_{10}$ ,  $d_{50}$  and  $d_{90}$  on the graphite fraction is shown in Table 7.3. The modal particle diameter of TIMREX KS44 is around  $35 \mu\text{m}$ . The powder mixtures show a bi-modal distribution with a first peak in the vicinity of  $10 \mu\text{m}$  and a second peak closer to  $30 \mu\text{m}$ , which corresponds respectively to the SiC F800 and TIMREX KS44 modal particle diameters. The skeletal densities measured using helium pycnometry along with the calculated theoretical density of the mixture using Equation (7.1) are also summarized in Table 7.3.

$$\rho_{mix} = \frac{M_{SiC}}{M_{SiC}/\rho_{SiC} + M_{gr}/\rho_{gr} + M_{pyr}/\rho_{pyr}} + \frac{M_{gr}}{M_{SiC}/\rho_{SiC} + M_{gr}/\rho_{gr} + M_{pyr}/\rho_{pyr}} + \frac{M_{pyr}}{M_{SiC}/\rho_{SiC} + M_{gr}/\rho_{gr} + M_{pyr}/\rho_{pyr}} \quad (7.1)$$

where,  $M_{SiC}$ ,  $M_{gr}$  and  $M_{pyr}$  are the mass fraction of SiC, graphite and pyrolytic carbon derived from bakelite, respectively, and  $\rho_{SiC} = 3.21 \text{ g/cm}^3$ ,  $\rho_{gr} = 2.25 \text{ g/cm}^3$  and  $\rho_{pyr} \approx 1.5 \text{ g/cm}^3$  are densities of the SiC, graphite and pyrolytic carbon derived from bakelite, respectively.

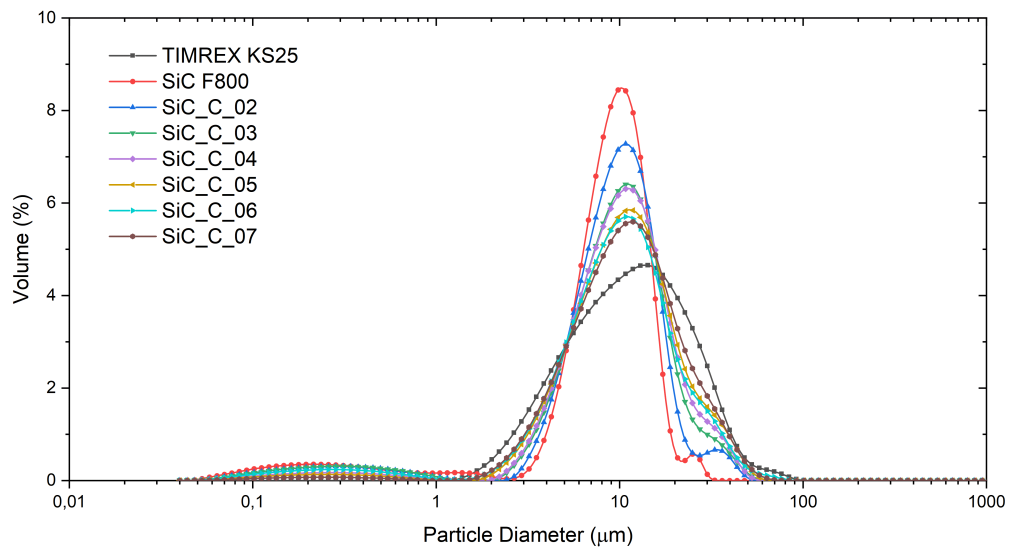


Figure 7.5 – The particle size distribution of SiC F800 and TIMREX KS25 powders and their mixtures listed in Table 7.2 as analyzed by laser diffraction.

Table 7.3 – The particle size distribution of SiC F800, TIMREX KS25, TIMREX KS44 powders and their mixtures with increasing graphite content analyzed after mixing step by laser diffraction along with their skeletal densities measured using He pycnometry and calculated theoretical densities using Equation (7.1).

legend	graphite content	particle size			skeletal density	
		d10	d50	d90	measured	calculated
	%		μm		g/cm <sup>3</sup>	
SiC_F800	0	4	9	16	3.21	-
SiC_C_02	5	4	10	18	2.75	2.94
SiC_C_03	10	4	10	21	2.71	2.88
SiC_C_04	15	5	11	23	2.67	2.82
SiC_C_05	20	4	11	25	2.63	2.77
SiC_C_06	25	4	10	25	2.59	2.72
SiC_C_07	30	5	11	27	2.54	2.67
TIMREX KS 25	100	4	12	30	2.25	-
SiC_C_08	20	6	14	39	2.64	2.77
SiC_C_09	25	6	13	37	2.60	2.72
SiC_C_10	30	5	14	42	2.56	2.67
TIMREX KS 44	100	6	18	49	2.25	-



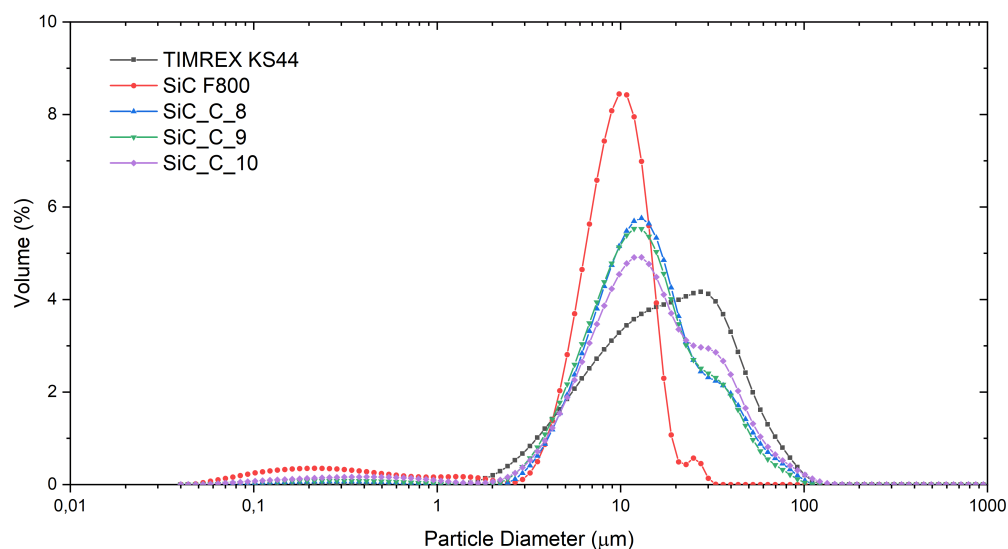


Figure 7.6 – The particle size distribution of SiC F800 and TIMREX KS44 powders and their mixtures listed in Table 7.2 as analyzed by laser diffraction.

### 7.5.2 Porosity and pore size distribution by mercury intrusion porosimetry (MIP)

The pore size distribution of the C-C preforms with various graphite particle sizes, pressing forces and pyrolysis temperatures was measured using mercury intrusion porosimetry. All of the C-C preforms exhibited a similar shape of the distribution, as seen in Figure 7.7 (a). The median pore diameter of the graphite powder preforms was observed to increase with increasing particle size of the used graphite powder. The total porosity measured by MIP was in the range of 34 to 46 % and was observed to be decreasing with decreasing particle size and increasing pressing force. Table 7.4 summarizes the modal pore diameter and total porosity measured by Hg intrusion for various C-C preforms with varying particle size, pressing force and pyrolysis temperature.

Table 7.4 – Modal pore size and total porosity of C-C preforms with various particle size, pressing force and pyrolysis temperature as measured by Hg intrusion.

	Pressing force kN	Pyrolysis temperature °C	Modal pore diameter μm	Porosity by Hg intrusion %
TIMREX KS10	110	1000	0.59	38
	110	1400	0.93	46
TIMREX KS25	110	1000	0.9	35
	110	1400	1.4	43
TIMREX KS44	90	1000	1.19	39
	90	1400	0.84	34
	110	1400	0.93	38
TIMREX KS75	110	1000	8.31	46

The sample pore size distribution of the SiC-C preforms with TIMREX KS25 and TIMREX KS44 graphite powder with varying composition and SiC F800 powder as mentioned in Table 7.2 measured by MIP is shown in Figure 7.7 (b). An uni-modal and very narrow distribution of pore size can be observed in all the SiC-C preforms.

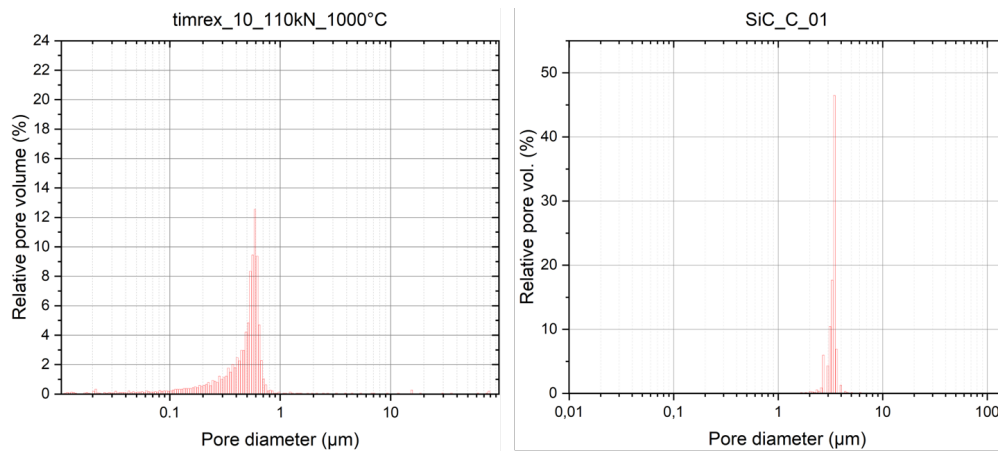


Figure 7.7 – Example of the pore size distribution measured via MIP (a) the C-C preform made up of graphite powder TIMREX KS 10 mix pressed at 110 kN and pyrolysed at 1000 °C (b) the SiC-C preform made from powder mix of SiC and C.

In Figure 7.8, the change in median diameter and percentage porosity measured by Hg intrusion is shown with increasing graphite fraction for both mixtures, i.e. with the TIMREX KS25 and TIMREX KS44 powder. The median pore diameter was in the range from 1.6 to 3.4 μm and was found to be decreasing with increasing graphite powder fraction. The porosity of the preforms ranged from 30 to 44 % and was additionally found to be decreasing with increasing

graphite powder fraction.

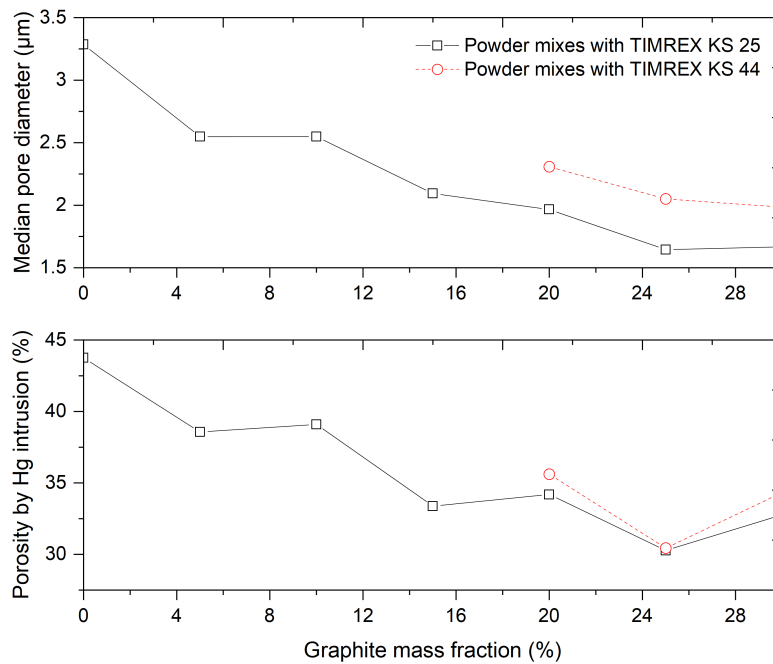
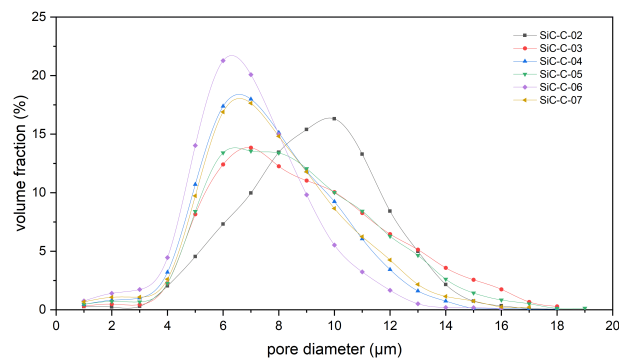


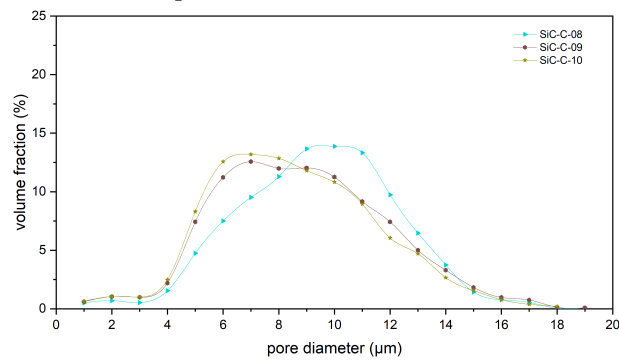
Figure 7.8 – Median pore size and total percentage porosity measure by Hg intrusion with increasing graphite fraction for SiC-C preforms.

### 7.5.3 Porosity and pore size distribution by X-ray CT

The distribution of the pore size for pyrolyzed SiC-C preforms made of the SiC F800 powder and TIMREX KS25 and TIMREX KS44 graphite powders with varying mass fractions, as measured by the X-ray CT technique, is shown in Figure 7.9. The resolution obtained in the X-ray CT scan was about 0.5 μm. To calculate the volume and equivalent diameter (diameter of a sphere with the same volume) of the pore in 3D, the pores are separated in 3D based on the voxels with a face in common. The extracted modal diameter and percentage porosity with varying graphite fraction is shown in Figure 7.10. From the X-ray CT analysis, it can be seen that the modal pore size ranges from ~ 6 to 10 μm and the porosity from ~ 14 to 26 %. Both modal pore size and porosity were higher for preforms with the TIMREX KS44 powder than those with the TIMREX KS25 powder. Furthermore, the preforms with TIMREX KS44 showed a broader pore size distribution compared to preforms with TIMREX KS25. The pore size distribution for preforms with TIMREX KS25 narrows with increasing graphite content, as seen in Figure 7.9 (a).



(a) preforms with TIMREX KS25



(b) preforms with TIMREX KS44

Figure 7.9 – Pore size distribution of SiC-C preforms measured by X-ray CT data for preforms made with mixture of SiC powder and (a) TIMREX KS25 and (b) TIMREX KS44 graphite powder.

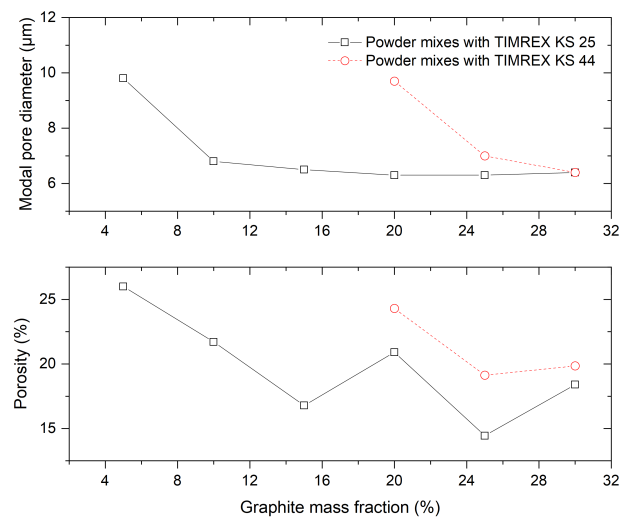


Figure 7.10 – Modal pore size and total porosity of SiC-C preforms with increasing graphite fraction as measured by X-ray CT analysis.

### 7.5.4 Infiltration of C-C preforms with near eutectic Si-Zr alloy

The C-C preforms made from the graphite powder with  $d_{90}$  of 5  $\mu\text{m}$  and 10  $\mu\text{m}$  could not be infiltrated by molten alloy. In Figure 7.11 the sample made from powder mix C\_C\_01 with and 110 kN pressing force is shown that could not be infiltrated using near eutectic Si-Zr alloy at 1500 °C. The alloy touches the bottom of the preform but was not penetrating the preform beyond a few hundred micron. The SEM image in Figure 7.11(c) shows the alloy stuck to the bottom of the preform and a reaction zone of a few hundred microns where formation of SiC can be seen.

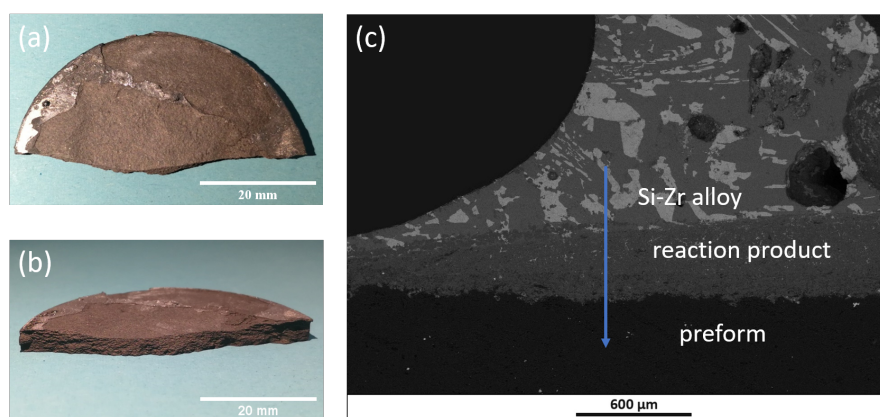


Figure 7.11 – Preform made with the powder mix C-C\_01 at 110 kN pressing force after infiltration (a) bottom surface (b) cross section (c) SEM image of the cross section at the surface where the infiltrating alloy first gets in contact. The arrow indicates the direction of the infiltration.

The C-C preform made using TIMREX KS25 ( $d_{90}$  of 25  $\mu\text{m}$ ) and 90 kN pressing force was partially infiltrated with visible cracks while the one pressed at 110 kN showed no infiltration by the molten alloy. Preforms made using TIMREX KS44 ( $d_{90}$  of 44  $\mu\text{m}$ ) with a pressing force 90 kN and 110 kN were infiltrated partially by the molten alloy. In Figure 7.12, both samples showed visible cracking after infiltration, however, the sample pressed at 90 kN force showed much more severe cracking compared to that pressed with 110 kN. The cracks were not filled with the alloy, as can be observed in the SEM images in Figure 7.13.

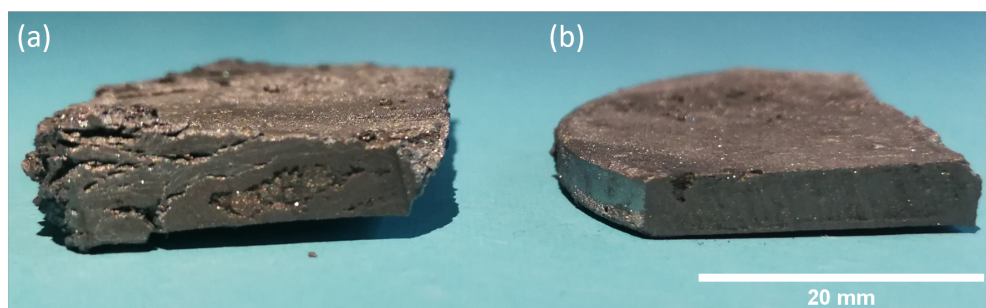


Figure 7.12 – Preforms made up from TIMREX KS44 powder showing cracking after infiltration preforms pressed at (a) 90 kN (b) 110 kN force.

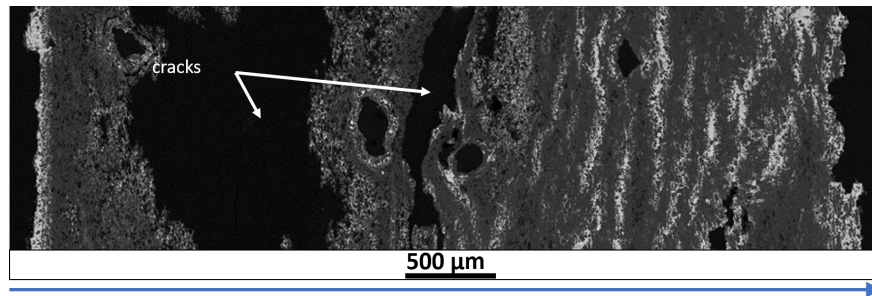


Figure 7.13 – SEM image of the preform made from TIMREX KS44 graphite powder after infiltration showing cracked sample after infiltration. The arrow at the bottom indicates the direction of the infiltration.

Preforms made with powder mix C\_C\_05 ( $d_{90} = 75 \mu\text{m}$ ), showed complete infiltration along the entire thickness of the preform. A few cracks are still visible, as seen in Figure 7.14 (a). The SEM image in Figure 7.14 (b), obtained by stitching the high resolution images together to image the whole thickness of the cross-section, shows that the preforms were completely infiltrated by the alloy, however, the conversion of carbon into SiC is incomplete. Upon closer inspection of the samples by SEM (Figure 7.14 (c)), it is possible to distinguish unreacted graphite, SiC, Zr silicide, as well as other Si phases with negligible porosity. The unreacted graphite phase was measured to be approx. 14 vol. % and the Zr silicide phase was 11 vol. %, based on thresholding the gray-scale image of the cross-section Figure 7.14 (b) using ImageJ [166] software. Correct thresholding to differentiate Si and SiC was hindered due to the low contrast. A gradient can be observed in the Zr-rich phase from the bottom and top side of the preform towards the centre, where the amount of the Zr-rich phase decreases.

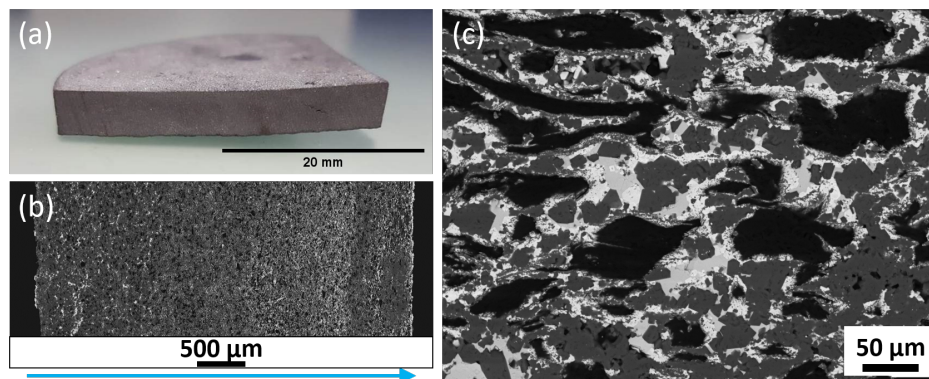


Figure 7.14 – Sample after infiltration of preforms made from TIMREX KS75 powder showing (a) complete infiltration in cross-section with few cracks (b) SEM image showing complete infiltration along the thickness and gradient structure of Zr rich bright phase. The arrow at the bottom indicates the direction of the infiltration. (c) SEM image with higher magnification showing unreacted graphite, SiC, Zr silicide and Si.

The results of the infiltration by near-eutectic Si-Zr alloy at 1500 °C of various preforms made

from graphite powder with varying particle size, pressing force and pyrolysis temperature are summarized in Table 7.5. The Si-Zr alloy could not infiltrate preforms made from graphite powder with a particle size of  $d_{90} = 25 \mu\text{m}$ .

Table 7.5 – Summary of the results after infiltration of various C-C preforms prepared with different pressing force and pyrolysis temperature.

Powder mix	Graphite powder $d_{90}$ ( $\mu\text{m}$ )	Pressing force (kN)	Pyrolysis temperature ( $^{\circ}\text{C}$ )	Infiltration result
C_C_01	5	90	1000	None
C_C_01	5	110	1000	None
C_C_02	10	90	1400	None
C_C_02	10	110	1400	None
C_C_03	25	90	1400	Partial with cracks
C_C_03	25	110	1400	None
C_C_04	44	90	1000	Partial with cracks
C_C_04	44	110	1000	Partial with cracks
C_C_04	44	90	1400	Partial with cracks
C_C_04	44	110	1400	Partial with cracks
C_C_05	75	110	1000	Complete with minor cracks

### 7.5.5 Infiltration of SiC-C preforms with near eutectic Si-Zr alloy

In Figure 7.15, SEM cross-section images are shown of SiC-C preforms fabricated with varying TIMREX KS25 graphite mass fractions from 5 to 30 % and are infiltrated by the near-eutectic Si-Zr alloy at 1500  $^{\circ}\text{C}$ . The samples show complete infiltration along the thickness of the preforms, except for the sample with 30% graphite powder, where the center is not reached by the liquid alloy. For samples with 5% and 10% graphite powder, banding of the Zr-rich phase can be seen, which decreases with increasing graphite content until reaching 20%. The sample with 25% graphite powder shows a single band at the center with a Zr-rich phase, while the sample with 30% graphite shows 2 bands of a Zr-rich phase close to the center and an uninfiltrated center with a thickness of slightly less than 1/3 of the total thickness. Porosity can be observed at the center of the samples with 5 and 10 % graphite powder, the latter being more porous. The samples with 15 and 20 % graphite powder show the most uniform structure considering the distribution of the Zr-rich phase and with minimal porosity.

The SEM cross-section images of the samples made from 20, 25 and 30 % TIMREX KS25 graphite powder and infiltrated by the near-eutectic Si-Zr alloy at 1700  $^{\circ}\text{C}$ , are shown in Figure 7.16. Only the sample with 20 % graphite was completely infiltrated by the alloy, whereas samples with 25 and 30 % graphite have approximately 1/3 and 3/4 of the total thickness at the core not infiltrated by the alloy. The banding with the Zr-rich phase can also be seen just before the alloy stops. The sample with 20 % of graphite powder shows a single



band of Zr-rich phase at the center, as well as a higher concentration of uninfiltrated porosity at the center. Apart from the uninfiltrated core, the samples with 25 and 30% graphite powder also show very high porosity in the infiltrated zones.

In Figure 7.17, the SEM cross-section images are shown of the preforms fabricated using the TIMREX KS44 graphite powder with mass fractions of 20, 25 and 30% and infiltrated by the near-eutectic Si-Zr alloy at 1500 °C. The preforms with 20 and 25 % graphite powder were completely infiltrated by the Si-Zr alloy. Both of the samples show a fair amount of uninfiltrated porosity, which is homogeneously distributed throughout the entire thickness of the preform. The samples showed a single band at the center with a Zr-rich phase. The molten Si-Zr alloy was not able to reach the core of the sample with 30 % graphite powder, where almost 1/3 of the total thickness remained uninfiltrated at the center. Two bands with a Zr-rich phase can be observed where the alloy stops infiltrating near the center from both top and bottom side. The infiltrated zone additionally showed a significant amount of homogeneously distributed uninfiltrated pores.

The summary of the results of the infiltration by the near-eutectic Si-Zr alloy at 1500 °C and 1700 °C for various preforms with varying graphite mass fractions and composition, along with the theoretical densities and silicide phase fraction of the completely infiltrated preform calculated by using the formulation in section 5.2 is shown in Table 7.6. The pore fraction and Si<sub>2</sub>Zr volume fraction are measured using the grayscale thresholding feature of Fiji software with high resolution SEM images stitched together to image the entire thickness of the preform. The contrast between SiC and Si was very low, therefore segmenting via grayscale thresholding proved to be challenging. Furthermore, in some cases it was also difficult to differentiate pores and unreacted graphite. Consequently, an approximation was used to set the threshold value.



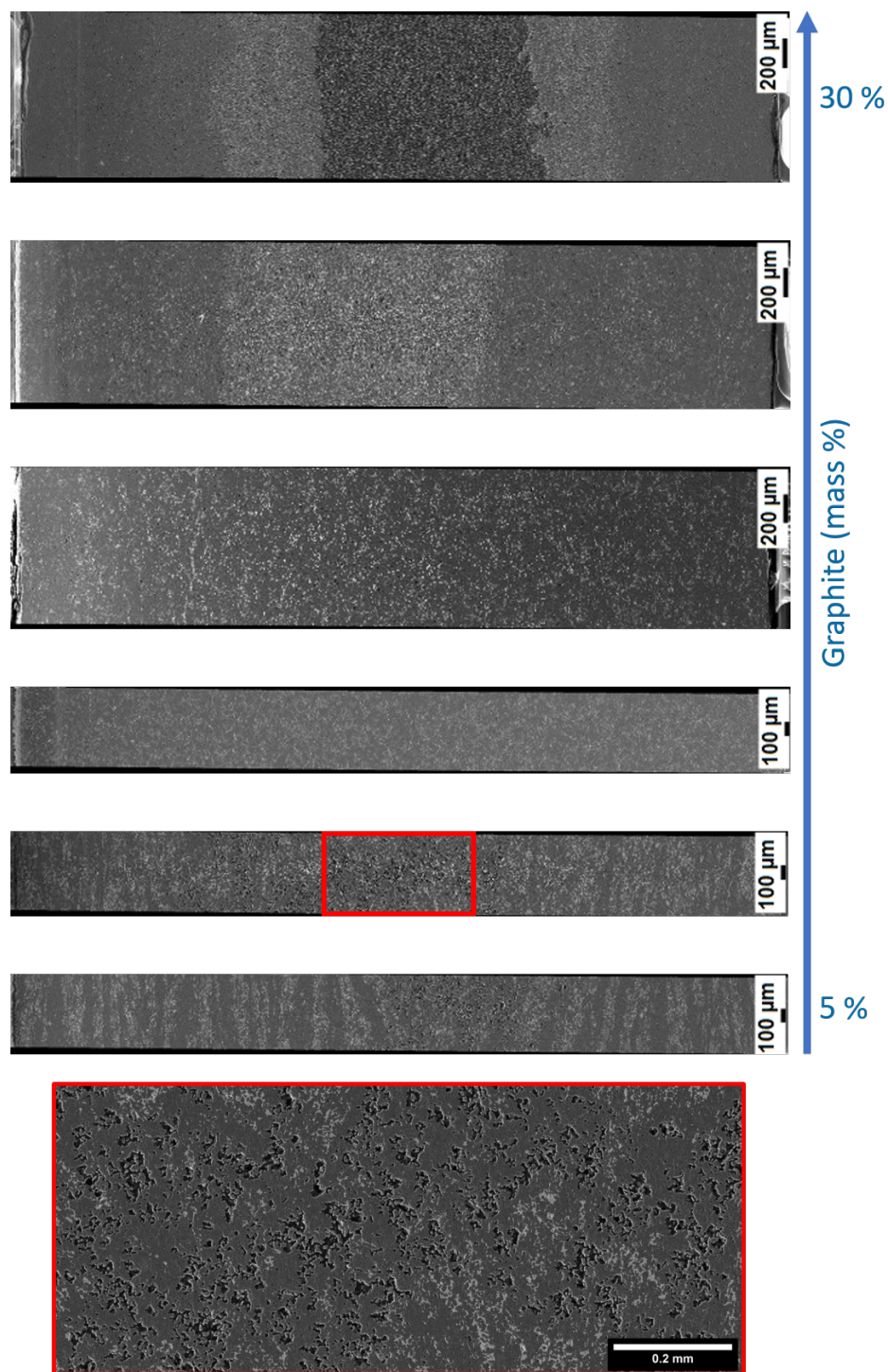


Figure 7.15 – The high resolution SEM images stitched to together to make panorama of the cross section of the SiC-C preforms with increasing mass fraction of TIMREX KS25 graphite powder from 5 to 30 % and infiltrated by near eutectic Si-Zr alloy at 1500 °C. A magnified portion is shown at the bottom marked by red rectangle to illustrate the observed porosity.

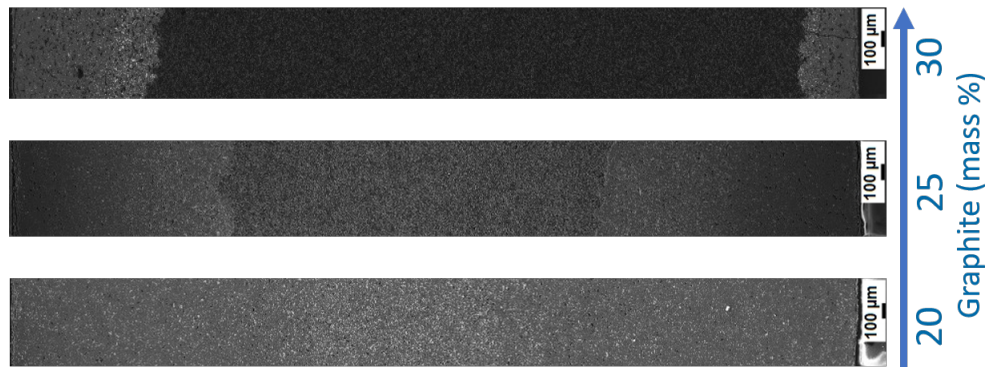


Figure 7.16 – The high resolution SEM images stitched to together to make panorama of the cross section of the SiC-C preforms with increasing mass fraction of TIMREX KS25 graphite powder from 20 to 30 % and infiltrated by near eutectic Si-Zr alloy at 1700 °C.

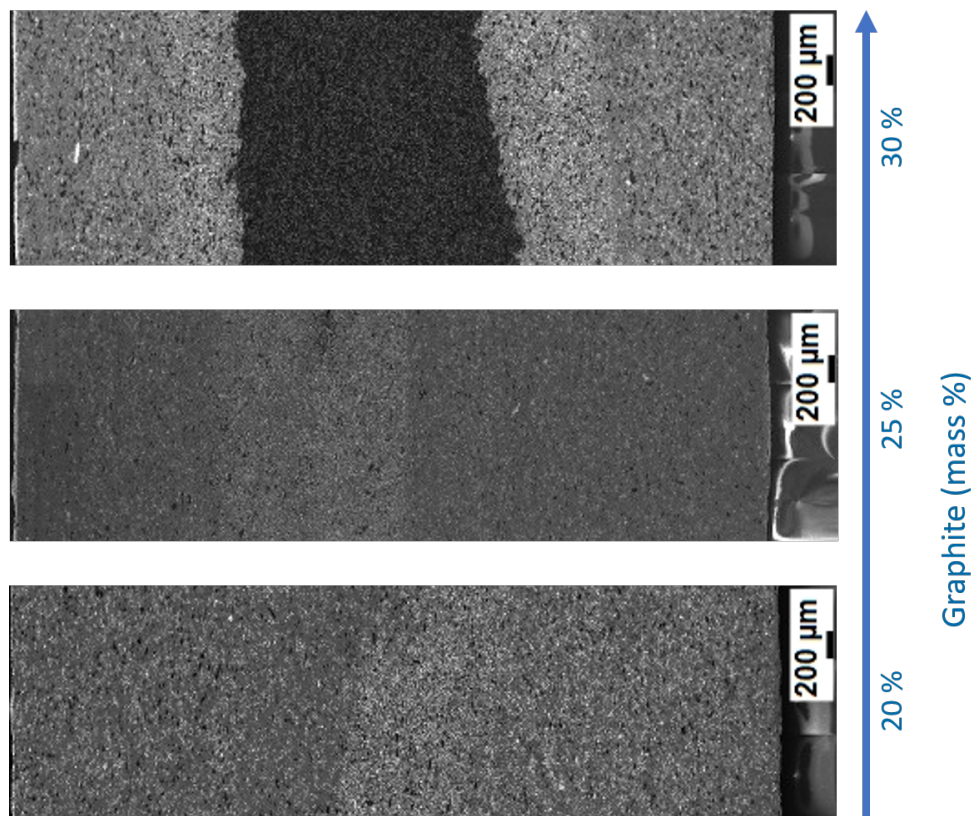


Figure 7.17 – The high resolution SEM images stitched to together to make panorama of the cross section of the SiC-C preforms with increasing mass fraction of TIMREX KS44 graphite powder from 20 to 30 % and infiltrated by near eutectic Si-Zr alloy at 1500 °C.

Table 7.6 – Summary of the results of infiltration of SiC-C preforms with near-eutectic Si-Zr alloy at 1500 °C and 1700 °C with their respective densities before and after infiltration calculated by measuring mass, diameter and thickness, and pore and ZrSi<sub>2</sub> volume fraction measured by SEM image grayscale thresholding using Fiji software. The theoretical densities and silicide phase fraction of the completely infiltrated preform calculated by using the formulation in section 5.2 are also given.

Powder mix	Graphite powder fraction (%)	infiltration temperature (°C)	density before infiltration (g/cm <sup>3</sup> )	density after infiltration (g/cm <sup>3</sup> )	pore (vol. %)	Si <sub>2</sub> Zr (vol. %)	Infiltration result (SEM)	Theo. Si <sub>2</sub> Zr or SiZr* vol. %	Theo. density (g/cm <sup>3</sup> )
SiC_C_01	0	1500	1.63	3.08	<0.5	11.6	Complete	11.1	3.15
SiC_C_02	5	1500	1.71	3.14	3.8	9.4	Complete	11.5	3.23
SiC_C_03	10	1500	1.76	3.26	4.5	10	Complete	11.6	3.31
SiC_C_04	15	1500	1.8	3.39	0.7	8.2	Complete	11.6	3.39
SiC_C_05	20	1500	1.81	3.32	0.8	6	Complete	8*	3.43
SiC_C_06	25	1500	1.86	3.16	5.2	10.1	Partial	-	-
SiC_C_07	30	1500	1.89	2.49	-	10	Partial	-	-
SiC_C_08	20	1500	1.79	3.43	<0.5	8.57	Complete	8*	3.45
SiC_C_09	25	1500	1.83	3.34	0.7	8.2	Complete	8*	3.35
SiC_C_10	30	1500	1.84	2.96	-	6.8	Partial	-	-
SiC_C_05	20	1700	1.81	3.33	<1	7.1	Complete	8.2*	3.45
SiC_C_06	25	1700	1.86	3.06	-	8	Partial	-	-
SiC_C_07	30	1700	1.89	2.65	-	1.2	Partial	-	-

The XRD analysis of the selected area from the infiltrated preforms are shown in Figure 7.18. The major phases observed are SiC, C, Si, Si<sub>2</sub>Zr, as well as some impurity phases containing Hf, Al and Fe. For the partially infiltrated samples only the reacted zones were chosen for analysis. Quantitative analysis was hindered due to two reasons. Firstly, caused by the amount of unidentified peaks of mostly complex phases of impurities, such as Al, Fe and Hf, and secondly, as some preforms were partially infiltrated, only the reacted regions were analyzed, inhibiting further comparison. The presence of peaks from Si and C in nearly all preforms, although in lower intensities, suggests the presence of residual Si and unreacted C.

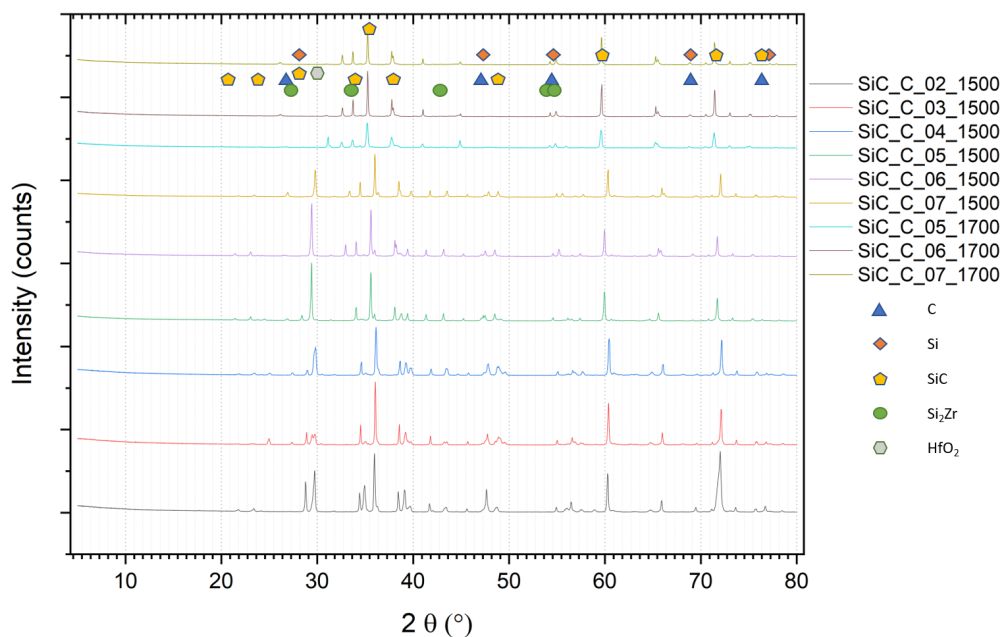


Figure 7.18 – XRD analysis of SiC/C preforms after infiltration at 1500 °C and 1700 °C showing major phases observed, which were C, Si, Si<sub>2</sub>Zr and some unidentified impurity phases containing Hf, Al and Fe.

## 7.6 Discussion

The successful reactive melt infiltration requires sufficient capillary forces, as the melt is pulled into the porous preform via capillary forces. Various parameters, such as the contact angle between the preform material and melt, pore size, atmosphere in the furnace during infiltration, and surface tension of the infiltrating melt all affect the capillary forces. Moreover, during the infiltration process, it is important that the capillary system remains open. The reactive infiltration of C-C/ SiC-C preforms is a very complex process due to the competing of simultaneously occurring processes, such as the pulling of the liquid by capillary action into the pores and the conversion of C into SiC by exothermic reaction. The extent of infiltration and conversion of C to SiC is decisive for the resulting properties of the composite. Several observations are made based on the various analyses carried out on the C-C and SiC-C preforms both before and after the infiltration by the near-eutectic Si-Zr alloy. The effect of

parameters, such as particle and porosity size and their distribution, graphite mass fraction and infiltration temperature exhibit an explicit influence on the extent of the infiltration of the preform, as well as the conversion of the graphite powder particles to SiC.

### 7.6.1 Infiltration of the C-C preforms

The porosity of the C-C preforms, as measured by mercury porosimetry, showed that the pore size distribution shifts towards higher pore sizes with increasing particle size, as well as pyrolysis temperature and shifts towards lower pore size with increasing pressure used when pressing the preforms. This behaviour was expected, as when the particle diameter increases, the inter particle distance at a given pressure will also increase resulting in bigger pores and increased porosity.

In this study, the C-C preforms made by pyrolysing cold-compacted graphite powder with bakelite resin, usually results in irregular porosity. One of the biggest limitations of the mercury porosimetry technique is that it measures the size of the entrance to the pore but not its actual inner size (Figure 7.19). This usually results in lower pore size values. Additionally, there is no way to determine if the preform has closed porosity using this technique [190].

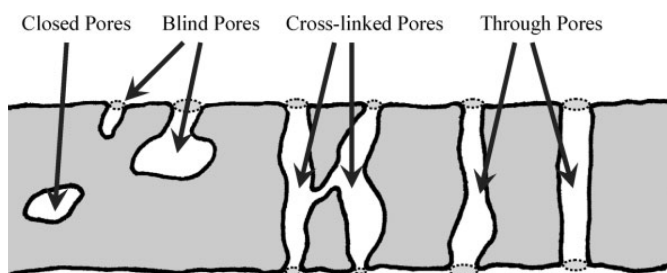


Figure 7.19 – Schematic representation of types of pores (reproduce from [190]).

The yield of pyrolytic carbon after pyrolysis of bakelite was about 60 %, as measured by TGA. Using this value, in Figure 7.20, the adequate porosity required for a C/C preform to obtain fully dense composites without residual Si or porosity is plotted against the increasing Zr concentration in the alloy according to the analytical model presented in section 5.1. As we can see for Si-8 at. pct Zr, the ideal porosity to obtain a fully dense composite with complete conversion of C to SiC and the remaining structure to be  $\text{Si}_2\text{Zr}$  is about 60 %. However, it is rather difficult if not impossible to manufacture such a preform with reasonable green strength for handling using graphite powders with particles sizes facilitating the complete conversion to SiC by reaction with liquid Si within a reasonable processing time. Using carbon short fibers, however, could make these high pore volume fractions accessible.

The C-C preforms fabricated using graphite powder with particle sizes  $d_{90}$  of 5 and 10  $\mu\text{m}$  were not infiltrated at all by the near-eutectic Si-Zr alloy. The alloy formed a thin SiC layer of a few hundred microns at the bottom surface of the preform where the alloy made first contact



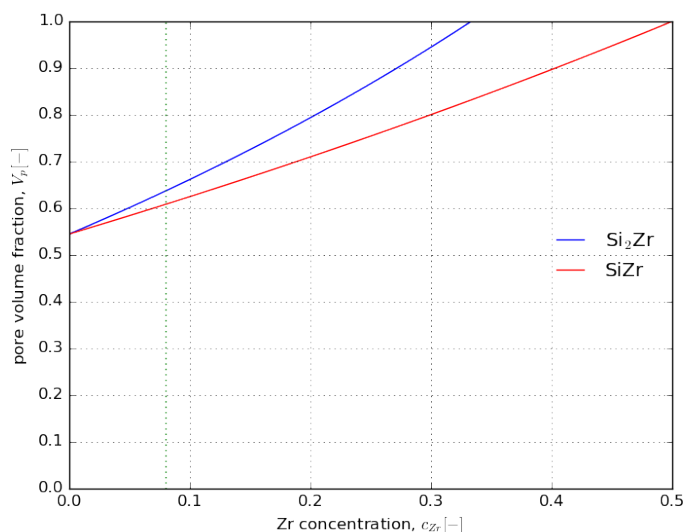


Figure 7.20 – Adequate porosity of a C/C preforms with increasing Zr concentration is plotted using Equation (5.19).

after wicking through the graphite foil, as seen in Figure 7.11. As the pore network formed by graphite particles of 5 or 10  $\mu\text{m}$  is very fine, the thin SiC layer acts as an impervious barrier stopping any further flow of the molten alloy. The C-C preforms made of graphite powder with particle sizes  $d_{90}$  of 25 and 44  $\mu\text{m}$  showed partial infiltration with cracks, while for preforms with  $d_{90}$  of 75  $\mu\text{m}$  the infiltration was complete and with fewer cracks. No relation can be established between the infiltration and porosity measured by mercury porosimetry when compared to the infiltration results summarised in Table 7.5 with the porosity measurements from Table 7.4. However, it might be expected that the porosity of the preforms increases with increasing particle size of the graphite powder when the pressing force and pyrolysis temperature are the same. The inaccuracy and inconsistency of porosity measurements by means of Hg porosimetry can be attributed to the inherent flaws of Hg porosimetry discussed earlier combined with the weak strength of the cold-pressed C-C preforms.

The partial infiltration of the C-C preforms made from TIMREX KS25 and TIMREX KS44 can be explained by the pore choking-off effect. Theoretically, the conversion of C to SiC by reaction with Si in a closed system results in a reduction in volume, as the molar volume of SiC (12.4  $\text{cm}^3/\text{mol}$ ) is less than that of the reactants graphite (5.3  $\text{cm}^3/\text{mol}$ ) and Si (11.1  $\text{cm}^3/\text{mol}$ ) combined. The resulting porosity by formation of SiC is filled by the liquid alloy as long as a fresh supply from the feed melt pool is guaranteed. However, there is an approximately 57 % theoretical increase in the solid volume fraction in conversion of solid graphite to solid SiC. Due to this much larger molar volume of SiC as compared to graphite, smaller pores tend to close shut, i.e. the so-called pore choke-off phenomenon. This effect reduces the permeability of the preform and inhibits the further flow of liquid alloy, in turn resulting in incomplete infiltration.

The cracks observed in the partially infiltrated samples made from the TIMREX KS44 graphite powder preform were not filled with molten alloy, which indicates that they were formed during solidification rather than during the infiltration phase when the alloy was still in liquid state, where it could easily accommodate the space created by cracks and voids. The Si exhibits an anomalous behaviour during the phase change from liquid to solid, where the increase in volume is approximately 11.7 %. The stresses caused by expansion during the solidification of Si can lead to severe cracking of loosely-compacted, partially-infiltrated graphite preforms.

The preform comprised of the TIMREX KS75 graphite powder exhibited complete infiltration along the whole thickness of the preform. However, the graphite did not undergo complete conversion ( $\sim 14$  vol. % residual C) to SiC, as seen in Figure 7.14 (b). The  $d_{90}$  particle size of the graphite powder is around  $75\text{ }\mu\text{m}$  for preforms made up of the TIMREX KS75 powder. From our previous study [167] and also shown by Voytovych et al. [136], the thickness of the reaction formed SiC layer has a threshold value of around 15 to  $20\text{ }\mu\text{m}$  for graphite and around  $10\text{ }\mu\text{m}$  for glassy carbon substrates when a droplet of molten Si or Si-Zr alloy reacts with the surface independent of the duration. The reaction-formed SiC layer is impermeable to liquid Si and the extremely slow grain-boundary diffusion of C or Si through the SiC layer is the reason for negligible growth of the reaction layer and only results in the coarsening and homogenization of the SiC layer's microstructure. It can be observed in Figure 7.14 that there are several large graphite particles (dark black) surrounded by an SiC layer and not being completely converted to SiC at the core, although the alloy was in liquid phase for well over an hour during the infiltration process. Only if the larger graphite particle has open intraparticle porosity then the alloy can be sucked into the pore and the whole graphite particle would be transformed into SiC by reaction between Si and C.

Considering the incomplete infiltration of preforms with graphite powder of particle size  $d_{90}$  less than  $25\text{ }\mu\text{m}$  and incomplete conversion of larger graphite particles to SiC in preforms made up of TIMREX KS75 graphite powder, the remainder of the study was performed with SiC-C preforms made by a mixture of TIMREX KS25 or TIMREX KS44 with SiC F800 powder with varying mass fractions.

### 7.6.2 Infiltration of the SiC-C preforms

The porosity and pore size distribution directly affects the so-called "pore choking-off" effect observed in reactive infiltration of liquid Si in microporous carbon preforms. In the case of infiltration of C/C preforms by Si-alloys, a higher amount of initial total porosity is needed, as the initial Zr content in the alloy increases, as seen in Figure 7.20. Additionally, Singh and Behrendt [70] reported the same for infiltration by Si-Mo alloys. However, the addition of SiC powder to the graphite powder considerably reduces the necessary initial porosity of preforms, as shown in the analytical model for adequate porosity in section 5.1. This is beneficial in making preforms with a higher green density, as the preforms do not need to have a porosity in the range of 60 %. The accurate and reliable measurement of porosity is rather

difficult when it comes to these kind of preforms. In Figure 7.21, the theoretical adequate porosity to attain composites without any residual porosity or Si and facilitate the complete conversion of graphite along with the measured porosity values of SiC/C preforms made from SiC F800 powder and TIMREX KS 25 graphite with varying mass fraction using three different methods, namely, MIP, X-Ray CT and physical dimensions and skeletal density measured by He pycnometry. The analytical model developed in section 5.1 is used for calculating the ideal porosity value and Bakelite's pyrolytic carbon yield was taken as 60 %.

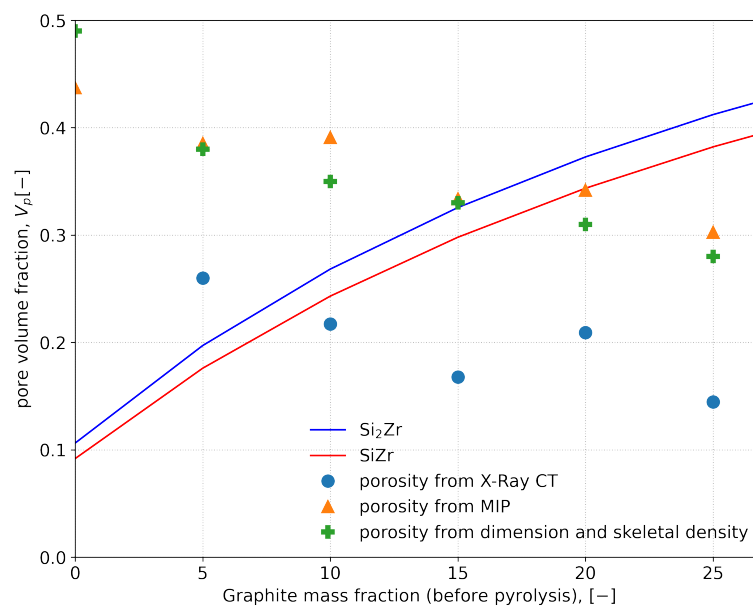


Figure 7.21 – Theoretical initial adequate porosity of the SiC/C preforms with varying graphite fractions to obtain fully dense preforms without residual Si or unreacted C and given silicide phase. Above the line one would expect to get free Si and below the line unreacted C. The measured porosity values are also shown for preforms with TIMREX KS 25 graphite powder mass fractions ranging from 5 to 25 %.

The porosimetry measurement of SiC-C preforms with mercury porosimetry showed a very narrow pore size distribution. The median pore diameter of the preforms decreased with increasing graphite percentage for both kinds of preforms, i.e. made from TIMREX KS25 and TIMREX KS44 and mixed with SiC F800. The total porosity measured by mercury intrusion seems to also decrease with increasing graphite mass fraction in SiC-C preforms. The preforms made with TIMREX KS44 have a higher median pore diameter, as well as total porosity measured by mercury intrusion owing to their larger particle size as compared to the preforms containing TIMREX KS25 for the same graphite mass fractions. However, the pores observed in the microstructure of the infiltrated specimens contradicts such a low value of median pore size measured by Hg porosimetry. In Figure 7.22, a sample SEM image of a SiC\_C\_07 preform and a X-ray CT frame of the preforms made from SiC\_C\_07 powder mix are shown. The pores



(with the darkest color in both images) have much larger sizes than the median pore size of  $2\text{ }\mu\text{m}$ ) measured by MIP.

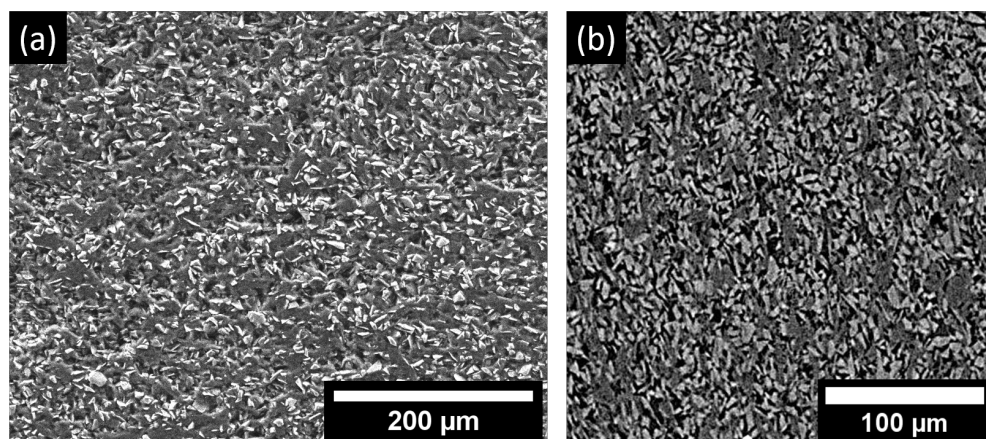


Figure 7.22 – (a) SEM image of the SiC\_C\_07 preform (b) X-ray CT frame showing much larger pores than measured by MIP (median pore diameter =  $2\text{ }\mu\text{m}$ ). The pores are darkest with both images.

The second set of porosity analysis done via X-ray CT technique showed completely different absolute values of the porosity distribution and modal pore size. However, the trend of decreasing porosity with increasing graphite content is similar in total porosity values measured by both Hg porosimetry and X-ray CT technique. The modal pore size values measured via X-ray CT are fairly constant irrespective of increasing mass fraction after decreasing to  $7\text{ }\mu\text{m}$  for 10 % graphite powder. The modal diameter values obtained via X-ray CT seem to be in line with observations via SEM. Moreover, the distribution of pore size is much broader for preforms with less graphite and shifts left to lower pore sizes with increasing graphite mass fractions. The particle size distribution of the SiC-C powder mixtures shows that the amount of sub-micron sized SiC particles decreases with increasing graphite mass fraction. It is possible that during the mixing the finer SiC particles form agglomerates together with the bakelite binder and/or graphite particles, which results in the bi-modal mixture with peaks corresponding to the modal diameters of SiC and graphite powder, respectively. As the graphite powder mass fraction increases, the second peak corresponding to the modal size of graphite powder gets more dominant. The graphite powders used in both mixtures, i.e. TIMREX KS25 and TIMREX KS44, have higher  $d_{90}$  than the SiC F800 powder. Therefore, with increasing amount of graphite powder, more SiC particles can occupy the inter-particle voids formed by graphite particles resulting in denser preforms with less porosity. However, the total porosity measured via CT are far off from the expected values as calculated by skeletal density of the powder mix, weight and physical dimensions of the preform, as seen in Figure 7.21. This can be explained by the resolution limit of the voxel in CT being  $0.5\text{ }\mu\text{m}$ . It appears that the pores closer to the size  $1\text{ }\mu\text{m}$  or sub-micron may not be imaged and isolated correctly, resulting in much lower measured total porosity. Therefore, care should be taken while using either of the techniques to analyse the porosity accurately and reliably.

The infiltration results of the SiC-C preforms with varying mass fractions of graphite powder are affected not only by the amount of graphite available for the reaction with the alloy but also the changing porosity distribution of the preforms. It is evident from the porosity analysis of the preforms that the porosity decreases with the increasing mass fraction of graphite powder in the preform. The equivalent radius  $R^*$  for the SiC/C preforms used in the experiments, calculated using Equation (5.63), developed in section 5.4 and the factor  $\phi$  accounting for the influence of the SiC particles in wetting, calculated by taking the ratio of the surface provided by the graphite to the surface per volume of graphite and SiC together are given in Table 7.7. The effect of pyrolysed carbon from bakelite was not considered for simplification. The value of specific surface of SiC F800 is taken as 1070 m<sup>2</sup>/kg from ref.[191], the values for TIMREX KS25 and TIMREX KS44 are taken, as mentioned in Table 7.1.

Table 7.7 – The calculated values of equivalent radius,  $R^*$  and SiC propensity factor,  $\phi$  in the SiC/C preforms as developed in section 5.4.

Sample	Graphite powder	Graphite mass fraction	$R^*$ [m]	$\phi$
SiC_C_01	TIMREX KS 25	0	5.6E-07	0.00
SiC_C_02	TIMREX KS 25	5	2.5E-07	0.37
SiC_C_03	TIMREX KS 25	10	1.6E-07	0.55
SiC_C_04	TIMREX KS 25	15	1.2E-07	0.66
SiC_C_05	TIMREX KS 25	20	9.3E-08	0.74
SiC_C_06	TIMREX KS 25	25	7.0E-08	0.79
SiC_C_07	TIMREX KS 25	30	5.6E-08	0.83
SiC_C_08	TIMREX KS 44	20	1.2E-07	0.68
SiC_C_09	TIMREX KS 44	25	9.5E-08	0.74
SiC_C_10	TIMREX KS 44	30	7.7E-08	0.78

The calculated terminal infiltration length  $L$ , using the differential model for non-isothermal infiltration experiments of the SiC/C preforms infiltrated by Si-8 at-pct Zr alloy (section 5.5) at 1500 °C and 1700 °C using the value of  $R^*$  and  $\phi$  from Table 7.7 are shown in Figure 7.23

The observed infiltration lengths follow the model more or less qualitatively when compared with the extent of the infiltration observed in the SEM analysis in Figure 7.15, Figure 7.16 and Figure 7.17, which are summarized in Table 7.6. The most desirable results, which include a homogeneous distribution of the Zr-rich phase, least porosity and maximum conversion of graphite into SiC, can be seen in sample with 15 % and 20 % mass fraction of graphite for preforms with both TIMREX KS25 and 20 % mas fraction of TIMREX KS44 powder (Table 7.6). The later, however, has approximately 4 to 6 % of unreacted graphite. The uncertainty is due to the difficulty in the segmentation of the pores and residual graphite due to low image contrast. The porosity values are very close to those calculated by the analytical model (Figure 7.21).

There is another interesting observation from the preforms with TIMREX KS25 powder infiltrated at 1700 °C, as seen in Figure 7.16: the preforms with 25 % and 30 % graphite show

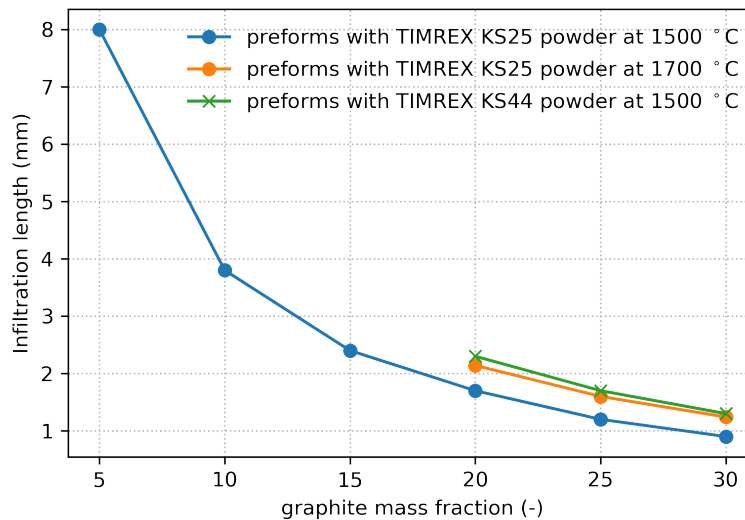


Figure 7.23 – The calculated terminal infiltration length of the SiC/C preforms for a non-isothermal case, inputting the graphite mass fraction and infiltration temperature values used in this study.

much less depth of infiltration as compared to those of the same preforms infiltrated at 1500 °C. As per the calculated terminal length in Figure 7.23, the preforms should actually show longer infiltration depths. As also observed in chapter 6, the increase in temperature in non-isothermal infiltration may increase the infiltration depth achieved for a given capillary size. However, in the case of the porous carbonaceous preform, the pore structure is more random and sometimes small enough to locally have a negative effect on the reactive infiltration process, as seen in the isothermal case (Figure 7.24). Again, the terminal length values are lower than that of those obtained in non-isothermal infiltration. This has to do with the fact that diffusion-mediated infiltration is possible in the incremental scheme used in the non-isothermal modelling, while in the isothermal model, the infiltration stops as soon as the defined critical concentration is attained for the first time. Furthermore, the model requires further development, as some of the basic assumptions do no longer hold when calculating short infiltrations at diffusion mediated "creeping" infiltration rates.

### 7.6.3 Banding of the Zr-rich phase

The banding of the Zr-rich phase observed in the cross-sections of SiC-C preforms infiltrated by the Si-Zr alloy may help in decoding the reactive infiltration process with binary alloys. In chapter 6, where we studied the reactive flow of molten pure Si and Si-Zr alloy in a single micron-size capillary channel made up of glassy carbon, we found two distinct mechanisms, which could cause the infiltration to stop during the reactive infiltration of molten Si-Zr alloy. The first is the widely suggested formation of solid SiC due to the reaction between carbon

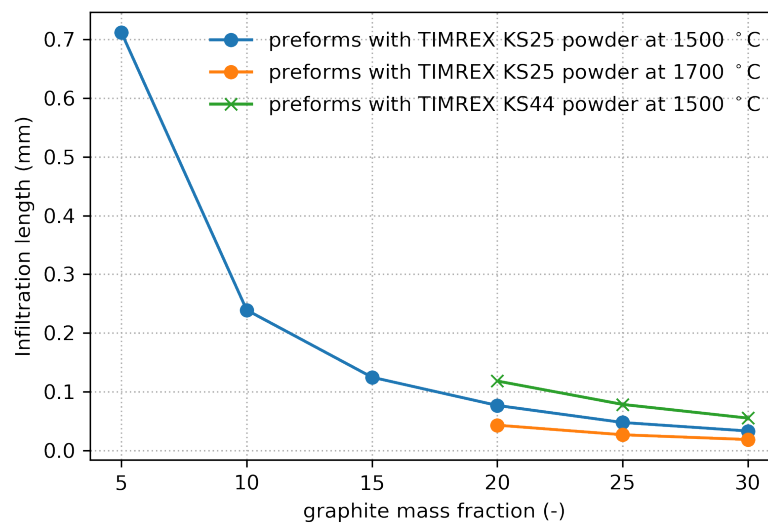


Figure 7.24 – The calculated terminal infiltration length for an isothermal infiltration case. The temperature has a negative effect on the terminal infiltration depth.

and molten silicon reducing the permeability of the channels until it blocks the further supply of fresh molten Si or alloy from the ingress to complete the infiltration of the preform. The second mechanism we found is the precipitation of solid zirconium silicides at the infiltration front due to the increase in Zr concentration in the alloy along the infiltration path as Si reacts with carbon to form SiC. These combined findings of the analytical model for ideal porosity and infiltration length suggests that as the graphite fraction increases the infiltration depth should also increase for a given porosity.

In Figure 7.15, the SEM cross-section image of the preform with 5% TIMREX KS25 graphite powder infiltrated at 1500 °C shows an alternating band structure of a Zr-rich phase and reaction-formed SiC along the length with a large amount of residual porosity at the core. Since the SEM image depicts only a small width (few 100  $\mu\text{m}$ ) compared to the whole thickness of the preform ( $\sim 5$  mm), it might give an impression of ordered banding of the Zr-rich phase. The lower magnification image (Figure 7.25), however, shows typical off-eutectic solidification. As the amount of C in the preform is much lower, the composition infiltrated alloy after reaction with C changes slightly and results in the observed off-eutectic solidification.

The preforms with 15 % and 20 % TIMREX KS25 graphite powder infiltrated at 1500 °C are characterised by a homogeneous distribution of Zr silicides without any banding and the least residual porosity as measured by grayscale thresholding of high resolution panoramic SEM images of the cross-sections in Figure 7.15. The measured densities after infiltration for preforms with 15 % and 20 % graphite powder are 3.39 g/cm<sup>3</sup> and 3.34 g/cm<sup>3</sup>, respectively. The homogeneous structure suggests that the preforms are infiltrated fast enough to avoid pore closure caused by Zr silicide precipitation, resulting in a homogeneous precipitation of

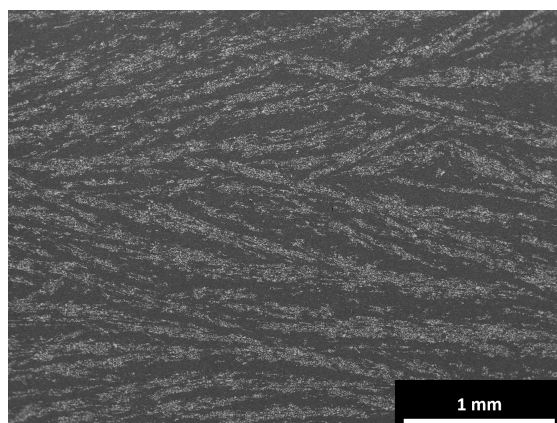


Figure 7.25 – SEM image of the SiC-C preforms with 5 % TIMREX KS25 graphite powder, showing the off-eutectic solidification of Si-8 at. pct Zr alloy in the SiC/C preforms with low C content.

Zr silicides after the Si from the alloy has reacted with the graphite particles to form SiC and, consequently, increasing the Zr concentration in the remaining liquid. When the concentration of graphite mass fraction is increased to 25 %, a single band with a high concentration of a Zr-rich phase can be seen at the core with slight residual porosity. Therefore, the density after infiltration is slightly lower than that of the preform with a graphite mass fraction of 20 %. The increase in graphite mass fraction in the preform with 25 % graphite powder increases the Zr concentration at the infiltration front more than that of preform with with graphite mass fraction of 20 %, as there is more C available to react with Si. When the graphite mass fraction is further increased to 30 %, the initial preform porosity value decreases considerably more compared to the ideal porosity and the amount of graphite to react with the Si from the alloy is high enough to increase the concentration of Zr at the infiltration front at a much shorter length, such that the precipitation of Zr silicides blocks further supplies of fresh alloy to the core of the preform. This can be seen as the two bright color bands of Zr-rich phase on both sides of the uninfiltrated preform core.

The experimental results obtained in the reactive flow of the Si-Zr alloy in a micron-sized single capillary channel of glassy carbon are mentioned in chapter 6; we observed that increasing the infiltration temperature to 1700 °C may facilitate in increasing the infiltration depth. The increased length of infiltration is caused by the non-isothermal infiltration of the 10 µm glassy carbon microchannel. The result of the infiltration of the preform with TIMREX KS 25 powder of mass fractions from 20 % to 30% and infiltrated at 1700 °C by the near-eutectic Si-Zr alloy showed, however, lower infiltration depth as compared to that of the similar preforms infiltrated at 1500 °C. This can also be confirmed with the lower density of the infiltrated preforms. The major difference between a single microchannel capillary and preform infiltration is the type of carbon; the carbon in the single microchannel experiment is glassy carbon and in preforms it's graphite. White et al. [168] and Voytovych et al. [136] have shown that the reaction rate of Si with C and the nature of the produced SiC are material-dependent. As graphite is

more reactive than glassy carbon when it comes to the formation of SiC by reaction of molten Si and C, the results from the microchannel experiments may not be directly translated to the infiltration of preforms made with graphite powder by the Si-Zr alloy. Secondly, as previously mentioned, the complexity of the pore structure and the presence of sub-10  $\mu\text{m}$  pores hinder longer infiltration length obtained for non-isothermal infiltration over the peritectic temperature.

Increasing the graphite particle size used to make the SiC-C preforms by changing the graphite powder from TIMREX KS 25 to TIMREX KS 44 resulted in preforms with a higher total porosity and modal pore size, as measured by X-ray CT analysis in Figure 7.10. The slightly higher porosity and modal pore size, as compared to preform with TIMREX KS25 graphite powder, helps steer the infiltration closer to the core. However, the preform with a graphite mass fraction of 30 % was still not completely infiltrated till the core. The similar banding effect at the core can be observed here as well. The measured densities after infiltration show that the preform with a mass fraction of 20 % TIMREX KS44 graphite powder produces discs with highest density of  $3.43 \text{ g/cm}^3$ . However, it is worth noting that the bigger graphite particles of TIMREX KS44 graphite powder did not completely convert to SiC by reaction with Si from the alloy. From our previous study [167] of sessile drop experiments of Si and near-eutectic Si-Zr alloy on glassy carbon plates, we found that the maximum reaction layer of SiC formed on glassy carbon was around 5  $\mu\text{m}$  for both pure Si and near-eutectic Si-Zr alloy. Additionally, Voytovych et al. [136], showed that the maximum reaction layer thickness on graphite is approximately 15 ~20  $\mu\text{m}$ . The liquid Si reacts with the C and forms a micron thick permeable layer of SiC, through which liquid Si can still diffuse through the pockets to rapidly form a thick layer of SiC until it reaches a threshold value of approximately 15 ~20  $\mu\text{m}$  on graphite substrates and 10  $\mu\text{m}$  on glassy carbon substrates. Further growth by grain-boundary diffusion of C is negligible and only results in coarsening of the SiC grains rather than increasing the thickness of the SiC layer. The shape of the graphite particles is flaky and when one considers an isolated particle, the smaller dimension of the particle may be much smaller than 20  $\mu\text{m}$ , however during compaction and pyrolysis process it is possible that some of the particles may agglomerate together and form a bigger particle with dimensions exceeding the critical maximum thickness of the C particle. Although the preform with 20 % TIMREX graphite powder is completely infiltrated with negligible porosity, the residual unreacted graphite may make it unsuitable for certain applications requiring high oxidation resistance.

## 7.7 Conclusion

The preforms containing only graphite powder can be infiltrated completely with minimal defects only when they are made with particle size  $d_{90}$  75  $\mu\text{m}$  or larger. The C-C preforms are more prone to defects, such as cracks and residual porosity due to large amounts of thermal stresses caused by the highly exothermic reaction between Si and C, as well as the expansion of residual Si in the pores. Larger graphite particles cannot be completely converted to SiC, which make these Si-Zr alloy infiltrated composites prone to oxidation and with lower ablation

resistance. However, fully dense composites can be made through the infiltration of near eutectic Si-Zr alloy in a porous preform made up of a mixture of carbon and SiC powder with residual porosity and unreacted graphite of less than 1 %.

The experiments with SiC/C preform infiltration with varying graphite mass fraction and particle size showed that only increasing the porosity is not sufficient in obtaining fully dense composites without residual Si, porosity and unreacted C. The infiltration results were in line with the analytical model developed in chapter 5 for ideal porosity of the preforms for a given SiC/C ratio. The best properties were obtained for preforms made from SiC F800 and 15 % TIMREX KS 25 graphite powder, having initial preform porosity of 33 % as measured by MIP. The infiltrated sample had less than 1 % of residual porosity and graphite with SiC being the predominant phase,  $\text{Si}_2\text{Zr}$  and minimal residual Si.

Precipitation of the solid Zr silicides at the infiltration front was the major cause of pore blocking in case of the carbonaceous preforms infiltrated by Si-8 at. pct Zr alloy, unlike the formation of SiC in the case of infiltration by pure Si. Increasing the processing temperature above the peritectic temperature did not enable higher infiltration as suggested by the differential non-isothermal model developed for the infiltration length of the alloy in a micro-channel. The much lower pore sizes and irregular pore structures of the preform resulted in faster pore clogging at higher temperatures, as suggested by the isothermal model.

## 8 Conclusion

### 8.1 Conclusions from this work

The thesis's work provided detailed insight into the fundamentals of the reactive infiltration of porous carbonaceous preforms by Si-X alloys. The key learnings of this work are as follows:

- **The viability of Zr as an alloy element for reactive infiltration of porous carbonaceous preform was established by sessile drop experiments.**
  - The choice of the Zr as a suitable alloying element was based on several criteria as outlined in the last section of the Literature review. A first study for suitability was concerned with the wettability of the Si-8 at. pct Zr alloy on SiC and glassy C substrates compared to pure Si by sessile drop experiments. Si-8 at. pct Zr alloy showed good wettability on both C and SiC substrates, although with a slower spreading rate than pure Si. The equilibrium contact angles were in the range of 29° and 39° at 1500 °C.
  - It was found that the evaporation could result in erroneous interpretation of the wetting angle for long term spreading experiments. The importance of the Si evaporation under vacuum was highlighted with regard to the infiltration process. The reaction layer at the interface was made up of SiC in both pure Si and Si-Zr alloy on C substrate, while SiC substrate was nonreactive. However, there was a slight erosion of the SiC substrate at the interface.
- **Analytical models describing infiltration kinetics, porous preform requirements, alloy composition, processing temperature and resulting phases in the reactive infiltration of porous carbonaceous preforms by Si alloys were developed.**
  - An analytical model for correctly evaluating the adequate pore volume fraction by taking into account the presence of silicide formers, as well as a model to predict theoretical density and phases present after infiltration based on preform composition and preform porosity, was devised. The analytical model's treatment is valid for an extensive range of silicide formers.



- The model showed that an increase in graphite mass fraction in the SiC-C preforms shifted the range of preform porosity leading to composites formed by SiC and silicides to higher values. A porosity above this range results in residual Si, and a porosity below this range results in unreacted graphite.
- For the first time, an analytical model was developed for pore channel closure due to alloying element enrichment at the infiltration front, both for individual straight channels and tortuous porosity under isothermal and non-isothermal processing conditions.
- For the SiC/C preforms, an effective pore radius was calculated in terms of the SiC and graphite powder's specific surface area.
- In isothermal conditions, the infiltration length decreases with increasing temperature, while in the non-isothermal condition, in a particular scenario, higher infiltration lengths can be reached. Good quantitative agreement between the experiments and the model was observed.
- **For the first time, reactive infiltration of the Si-Zr alloy in micron-sized carbon capillaries has been experimentally studied. A new mechanism for the closure of pores based on enrichment of the silicide former at the infiltration front was proposed conceptually, quantified using analytical models, and verified experimentally.**
  - A clean method was devised to study phenomena pertaining to LSI in a macroscopic sample with simple geometry but with length scale relevant to preform infiltration. In the glassy carbon microchannel experiments, the pore closure observed at the infiltration front was due to the precipitation of Zr silicides.
  - The basic mechanism is that the Si from the alloy reacts with the C from the wall of the microchannel forming the SiC layer, the diffusion of Si from the receding alloy is not fast enough to compensate for the loss of Si, which results in continuous enrichment of the Zr at the infiltration front. Once the Zr concentration is higher than the critical value defined by a solid mass fraction at the given temperature, precipitation of Zr silicides at the infiltration front restricts the further flow of molten alloy.
  - The increase in infiltration temperature above the alloy's peritectic temperature in a non-isothermal condition leads to higher infiltration depth for the 10  $\mu\text{m}$  deep channel.
  - The pore-clogging due to the growth of the SiC layer at the ingress was observed neither in pure Si nor in Si-8 at. pct Zr alloy in case of 10  $\mu\text{m}$  thick and 465 mm long glassy carbon channel. The pore clogging may have however operated in the porous preform infiltration experiments where bottlenecks may have significantly smaller characteristic dimensions than in the microchannel experiments conducted here. The results were in good agreement with the developed model.
- **The sweet spot for infiltration of disk-shaped porous carbonaceous preform by Si-Zr alloy in terms of C and SiC powder size and composition, preform porosity, alloy composition and processing temperature analytically predicted and experimentally verified. The results were consistent with the analytical model.**

- The disc-shaped composites were manufactured by infiltration of Si-8 at. pct Zr alloy in carbonaceous C/C and SiC/C preforms to verify predictions of the various models presented, pertaining to i) the relation between preform composition and porosity and the resulting phases (semi-quantitative in the analysis); ii) sweet spot calculation of full conversion without free silicon; iii) quantitative analysis of infiltration length as a function of preform composition and porosity; iv) limit of length scale, the model, would indicate that infiltration gets deeper when the characteristic length scale of the carbonaceous phase gets larger. Exploring this venue is limited by the difficulty in obtaining full conversion of C to SiC within reasonable reaction time. The C/C preforms with particle size  $d_{90} = 75 \mu\text{m}$ , or larger could be infiltrated entirely to form dense composite but with incomplete conversion of the graphite to the reaction formed SiC. The C/C preforms were also more prone to cracking. The use of SiC/C preforms can reduce the ideal initial preform porosity as outlined in the analytical model.
- The best results were obtained for the preforms made from SiC F800 and 15 % mass fraction of the TIMREX KS 22 graphite powder with 33 % initial preform porosity. The infiltrated sample had less than 1 % of residual porosity and graphite with major phases consisting SiC,  $\text{Si}_2\text{Zr}$  and minimal residual Si. The results obtained for the SiC/C preforms were in agreement with the model's prediction.

Overall, it is all but simple to actually achieve dense, volume conserving LSI composites without free silicon and free graphite. Understanding the pore closure mechanism due to the precipitation of the solid silicide phase with the help of an analytical model and the microchannel experiments is the highlight of the work. The thesis provides a wide variety of tools and general guidelines to manufacture dense SiC matrix composites using reactive infiltration of porous carbonaceous preforms by Si alloys, not limited to the Si-Zr system studied here.

## 8.2 Outlook

Although we were able to get some insights into the wetting of C by Si-Zr alloy by sessile drop experiments, the work can be further extended by understanding the very early stage wetting of C by Si alloys by using the dispensing drop technique coupled with a high-speed digital camera system. The early stage of wetting by forming a very thin SiC layer is believed to happen within a fraction of seconds. The experiments might also provide vital information regarding the Si and C reaction rate.

The microchannel experiment helped us verify the pore-clogging by silicide precipitation at the infiltration front hypothesis. However, the furnace setup did not allow any in situ observations of the infiltration front which would be necessary to substantiate the predicted slow-down of the liquid metal ingress once the diffusion limit, i.e the situation where further ingress of the liquid is only possible at a rate controlled by the diffusive transport of the silicide former away from the infiltration front, is reached. Designing the experiment to observe the

in situ rise of the meniscus in microchannels, something along the lines of the experiments by Hofbauer et al. [141], will give a direct access to instantaneous infiltration velocity, which in turn can be used to decide the processing parameters for the composite processing. Also, by mechanically controlling when the liquid alloy is introduced into the samples, the experiments can be performed in an isothermal condition and the start and the end of the process can be controlled more precisely. A cold-wall reaction chamber as, e.g. an induction heated furnace with quartz wall for visual observation, seems a good start both for potential visual inspection and the potential ease of instrumentation of the setup.

An induction furnace can be an excellent option to perform infiltration experiments as well. The processing time can be reduced to as low as a few minutes. On the downside, the appropriate heating up of the preform (due to different coupling with the induction heating) may require some additional thought. At any rate, our preliminary study on the viability of infiltration by induction melting was rather promising. Figure 8.1 shows an experimental setup used for the induction infiltration and an SEM image of the induction infiltrated SiC-C preform with 5 wt.% TIMREX KS 25 graphite powder. The whole heating cycle took about 15 min to reach the infiltration temperature of 1500 °C, manually controlling the heating rate.

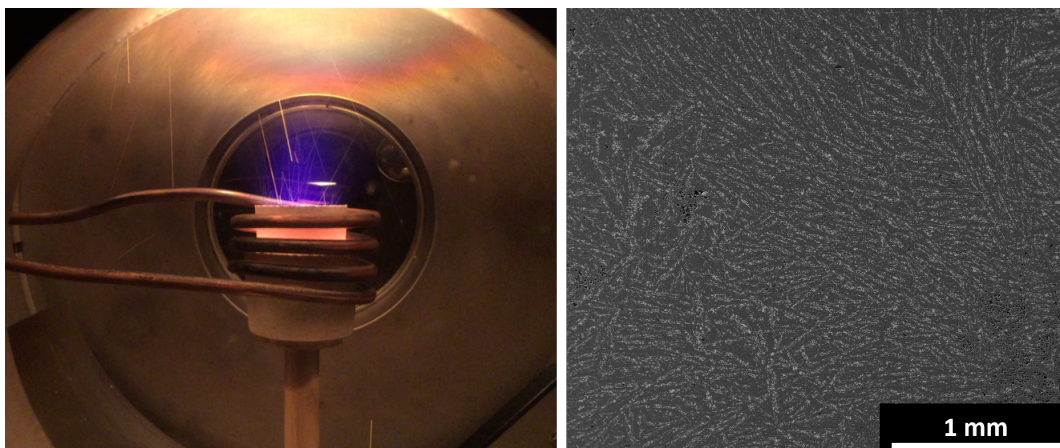


Figure 8.1 – Experimental setup for induction infiltration experiment (left) and SEM image of the cross-section of the induction infiltrated SiC/C preform with 5 wt.% TIMREX KS 25 graphite powder (right).

The current analytical model of pore clogging by enrichment of silicide former at the infiltration front neglects some complicating issues, e.g. the effect of the thickness of the reaction formed SiC layer, for numerical simplicity. In its closed form, it simply describes the moment at which the critical silicide former concentration is reached for the first time at the infiltration front and does not take into account the "creeping" ingress enabled by the diffusion of the silicide former away from the infiltration front. In general terms, the silicide former concentration profile behind the infiltration front is a complicated issue that needs to be studied in detail by numerical means. The current model can thus further be improved along these lines. The model also predicts that higher Si content in the alloy leads to deeper infiltration,

which was also observed experimentally in the microchannel experiments. Verification for the infiltration of carbonaceous preforms by an alloy with higher Si content is needed. Such reduction of silicide forming elements would, however, come at the price of requiring higher initial preform porosity (for a given preform composition) and would constitute a typical trade-off.

This page is intentionally left blank.

# A Python codes

Listing A.1 – Adequate theoretical porosity model

```
1 # -*- coding: utf-8 -*-
2 """
3 @author: manoj
4 """
5 import matplotlib.pyplot as plt
6 import numpy as np
7 density_SiC=3.21 #g/cc
8
9 density_C_P=1.5 #g/cc pyrolyzed
10 density_C_G=2.2 #g/cc graphite
11 density_Si=2.5
12 density_SiZr= 5.590 #g/cc Lang cheng et al. alpha SiZr
13 density_Si2Zr=4.88 #g/cc
14
15 molar_weight_C=12
16 molar_weight_Si=28
17 molar_weight_SiC=40
18 molar_weight_SiZr=28+91
19 molar_weight_Si2Zr=2*28+91
20 def adequate_pore_fraction(c_Si, weight_SiC, weight_C_G, weight_C_P,n):
21     if n==1:
22         V_m_Si_n_X=molar_weight_SiZr/density_SiZr
23     else:
24         V_m_Si_n_X=molar_weight_Si2Zr/density_Si2Zr
25
26     V_m_SiC =molar_weight_SiC/density_SiC
27     V_m_C_G =molar_weight_C/density_C_G
28     V_m_C_P =molar_weight_C/density_C_P
29     c=c_Si
30     term_m=(weight_C_P*density_C_G)/(weight_C_G*density_C_P)
31     term_a=(V_m_SiC/V_m_C_G)-1+term_m*(V_m_SiC/V_m_C_P-1)
32     A=1/(term_a+(1-c)*V_m_Si_n_X/((n+1)*c-n)*(1/V_m_C_G+term_m/V_m_C_P))
33     B=1+(weight_SiC*density_C_G)/(weight_C_G*density_SiC)+(weight_C_P*
34         density_C_G)/(weight_C_G*density_C_P)
35     return (1/(1+A*B))
```

```

35 #plots
36 plt.figure(dpi=300)
37 # plt.style.use('classic')
38 c_Si=np.arange(0.01,1.01,0.01)
39 weight_SiC=90
40 weight_C_G=.1
41 weight_C_P=6
42 plt.plot (1-c_Si,adequate_pore_fraction(c_Si, weight_SiC, weight_C_G,
    weight_C_P,2),label='Si$_2$Zr', color='b')
43 plt.plot (1-c_Si,adequate_pore_fraction(c_Si, weight_SiC, weight_C_G,
    weight_C_P,1),label='SiZr',color='r')
44 plt.xlabel('Zr concentration, $c_{Zr}$ [-]$ ')
45 plt.ylabel('pore volume fraction, $V_p$ [-]$ ')
46 plt.legend(loc='center right',frameon=False)
47 plt.ylim([0.0, 1])
48 plt.tick_params(axis='y')
49 plt.xlim([0, 0.5])
50 plt.grid(axis='both')
51 plt.yticks(np.arange(0, 1.1, step=0.1))
52 plt.savefig('adequate_pore_fraction_vs_Zr_conc.png',transparent=1)

```

Listing A.2 – infiltration length model

```

1 # -*- coding: utf-8 -*-
2 """
3 @author: manoj
4 """
5 import math
6 import matplotlib.pyplot as plt
7 import numpy as np
8 #constants
9 molar_volume_SiC = 1.25e-5 #m^3/mol Calculated from
    density and molecular mass from Pubchem
10 molar_volume_liquid = 1.31e-5 #m^3/mol CODATA Si=12.01,
    Zr=14.02
11 universal_gas_constant=8.3145
12 diffusion_Si_liq = 15e-9 # 8e3 m^2/s Birnie 1986 #
    Pommrich 2008, Jingyu Qin 2019
13 triple_line_velocity= 2e-4 #m/s Giuranno 2020
14 activation_energy_SiC =200e3 #J/mol Dezellus 2002
15 activation_energy_triple_line=185e3 #assumption
16 activation_energy_diffusion=28e3 # 850e3 J/mol Birnie 1986 #
    Pommrich 2008
17 # calculation for triple line velocity prefactor
18 triple_line_velocity_prefactor=triple_line_velocity/(math.exp(-
    activation_energy_triple_line/(universal_gas_constant*1773)))
19 print(triple_line_velocity_prefactor)
20 #calculation for thickness_SiC_prefactor
21 known_thickness_SiC=1e-6 #m
22 known_time=900 #s
23 known_temperature=1773 #K
24 thickness_SiC_prefactor=known_thickness_SiC/(math.exp(-

```

```

        activation_energy_SiC/(universal_gas_constant*known_temperature))*math.
        pow(known_time,1/2))
25 # thickness_SiC_prefactor=0.3
26 print (thickness_SiC_prefactor)
27 #Critical Si calculation , 27.8 Zr at 1500 deg C, 43.6 Zr at 1620
28 def critical_Si(temperature):
29     return 0.72 if temperature<=1620 else 0.564
30 # infiltration length calcuclation
31 def infiltration_length_SiZr(C_Si_initial, temperature,
    microchannel_thickness, order_n):
32     n=order_n
33     T=temperature +273
34     e=microchannel_thickness*1e-6 #micrometer to m
35     C_Si_crit= critical_Si(temperature) # 80% of solid phase at
    1500 deg C - 0.34 Si2Zr line
36     if C_Si_initial<=C_Si_crit:
37         L=0
38     else:
39         L=math.pow(((C_Si_initial-C_Si_crit)*molar_volume_SiC*e*math.pow(
    diffusion_Si_liq,(n-1)/(2*n))/((1-C_Si_initial)*molar_volume_liquid*2*
    thickness_SiC_prefactor*math.pow(triple_line_velocity_prefactor,(n-3)
    /(2*n))))*math.exp((2*n*activation_energy_SiC-(n-1)*
    activation_energy_diffusion-(3-n)*activation_energy_triple_line)/(2*n*
    universal_gas_constant*T)),(2*n/(n+1)))
40
41     return L *1000
42 def infiltration_length_SiZr_preform(C_Si_initial, temperature,
    effective_radius, order_n):
43     n=order_n
44     T=temperature +273
45     e=effective_radius*1e-6 #micrometer to m
46     C_Si_crit= critical_Si(temperature) # 80% of solid phase
    at 1500 deg C - 0.34 Si2Zr line
47     local_surface_inclination_factor=1/3 #assumption
48     SiC_presence_compensation=0.5 #assumption
49     if C_Si_initial<=C_Si_crit:
50         L=0
51     else:
52         L=math.pow(((C_Si_initial-C_Si_crit)*molar_volume_SiC*e*math.pow(
    diffusion_Si_liq,(n-1)/(2*n))/((1-C_Si_initial)*molar_volume_liquid*2*
    SiC_presence_compensation*math.pow(local_surface_inclination_factor,((n
    -3)/(2*n)))*thickness_SiC_prefactor*math.pow(
    triple_line_velocity_prefactor,(n-3)/(2*n))))*math.exp((2*n*
    activation_energy_SiC-(n-1)*activation_energy_diffusion-(3-n)*
    activation_energy_triple_line)/(2*n*universal_gas_constant*T)),(2*n/(n
    +1)))
53     return L*1000
54 #plots microchannel
55 #infiltration length vs temperature
56 n=2
57 lengthvstemp=[]
58 temperature=np.arange(1500,1800,5)

```



```

59 for temp in temperature:
60     lengthvstemp.append(infiltration_length_SiZr(0.9,temp,10,n))
61 #infiltration length vs concentration
62 lengthvsconc=[]
63 conc=np.arange(.5,1,0.01)
64 for c in conc:
65     lengthvsconc.append(infiltration_length_SiZr(c,1500,10,n))
66 plt.style.use('classic')
67 fig, (ax1,ax2) = plt.subplots(nrows=1, ncols=2)
68 fig.set_size_inches(10, 6)
69 ax1.plot(temperature, lengthvstemp)
70 ax1.grid(True)
71 ax1.set_xlabel('Temperature($^\circ$C)')
72 ax1.set_ylabel('Infiltration length (mm)')
73 ax1.set_title('(a)')
74 ax2.plot(conc, lengthvsconc)
75 ax2.set_xlabel('Concentration of Si')
76 ax2.grid(True)
77 ax2.set_title('(b)')
78 plt.savefig('model_microchannel_infiltration.png',transparent=1)
79 # plot preform
80 n=2
81 lengthvstemp=[]
82 temperature=np.arange(1500,1800,5)
83 for temp in temperature:
84     lengthvstemp.append(infiltration_length_SiZr_preform(0.9,temp,0.5,n))
85 #infiltration length vs concentration
86 lengthvsconc=[]
87 conc=np.arange(.5,1,0.01)
88 for c in conc:
89     lengthvsconc.append(infiltration_length_SiZr_preform(c,1500,0.5,n))
90 fig, (ax1,ax2) = plt.subplots(nrows=1, ncols=2)
91 fig.set_size_inches(10, 6)
92 ax1.plot(temperature, lengthvstemp)
93 ax1.grid(True)
94 ax1.set_xlabel('Temperature($^\circ$C)')
95 ax1.set_ylabel('Infiltration length (mm)')
96 ax1.set_title('(a)')
97 ax2.plot(conc, lengthvsconc)
98 ax2.set_xlabel('Concentration of Si')
99 ax2.grid(True)
100 ax2.set_title('(b)')
101 plt.savefig('model_preform_infiltration.png',transparent=1)

```

Listing A.3 – Differential non-isothermal infiltration length model

```

1 # -*- coding: utf-8 -*-
2 """
3 @author: manoj
4 """
5 import math
6 import matplotlib.pyplot as plt

```

```

7 import numpy as np
8 #constants
9 molar_volume_SiC = 1.25e-5 #m^3/mol Calculated from
    density and molecular mass from Pubchem
10 molar_volume_liquid = 1.31e-5 #m^3/mol CODATA Si=12.01,
    Zr=14.02
11 universal_gas_constant=8.3145
12 diffusion_Si_liq = 15e-9 # 8e3 m^2/s Birnie 1986 #
    Pommrich 2008, Jingyu Qin 2019
13 triple_line_velocity= 2e-4 #m/s Giuranno 2020
14 activation_energy_SiC =200e3 #J/mol Dezellus 2002
15 activation_energy_triple_line=185e3 #assumption
16 activation_energy_diffusion=28e3 # 850e3 J/mol Birnie 1986 #
    Pommrich 2008
17 # calculation for triple line velocity prefactor
18 triple_line_velocity_prefactor=triple_line_velocity/(math.exp(-
    activation_energy_triple_line/(universal_gas_constant*1773)))
19 print(triple_line_velocity_prefactor)
20 #calculation for thickness_SiC_prefactor
21 known_thickness_SiC=1e-6 #m
22 known_time=900 #s
23 known_temperature=1773 #K
24 thickness_SiC_prefactor=known_thickness_SiC/(math.exp(-
    activation_energy_SiC/(universal_gas_constant*known_temperature))*math.
    pow(known_time,1/2))
25 # thickness_SiC_prefactor=0.3
26 print (thickness_SiC_prefactor)
27 #Critical Si calculation , 27.8 Zr at 1500 deg C, 43.6 Zr at 1620
28 def critical_Si(temperature):
29     return 0.72 if temperature<=1620 else 0.564
30 # infiltration length calcuclation
31 def infiltration_length_SiZr(C_Si_initial, temperature,
    microchannel_thickness,order_n):
32     n=order_n
33     T=temperature +273
34     e=microchannel_thickness*1e-6 #micrometer to m
35     C_Si_crit= critical_Si(temperature) # 80% of solid phase at
    1500 deg C - 0.34 Si2Zr line
36     if C_Si_initial<=C_Si_crit:
37         L=0
38     else:
39         L=math.pow(((C_Si_initial-C_Si_crit)*molar_volume_SiC*e*math.pow(
            diffusion_Si_liq,(n-1)/(2*n)))/((1-C_Si_initial)*molar_volume_liquid*2*
            thickness_SiC_prefactor*math.pow(triple_line_velocity_prefactor,(n-3)
            /(2*n))))*math.exp((2*n*activation_energy_SiC-(n-1)*
            activation_energy_diffusion-(3-n)*activation_energy_triple_line)/(2*n*
            universal_gas_constant*T)),(2*n/(n+1)))
40
41     return L *1000
42 def infiltration_length_SiZr_preform(C_Si_initial, temperature,
    effective_radius,order_n):
43     n=order_n

```

```

44     T=temperature +273
45     e=effective_radius*1e-6                                     #micrometer to m
46     C_Si_crit= critical_Si(temperature)                         # 80% of solid phase
47     at 1500 deg C - 0.34 Si2Zr line
48     local_surface_inclination_factor=1/3                       #assumption
49     SiC_presence_compensation=0.5                              #assumption
50     if C_Si_initial<=C_Si_crit:
51         L=0
52     else:
53         L=math.pow(((C_Si_initial-C_Si_crit)*molar_volume_SiC*e*math.pow(
54             diffusion_Si_liq,(n-1)/(2*n))/((1-C_Si_initial)*molar_volume_liquid*2*
55             SiC_presence_compensation*math.pow(local_surface_inclination_factor,((n
56             -3)/(2*n))))*thickness_SiC_prefactor*math.pow(
57             triple_line_velocity_prefactor,(n-3)/(2*n))))*math.exp((2*n*
58             activation_energy_SiC-(n-1)*activation_energy_diffusion-(3-n)*
59             activation_energy_triple_line)/(2*n*universal_gas_constant*T)),(2*n/(n
60             +1)))
61     return L*1000
62 #plots microchannel
63 #infiltration length vs temperature
64 n=2
65 lengthvstemp=[]
66 temperature=np.arange(1500,1800,5)
67 for temp in temperature:
68     lengthvstemp.append(infiltration_length_SiZr(0.9,temp,10,n))
69 #infiltration length vs concentration
70 lengthvsconc=[]
71 conc=np.arange(.5,1,0.01)
72 for c in conc:
73     lengthvsconc.append(infiltration_length_SiZr(c,1500,10,n))
74 plt.style.use('classic')
75 fig, (ax1,ax2) = plt.subplots(nrows=1, ncols=2)
76 fig.set_size_inches(10, 6)
77 ax1.plot(temperature, lengthvstemp)
78 ax1.grid(True)
79 ax1.set_xlabel('Temperature($^\circ$C)')
80 ax1.set_ylabel('Infiltration length (mm)')
81 ax1.set_title('(a)')
82 ax2.plot(conc, lengthvsconc)
83 ax2.set_xlabel('Concentration of Si')
84 ax2.grid(True)
85 ax2.set_title('(b)')
86 plt.savefig('model_microchannel_infiltration.png',transparent=1)
87 # plot preform
88 n=2
89 lengthvstemp=[]
90 temperature=np.arange(1500,1800,5)
91 for temp in temperature:
92     lengthvstemp.append(infiltration_length_SiZr_preform(0.9,temp,0.5,n))
93 #infiltration length vs concentration
94 lengthvsconc=[]
95 conc=np.arange(.5,1,0.01)

```

```
88 for c in conc:
89     lengthvsconc.append(infiltration_length_SiZr_preform(c,1500,0.5,n))
90 fig, (ax1,ax2) = plt.subplots(nrows=1, ncols=2)
91 fig.set_size_inches(10, 6)
92 ax1.plot(temperature, lengthvstemp)
93 ax1.grid(True)
94 ax1.set_xlabel('Temperature($^\circ$C)')
95 ax1.set_ylabel('Infiltration length (mm)')
96 ax1.set_title('(a)')
97 ax2.plot(conc, lengthvsconc)
98 ax2.set_xlabel('Concentration of Si')
99 ax2.grid(True)
100 ax2.set_title('(b)')
101 plt.savefig('model_preform_infiltration.png',transparent=1)
```

This page is intentionally left blank.

## Bibliography

- [1] D. Aleksendrić and P. Carlone, “Introduction to composite materials”, in *Soft Computing in the Design and Manufacturing of Composite Materials*, D. Aleksendrić and P. Carlone, Eds. Oxford: Woodhead Publishing, 2015, pp. 1–5, ISBN: 9781782421795. DOI: 10.1533/9781782421801.1.
- [2] K. K. Chawla, *Ceramic Matrix Composites*. 1993, ISBN: 9781475722185. DOI: 10.1007/978-1-4757-2216-1.
- [3] N. P. Bansal and J. Lamon, *Ceramic matrix composites : materials, modeling and technology*. 2015, ISBN: 9781118832899.
- [4] S. Hampshire, *Non-Oxide Technical and Engineering Ceramics*. Name Springer, Dordrecht, 1987, ISBN: 9789401080316. DOI: 10.1007/978-94-009-3423-8.
- [5] M. Bengisu, *Engineering Ceramics*, ser. Engineering Materials. Springer, Berlin, Heidelberg, 2001, ISBN: 9783642087196. DOI: 10.1007/978-3-662-04350-9.
- [6] A. H. Cowles and E. H. Cowles, “Electric smelting furnace”, Patent U.S.319945, 1885.
- [7] E. G. Acheson, “Carborundum: its history, manufacture and uses”, *Journal of the Franklin Institute*, vol. 136, no. 4, pp. 279–289, 1893, ISSN: 0016-0032. DOI: 10.1016/0016-0032(93)90369-6.
- [8] E. G. Acheson, “Production of artificial, crystalline carbonaceous material”, Patent US492767A, 1893.
- [9] N. P. Bansal, *Handbook of Ceramic Composites*. Springer US, 2006, ISBN: 9780387239866.
- [10] M. Belmonte, “Advanced ceramic materials for high temperature applications”, *Advanced Engineering Materials*, vol. 8, no. 8, pp. 693–703, Aug. 2006, ISSN: 1438-1656. DOI: 10.1002/adem.200500269.
- [11] Y. D. Blum, J. Marschall, D. Hui, and S. Young, “Thick protective uhtc coatings for SiC-based structures: process establishment”, *Journal of the American Ceramic Society*, vol. 91, no. 5, pp. 1453–1460, May 2008. DOI: 10.1111/j.1551-2916.2008.02360.x.
- [12] O. P. Chakrabarti and P. K. Das, “High temperature load–deflection behaviour of reaction bonded SiC (RBSC)”, *Ceramics International*, vol. 27, no. 5, pp. 559–563, 2001, ISSN: 0272-8842. DOI: 10.1016/S0272-8842(00)00120-6.

- [13] N. S. Jacobson, "Corrosion of silicon-based ceramics in combustion environments", *Journal of the American Ceramic Society*, vol. 76, no. 1, pp. 3–28, Jan. 1993, ISSN: 0002-7820. DOI: 10.1111/j.1151-2916.1993.tb03684.x.
- [14] N. S. Jacobson and D. L. Myers, "Active oxidation of SiC", *Oxidation of Metals*, vol. 75, no. 1-2, pp. 1–25, 2010, ISSN: 0030-770X 1573-4889. DOI: 10.1007/s11085-010-9216-4.
- [15] N. Jacobson, B. Harder, D. Myers, and M. Cinibulk, "Oxidation transitions for SiC part i. active-to-passive transitions", *Journal of the American Ceramic Society*, vol. 96, no. 3, pp. 838–844, 2013, ISSN: 0002-7820. DOI: 10.1111/jace.12108.
- [16] J. Magnant, L. Maillé, R. Paillet, J.-C. Ichard, A. Guette, F. Rebillat, and E. Philippe, "Carbon fiber/reaction-bonded carbide matrix for composite materials – manufacture and characterization", *Journal of the European Ceramic Society*, vol. 32, no. 16, pp. 4497–4505, 2012, ISSN: 0955-2219. DOI: 10.1016/j.jeurceramsoc.2012.06.009.
- [17] N. D. Shcherban, "Review on synthesis, structure, physical and chemical properties and functional characteristics of porous silicon carbide", *Journal of Industrial and Engineering Chemistry*, vol. 50, pp. 15–28, Jun. 2017, ISSN: 1226-086X. DOI: 10.1016/j.jiec.2017.02.002.
- [18] E. P. Simonenko, D. V. Sevast'yanov, N. P. Simonenko, V. G. Sevast'yanov, and N. T. Kuznetsov, "Promising ultra-high-temperature ceramic materials for aerospace applications", *Russian Journal of Inorganic Chemistry*, vol. 58, no. 14, pp. 1669–1693, Dec. 2013, ISSN: 0036-0236. DOI: 10.1134/s0036023613140039.
- [19] R. Naslain, "Design, preparation and properties of non-oxide CMCs for application in engines and nuclear reactors: an overview", *Composites Science and Technology*, vol. 64, no. 2, pp. 155–170, 2004, ISSN: 0266-3538. DOI: 10.1016/s0266-3538(03)00230-6.
- [20] W. J. Choyke, H. Matsunami, and G. Pensl, *Silicon carbide: recent major advances*, ser. Advanced Texts in Physics. Springer Science & Business Media, 2004, ISBN: 3642188702. DOI: 10.1007/978-3-642-18870-1.
- [21] V. A. Izhevskiy, L. A. Genova, J. C. Bressiani, and A. H. A. Bressiani, "Review article: silicon carbide. structure, properties and processing", *Cerâmica*, vol. 46, pp. 4–13, 2000, ISSN: 0366-6913.
- [22] N. W. Jepps and T. F. Page, "Polytypic transformations in silicon carbide", *Progress in Crystal Growth and Characterization*, vol. 7, no. 1-4, pp. 259–307, 1983, ISSN: 0146-3535. DOI: 10.1016/0146-3535(83)90034-5.
- [23] H. Matsunami, "Chemical vapor epitaxy of silicon carbide", in *Encyclopedia of Materials: Science and Technology*, K. H. J. Buschow, R. W. Cahn, M. C. Flemings, B. Ilschner, E. J. Kramer, S. Mahajan, and P. Veyssi re, Eds. Oxford: Elsevier, 2001, pp. 1192–1197, ISBN: 9780080431529. DOI: 10.1016/b0-08-043152-6/00223-0.
- [24] A. L. Ortiz, F. S nchez-Bajo, F. L. Cumbre ra, and F. Guiberteau, "The prolific polytypism of silicon carbide", *Journal of Applied Crystallography*, vol. 46, no. 1, pp. 242–247, 2013, ISSN: 0021-8898. DOI: 10.1107/s0021889812049151.

- [25] S. Sömiya and Y. Inomata, *Silicon Carbide Ceramics—1*. Name Springer, Dordrecht, 1991, ISBN: 9781851665600. DOI: 10.1007/978-94-011-3842-0.
- [26] M. Nader, F. Aldinger, and M. J. Hoffmann, “Influence of the  $\alpha/\beta$ -SiC phase transformation on microstructural development and mechanical properties of liquid phase sintered silicon carbide”, *Journal of Materials Science*, vol. 34, no. 6, pp. 1197–1204, 1999, ISSN: 0022-2461. DOI: 10.1023/a:1004552704872.
- [27] P. Eveno, J. Li, A. M. Huntz, and J. Chaumont, “Diffusion of C-13 and Si-29 implanted ions in SiC”, *Materials Science and Engineering B-Solid State Materials for Advanced Technology*, vol. 11, no. 1-4, pp. 331–336, Jan. 1992, ISSN: 0921-5107. DOI: 10.1016/0921-5107(92)90235-2.
- [28] M. H. Hon and R. F. Davis, “Self-diffusion of  $^{14}\text{C}$  in polycrystalline  $\beta$ -SiC”, *Journal of Materials Science*, vol. 14, no. 10, pp. 2411–2421, Oct. 1979. DOI: 10.1007/bf00737031.
- [29] F. F. Lange and T. K. Gupta, “Sintering of SiC with Boron compounds”, *Journal of the American Ceramic Society*, vol. 59, no. 11-12, pp. 537–538, 1976, ISSN: 0002-7820. DOI: 10.1111/j.1151-2916.1976.tb09435.x.
- [30] S. Prochazka, “Special ceramics 6”, *British Ceramic Res. Assoc., Stoke-on-Trent*, pp. 171–181, 1975.
- [31] N. L. Hecht, D. E. McCullum, and G. A. Graves, “Investigation of selected silicon nitride and silicon carbide ceramics”, in *12th Annual Conference on Composites and Advanced Ceramic Materials, Part 2 of 2: Ceramic Engineering and Science Proceedings, Volume 9, Issue 9/10*, ser. Ceramic Engineering and Science Proceedings. 1988, pp. 1313–1332, ISBN: 9780470310502. DOI: 10.1002/9780470310502.ch26.
- [32] D. E. McCullum, N. L. Hecht, L. Chuck, and S. M. Goodrich, “Summary of results of the effects of environment on mechanical behavior of high-performance ceramics”, in *Proceedings of the 15th Annual Conference on Composites and Advanced Ceramic Materials, Part 2 of 2: Ceramic Engineering and Science Proceedings, Volume 12, Issue 9/10*, ser. Ceramic Engineering and Science Proceedings. 1991, pp. 1886–1913, ISBN: 9780470313848. DOI: 10.1002/9780470313848.ch20.
- [33] G. R. Anstis, P. Chantikul, B. R. Lawn, and D. B. Marshall, “A critical evaluation of indentation techniques for measuring fracture toughness: i, direct crack measurements”, *Journal of the American Ceramic Society*, vol. 64, no. 9, pp. 533–538, 1981, ISSN: 0002-7820 1551-2916. DOI: 10.1111/j.1151-2916.1981.tb10320.x.
- [34] K. Suzuki and M. Sasaki, *Fundamental Structural Ceramics*. Terra Scientific Publishing Company, Tokyo, Japan, 1987.
- [35] C. A. Handwerker, J. E. Blendell, and W. Kaysser, *Sintering of advanced ceramics*, ser. Conference: 90. annual meeting of the American Ceramic Society, Cincinnati, OH (USA), 1-5 May 1988; Related Information: Ceramic transactions. Columbus, OH (USA); American Ceramic Society Inc.; None, 1990, p. 789, ISBN: 0-944904-20-3.



- [36] D. H. Kim, C. W. Jang, B. H. Park, and S. Baik, "Pressureless-sintering of silicon carbide with additions of yttria and alumina", *Journal of the Korean Ceramic Society*, vol. 26, no. 2, pp. 228–34, 1989.
- [37] M. A. Mulla and V. D. Krstic, "Low-temperature pressureless sintering of  $\beta$ -silicon carbide with aluminum oxide and yttrium oxide additions", *American Ceramic Society Bulletin*, vol. 70, no. 3, pp. 439–443, 1991, ISSN: 0002-7812.
- [38] M. Omori, H. Takei, and M. Omori, "Method of preparing sintered shapes of silicon carbide", Patent US4564490A, 1986.
- [39] R. Ruh and A. Zangvil, "Composition and properties of hot-pressed SiC-AlN solid solutions", *Journal of the American Ceramic Society*, vol. 65, no. 5, pp. 260–265, May 1982, ISSN: 0002-7820. DOI: 10.1111/j.1151-2916.1982.tb10429.x.
- [40] V. J. Tennery, *Ceramic materials and components for engines; Proceedings of the Third International Symposium, Las Vegas, NV, Nov. 27-30, 1988*, ser. Conference: 3. international symposium on ceramic materials and components for engines, Las Vegas, NV (USA), 27-30 Nov 1988. Westerville, OH (US); American Ceramic Society, Inc.; None, 1989.
- [41] A. O. Konstantinov, C. I. Harris, A. Henry, and E. Janzén, "Fabrication and properties of high-resistivity porous silicon carbide for SiC power device passivation", *Materials Science and Engineering: B*, vol. 29, no. 1-3, pp. 114–117, Jan. 1995, ISSN: 0921-5107. DOI: 10.1016/0921-5107(94)04009-s.
- [42] K. Koumoto, M. Shimohigoshi, S. Takeda, and H. Yanagida, "Thermoelectric energy-conversion by porous SiC ceramics", *Journal of Materials Science Letters*, vol. 6, no. 12, pp. 1453–1455, 1987, ISSN: 0261-8028. DOI: 10.1007/Bf01689320.
- [43] T. Matsumoto, J. Takahashi, T. Tamaki, T. Futagi, H. Mimura, and Y. Kanemitsu, "Blue-green luminescence from porous silicon carbide", *Applied Physics Letters*, vol. 64, no. 2, p. 226, Jan. 1994, ISSN: 0003-6951. DOI: 10.1063/1.111979.
- [44] H. Suda, H. Yamauchi, Y. Uchimarui, I. Fujiwara, and K. Haraya, "Preparation and gas permeation properties of silicon carbide-based inorganic membranes for hydrogen separation", *Desalination*, vol. 193, no. 1-3, pp. 252–255, 2006, ISSN: 0011-9164. DOI: 10.1016/j.desal.2005.04.143.
- [45] T. E. Wilkes, M. L. Young, R. E. Sepulveda, D. C. Dunand, and K. T. Faber, "Composites by aluminum infiltration of porous silicon carbide derived from wood precursors", *Scripta Materialia*, vol. 55, no. 12, pp. 1083–1086, Dec. 2006, ISSN: 1359-6462. DOI: 10.1016/j.scriptamat.2006.08.040.
- [46] J.-H. Eom, Y.-W. Kim, and S. Raju, "Processing and properties of macroporous silicon carbide ceramics: a review", *Journal of Asian Ceramic Societies*, vol. 1, no. 3, pp. 220–242, 2013, ISSN: 2187-0764. DOI: 10.1016/j.jascer.2013.07.003.

- [47] W. B. Hillig, R. L. Mehan, C. R. Morelock, V. J. Decarlo, and W. Laskow, "Silicon-silicon carbide composites", *American Ceramic Society Bulletin*, vol. 54, no. 12, pp. 1054–1056, 1975, ISSN: 0002-7812.
- [48] G. S. Corman and K. L. Luthra, "Silicon melt infiltrated ceramic composites (HiPer-Comp™)", in *Handbook of Ceramic Composites*, N. P. Bansal, Ed. Boston, MA: Springer US, 2005, ch. Chapter 5, pp. 99–115, ISBN: 978-0-387-23986-6. DOI: 10.1007/0-387-23986-3\_5.
- [49] G. Bianchi, P. Vavassori, B. Vila, G. Annino, M. Nagliati, M. Mallah, S. Gianella, M. Valle, M. Orlandi, and A. Ortona, "Reactive silicon infiltration of carbon bonded preforms embedded in powder field modifiers heated by microwaves", *Ceramics International*, vol. 41, no. 9, pp. 12 439–12 446, 2015, ISSN: 0272-8842. DOI: 10.1016/j.ceramint.2015.06.087.
- [50] W. Krenkel and F. Berndt, "C/C-SiC composites for space applications and advanced friction systems", *Materials Science and Engineering a-Structural Materials Properties Microstructure and Processing*, vol. 412, no. 1-2, pp. 177–181, 2005, ISSN: 0921-5093. DOI: 10.1016/j.msea.2005.08.204.
- [51] W. Krenkel, B. Heidenreich, and R. Renz, "C/C-SiC composites for advanced friction systems", *Advanced Engineering Materials*, vol. 4, no. 7, pp. 427–436, Jul. 2002, ISSN: 1438-1656. DOI: 10.1002/1527-2648(20020717)4:7<427::AID-ADEM427>3.0.CO;2-C.
- [52] W. Krenkel, "Cost effective processing of CMC composites by melt infiltration (LSI-Process)", in *25th Annual Conference on Composites, Advanced Ceramics, Materials, and Structures: A: Ceramic Engineering and Science Proceedings, Volume 22, Issue 3*, ser. Ceramic Engineering and Science Proceedings. John Wiley & Sons, Inc., 2001, pp. 443–454, ISBN: 9780470294680. DOI: 10.1002/9780470294680.ch52.
- [53] Y. Xu, L. Cheng, and L. Zhang, "Carbon/silicon carbide composites prepared by chemical vapor infiltration combined with silicon melt infiltration", *Carbon*, vol. 37, no. 8, pp. 1179–1187, 1999, ISSN: 0008-6223. DOI: 10.1016/S0008-6223(98)00310-8.
- [54] M. Patel, K. Saurabh, V. V. B. Prasad, and J. Subrahmanyam, "High temperature C/C-SiC composite by liquid silicon infiltration: a literature review", *Bulletin of Materials Science*, vol. 35, no. 1, pp. 63–73, 2012, ISSN: 0250-4707 0973-7669. DOI: 10.1007/s12034-011-0247-5.
- [55] J. C. Margiotta, D. J. Zhang, and D. C. Nagle, "Microstructural evolution during silicon carbide (SiC) formation by liquid silicon infiltration using optical microscopy", *International Journal of Refractory Metals & Hard Materials*, vol. 28, no. 2, pp. 191–197, 2010, ISSN: 0263-4368. DOI: 10.1016/j.ijrmhm.2009.09.002.
- [56] M. W. Chase, *NIST-JANAF Thermochemical tables fourth edition (Journal of physical and chemical reference data)*. American Institute of Physics for the National Institute of Standards and Technology, 1998, ISBN: 9781563968204.

- [57] S. Kumar, A. Kumar, R. Devi, A. Shukla, and A. K. Gupta, "Capillary infiltration studies of liquids into 3d-stitched C-C preforms part b: kinetics of silicon infiltration", *Journal of the European Ceramic Society*, vol. 29, no. 12, pp. 2651–2657, 2009, ISSN: 0955-2219. DOI: 10.1016/j.jeurceramsoc.2009.03.006.
- [58] S. Kumar, A. Kumar, A. Shukla, G. R. Devi, and A. K. Gupta, "Thermal-diffusivity measurement of 3d-stitched C-SiC composites", *Journal of the European Ceramic Society*, vol. 29, no. 3, pp. 489–495, 2009, ISSN: 0955-2219. DOI: 10.1016/j.jeurceramsoc.2008.06.028.
- [59] P. Sangsuwan, J. A. Orejas, J. E. Gatica, S. N. Tewari, and M. Singh, "Reaction-bonded silicon carbide by reactive infiltration", *Industrial & Engineering Chemistry Research*, vol. 40, no. 23, pp. 5191–5198, 2001, ISSN: 0888-5885. DOI: 10.1021/ie001029e.
- [60] A. A. Galiguzov, A. M. Kenigfest, A. P. Malakho, A. N. Seleznev, and V. V. Avdeev, "Study of process of erosion of various types of carbon fibres by molten silicon", *Fibre Chemistry*, vol. 44, no. 2, pp. 101–105, 2012, ISSN: 0015-0541. DOI: 10.1007/s10692-012-9407-7.
- [61] V. Bougiouri, R. Voytovych, N. Rojo-Calderon, J. Narciso, and N. Eustathopoulos, "The role of the chemical reaction in the infiltration of porous carbon by NiSi alloys", *Scripta Materialia*, vol. 54, no. 11, pp. 1875–1878, 2006, ISSN: 1359-6462. DOI: 10.1016/j.scriptamat.2006.02.015.
- [62] R. Voytovych, V. Bougiouri, N. R. Calderon, J. Narciso, and N. Eustathopoulos, "Reactive infiltration of porous graphite by nisi alloys", *Acta Materialia*, vol. 56, no. 10, pp. 2237–2246, 2008, ISSN: 1359-6454. DOI: 10.1016/j.actamat.2008.01.011.
- [63] Y. G. Tong, S. X. Bai, and K. Chen, "C/C-ZrC composite prepared by chemical vapor infiltration combined with alloyed reactive melt infiltration", *Ceramics International*, vol. 38, no. 7, pp. 5723–5730, 2012, ISSN: 0272-8842. DOI: 10.1016/j.ceramint.2012.04.017.
- [64] Y. Tong, Z. Cai, S. Bai, Y. Hu, M. Hua, W. Xie, Y. Ye, and Y. Li, "Microstructures and properties of Si-Zr alloy based CMCs reinforced by various porous C/C performs", *Ceramics International*, vol. 44, no. 14, pp. 16 577–16 582, 2018, ISSN: 02728842. DOI: 10.1016/j.ceramint.2018.06.081.
- [65] Y. Tong, S. Bai, H. Zhang, and K. Chen, "C/C-SiC composite prepared by Si-10Zr alloyed melt infiltration", *Ceramics International*, vol. 38, no. 4, pp. 3301–3307, 2012, ISSN: 0272-8842. DOI: 10.1016/j.ceramint.2011.12.038.
- [66] R. P. Messner and Y.-M. Chiang, "Liquid-phase reaction-bonding of silicon carbide using alloyed silicon-molybdenum melts", *Journal of the American Ceramic Society*, vol. 73, no. 5, pp. 1193–1200, 1990, ISSN: 1551-2916. DOI: 10.1111/j.1151-2916.1990.tb05179.x.
- [67] Y. G. Wang, X. J. Zhu, L. T. Zhang, and L. F. Cheng, "C/C-SiC-ZrC composites fabricated by reactive melt infiltration with Si<sub>0.87</sub>Zr<sub>0.13</sub> alloy", *Ceramics International*, vol. 38, no. 5, pp. 4337–4343, 2012, ISSN: 0272-8842. DOI: 10.1016/j.ceramint.2012.02.016.

- [68] Y. M. Chiang and R. P. Messner, "Method of preparing refractory silicon carbide composites and coatings", Patent US5079195A, 1992.
- [69] M. Singh and D. R. Behrendt, "Reactive melt infiltration of silicon-molybdenum alloys into microporous carbon preforms", *Materials Science and Engineering a-Structural Materials Properties Microstructure and Processing*, vol. 194, no. 2, pp. 193–200, 1995, ISSN: 0921-5093. DOI: 10.1016/0921-5093(94)09663-5.
- [70] M. Singh and D. R. Behrendt, "Studies on the reactive melt infiltration of silicon and silicon-molybdenum alloys in porous carbon", NASA Lewis Research Center; Cleveland, OH, United States, Report, 1992.
- [71] M. Hansen and K. Anderko, *Constitution of binary alloys, SECOND EDITION*. New York: McGraw Hill Book Company, 1958, ISBN: 9780070260504.
- [72] O. Chakrabarti and P. K. Das, "Reactive infiltration of Si-Mo alloyed melt into carbonaceous preforms of silicon carbide", *Journal of the American Ceramic Society*, vol. 83, no. 6, pp. 1548–1550, 2000, ISSN: 0002-7820. DOI: 10.1111/j.1151-2916.2000.tb01430.x.
- [73] S. Meier and J. G. Heinrich, "Processing-microstructure-properties relationships of MoSi<sub>2</sub>-SiC composites", *Journal of the European Ceramic Society*, vol. 22, no. 13, pp. 2357–2363, Dec. 2002, ISSN: 0955-2219. DOI: 10.1016/S0955-2219(02)00035-3.
- [74] Z. Hao, W. Sun, X. Xiong, Y. Xu, Y. Chang, Z. Peng, Z. Chen, and Y. Wang, "Comparison of microstructure and ablation behavior of Si-Mo-Ti/Al/Zr infiltrated C/C composites prepared at different infiltration temperature", *Ceramics International*, vol. 43, no. 2, pp. 2765–2773, 2017, ISSN: 0272-8842. DOI: 10.1016/j.ceramint.2016.11.107.
- [75] R. B. Reitz, F. W. Zok, and C. G. Levi, "Reactive alloy melt infiltration for SiC composite matrices: mechanistic insights", *Journal of the American Ceramic Society*, vol. 100, no. 12, pp. 5471–5481, 2017, ISSN: 0002-7820. DOI: 10.1111/jace.15167.
- [76] M. Singh and D. R. Behrendt, "Reactive melt infiltration of silicon-niobium alloys in microporous carbons", *Materials Research Society*, vol. 9, no. 07, pp. 1701–1708, 1994, ISSN: 0884-2914. DOI: 10.1557/jmr.1994.1701.
- [77] T. Aoki, T. Ogasawara, Y. Okubo, K. Yoshida, and T. Yano, "Fabrication and properties of Si-Hf alloy melt-infiltrated tyranno ZMI fiber/SiC-based matrix composites", *Composites Part A: Applied Science and Manufacturing*, vol. 66, pp. 155–162, 2014, ISSN: 1359-835X. DOI: 10.1016/j.compositesa.2014.07.009.
- [78] T. Aoki and T. Ogasawara, "Tyranno ZMI fiber/TiSi<sub>2</sub>-Si matrix composites for high-temperature structural applications", *Composites Part A: Applied Science and Manufacturing*, vol. 76, pp. 102–109, 2015, ISSN: 1359-835X. DOI: 10.1016/j.compositesa.2015.05.018.
- [79] A. J. Whitehead and T. F. Page, "Fabrication and characterization of some novel reaction-bonded silicon carbide materials", *Journal of Materials Science*, vol. 27, no. 3, pp. 839–852, 1992, ISSN: 0022-2461 1573-4803. DOI: 10.1007/bf02403904.

- [80] Y. G. Wang, X. J. Zhu, L. T. Zhang, and L. F. Cheng, "Reaction kinetics and ablation properties of C/C-ZrC composites fabricated by reactive melt infiltration", *Ceramics International*, vol. 37, no. 4, pp. 1277–1283, 2011, ISSN: 0272-8842. DOI: 10.1016/j.ceramint.2010.12.002.
- [81] A. J. Deutsch, "The abundance of the elements", *Scientific American*, vol. 183, no. 4, pp. 14–17, 1950, ISSN: 00368733, 19467087.
- [82] M. J. Assael, I. J. Armyra, J. Brillo, S. V. Stankus, J. Wu, and W. A. Wakeham, "Reference data for the density and viscosity of liquid cadmium, cobalt, gallium, indium, mercury, silicon, thallium, and zinc", *Journal of Physical and Chemical Reference Data*, vol. 41, no. 3, p. 033 101, 2012, ISSN: 0047-2689. DOI: 10.1063/1.4729873.
- [83] R. A. Logan and W. L. Bond, "Density change in silicon upon melting", *Journal of Applied Physics*, vol. 30, no. 3, pp. 322–322, 1959. DOI: 10.1063/1.1735159.
- [84] V. M. Glazov and O. D. Shchelikov, "Volume changes during melting and heating of silicon and germanium melts", *High Temperature*, vol. 38, no. 3, pp. 405–412, 2000, ISSN: 1608-3156. DOI: 10.1007/BF02756000.
- [85] H. Sasaki, E. Tokizaki, K. Terashima, and S. Kimura, "Density variation of molten silicon measured by an improved archimedian method", *Japanese Journal of Applied Physics*, vol. 33, no. Part 1, No. 7A, pp. 3803–3807, 1994, ISSN: 0021-4922 1347-4065. DOI: 10.1143/jjap.33.3803.
- [86] M. Langen, T. Hibiya, M. Eguchi, and I. Egry, "Measurement of the density and the thermal expansion coefficient of molten silicon using electromagnetic levitation", *Journal of Crystal Growth*, vol. 186, no. 4, pp. 550–556, 1998, ISSN: 0022-0248. DOI: Doi10.1016/S0022-0248(97)00619-2.
- [87] W. K. Rhim, S. K. Chung, A. J. Rulison, and R. E. Spjut, "Measurements of thermo-physical properties of molten silicon by a high-temperature electrostatic levitator", *International Journal of Thermophysics*, vol. 18, no. 2, pp. 459–469, 1997. DOI: 10.1007/BF02575175.
- [88] W.-K. Rhim and K. Ohsaka, "Thermophysical properties measurement of molten silicon by high-temperature electrostatic levitator: density, volume expansion, specific heat capacity, emissivity, surface tension and viscosity", *Journal of crystal growth*, vol. 208, no. 1-4, pp. 313–321, 2000, ISSN: 0022-0248. DOI: Doi10.1016/S0022-0248(99)00437-6.
- [89] C. Wagner, "Passivity during the oxidation of silicon at elevated temperatures", *Journal of Applied Physics*, vol. 29, no. 9, pp. 1295–1297, 1958, ISSN: 0021-8979. DOI: 10.1063/1.1723429.
- [90] B. Drevet and N. Eustathopoulos, "Wetting of ceramics by molten silicon and silicon alloys: a review", *Journal of Materials Science*, vol. 47, no. 24, pp. 8247–8260, 2012, ISSN: 0022-2461 1573-4803. DOI: 10.1007/s10853-012-6663-0.
- [91] J. N. Israelachvili, *Intermolecular and surface forces*. Academic press, 2015, ISBN: 0080923631. DOI: 10.1016/C2009-0-21560-1.

- [92] R. Israel, "Etude des interactions entre silicium liquide et graphite pour application à l'élaboration du silicium photovoltaïque", Theses, Institut National Polytechnique de Grenoble - INPG, Sep. 2009.
- [93] O. Maillart, F. Hodaj, V. Chaumat, and N. Eustathopoulos, "Influence of oxygen partial pressure on the wetting of SiC by a Co-Si alloy", *Materials Science and Engineering a-Structural Materials Properties Microstructure and Processing*, vol. 495, no. 1-2, pp. 174–180, 2008, ISSN: 0921-5093. DOI: 10.1016/j.msea.2007.11.090.
- [94] P. H. Keck and W. Van Horn, "The surface tension of liquid silicon and germanium", *Physical Review*, vol. 91, no. 3, p. 512, 1953.
- [95] B. J. Keene, "A review of the surface tension of silicon and its binary alloys with reference to marangoni flow", *Surface and Interface Analysis*, vol. 10, no. 8, pp. 367–383, 1987, ISSN: 0142-2421. DOI: 10.1002/sia.740100802.
- [96] N. K. Dzhemilev, S. I. Popel, and B. V. Tsarevskii, "Isotherm of the density and surface tension of iron–silicon melts", *Fiz. Met. Metalloved*, vol. 18, no. 1, pp. 83–87, 1964.
- [97] E. S. Levin, P. V. Geld, and B. A. Baum, "Effect of temperature and composition on density and surface energy of silicon-iron melts", *Russian Journal of Physical Chemistry, USSR*, vol. 40, no. 11, p. 1455, 1966, ISSN: 0036-0244.
- [98] W. D. Kingery and M. Humenik Jr, "Surface tension at elevated temperatures. i. furnace and method for use of the sessile drop method; surface tension of silicon, iron and nickel", *The Journal of Physical Chemistry*, vol. 57, no. 3, pp. 359–363, 1953, ISSN: 0022-3654.
- [99] F. N. Tavadze, M. G. Kekus, D. V. Khantadze, and T. G. Tsverdvase, *Poverkh yavleniya rasp., ed. by vn eremenko (in russian)*, Journal Article, 1968.
- [100] V. P. Elyutin, V. I. Kostikov, and V. Y. Levin, "Si-zr, in fiz. khim. poverkh yavleni rasp. (ed.) v. n. eremenko", *Naukova Dumka, Kiev (in Russian)*, pp. 153–156, 1971.
- [101] Y. V. Naidich, V. M. Perevertailo, and L. P. Obushchak, "Density and surface tension of alloys of the systems Au-Si and Au-Ge", *Soviet Powder Metallurgy and Metal Ceramics*, vol. 14, no. 5, pp. 403–404, 1975, ISSN: 0038-5735. DOI: 10.1007/bf00807814.
- [102] S. V. Lukin, V. I. Zhuchkov, N. A. Vatolin, and Y. S. Kozlov, "The physicochemical properties of si-b alloys", *Journal of the Less Common Metals*, vol. 67, no. 2, pp. 407–413, 1979, ISSN: 0022-5088. DOI: 10.1016/0022-5088(79)90019-5.
- [103] S. C. Hardy, "The surface tension of liquid silicon", *Journal of crystal growth*, vol. 69, no. 2-3, pp. 456–460, 1984, ISSN: 0022-0248. DOI: 10.1016/0022-0248(84)90355-5.
- [104] K. C. Mills and L. Courtney, "Thermophysical properties of silicon", *ISIJ International*, vol. 40, no. Suppl, pp. 130–138, 2000, ISSN: 0915-1559. DOI: 10.2355/isijinternational.40.suppl\_s130.
- [105] S. Kimura and K. Terashima, "A review of measurement of thermophysical properties of silicon melt", *Journal of Crystal Growth*, vol. 180, no. 3-4, pp. 323–333, 1997, ISSN: 0022-0248. DOI: 10.1016/S0022-0248(97)00263-7.

- [106] X. Huang, S. Togawa, S.-I. Chung, K. Terashima, and S. Kimura, "Surface tension of a si melt: influence of oxygen partial pressure", *Journal of Crystal Growth*, vol. 156, no. 1-2, pp. 52–58, Nov. 1995, ISSN: 0022-0248. DOI: 10.1016/0022-0248(95)00207-3.
- [107] S.-I. Chung, K. Izunome, A. Yokotani, and Shigeyukikimura, "Estimation of surface tension of molten silicon using a dynamic hanging drop", *Japanese Journal of Applied Physics*, vol. 34, no. Part 2, No. 5B, pp. L631–L634, 1995, ISSN: 0021-4922. DOI: 10.1143/jjap.34.l631.
- [108] M. Przyborowski, T. Hibiya, M. Eguchi, and I. Egry, "Surface tension measurement of molten silicon by the oscillating drop method using electromagnetic levitation", *Journal of Crystal Growth*, vol. 151, no. 1-2, pp. 60–65, 1995, ISSN: 0022-0248. DOI: 10.1016/0022-0248(95)00056-9.
- [109] N. Kawasaki, K. Watanabe, and Y. Nagasaka, "Measurement of the surface tension of molten silicon by the use of ripplon", *High Temperatures - High Pressures*, vol. 30, no. 1, pp. 91–96, 1998. DOI: 10.1068/htec203.
- [110] K. Mukai, Z. Yuan, K. Nogi, and T. Hibiya, "Effect of the oxygen partial pressure on the surface tension of molten silicon and its temperature coefficient", *Isij International*, vol. 40, no. Suppl, pp. 148–152, 2000, ISSN: 0915-1559.
- [111] Z. Zhou, S. Mukherjee, and W.-K. Rhim, "Measurement of thermophysical properties of molten silicon using an upgraded electrostatic levitator", *Journal of Crystal Growth*, vol. 257, no. 3-4, pp. 350–358, 2003, ISSN: 0022-0248. DOI: 10.1016/s0022-0248(03)01430-1.
- [112] S. V. Gupta, "Oscillating viscometers", in *Viscometry for Liquids*, Springer International Publishing, 2014, pp. 107–136. DOI: 10.1007/978-3-319-04858-1\_5.
- [113] Y. Sato, Y. Kameda, T. Nagasawa, T. Sakamoto, S. Moriguchi, T. Yamamura, and Y. Waseda, "Viscosity of molten silicon and the factors affecting measurement", *Journal of Crystal Growth*, vol. 249, no. 3-4, pp. 404–415, Mar. 2003, ISSN: 0022-0248. DOI: 10.1016/S0022-0248(02)02153-X.
- [114] K. Kakimoto, M. Eguchi, H. Watanabe, and T. Hibiya, "Natural and forced convection of molten silicon during czochralski single crystal growth", *Journal of Crystal Growth*, vol. 94, no. 2, pp. 412–420, 1989, ISSN: 0022-0248. DOI: 10.1016/0022-0248(89)90016-x.
- [115] H. Sasaki, E. Tokizaki, X. M. Huang, K. Terashima, and S. Kimura, "Temperature dependence of the viscosity of molten silicon measured by the oscillating cup method", *Japanese Journal of Applied Physics*, vol. 34, no. Part 1, No. 7A, pp. 3432–3436, 1995, ISSN: 0021-4922. DOI: 10.1143/jjap.34.3432.
- [116] A. W. Adamson and A. P. Gast, *Physical chemistry of surfaces*. Wiley, 1997, ISBN: 9780471148739.
- [117] P. Lambert, *Surface Tension in Microsystems*, ser. Microtechnology and MEMS. 2013, ISBN: 978-3-642-37551-4. DOI: 10.1007/978-3-642-37552-1.

- [118] J. V. Naidich, "The wettability of solids by liquid metals", in *Progress in Surface and Membrane Science*, D. A. Cadenhead and J. F. Danielli, Eds., ser. Progress in Surface and Membrane Science. Elsevier, 1981, vol. 14, pp. 353–484, ISBN: 9780125718141. DOI: 10.1016/b978-0-12-571814-1.50011-7.
- [119] N. Eustathopoulos, M. G. Nicholas, and B. Drevet, *Wettability at high temperatures*. Elsevier, 1999, vol. 3, ch. 3, ISBN: 0080543782.
- [120] A. Ciftja, T. A. Engh, and M. Tangstad, "Wetting properties of molten silicon with graphite materials", *Metallurgical and Materials Transactions A*, vol. 41, no. 12, pp. 3183–3195, 2010, ISSN: 1073-5623 1543-1940. DOI: 10.1007/s11661-010-0362-8.
- [121] S. Amore, E. Ricci, G. Borzone, and R. Novakovic, "Wetting behaviour of lead-free Sn-based alloys on Cu and Ni substrates", *Materials Science and Engineering: A*, vol. 495, no. 1-2, pp. 108–112, 2008, ISSN: 0921-5093. DOI: 10.1016/j.msea.2007.10.110.
- [122] P. G. De Gennes, "Wetting: statics and dynamics", *Reviews of Modern Physics*, vol. 57, no. 3, pp. 827–863, 1985, ISSN: 0034-6861. DOI: 10.1103/revmodphys.57.827.
- [123] V. H. López and A. R. Kennedy, "Flux-assisted wetting and spreading of al on TiC", *Journal of Colloid and Interface Science*, vol. 298, no. 1, pp. 356–362, Jun. 2006, ISSN: 0021-9797. DOI: 10.1016/j.jcis.2005.12.040.
- [124] D. R. Milner, "A survey of the scientific principles related to wetting and spreading", *British Welding Journal*, vol. 5, no. 3, pp. 90–105, 1958.
- [125] A. Shafiei, P. Abachi, K. Dehghani, and K. Pourazarang, "On the formation of inter-metallics during the furnace brazing of pure titanium to 304 stainless steel using ag (30–50%)–Cu filler metals", *Materials and Manufacturing Processes*, vol. 25, no. 11, pp. 1333–1340, Dec. 2010, ISSN: 1042-6914. DOI: 10.1080/10426914.2010.523911.
- [126] V. Bougiouri, R. Voytovych, O. Dezellus, and N. Eustathopoulos, "Wetting and reactivity in Ni–Si/C system: experiments versus model predictions", *Journal of Materials Science*, vol. 42, no. 6, pp. 2016–2023, 2007, ISSN: 0022-2461 1573-4803. DOI: 10.1007/s10853-006-1483-8.
- [127] O. Dezellus, R. Voytovych, A. P. H. Li, G. Constantin, F. Bosselet, and J. C. Viala, "Wettability of Ti<sub>3</sub>SiC<sub>2</sub> by Ag–Cu and Ag–Cu–Ti melts", *Journal of Materials Science*, vol. 45, no. 8, pp. 2080–2084, 2009, ISSN: 0022-2461 1573-4803. DOI: 10.1007/s10853-009-3941-6.
- [128] D. A. Krivoshein, I. A. Sobol', N. A. Maurakh, V. S. Dergunova, and Y. N. Petrov, "Wetting of carbon materials with eutectic alloy of the ZrB<sub>2</sub>–Si–C system", *Poroshkovaya Metallurgiya (Kiev)*, pp. 50–53, 2017, ISSN: 0032-4795.
- [129] G. W. Liu, M. L. Muolo, F. Valenza, and A. Passerone, "Survey on wetting of SiC by molten metals", *Ceramics International*, vol. 36, no. 4, pp. 1177–1188, 2010, ISSN: 0272-8842. DOI: 10.1016/j.ceramint.2010.01.001.



- [130] Y. V. Naidich, V. Zhuravlev, and N. Krasovskaya, "The wettability of silicon carbide by au-si alloys", *Materials Science and Engineering a-Structural Materials Properties Microstructure and Processing*, vol. 245, no. 2, pp. 293–299, 1998, ISSN: 0921-5093. DOI: 10.1016/S0921-5093(97)00718-1.
- [131] B. R. Bathey, G. F. Hurley, and H. E. Bates, "Observations of efg die material interactions with liquid silicon", *Journal of Materials Science*, vol. 15, no. 9, pp. 2192–2196, 1980. DOI: 10.1007/bf00552306.
- [132] O. Dezellus, S. Jacques, F. Hodaj, and N. Eustathopoulos, "Wetting and infiltration of carbon by liquid silicon", *Journal of Materials Science*, vol. 40, no. 9-10, pp. 2307–2311, 2005, ISSN: 0022-2461. DOI: DOI10.1007/s10853-005-1950-7.
- [133] R. Israel, R. Voytovych, P. Protsenko, B. Drevet, D. Camel, and N. Eustathopoulos, "Capillary interactions between molten silicon and porous graphite", *Journal of Materials Science*, vol. 45, no. 8, pp. 2210–2217, 2009, ISSN: 0022-2461 1573-4803. DOI: 10.1007/s10853-009-3889-6.
- [134] J. G. Li and H. Hausner, "Reactive wetting in the liquid-silicon/solid-carbon system", *Journal of the American Ceramic Society*, vol. 79, no. 4, pp. 873–880, 1996, ISSN: 0002-7820. DOI: 10.1111/j.1151-2916.1996.tb08519.x.
- [135] J.-G. Li and H. Hausner, "Wetting and infiltration of graphite materials by molten silicon", *Scripta Metallurgica et Materialia*, vol. 32, no. 3, pp. 377–382, 1995, ISSN: 0956-716X. DOI: 10.1016/S0956-716X(99)80068-5.
- [136] R. Voytovych, R. Israel, N. Calderon, F. Hodaj, and N. Eustathopoulos, "Reactivity between liquid Si or Si alloys and graphite", *Journal of the European Ceramic Society*, vol. 32, no. 14, pp. 3825–3835, 2012, ISSN: 0955-2219. DOI: 10.1016/j.jeurceramsoc.2012.05.020.
- [137] T. J. Whalen and A. T. Anderson, "Wetting of Sic, Si<sub>3</sub>N<sub>4</sub>, and carbon by Si and binary Si alloys", *Journal of the American Ceramic Society*, vol. 58, no. 9-10, pp. 396–399, 1975, ISSN: 0002-7820. DOI: 10.1111/j.1151-2916.1975.tb19006.x.
- [138] Z. Yuan, W. L. Huang, and K. Mukai, "Wettability and reactivity of molten silicon with various substrates", *Applied Physics a-Materials Science & Processing*, vol. 78, no. 4, pp. 617–622, 2004, ISSN: 0947-8396. DOI: 10.1007/s00339-002-2001-8.
- [139] H. Zhou and R. N. Singh, "Kinetics model for the growth of silicon carbide by the reaction of liquid silicon with carbon", *Journal of the American Ceramic Society*, vol. 78, no. 9, pp. 2456–2462, Sep. 1995, ISSN: 0002-7820. DOI: 10.1111/j.1151-2916.1995.tb08685.x.
- [140] B. Komolafe and M. Medraj, "Progress in wettability study of reactive systems", *Journal of Metallurgy*, vol. 2014, p. 14, 2014. DOI: 10.1155/2014/387046.
- [141] P. J. Hofbauer, E. Radlein, and F. Raether, "Fundamental mechanisms with reactive infiltration of silicon melt into carbon capillaries", *Advanced Engineering Materials*, vol. 21, no. 8, p. 1900184, 2019, ISSN: 1438-1656. DOI: 10.1002/adem.201900184.

- [142] J. A. Champion, B. J. Keene, and S. Allen, "Wetting of refractory materials by molten metallides", *Journal of Materials Science*, vol. 8, no. 3, pp. 423–426, 1973, ISSN: 0022-2461. DOI: 10.1007/Bf00550164.
- [143] J. G. Li and H. Hausner, "Wettability of silicon-carbide by gold, germanium and silicon", *Journal of Materials Science Letters*, vol. 10, no. 21, pp. 1275–1276, 1991, ISSN: 0261-8028. DOI: 10.1007/Bf00720944.
- [144] P. Nikolopoulos, S. Agathopoulos, G. N. Angelopoulos, A. Naoumidis, and H. Grubmeier, "Wettability and interfacial energies in SiC-liquid metal systems", *Journal of Materials Science*, vol. 27, no. 1, pp. 139–145, 1992, ISSN: 0022-2461. DOI: 10.1007/Bf02403656.
- [145] C. Rado, S. Kalogeropoulou, and N. Eustathopoulos, "Wetting and adhesion in metal-silicon carbide systems: the effect of surface polarity of SiC", *Scripta Materialia*, vol. 42, no. 2, pp. 203–208, 1999, ISSN: 1359-6462. DOI: 10.1016/S1359-6462(99)00325-5.
- [146] M. Syväjärvi, R. Yakimova, and E. Janzén, "Growth of SiC from the liquid phase: wetting and dissolution of SiC", *Diamond and Related Materials*, vol. 6, no. 10, pp. 1266–1268, 1997, ISSN: 0925-9635. DOI: 10.1016/S0925-9635(97)00081-2.
- [147] R. Warren and C. H. Andersson, "Silicon carbide fibres and their potential for use in composite materials. part ii", *Composites*, vol. 15, no. 2, pp. 101–111, 1984, ISSN: 0010-4361. DOI: 10.1016/0010-4361(84)90721-3.
- [148] V. L. Yupko, G. G. Gnesin, Y. P. Dyban, T. I. Kuz'mina, I. E. Polomoshnov, and Z. V. Sichkar, "The wetting of self-bonded polycrystalline silicon carbide by silicon", *Soviet Powder Metallurgy and Metal Ceramics*, vol. 16, no. 11, pp. 860–862, 1977, ISSN: 0038-5735 1573-9066. DOI: 10.1007/bf00797043.
- [149] R. Israel, G. De Combarieu, B. Drevet, D. Camel, N. Eustathopoulos, and O. Raymond, "Resistance to oxidation of graphite silicided by reactive infiltration", *Journal of the European Ceramic Society*, vol. 31, no. 12, pp. 2167–2174, Oct. 2011, ISSN: 0955-2219. DOI: 10.1016/j.jeurceramsoc.2011.05.005.
- [150] J. Roger, A. Marchais, and Y. Le Petitcorps, "Examination of the interaction between liquid silicon and bulk silicon carbide", *Journal of Crystal Growth*, vol. 426, pp. 1–8, 2015, ISSN: 0022-0248. DOI: 10.1016/j.jcrysgro.2015.05.013.
- [151] E. O. Einset, "Capillary infiltration rates into porous media with applications to Silcomp processing", *Journal of the American Ceramic Society*, vol. 79, no. 2, pp. 333–338, 1996, ISSN: 0002-7820 1551-2916. DOI: 10.1111/j.1151-2916.1996.tb08125.x.
- [152] F. A. L. Dullien, M. S. Elsayed, and V. K. Batra, "Rate of capillary rise in porous-media with nonuniform pores", *Journal of Colloid and Interface Science*, vol. 60, no. 3, pp. 497–506, 1977, ISSN: 0021-9797. DOI: 10.1016/0021-9797(77)90314-9.
- [153] E. O. Einset, "Analysis of reactive melt infiltration in the processing of ceramics and ceramic composites", *Chemical Engineering Science*, vol. 53, no. 5, pp. 1027–1039, 1998, ISSN: 0009-2509. DOI: 10.1016/S0009-2509(97)00379-5.

- [154] D. Sergi, A. Camarano, J. M. Molina, A. Ortona, and J. Narciso, "Surface growth for molten silicon infiltration into carbon millimeter-sized channels: lattice-boltzmann simulations, experiments and models", *International Journal of Modern Physics C*, vol. 27, no. 6, 2016, ISSN: 0129-1831. DOI: 10.1142/S0129183116500625.
- [155] N. Eustathopoulos, R. Israel, B. Drevet, and D. Camel, "Reactive infiltration by Si: infiltration versus wetting", *Scripta Materialia*, vol. 62, no. 12, pp. 966–971, 2010, ISSN: 1359-6462. DOI: 10.1016/j.scriptamat.2010.02.030.
- [156] H. M. Chen, F. Zheng, H. S. Liu, L. B. Liu, and Z. P. Jin, "Thermodynamic assessment of B-Zr and Si-Zr binary systems", *Journal of Alloys and Compounds*, vol. 468, no. 1-2, pp. 209–216, 2009, ISSN: 0925-8388. DOI: 10.1016/j.jallcom.2008.01.001.
- [157] C. Gueneau, C. Servant, I. Ansara, and N. Dupin, "Thermodynamic assessment of the Si-Zr system", *Calphad - Computer Coupling of Phase Diagrams and Thermochemistry*, vol. 18, no. 3, pp. 319–327, 1994, ISSN: 0364-5916. DOI: 10.1016/0364-5916(94)90036-1.
- [158] H. Okamoto, "The Si-Zr (Silicon-Zirconium) system", *Journal of Phase Equilibria*, vol. 11, no. 5, pp. 513–519, 1990, ISSN: 1054-9714. DOI: 10.1007/bf02898272.
- [159] M. E. Schlesinger, "Thermodynamics of solid transition-metal silicides", *Chemical Reviews*, vol. 90, no. 4, pp. 607–628, 1990, ISSN: 0009-2665. DOI: 10.1021/cr00102a003.
- [160] H. M. Chen, Y. Xiang, S. Wang, F. Zheng, L. B. Liu, and Z. P. Jin, "Thermodynamic assessment of the C–Si–Zr system", *Journal of Alloys and Compounds*, vol. 474, no. 1–2, pp. 76–80, 2009, ISSN: 0925-8388. DOI: 10.1016/j.jallcom.2008.06.086.
- [161] Y. Wang and A. H. Carim, "Ternary phase equilibria in the Zr-Si-C system", *Journal of the American Ceramic Society*, vol. 78, no. 3, pp. 662–666, 1995, ISSN: 1551-2916. DOI: 10.1111/j.1151-2916.1995.tb08229.x.
- [162] N. R. Calderon, M. Martinez-Escandell, J. Narciso, and F. Rodriguez-Reinoso, "The combined effect of porosity and reactivity of the carbon preforms on the properties of SiC produced by reactive infiltration with liquid si", *Carbon*, vol. 47, no. 9, pp. 2200–2210, 2009, ISSN: 0008-6223. DOI: 10.1016/j.carbon.2009.04.002.
- [163] T. Liensdorf, R. Schoch, M. Lang, N. Langhof, T. Hochrein, M. Bastian, and W. Krenkel, "Silicon infiltrated silicon carbide from extruded thermoplastic wood polymer composites", *International Journal of Applied Ceramic Technology*, vol. 17, no. 1, pp. 3–10, 2019, ISSN: 1546-542X 1744-7402. DOI: 10.1111/ijac.13404.
- [164] M. Striegler, B. Matthey, U. Mühle, A. Michaelis, and M. Herrmann, "Corrosion resistance of silicon-infiltrated silicon carbide (sisic)", *Ceramics International*, vol. 44, no. 9, pp. 10 111–10 118, 2018, ISSN: 0272-8842. DOI: 10.1016/j.ceramint.2018.02.229. [Online]. Available: <https://dx.doi.org/10.1016/j.ceramint.2018.02.229>.
- [165] L. Cornolti, S. Martinelli, G. Bianchi, and A. Ortona, "Microwave heating controlled reactive melt infiltration for graphite-Si-SiC ceramics manufacturing", *Journal of the American Ceramic Society*, 2018, ISSN: 1551-2916. DOI: 10.1111/jace.16124. [Online]. Available: <https://ceramics.onlinelibrary.wiley.com/doi/full/10.1111/jace.16124>.

- [166] J. Schindelin, I. Arganda-Carreras, E. Frise, V. Kaynig, M. Longair, T. Pietzsch, S. Preibisch, C. Rueden, S. Saalfeld, B. Schmid, J.-Y. Tinevez, D. J. White, V. Hartenstein, K. Eliceiri, P. Tomancak, and A. Cardona, "Fiji: an open-source platform for biological-image analysis", *Nature Methods*, vol. 9, no. 7, pp. 676–682, 2012, ISSN: 1548-7105. DOI: 10.1038/nmeth.2019. [Online]. Available: <https://doi.org/10.1038/nmeth.2019>.
- [167] M. Naikade, B. Fankhanel, L. Weber, A. Ortona, M. Stelter, and T. Graule, "Studying the wettability of Si and eutectic Si-Zr alloy on carbon and silicon carbide by sessile drop experiments", *Journal of the European Ceramic Society*, vol. 39, no. 4, pp. 735–742, 2019, ISSN: 0955-2219. DOI: 10.1016/j.jeurceramsoc.2018.11.049.
- [168] J. F. White, L. Ma, K. Forwald, and D. Sichen, "Reactions between silicon and graphite substrates at high temperature: in situ observations", *Metallurgical and Materials Transactions B*, vol. 45, no. 1, pp. 150–160, Sep. 2013, ISSN: 1073-5615. DOI: 10.1007/s11663-013-9947-0.
- [169] N. R. Calderon, R. Voytovych, J. Narciso, and N. Eustathopoulos, "Wetting dynamics versus interfacial reactivity of AlSi alloys on carbon", *Journal of Materials Science*, vol. 45, no. 8, pp. 2150–2156, 2009, ISSN: 0022-2461 1573-4803. DOI: 10.1007/s10853-009-3909-6.
- [170] H. Li, L. Zhang, L. Cheng, and Y. Wang, "Fabrication of 2d C/ZrC–SiC composite and its structural evolution under high-temperature treatment up to 1800°C", *Ceramics International*, vol. 35, no. 7, pp. 2831–2836, 2009, ISSN: 0272-8842. DOI: 10.1016/j.ceramint.2009.03.030.
- [171] H. Pi, S. Fan, and Y. Wang, "C/SiC–ZrB<sub>2</sub>–ZrC composites fabricated by reactive melt infiltration with ZrSi<sub>2</sub> alloy", *Ceramics International*, vol. 38, no. 8, pp. 6541–6548, 2012, ISSN: 0272-8842. DOI: 10.1016/j.ceramint.2012.05.035.
- [172] K. Landry, C. Rado, and N. Eustathopoulos, "Influence of interfacial reaction rates on the wetting driving force in metal/ceramic systems", *Metallurgical and Materials Transactions A*, vol. 27, no. 10, pp. 3181–3186, 1996, ISSN: 1073-5623 1543-1940. DOI: 10.1007/bf02663868.
- [173] K. Landry, C. Rado, R. Voitchovich, and N. Eustathopoulos, "Mechanisms of reactive wetting: the question of triple line configuration", *Acta Materialia*, vol. 45, no. 7, pp. 3079–3085, 1997, ISSN: 1359-6454. DOI: 10.1016/S1359-6454(96)00372-2.
- [174] P. J. Yunes Rubio, L. Hong, N. Saha-Chaudhury, R. Bush, and V. Sahajwalla, "Dynamic wetting of graphite and SiC by ferrosilicon alloys and silicon at 1550°C", *ISIJ International*, vol. 46, no. 11, pp. 1570–1576, 2006, ISSN: 0915-1559 1347-5460. DOI: 10.2355/isijinternational.46.1570.
- [175] A. I. Pommrich, A. Meyer, D. Holland-Moritz, and T. Unruh, "Nickel self-diffusion in silicon-rich Si-Ni melts", *Applied Physics Letters*, vol. 92, no. 24, p. 241 922, 2008, ISSN: 0003-6951. DOI: Artn24192210.1063/1.2947592. [Online]. Available: %3CGo%20to%20ISI%3E://WOS:000256934900046.

- [176] D. Giuranno, A. Polkowska, W. Polkowski, and R. Novakovic, "Wetting behavior and reactivity of liquid Si-10Zr alloy in contact with glassy carbon", *Journal of Alloys and Compounds*, vol. 822, p. 153 643, 2020, ISSN: 0925-8388. DOI: ARTN15364310.1016/j.jallcom.2020.153643.
- [177] J. Qin, X. Li, J. Wang, and S. Pan, "The self-diffusion coefficients of liquid binary M-Si (M=Al, Fe, Mg and Au) alloy systems by first principles molecular dynamics simulation", *AIP Advances*, vol. 9, no. 3, p. 035 328, 2019, ISSN: 2158-3226. DOI: 10.1063/1.5067295. [Online]. Available: <https://aip.scitation.org/doi/abs/10.1063/1.5067295>.
- [178] A. Ortona, D. Trimis, V. Uhlig, R. Eder, S. Gianella, P. Fino, G. D'Amico, E. Boulet, C. Chazelas, T. Grämer, E. Cresci, J. G. Wünnig, H. Altena, F. Beneke, and M. Debier, "SiSiC heat exchangers for recuperative gas burners with highly structured surface elements", *International Journal of Applied Ceramic Technology*, vol. 11, no. 5, pp. 927–937, 2013, ISSN: 1546-542x. DOI: 10.1111/ijac.12087.
- [179] Y. Zhang, S. Li, J. Han, and Y. Zhou, "Fabrication and characterization of random chopped fiber reinforced reaction bonded silicon carbide composite", *Ceramics International*, vol. 38, no. 2, pp. 1261–1266, 2012, ISSN: 0272-8842. DOI: 10.1016/j.ceramint.2011.08.058.
- [180] R. Pampuch, E. Walasek, and J. Bialoskórski, "Reaction mechanism in carbon-liquid silicon systems at elevated temperatures", *Ceramics International*, vol. 12, no. 2, pp. 99–106, 1986, ISSN: 0272-8842. DOI: 10.1016/0272-8842(86)90023-4.
- [181] B. L. Wing, F. Esmonde-White, and J. W. Halloran, "Microstress in reaction-bonded SiC from crystallization expansion of silicon", *Journal of the American Ceramic Society*, vol. 99, no. 11, V. Jayaram, Ed., pp. 3705–3711, 2016, ISSN: 0002-7820. DOI: 10.1111/jace.14398.
- [182] T. Tsunoura, K. Yoshida, T. Yano, T. Aoki, and T. Ogasawara, "Fabrication and bending behavior of amorphous SiC-fiber-reinforced Si-Co eutectic alloy composites at elevated temperatures", *Composites Part B: Engineering*, vol. 164, pp. 769–777, 2019, ISSN: 1359-8368. DOI: 10.1016/j.compositesb.2019.01.103.
- [183] T. TSUNOURA, Y. OKUBO, K. YOSHIDA, T. YANO, T. AOKI, and T. OGASAWARA, "Oxidation behavior of monolithic HfSi<sub>2</sub> and SiC fiber-reinforced composites fabricated by melt infiltration using Si-8.5 at% Hf alloy at 800-1200°C in dry air", *Journal of the Ceramic Society of Japan*, vol. 126, no. 1, pp. 27–33, 2018, ISSN: 1348-6535. DOI: 10.2109/jcersj2.17136.
- [184] J. Roger, L. Guesnet, A. Marchais, and Y. L. Petitcorps, "SiC/Si composites elaboration by capillary infiltration of molten silicon", *Journal of Alloys and Compounds*, vol. 747, pp. 484–494, 2018, ISSN: 0925-8388. DOI: 10.1016/j.jallcom.2018.03.024.
- [185] M. Bahraini, J. M. Molina, M. Kida, L. Weber, J. Narciso, and A. Mortensen, "Measuring and tailoring capillary forces during liquid metal infiltration", *Current Opinion in Solid State & Materials Science*, vol. 9, no. 4-5, pp. 196–201, 2005, ISSN: 1359-0286. DOI: 10.1016/j.cossms.2006.02.007.

- [186] Y. Yuan and T. R. Lee, "Contact angle and wetting properties", in *Surface Science Techniques*, G. Bracco and B. Holst, Eds., ser. Springer Series in Surface Sciences. Berlin, Heidelberg: Springer Berlin Heidelberg, 2013, ch. Chapter 1, pp. 3–34, ISBN: 9783642342424. DOI: 10.1007/978-3-642-34243-1\_1.
- [187] R. Deike and K. Schwerdtfeger, "Reactions between liquid silicon and different refractory materials", *Journal of The Electrochemical Society*, vol. 142, no. 2, 1995, ISSN: 00134651. DOI: 10.1149/1.2044109.
- [188] F. H. Gern and R. Kochendorfer, "Liquid silicon infiltration: description of infiltration dynamics and silicon carbide formation", *Composites Part a-Applied Science and Manufacturing*, vol. 28, no. 4, pp. 355–364, 1997, ISSN: 1359-835x. DOI: 10.1016/S1359-835x(96)00135-2.
- [189] M. H. Hon, R. F. Davis, and D. E. Newbury, "Self-diffusion of 30Si in polycrystalline  $\beta$ -SiC", *Journal of Materials Science*, vol. 15, no. 8, pp. 2073–2080, 1980, ISSN: 1573-4803. DOI: 10.1007/bf00550634.
- [190] H. Giesche, "Mercury porosimetry: a general (practical) overview", *Particle & Particle Systems Characterization*, vol. 23, no. 1, pp. 9–19, 2006, ISSN: 0934-0866. DOI: 10.1002/ppsc.200601009.
- [191] J. M. Molina, R. Arpon, R. A. Saravanan, C. Garcia-Cordovilla, E. Louis, and J. Narciso, "Threshold pressure for infiltration and particle specific surface area of particle compacts with bimodal size distributions", *Scripta Materialia*, vol. 51, no. 6, pp. 623–627, 2004, ISSN: 1359-6462. DOI: 10.1016/j.scriptamat.2004.05.009. [Online]. Available: %3CGo%20to%20ISI%3E://WOS:000222703200028.

This page is intentionally left blank.

# Manoj Naikade

25 Juli 1989

Heugatterstrasse 35, 8600 Dübendorf

manojknaikade@gmail.com

+41 79 637 63 48

Indian

www.manojnaikade.com

manoj-naikade-08a24157

manojknaikade

Single

Work permit B

A, B

Fluent :German; Business fluent: English, Hindi; Mother tongue: Marathi



## Professional career

Mai 2016 - Dec 2020

PhD Student

High Performance Ceramic Lab, Empa, Switzerland

Study and characterization of silicon-metal alloy systems for the reactive infiltration process of ceramic matrix composites

October 2013– August 2014

Intern

Max-Planck-Institut für Eisenforschung GmbH, Düsseldorf, Germany

- Development of testing method for characterization of mechanical properties of Aerogel
- Investigation of the mechanical properties of resorcinol formaldehyde aerogels using digital image correlation

August 2010 – August 2012

Executive Engineer (Quality Assurance)

Larson & Tubro Komatsu Pvt. Ltd., Bangalore, India

- Raw material testing as per ASTM, DIN, EN, ISO or JIS standards
- Failure analysis of components at work site
- Statistical analysis of failure data analysis to identify area of improvements
- Supporting design team in improvement and selection of material and manufacturing process
- Casting and welding quality analysis
- Internal quality audits
- New supplier development and supplier quality audits for foundry, heat treatment, surface treatment, welding and machining shop

January 2010 – June 2010

Intern

Volkswagen India Pvt. Ltd., Pune, India

- Cyclic corrosion behaviour of suspension parts
- Study of high strength automotive steel qualification

June 2008 – December 2008

Intern

Speciality Sintered products Pvt. Ltd., Pune, India

- Atmosphere optimization for sintering furnace
- Cost reduction in zinc plating of sintered components
- Valve Seat manufacturing by powder metallurgy route



## Education

2012 – 2015

Master of Science in Metallurgical Engineering  
RWTH Aachen, Germany

Note : 1.8

Thesis: Testing of a new software tool for the determination of the amount of recrystallized and recovered volume fraction and its application to different annealed aluminium alloys

2006 – 2010

Bachelor of Technology in Metallurgy Engineering

Note: 7.92 /10

College of Engineering, Pune, India



## Workshops and trainings

2019: Technical and professional development workshop, ACerS, Florida, USA

2018: TOPSTARS innovaTion challenge, Trento, Italy

2017: Failure analysis of materials, ETH, Zürich

2016: Surface tension and wetting, ULB, Belgium

2011:Fracture mechanics, IISC, Bangalore, Indien



## Material characterisation techniques

Metallography, optical microscopy, SEM, TEM, EDX, XRD, EBSD, tensile and compression testing, digital image correlation, X-ray tomography, mercury porosimetry, ultrasonic testing



## Software

MS-Office, Origin, MS project, SAP ●●●●●●

Auto-CAD, Pro-E, CATIA, Autodesk Inventor, Fusion 360 ●●●●○○

ARAMIS, TSL-OIM, Image-Access ●●●●●●

Adobe Photoshop, Illustrator, InDesign, Blender ●●●●●●

MATLAB, python, C/C++ ●●●●○○

HTML, Arduino, Java ●●●●○○



## Publications

M. Naikade, B. Fankhanel, L. Weber, A. Ortona, M. Stelter, T. Graule, Studying the wettability of Si and eutectic Si-Zr alloy on carbon and silicon carbide by sessile drop experiments, Journal of the European Ceramic Society 39(4) (2019) 735-742.

M. Schwan, M. Naikade, D. Raabe, L. Ratke, From hard to rubber-like: mechanical properties of resorcinol-formaldehyde aerogels, Journal of Materials Science (2015) 1-12.



## Awards and grants

2019: Winter workshop grant, Euro. Ceramic Society

2019: Research Travel grant, American Ceramic Society

2018: TOP STARS Innovation challenge, Trento, Italien

2017: Mobility support grant, European Ceramic Society



## Hobbies and others

Sketching, Painting, Photography, Badminton

Guinness book of World record for "Longest painting by numbers", 599.94 m, with 135 students of college of engineering Pune, on 08 March 2008